

HARVARD UNIVERSITY  
Graduate School of Arts and Sciences



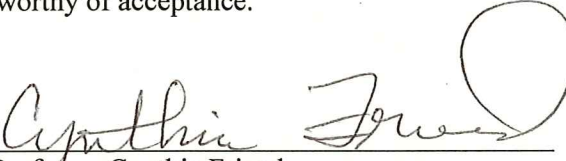
DISSERTATION ACCEPTANCE CERTIFICATE

The undersigned, appointed by the  
Department of Chemistry & Chemical Biology  
have examined a dissertation entitled:

Correlation of Catalytic Activity to Material Structure and Surface Composition for  
Sustainable Catalysis

presented by : Nare Janvelyan

candidate for the degree of Doctor of Philosophy and hereby  
certify that it is worthy of acceptance.

Signature   
Typed name: Professor Cynthia Friend

Signature   
Typed name: Professor Efthimios Kaxiras

Signature   
Typed name: Professor Michael Aziz

Date: 1 May 2018





# Correlation of Catalytic Activity to Material Structure and Surface Composition for Sustainable Catalysis

A dissertation presented

by

Nare Janvelyan

to

The Department of Chemistry and Chemical Biology

in partial fulfillment of the requirements

for the degree of

Doctor of Philosophy

in the subject of

Chemical Physics

Harvard University

Cambridge, Massachusetts

May 2018

©2018 – Nare Janvelyan

All rights reserved.

Dissertation Advisor

Author

**Cynthia M. Friend**

**Nare Janvelyan**

# Correlation of Catalytic Activity to Material Structure and Surface Composition for Sustainable Catalysis

## Abstract

This thesis investigates the relation between the catalytic activity and catalyst material to develop a predictive framework for the rational design of catalytic systems. More specifically, catalyst morphology, surface structure, and surface composition are probed to understand their impact on catalyst activity and selectivity for sustainable catalysis applications. We begin with an introduction of sustainable catalysis, with an emphasis on the use of copper catalysts and alloy materials (Chapter 1). The details of the methods used in this thesis are then presented (Chapter 2). Next, the role of defects and step edge sites in elementary reaction steps is studied for methanol oxidation on titania (Chapter 3) and ethanol dehydrogenation on copper (Chapter 4). The study of ethanol dehydrogenation reaction is further expanded to understand the effect of alloying nickel with copper materials on the catalyst activity and selectivity (Chapter 5). A thorough investigation is undertaken to understand surface compositional (Chapter 6) and structural (Chapter 7) changes induced by different gas exposures of a nanoporous nickel-copper catalyst. The changes in surface composition and structure using in situ techniques are correlated to changes in catalytic activity and stability (Chapters 6 – 7). The use of reactive gases to alter

catalytic materials is further investigated on a bulk silver-gold alloy as a model for nanoporous gold catalysts (Chapter 8).

# Contents

Title page	i
Abstract	iii
Table of Contents	v
Citations to Published Work	xi
Acknowledgements	xii
<b>1 Introduction – Sustainable Catalysis</b>	<b>1</b>
1.1 Abstract	1
1.2 Motivation: Sustainable Production of Valuable Chemicals	1
1.2.1 Acetaldehyde: Current Production	3
1.2.2 Ethanol Dehydrogenation as an Alternative	5
1.2.3 The Plague: Deactivation	7
1.3 Cu-based Catalysts for Alcohol Dehydrogenation Reactions	8
1.3.1 Role of Step Edge Sites in Cu	8
1.3.2 Supported Cu Catalysts	10
1.3.3 Promoters and Alloys	11
1.4 Alloy Catalysts	12
1.4.1 Bulk Alloys	12
1.4.2 Dilute Metal Alloys	13
1.4.3 Ni-Cu Catalysts for Ethanol Dehydrogenation	15
1.4.4 Manipulation of Active Structures	16
1.5 Specific Aims of Thesis	18

1.6 References	19
<b>2 Methods</b>	<b>28</b>
2.1 Abstract	28
2.2 Catalyst Pretreatments	28
2.2.1 H <sub>2</sub> and O <sub>2</sub> Pretreatments of Cu-based Catalysts	28
2.2.2 Pretreatments of Bulk Ag-Au Alloys	29
2.3 Catalytic Activity Tests	29
2.3.1 Steady-State Ethanol Dehydrogenation Reaction Tests	29
2.3.2 Activation Energy Measurements	32
2.3.3 Temperature-Programmed Ethanol Dehydrogenation Reaction Tests	32
2.4 Catalyst Characterization	33
2.4.1 X-ray Photoelectron Spectroscopy	33
2.4.2 Ambient-Pressure X-ray Photoelectron Spectroscopy (AP-XPS)	34
2.4.3 AP-XPS Spectral Analysis	35
2.4.4 Near-Edge X-ray Absorption Fine Structure (NEXAFS)	36
2.4.5 Raman Spectroscopy	36
2.4.6 Electron Microscopy – SEM and TEM	37
2.4.7 Environmental Transmission Electron Microscopy (E-TEM)	39
2.4.8 TEM Imaging of Twinned Pd Nanostructures	39
2.4.9 TEM Imaging of AuPt Nanostructures	41
2.5 References	52

<b>3 Methanol Photo-Oxidation on Rutile TiO<sub>2</sub> Nanowires: Probing Reaction Pathways</b>	
<b>on Complex Materials</b>	<b>53</b>
3.1 Abstract	53
3.2 Introduction	54
3.3 Methods	58
3.4 Results and Discussion	60
3.4.1 Nanowire Characterization	60
3.4.2 Oxygen Adsorption and Photodesorption	62
3.4.3 Methanol Thermal and Photocatalysis on TiO <sub>2</sub> Nanowires	64
3.5 Conclusions	77
3.6 Supporting Information	78
3.6.1 Characterization	78
3.6.2 Reactivity	81
3.7 References	84
<b>4 Multiscale Morphology of Nanoporous Copper Made from Intermetallic Phases</b>	<b>88</b>
4.1 Abstract	88
4.2 Introduction	89
4.3 Methods	92
4.4 Results and Discussion	95
4.5 Conclusions	108
4.6 Supporting Information	109
4.6.1 Standard Potentials	109

4.6.2 Crystallographic parameters for Rietveld refinement and the EBSD study	110
4.6.3 Ligament size distribution/ Histograms	113
4.6.4 Structural and compositional changes during dealloying of Zn <sub>50</sub> Cu <sub>50</sub>	115
4.6.5 Ethanol dehydrogenation	116
4.6.6 Cu/Zn ratios	117
4.6.7 Electron backscatter diffraction	118
4.6.8 Effects of sample geometry and concentration of etching solution	119
4.6.9 Conversion of samples compared to equilibrium conversion	120
4.7 References	120
<b>5 Selective Non-Oxidative Dehydrogenation of Ethanol to Acetaldehyde and Hydrogen on Highly Dilute NiCu Alloys</b>	<b>123</b>
5.1 Abstract	123
5.2 Introduction	124
5.3 Methods	128
5.3.1 Catalyst Preparation	128
5.3.2 Characterization Techniques	131
5.4 Results and Discussion	134
5.5 Conclusions	154
5.6 References	155
<b>6 Surface Compositional Evolution of Nanoporous NiCu</b>	<b>160</b>
6.1 Abstract	160
6.2 Introduction	161



6.3 Methods	164
6.3.1 Catalyst Preparation	164
6.3.2 Catalytic Activity	165
6.3.3 Ex situ Characterization Techniques	166
6.3.4 Environmental Transmission Electron Microscopy (E-TEM)	167
6.3.5 Ambient-pressure XPS (AP-XPS)	167
6.3.6 AP-XPS Spectral Analysis	169
6.3.7 Near-Edge X-ray Absorption Fine Structure (NEXAFS)	170
6.3.8 Density Functional Theory (DFT)	170
6.4 Results and Discussion	171
6.4.1 Reactivity of npCu for Ethanol Dehydrogenation Reaction	171
6.4.2 Reactivity of npNiCu for Ethanol Dehydrogenation Reaction	173
6.4.3 Compositional and Chemical State Changes of the npNiCu Surface	176
6.4.4 Long-term Compositional and Chemical State Changes	201
6.4.5 Characterization of Carbon Species	206
6.4.6 Ni Oxidation State and Deactivation	210
6.5 Conclusions	213
6.6 Supporting Information	215
6.7 References	223
<b>7 Structural Evolution of Nanoporous NiCu</b>	<b>234</b>
7.1 Introduction	234
7.2 Methods	235

7.2.1 Ex situ Characterization Techniques	235
7.2.2 Environmental Transmission Electron Microscopy (E-TEM)	236
7.2.3 Surface Area Approximation	236
7.3 Results and Discussion	237
7.3.1 Characterization of npCu	237
7.3.2 Characterization of H <sub>2</sub> -treated npNiCu	242
7.3.3 Characterization of O <sub>2</sub> -treated npNiCu	250
7.3.4 Reduction-Oxidation Behavior of npNiCu	256
7.4 Conclusions	261
7.5 Supporting Information	262
7.6 References	269
<b>8 Macroscopic 3D Nanoporosity Formation by Dry Oxidation of AgAu Alloys</b>	<b>271</b>
8.1 Abstract	271
8.2 Introduction	272
8.3 Methods	275
8.3.1 Physicochemical Treatments	275
8.3.2 FIB-SEM Studies and Analysis	276
8.3.3 Density Functional Theory and Kinetic Monte Carlo	276
8.4 Results and Discussion	278
8.5 Conclusions	292
8.6 Supporting Information	293
8.7 References	297

## Citations to Published Work

Parts of this dissertation cover research reported in the following articles:

*Methanol Photo-Oxidation on Rutile TiO<sub>2</sub> Nanowires: Probing Reaction Pathways on Complex Materials*

Crampton, A. S.; Cai, L.; [Janvelyan, N.](#); Zheng, X.; Friend, C. M.

*The Journal of Physical Chemistry C* **2017**, *121*, 9910-9919. (Chapter 3)

*Multiscale Morphology of Nanoporous Copper Made from Intermetallic Phases*

Egle, T.; Barroo, C.; [Janvelyan, N.](#); Baumgaertel, A. C.; Akey, A. J.; Biener, M. M.; Friend, C. M.; Bell, D. C.; Biener, J.

*ACS Applied Materials and Interfaces* **2017**, *9*, 25615-25622. (Chapter 4)

*Selective Non-Oxidative Dehydrogenation of Ethanol to Acetaldehyde and Hydrogen on Highly Diluted NiCu Alloys*

Shan, J.\*; [Janvelyan, N.\\*](#); Li, H.; Liu, J.; Egle, T.; Ye, J.; Biener, M. M.; Biener, J.; Friend, C. M.; Flytzani-Stephanopoulos, M.

*Applied Catalysis B: Environmental*, **2017**, *205*, 541-550. (Chapter 5)

*Surface Compositional Evolution of Nanoporous NiCu*

[Janvelyan, N.](#); Wu, C. H.; van Spronsen, M. A.; Montemore, M. M.; Shan, J.; Qi, Z.; Xu, F.;

Zakharov, D. N.; Stach, E. A.; Biener, J.; Kaxiras, E.; Flytzani-Stephanopoulos, M.; Friend, C. M.

*Under preparation* (Chapter 6)

*Structural Evolution of Nanoporous NiCu*

[Janvelyan, N.](#); Stevanovic, A.; Qi, Z.; Zakharov, D. N.; Stach, E. A.; Biener, J.; Friend, C. M.

*Under preparation* (Chapter 7)

*Macroscopic 3D Nanoporosity Formation by Dry Oxidation of AgAu Alloys*

Barroo, C.; Montemore, M. M.; [Janvelyan, N.](#); Zugic, B.; Akey, A. J.; Magyar, A. P.; Ye, J.;

Kaxiras, E.; Biener, J.; Bell, D. C.

*The Journal of Physical Chemistry C* **2017**, *121*, 5115-5122. (Chapter 8)

# Acknowledgements

I owe my deepest gratitude to my advisor, Cynthia Friend, for her endless support and guidance in my development as an independent scientist. Her dedication to science, mentorship, and teaching has been truly inspiring. I would also like to thank Robert Madix, who like a second advisor to me. I thank you both for your invaluable insights and thought-provoking discussions. It has been an honor to work under your mentorship.

Thank you to my committee, Professors Tim Kaxiras and Mike Aziz, for your valuable feedback and support in my annual meetings, qualifying exam, and defense, and for all the time you have spent evaluating my progress and thesis.

I am indebted to my collaborators for their teamwork and dedication towards doing great science with me: Dr. Junjun Shan and Professor Maria Flytzani-Stephanopoulos for their support in catalytic experiments; Dr. Cedric Barroo, Dr. Zhen Qi, Dr. Jianchao Ye, Mr. Tobias Egle, and Dr. Juergen Biener for their efforts in materials preparation; Dr. Matt Montemore for his endless support with theoretical work and insightful discussions; Dr. Cheng Hao Wu for his contribution and support in the ambient pressure XPS data analysis and publication development; Dr. Dmitri N. Zakharov for his help in doing environmental TEM and Professor Eric A. Stach for his invaluable insight and encouragement in helping me wrap up what felt like an impossible Ph.D project.

Thank you to all my lab members who have made the Friend Lab such a joy to walk into every day. It has been a pleasure Mr. Chris O'Conner, Ms. Amanda Filie, Mr. Tobias Egle, Dr. Andrew Crampton, Dr. Ana Stevanovic, Dr. Christian Reece, Dr. Fang Xu, Ms. Eri Muramoto, Dr. Judith Lattimer, Dr. Mathilde Luneau, Dr. Matthijs A. van Spronsen, Dr.

Yunfei Xu, Ms. Leah DeFrancesco, and other group members over the years for the enjoyable and cooperative atmosphere.

I would also like to thank Professor Michelle L. Personick and Dr. Branko Zucig for their mentorship and friendship since I joined the lab. I am forever grateful to all the help the CNS staff members have provided me: Mr. Adam Graham, Professor David C. Bell, Mr. Tim Cavanaugh, Dr. Arthur McClelland, Dr. Greg Lin, Ms. Carolyn Marks, and especially Dr. Jules Gardner. I would not have learned TEM without her guidance and constant support.

I am indebted to Susan Zawalich, Jeff Shenette, and Professor Jim Hogle for bringing me into the Dudley House community as a Dudley Fellow for three years. Thank you all for giving me the opportunity to pour my energy into this non-academic and rewarding avenue, the encouragement and support in all aspects of grad life, and the community you built for all graduate students. Being a Dudley Fellow has been one of my most cherished experiences at Harvard and led me to meet some of my closest friends making Harvard and Cambridge truly feel like home.

I feel grateful for the unconditional love, support, and encouragement my parents and sister have given me throughout the years. I would not have completed this journey without their support. I would also like to thank all my friends for their constant companionship, encouragement, intellectual engagement, and laughter. You have all expanded my horizons and made me a better person and I thank Harvard for bringing us together.

My research was supported as part of the Integrated Mesoscale Architectures for Sustainable Catalysis (IMASC), an Energy Frontier Research Center funded by the U.S. Department of Energy, Office of Science, Office of Basic Energy Sciences under Award

Number DE-SC0012573. I also appreciate the financial support from the Harvard University Center for the Environment and Duff Family Endowed Graduate Support Award.

# Chapter 1.

## Introduction - Sustainable Catalysis

### **1.1 Abstract**

To meet the rising global demand for energy, it is crucial to reduce the energy footprint of the chemical production industry. The development of more energy-efficient catalysts and catalytic processes is imperative to reaching this goal. The production of acetaldehyde, an important industrial chemical, is one such process that can be made more sustainable with the use of an alternative production process, ethanol dehydrogenation reaction. With the development of a robust catalyst, ethanol dehydrogenation can be used to produce acetaldehyde alongside hydrogen, a clean fuel. Copper-based catalysts provide a strong starting point towards this endeavor given their inherent high selectivity for dehydrogenation reactions. This report explores alloying as a strategy for improving the catalytic reactivity and stability of copper-based catalysts for the ethanol dehydrogenation reaction.

### **1.2 Motivation: Sustainable Production of Valuable Chemicals**

Global energy use is growing lightning fast. Total world consumption of energy is projected to increase from 549 quadrillion Btu in 2012 to 815 quadrillion Btu in 2040, a 48% increase<sup>1</sup>. The industrial sector is the largest consumer of delivered energy, consuming ~54% of the world's total delivered energy, in addition to being a heavy

## *Chapter 1. Introduction - Sustainable Catalysis*

emitter of carbon dioxide, which contributes to global warming<sup>1</sup>. Within the industrial sector, the basic chemicals industry, including bulk chemical manufacturing, accounted for 19% of total delivered energy consumption in 2012, making the basic chemicals industry the largest consumer of delivered energy<sup>1</sup>. Given that the chemical industry is such a large energy consumer, it is crucial that more energy efficient production processes are developed to minimize its energy footprint and help mitigate climate change.

In the chemical production industry, approximately 90% of all commercially produced chemicals utilize catalysts at some step in the process<sup>2</sup>. In chemistry, a catalyst is a material that increases the rate of a reaction, allowing certain reactions to take place that would otherwise not occur in the same conditions. Ammonia synthesis, one of society's greatest innovations, is an example of such a reaction. Developed by Haber and Bosch, the process takes atmospheric nitrogen and hydrogen and produces ammonia, a fertilizer, over an iron-based catalyst at elevated temperatures and pressures. The process has been dubbed the "detonator of the population explosion" as it has exponentially expanded society's ability to grow food<sup>3</sup>. If it wasn't for the development of this iron-based catalyst, much of society would not be here today.

Inspired by the impact of the Haber-Bosch process, this thesis primarily investigates the development of new catalysts for the production of acetaldehyde with the goal of making the production process more energy-efficient and environmentally sustainable. Current production methods of acetaldehyde utilize two main reactions that consume large quantities of energy. An alternative route to acetaldehyde



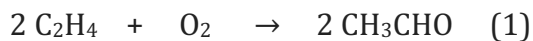
production is a reaction called ethanol dehydrogenation, an advantageous reaction that produces hydrogen in conjunction with the acetaldehyde. Although ethanol dehydrogenation is an environmentally friendlier pathway than the other two reaction methods, it is not currently viable in the chemical industry as a suitable catalyst is yet to be developed. Methanol oxidation to methyl formate and formaldehyde is also briefly studied in this thesis.

Specifically, this work examines the use of unsupported copper and nickel-copper (Ni-Cu) alloy materials for ethanol dehydrogenation reaction in addition to titania (TiO<sub>2</sub>) nanowires and silver-gold (AgAu) alloys for methanol oxidation.

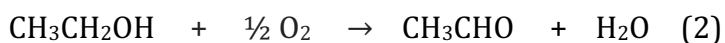
### **1.2.1 Acetaldehyde: Current Production**

Acetaldehyde is an important chemical in the global industry, which is widely found in nature and produced on the industrial scale. In 2003, 1 million tonnes of acetaldehyde were produced globally<sup>4</sup>. Acetaldehyde is a platform chemical, because it is used as a starting material for the production of other high value chemicals. It is used as a starting material for acetic acid, acetate esters, pentaerythritol, pyridine, and other pyridine based compounds<sup>4-5</sup> among many others. These molecules are high value chemicals used to produce polymers, explosives, resins, plastics, cosmetics, and many other chemicals for commercial applications.

Currently, acetaldehyde is mainly produced via the Wacker process using a homogenous palladium-copper chloride catalyst in the oxidation of ethylene (Reaction 1). Smaller quantities are manufactured by the partial oxidation of ethanol over silver catalysts at 500 – 650 °C (Reaction 2)<sup>4-5</sup>.



ethylene      oxygen      acetaldehyde



ethanol      oxygen      acetaldehyde      water

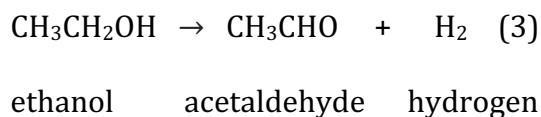
Although the Wacker process produces high yields of acetaldehyde, it has several disadvantages. First, it uses a corrosive catalyst which rusts the steel reactors and tubing used in the chemical industry. To prevent corrosion, reactors are lined with a ceramic material and titanium tubing is used instead of stainless steel, which is more expensive. Second, the process is conducted above atmospheric pressure, which requires more energy. Similarly, the partial oxidation of ethanol (Reaction 2) requires high temperatures for the reaction to occur.

Lastly and most significantly, the Wacker process is conducted in the liquid phase with water which requires several separation steps to purify the acetaldehyde from unwanted by-products and water. In the partial oxidation of ethanol (Reaction 2), water is produced as a by-product and thus, also needs to be separated. For both processes, a separation method called distillation is used, which is inefficient and consumes a considerable amount of energy. Specifically, chemical separation processes, including distillation, account for 10-15% of the world's energy consumption<sup>6</sup>. In the United States, separation processes account for ~50% of the energy used by the industrial sector, of which the distillation methods consume 49%

of energy<sup>6</sup>. Consequently, by reducing the number of separation steps in a procedure or by using a lower temperatures/pressures, the amount of energy consumed by a process is reduced. Ethanol dehydrogenation provides this opportunity for acetaldehyde production.

### **1.2.2 Ethanol Dehydrogenation as an Alternative**

Ethanol dehydrogenation is a potential alternative to the current methods of acetaldehyde production that is more energy-efficient and environmentally sustainable. The reaction proceeds at relatively low temperatures of 260-290 °C in atmospheric pressure on copper (Cu) catalysts (Reaction 3)<sup>4</sup>, thus using less energy than the current methods. Since acetaldehyde can be condensed into a liquid, it can be easily separated from the hydrogen gas.



A great benefit of the ethanol dehydrogenation reaction is the production of hydrogen as a co-product with the acetaldehyde. Hydrogen is advantageous as a fuel over other common fuels such as gasoline and natural gas because it has a high energy content by weight. The energy density of gasoline and natural gas are ~45-50 MJ/kg, while hydrogen's energy density is a steeping ~125 MJ/kg in comparison. Furthermore, hydrogen is considered a zero-emission fuel since it only produces water – a benign by-product – when burned with oxygen for energy. When employed

## *Chapter 1. Introduction - Sustainable Catalysis*

in an electrochemical cell coupled with an electric motor, it is two to three times more efficient than an internal combustion engine running on gasoline<sup>7</sup>. In addition, fuel cells operate at lower temperatures and are more compact in size compared to internal combustion engines. Because of these benefits, demand for hydrogen is increasing globally and extends into the consumer market through the development of hydrogen-powered vehicles. In this regard, the ethanol dehydrogenation reaction could prove a critical means of meeting demand due to its hydrogen gas co-product, while still producing the highly useful acetaldehyde.

With the use of ethanol derived from biomass (bioethanol or biofuel), the ethanol dehydrogenation process has the potential to be a completely renewable process as biomass is a renewable resource. With recent advances in chemical and biological processing technologies, the fermentation process to producing bioethanol is becoming more efficient and the ultimate goal of reaching a 'zero waste' biofuel production process is becoming ever more promising<sup>8-9</sup>. In just about 10 years, from 2007 to 2016, global bioethanol production has doubled from 13.12 billion gallons to 26.58 billion gallons with production still increasing<sup>10</sup>.

Biofuels seem incredibly attractive, because crops sequester carbon dioxide from the atmosphere as they grow. However, studies have shown that converting land for biofuel production releases more carbon dioxide than is saved by using biofuels instead of fossil fuels<sup>11-12</sup>. To truly reduce greenhouse gas emissions, biofuels should be produced from biomass waste or from biomass grown on abandoned agricultural lands<sup>12-13</sup>. Thus, the use of sustainably sourced and produced bioethanol,

would not only lead to a renewable ethanol dehydrogenation reaction, but it would also help mitigate global climate change.

As these examples demonstrate, ethanol dehydrogenation stands as an advantageous and sustainable industrial process. Ethanol from biomass provides an environmentally friendly resource. Acetaldehyde is produced and used as a starting material for other important chemicals and hydrogen is produced as a clean fuel with rising demand. In addition, the reaction takes place at relatively low temperatures and can be highly selective towards the acetaldehyde product with certain catalysts such as copper, which is also relatively inexpensive. While the benefits are unquestionable, the next sections will discuss the issues that prevent this reaction from being realized on the industrial scale and the research being conducted to develop new and improved catalysts for the reaction.

### **1.2.3 The Plague: Deactivation**

Although ethanol dehydrogenation is an attractive process, it is not currently economically viable due to the lack of a robust catalyst that meets all the criteria for industrial scale production. In chemical production, high selectivity is preferred over high activity as it reduces the number of separations required. Of course, a catalyst with high selectivity and high activity is ideal. Another criterion for industrial processes is long-term stability. Catalysts need to have stable activity for weeks, if not months, to be viable for industrial applications. The iron-based catalyst used for ammonia synthesis, for example, is used for 10 years or more<sup>14</sup>. In industry, it is better for a catalyst to have a lower activity and be stable for a long period of time than for

it to have higher activity and deactivate over time. Thus, the three main criteria for a viable catalyst in the industry are: high activity, selectivity, and stability.

With the development of a stable and highly active catalyst, ethanol dehydrogenation could become an efficient and sustainable source of hydrogen and acetaldehyde. Cu-based catalysts have been widely studied for ethanol and other alcohol dehydrogenation reactions<sup>15-46</sup>. Cu is highly selective for dehydrogenating the alcohol to its respective aldehyde, unlike more reactive metals which cleave the carbon-carbon bonds leading to decomposition of the reactants, an unwanted outcome. This quality of high selectivity has posed Cu to be an excellent catalyst for dehydrogenation reactions. Unfortunately, though, Cu catalysts were found to deactivate in ethanol and other alcohol dehydrogenation reactions.

Due to this issue of deactivation, copper-based catalysts have not been feasible on the industrial scale for the ethanol dehydrogenation reaction. This work aims to improve the stability and reactivity of Cu-based materials for the ethanol dehydrogenation reaction with the development of new, unsupported nanoporous copper and copper-nickel materials (Chapters 4 - 7).

## **1.3 Cu-based Catalysts for Alcohol Dehydrogenation Reactions**

### **1.3.1 Role of Step Edge Sites in Cu**

Copper was first demonstrated to be highly selective for dehydrogenating the C-O bond without cleaving the C-C bond in single crystal studies using methanol and ethanol, though they generally demonstrated low conversions to the respective aldehydes<sup>15-18</sup>. Supported copper catalysts have demonstrated modest activity for the

direct conversion of alcohols to the corresponding aldehydes. However, single crystal studies have shown much less activity. Further investigations on Cu single crystals have led to an understanding of this discrepancy.

Investigation of methanol on Cu (210) has demonstrated that methoxy formation is more facile on step edges than on terraces<sup>19</sup>. More recently, non-oxidative methanol and ethanol dehydrogenation was shown to occur at step and kink sites on Cu (111) and Cu (110) single crystals using scanning tunneling microscopy (STM) to locate the sites. In addition, the study also demonstrated that the activity of the single crystal could be increased by increasing the density of surface defects using thermal annealing and argon ion sputtering<sup>20</sup>. These studies have provided an explanation for the low conversions previously observed on Cu single crystals. Similarly, the contribution of step sites for non-oxidative ethanol dehydrogenation on Au nanoparticle catalysts has also been previously noted<sup>47</sup>. These studies demonstrate the efficacy of surface defects for catalyzing reactions and suggest that highly defective metal catalysts may be more active for dry ethanol dehydrogenation of alcohols.

Investigating this hypothesis further, Chapter 4 of this thesis demonstrates that step edge sites do not affect the activation energy of the ethanol dehydrogenation reaction on copper catalysts, because the rate-determining step is cleavage of the C-H bond and not the O-H bond. Based on this work, it can be concluded that defective metal catalysts may be more active catalysts for reactions where the rate-determining step is catalyzed by under-coordinated sites. For example, Chapter 3 of this thesis

demonstrates that oxygen adatom defects on TiO<sub>2</sub> nanowires enhance the production of formaldehyde and methyl formate in the oxidation of methanol.

### **1.3.2 Supported Cu Catalysts**

Although these single crystal studies show that step sites are the active site in copper single crystals for alcohol dehydrogenation, there is no agreement upon the active site when it comes to non-model Cu-based catalysts used in operating conditions, such as elevated temperatures and atmospheric pressure. With regards to Cu oxidation state, the on-going discussion is evident. Many studies report metallic Cu to be the most active species<sup>21-23</sup>, whereas others cite Cu<sup>+</sup> or a mixture of Cu<sup>0</sup>/Cu<sup>+</sup> as the most active species for the dehydrogenation of ethanol<sup>24-27</sup> and cyclohexanol<sup>28</sup>. One study used in situ X-ray absorption near edge structure (XANES) to correlate dehydrogenation and esterification selectivities to the distribution of Cu oxidation states. The study demonstrated that Cu<sup>0</sup> sites catalyze the dehydrogenation reaction to acetaldehyde, whereas Cu<sup>2+</sup> + Cu<sup>1+</sup> sites catalyze the esterification reaction to ethyl acetate. The study concluded that the relative populations of Cu<sup>0</sup> and Cu<sup>2+</sup>/Cu<sup>1+</sup> depend on cluster size and support and thus, the selectivity for dehydrogenation could be manipulated by altering either parameter<sup>23</sup>. In this vein, previous reports have also investigated the effects of Cu cluster size<sup>23, 26, 29</sup>, support<sup>22-23, 29-30</sup>, preparation methods<sup>31-32</sup>, and pressure<sup>33</sup>, though no decisive conclusion about the active site has been reached.



### **1.3.3 Promoters and Alloys**

Regardless of the ongoing discussion on the active site, Cu catalysts have been generally found to deactivate in alcohol dehydrogenation conditions, predominantly due to sintering<sup>34-42</sup>. To improve the stability of Cu catalysts, the addition of chromium<sup>21, 40-41, 43-45</sup>, magnesium<sup>28, 39</sup>, aluminum<sup>28, 30, 33</sup>, zinc<sup>46</sup>, and alkali metals<sup>37</sup> as promoters has been investigated. Chromium was reported to improve the stability of copper for the reaction; however, environmental issues related to the use of chromium have discouraged its use<sup>21, 40-41, 43-45</sup>. Potassium was found to be comparable to chromium as a promoter, increasing the activity and stability of silica-supported Cu catalysts for the dehydrogenation of ethanol. In the same study, sodium and rubidium was found not to impact the stability, however, they did increase the activity compared to Cu/SiO<sub>2</sub><sup>37</sup>.

Though the distinction between promoters and alloys is unclear, these studies on multi-component materials indicate an important principle: that the addition of a second component changes the inherent materials properties and thus, catalytic function. Bimetallic catalysts already open new opportunities for tuning the reactivity and selectivity of a catalyst for improved energy efficiency and sustainability. Because the primary motivation of this thesis is understanding the interplay between materials, especially alloys, and their catalytic properties, it is necessary to expand on the background of alloy materials to fully appreciate their unique properties and advantages in catalysis.

## 1.4 Alloy Catalysts

### 1.4.1 Bulk Alloys

Metal alloys demonstrate different and at times improved activity, selectivity, and stability compared to their individual components for many reactions. Alloying catalysts is particularly attractive for noble metals as the expensive noble metal can be diluted in a less expensive one, while maintaining the function of the noble metal. Bimetallic catalysts with noble components have been extensively studied for ethanol steam reforming and ethanol oxidation reactions including Au-Cu<sup>48-50</sup>, Co-Cu<sup>51-52</sup>, Co-Ni<sup>51, 53-54</sup>, Ni-Cu<sup>55-60</sup>, Ni-Zn<sup>61-63</sup>, Pd-Zn<sup>64</sup>, Pt-Cu<sup>65</sup>, Pt-Ni<sup>65-67</sup>, and Pt-Ru<sup>65, 68</sup>. Ethanol steam reforming (ESR) and ethanol oxidation reaction (EOR) produce CO and H<sub>2</sub> from ethanol and steam or ethanol and oxygen, respectively. Some of the elementary reactions in ESR and EOR overlap with non-oxidative ethanol dehydrogenation thus, the literature can be used to gain insight about materials and their catalytic properties.

Though the previous section on promoters/alloys alludes to some work on alloy materials for alcohol dehydrogenation reactions, the use of more noble components for non-oxidative alcohol dehydrogenation reactions has been limited to Ag-Cu<sup>69</sup>, Au-Cu<sup>49</sup>, and Pd-Zn<sup>70-72</sup>. The studies listed in this section utilize bulk alloys with each component comprising at least 5% of the alloy composition. Considering the large scale of industrial catalysis, this may still require a substantial amount of precious metals which are not only expensive, but also are at risk of resource depletion (Zn, Pt, Ag, Ru, Ir)<sup>73</sup>. Recently, studies have demonstrated that even dilute metal alloys, where one of the metal components comprises less than ~5% of the total

concentration, are still active and selective for catalytic reactions. These materials are of course attractive due to the small amount of precious metals used and thus warrant further investigation.

### **1.4.2 Dilute Metal Alloys**

Studies of dilute metal alloys are few as synthesizing dilute alloys (<5%) can be more difficult than bulk alloys (>5%), though the literature is growing. Dilute alloy materials display remarkable cases of improved performance compared to their monometallic counterparts, because the more reactive, minority component is used to drive the reaction on the majority host component. Nanoporous Au, for example, is a sponge-like structure with ~3 at% Ag that can catalyze numerous complex oxygen-assisted alcohol coupling reactions with high reactivity, selectivity, and long-term stability<sup>74-76</sup>. On its own, Au is highly selective for coupling reactions, but is relatively inert for dissociating O<sub>2</sub>, which is required for initiation of the reaction. Ag on its own promotes combustion of the alcohol reactants to carbon dioxide (CO<sub>2</sub>). The key to the high performance of nanoporous Au is a mixed Au-Ag oxide at the surface, which facilitates O<sub>2</sub> dissociation and spillover of oxygen atoms to the Au host, where the selective coupling of reactants occur<sup>77</sup>.

Further dilution of bimetallic catalysts still results in highly active catalysts. Single atom alloys are novel materials where single atoms of an active species, such as Pd or Pt, are dispersed on the surface of a less reactive host metal, such as Cu, which can be in the form of a single crystal or nanoparticle. The fundamental features of single atom alloys are that the more active component is present in very low

concentrations at the surface of the host metal and that it is thermodynamically stable as a single atom and does not form dimers or trimers.

Pd-Cu and Pt-Cu single atom alloys are capable of dissociating H<sub>2</sub> and catalyzing alkyne and alkadiene hydrogenation reactions with higher activity and selectivity compared to their monometallic counterparts, respectively<sup>78-79</sup>. Pt-Cu single atom alloys are also capable of dissociating C-H bonds and assisting in dehydrogenation reactions of methanol<sup>80</sup> and formic acid<sup>81</sup>. Similar to nanoporous Au, Cu on its own is inert for dissociating H<sub>2</sub> for hydrogenation reactions, whereas Pd and Pt are notoriously active for H<sub>2</sub> activation and hydrogenation reactions though unselective. Scanning tunneling microscopy (STM) of atomically dispersed Pd (~1 at%) on Cu (111) demonstrated that the dispersed Pd atoms on the Cu (111) surface dissociate H<sub>2</sub> molecules into adsorbed hydrogen atoms<sup>82</sup>. The STM study directly visualized the hydrogen atoms spilling over onto the Cu surface from the Pd atoms allowing hydrogenation reactions to proceed on the Cu surface, where it is highly selective.

These investigations on single atom alloys and nanoporous Au identify the crucial aspect in the success of dilute metal alloys: the synergistic effect of two different components where each performs a particular function in the overall reaction mechanism. Based on these principles, numerous catalytic materials can be strategically designed to improve their reactivity, selectivity, and stability for a given reaction. Chapter 5 of this thesis specifically investigates the development of dilute Ni-Cu alloy materials to demonstrate its improved activity compared to Cu for the ethanol dehydrogenation reaction.

### 1.4.3 Ni-Cu Alloys for Ethanol Dehydrogenation

Ni-Cu bulk alloys have been widely studied for the ethanol steam reforming or ethanol oxidation reactions<sup>55-60</sup>. Many studies demonstrate that the Cu preferentially dehydrogenates ethanol to acetaldehyde, whereas Ni is too reactive, promoting C-C bond scission reactions to H<sub>2</sub>, CO<sub>2</sub>, CO, and CH<sub>4</sub><sup>56, 59-60</sup>. Because Ni promotes C-C bond scission reactions, it is infamous for decomposing reactants into carbon leading to the deactivation<sup>57-58, 61-63, 83-84</sup>. With Ni-Cu catalysts, studies reported decreased carbon deposition compared to pure Ni catalysts, though it was not completely eliminated<sup>55, 57-58</sup>.

Building on the principles of dilute metal alloys, this thesis investigated dilute Ni-Cu alloy materials as they were theorized to be better materials for the ethanol dehydrogenation reaction than their pure components. Because Ni is more reactive than Cu, adding a small amount of it to Cu may improve the activity without sacrificing the selectivity to acetaldehyde. In addition to improving the activity, Ni may also stabilize the Cu structure from sintering. Sintering is a common method of deactivation. However, the more stable the metal, the less likely it is to sinter. The following is the increasing order of stability for metals<sup>85-86</sup>:



The lower the metal is in the series, the more susceptible it is to deactivate by sintering. Since Ni is a more stable metal than Cu, we speculated that doping Cu with

Ni would improve the stability of the catalyst and prevent deactivation by sintering. Furthermore, Cu and Ni are both inexpensive and earth abundant elements, making them cost-effective to implement on the industrial scale.

Based on these ideas, this work synthesized and tested novel Ni-Cu alloy nanoparticles and several nanoporous materials (sponge-like structures) for the ethanol dehydrogenation reaction. Chapter 5 demonstrates that dilute Ni-Cu alloys are highly active and selective for ethanol dehydrogenation to acetaldehyde and hydrogen. The study found that dilute Ni-Cu catalysts, regardless of form, lower the activation barrier for the ethanol dehydrogenation reaction and thus, have higher activity while maintaining high selectivity for acetaldehyde and hydrogen. Additional studies by collaborators demonstrated that Ni facilitates C-H bond cleavage, the rate-determining step in ethanol dehydrogenation, improving the activity of Cu in Ni-Cu single atom alloy nanoparticles and demonstrating the synergistic function of the metals<sup>87</sup>.

#### **1.4.4 Manipulation of Active Structures**

A crucial feature of dilute metal alloys that is often overlooked is the surface features of the catalyst. As alluded to in the dilute metal alloys section, the active component of the alloy must be at the surface as it will have no effect on the reactivity if it is located in the bulk. In the case of single atom alloys, the active component must also be stable as a single atom at the surface and not form dimers and trimers as the catalytic function of a single atom will differ from a dimer or trimer structure. Thus,

it is essential to control the surface features of a catalyst as the bulk composition does not reflect the surface composition or structure.

For working catalysts, the active surface can be manipulated by different pretreatments that lead to different catalytic behavior. For example, as prepared nanoporous Au (npAu) is highly active for CO oxidation to CO<sub>2</sub><sup>88</sup>, whereas ozone-pretreated npAu is inactive for CO oxidation<sup>89</sup>. Additionally, as prepared npAu becomes inactive for methanol oxidation and higher alcohols, whereas ozone-pretreated npAu is highly active, selective, and stable for alcohol oxidation reactions<sup>89</sup>. As stated previously, the key to ozone-activated npAu is a mixed Ag-Au oxide at the surface that is capable of dissociating O<sub>2</sub>. This structure is only created upon ozone treating the material which brings more Ag to the surface and oxidizes the Ag and Au<sup>77</sup>. On the other hand, the CO oxidation activity of as prepared npAu is attributed to surface defects with the role Ag being to stabilize the step sites and facilitate O<sub>2</sub> dissociation<sup>90</sup>. Clearly, the as prepared and ozone-treated npAu materials are fundamentally different materials with distinct catalytic activities. Ozone pretreatment is an example of a transformation agent, turning an inactive structure into an active one and vice versa, and demonstrates how materials can be manipulated and tuned for their best performance using carefully chosen pretreatments.

As a means to understanding npAu, Chapter 8 explores the effect of ozone treatment and methanol oxidation reaction on bulk Ag<sub>70</sub>Au<sub>30</sub>, which is the precursory alloy used to fabricate npAu by selective dissolution of Ag. The study demonstrates a similar diffusion of Ag to the surface by ozone exposure. Upon further exposure to

methanol oxidation reaction conditions, a nanoporous morphology develops illustrating that even large-scale compositional and morphological changes can be initiated by surface chemical reactions (Chapter 8).

Following up on the Ni-Cu studies presented in Chapter 5, Chapters 6 and 7 present an extensive investigation of different pretreatments on nanoporous Ni-Cu (npNiCu). These chapters demonstrate that H<sub>2</sub> pretreatment of npNiCu transforms the material such that it deactivates the catalyst for ethanol dehydrogenation, whereas O<sub>2</sub> pretreatment forms an active and more stable catalyst for the reaction. The work follows surface compositional (Chapter 6) and structural (Chapter 7) changes to demonstrate that the inactive and active forms of the catalyst are tied to the presence of metallic and oxidized Ni at the surface, respectively, with the presence metallic Ni leading to deactivation due to carbon deposition.

## **1.5 Specific Aims of Thesis**

The overarching focus of this thesis is on understanding the relationship between catalyst activity and catalyst material at a fundamental level. The effect of catalyst morphology on elementary reactions steps are probed on titania (TiO<sub>2</sub>) nanowires for methanol oxidation (Chapter 3) and nanoporous copper for ethanol dehydrogenation (Chapter 4). The effect of alloying nickel with various copper-based materials is explored for ethanol dehydrogenation reaction (Chapter 5). Furthermore, the transformation of catalytic materials with reactive gases is investigated on bulk Ag-Au (Chapter 8) as well as for nanoporous Ni-Cu with an extensive investigation on reactivity changes in the ethanol dehydrogenation



reaction correlated with structural (Chapter 6) and surface compositional (Chapter 7) changes. The insights gained from this work can be applied to tailor new catalysts with improved activity and stability for energy efficient and environmentally sustainable catalytic applications.

## 1.6 References

1. EIA, International Energy Outlook 2016. *U.S. Energy Information Administration* **2016**, 1-290.
2. PNNL Studying the chemistry as it happens in catalytic reactions. <https://phys.org/news/2012-01-chemistry-catalytic-reactions.html>.
3. Smil, V., Detonator of the population explosion. *Nature* **1999**, *400*, 415.
4. Eckert, M.; Fleischmann, G.; Jira, R.; Bolt, H. M.; Golka, K., Acetaldehyde. In *Ullmann's Encyclopedia of Industrial Chemistry*, Wiley-VCH Verlag GmbH & Co. KGaA: 2000.
5. Hagemeyer, H. J.; Staff, U. b., Acetaldehyde. In *Kirk-Othmer Encyclopedia of Chemical Technology*, John Wiley & Sons, Inc.: 2000.
6. Scholl, D. S. L., Ryan P., Seven chemical separations to change the world. *Nature* **2016**, *532*, 435-437.
7. EERE, Fuel Cell Technologies Program. *U.S. Department of Energy, Energy Efficiency & Renewable Energy (EERE)* **2010**.
8. Zeng, Y.; Zhao, S.; Yang, S.; Ding, S.-Y., Lignin plays a negative role in the biochemical process for producing lignocellulosic biofuels. *Current Opinion in Biotechnology* **2014**, *27* (Supplement C), 38-45.
9. Perlack, R. D. S., B. J., U.S. Billion-Ton Update: Biomass Supply for a Bioenergy and Bioproducts Industry. *U.S. Department of Energy* **2011**.
10. RFA, World Fuel Ethanol Production. *Renewables Fuel Association (RFA)* **2016**.
11. Searchinger, T.; Heimlich, R.; Houghton, R. A.; Dong, F.; Elobeid, A.; Fabiosa, J.; Tokgoz, S.; Hayes, D.; Yu, T.-H., Use of U.S. Croplands for Biofuels Increases

Greenhouse Gases Through Emissions from Land-Use Change. *Science* **2008**, *319* (5867), 1238-1240.

12. Fargione, J.; Hill, J.; Tilman, D.; Polasky, S.; Hawthorne, P., Land Clearing and the Biofuel Carbon Debt. *Science* **2008**, *319* (5867), 1235-1238.

13. Tilman, D.; Hill, J.; Lehman, C., Carbon-Negative Biofuels from Low-Input High-Diversity Grassland Biomass. *Science* **2006**, *314* (5805), 1598-1600.

14. Brown, D. E. E., T.; Joyner, R.W.; McCarroll, J.J.; Tennison, S.R., The genesis and development of the commercial BP doubly promoted catalyst for ammonia synthesis. *Catalysis Letters* **2014**, *144*, 545-552.

15. Bowker, M.; Madix, R. J., XPS, UPS and thermal desorption studies of alcohol adsorption on Cu(110) II. Higher Alcohols. *Surface Science* **1982**, *116* (3), 549-572.

16. Bowker, M.; Madix, R. J., XPS, UPS and thermal desorption studies of alcohol adsorption on Cu(110) I. Methanol. *Surface Science* **1980**, *95* (1), 190-206.

17. Wachs, I. E.; Madix, R. J., The selective oxidation of CH<sub>3</sub>OH to H<sub>2</sub>CO on a copper(110) catalyst. *Journal of Catalysis* **1978**, *53* (2), 208-227.

18. Sexton, B. A.; Hughes, A. E.; Avery, N. R., Surface intermediates in the reaction of methanol, formaldehyde and methyl formate on copper (110). *Applications of Surface Science* **1985**, *22*, 404-414.

19. Chen, A. K.; Masel, R., Direct conversion of methanol to formaldehyde in the absence of oxygen on Cu(210). *Surface Science* **1995**, *343* (1), 17-23.

20. Wang, Z.-T.; Xu, Y.; El-Soda, M.; Lucci, F. R.; Madix, R. J.; Friend, C. M.; Sykes, E. C. H., Surface Structure Dependence of the Dry Dehydrogenation of Alcohols on Cu(111) and Cu(110). *The Journal of Physical Chemistry C* **2017**, *121* (23), 12800-12806.

21. Colley, S. W.; Tabatabaei, J.; Waugh, K. C.; Wood, M. A., The detailed kinetics and mechanism of ethyl ethanoate synthesis over a Cu/Cr<sub>2</sub>O<sub>3</sub> catalyst. *Journal of Catalysis* **2005**, *236* (1), 21-33.

22. Iwasa, N.; Takezawa, N., Reforming of Ethanol -Dehydrogenation to Ethyl Acetate and Steam Reforming to Acetic Acid over Copper-Based Catalysts-. *Bulletin of the Chemical Society of Japan* **1991**, *64* (9), 2619-2623.

23. Witzke, M. E.; Dietrich, P. J.; Ibrahim, M. Y. S.; Al-Bardan, K.; Triezenberg, M. D.; Flaherty, D. W., Spectroscopic evidence for origins of size and support effects on selectivity of Cu nanoparticle dehydrogenation catalysts. *Chemical Communications* **2017**, *53* (3), 597-600.

24. Cassinelli, W. H.; Martins, L.; Magnani, M.; Pulcinelli, S. H.; Briois, V.; Santilli, C. V., Time-resolved XAS/MS/Raman monitoring of mutual copper self-reduction and ethanol dehydrogenation reactions. *RSC Advances* **2016**, 6 (25), 20453-20457.
25. Cassinelli, W. H.; Martins, L.; Passos, A. R.; Pulcinelli, S. H.; Rochet, A.; Briois, V.; Santilli, C. V., Correlation between Structural and Catalytic Properties of Copper Supported on Porous Alumina for the Ethanol Dehydrogenation Reaction. *ChemCatChem* **2015**, 7 (11), 1668-1677.
26. Freitas, I. C.; Damyanova, S.; Oliveira, D. C.; Marques, C. M. P.; Bueno, J. M. C., Effect of Cu content on the surface and catalytic properties of Cu/ZrO<sub>2</sub> catalyst for ethanol dehydrogenation. *Journal of Molecular Catalysis A: Chemical* **2014**, 381, 26-37.
27. Sato, A. G.; Volanti, D. P.; de Freitas, I. C.; Longo, E.; Bueno, J. M. C., Site-selective ethanol conversion over supported copper catalysts. *Catalysis Communications* **2012**, 26, 122-126.
28. Fridman, V. Z.; Davydov, A. A., Dehydrogenation of Cyclohexanol on Copper-Containing Catalysts. *Journal of Catalysis* **2000**, 195 (1), 20-30.
29. Gao, D.; Feng, Y.; Yin, H.; Wang, A.; Jiang, T., Coupling reaction between ethanol dehydrogenation and maleic anhydride hydrogenation catalyzed by Cu/Al<sub>2</sub>O<sub>3</sub>, Cu/ZrO<sub>2</sub>, and Cu/ZnO catalysts. *Chemical Engineering Journal* **2013**, 233, 349-359.
30. Inui, K.; Kurabayashi, T.; Sato, S., Direct synthesis of ethyl acetate from ethanol over Cu-Zn-Zr-Al-O catalyst. *Applied Catalysis A: General* **2002**, 237 (1), 53-61.
31. Fujita, S.-i.; Iwasa, N.; Tani, H.; Nomura, W.; Arai, M.; Takezawa, N., Dehydrogenation of Ethanol Over Cu/ZnO Catalysts Prepared from Various Coprecipitated Precursors. *Reaction Kinetics and Catalysis Letters* **2001**, 73 (2), 367-372.
32. Gole, J. L.; White, M. G., Nanocatalysis: Selective Conversion of Ethanol to Acetaldehyde Using Mono-atomically Dispersed Copper on Silica Nanospheres. *Journal of Catalysis* **2001**, 204 (1), 249-252.
33. Inui, K.; Kurabayashi, T.; Sato, S., Direct Synthesis of Ethyl Acetate from Ethanol Carried Out under Pressure. *Journal of Catalysis* **2002**, 212 (2), 207-215.
34. Chladek, P.; Croiset, E.; Epling, W.; Hudgins, R. R., Characterization of Copper Foam as Catalytic Material in Ethanol Dehydrogenation. *The Canadian Journal of Chemical Engineering* **2007**, 85 (6), 917-924.

35. Jung, K.-D.; Joo, O.-S.; Han, S.-H.; Uhm, S.-J.; Chung, I.-J., Deactivation of Cu/ZnO catalyst during dehydrogenation of methanol. *Catalysis Letters* **1995**, *35* (3), 303-311.
36. Marchi, A. J.; Fierro, J. L. G.; Santamaría, J.; Monzon, A., *Dehydrogenation of isopropyl alcohol on a Cu/SiO<sub>2</sub> catalyst: A study of the activity evolution and reactivation of the catalyst*. 1996; Vol. 142, p 375-386.
37. Tu, Y.-J.; Chen, Y.-W., Effects of Alkali Metal Oxide Additives on Cu/SiO<sub>2</sub> Catalyst in the Dehydrogenation of Ethanol. *Industrial & Engineering Chemistry Research* **2001**, *40* (25), 5889-5893.
38. Pepe, F.; Polini, R., Catalytic behavior and surface chemistry of Copper/ZnO/Al<sub>2</sub>O<sub>3</sub> catalysts for the decomposition of 2-propanol. *Journal of Catalysis* **1992**, *136* (1), 86-95.
39. Tu, Y.-J.; Chen, Y.-W., Effects of Alkaline-Earth Oxide Additives on Silica-Supported Copper Catalysts in Ethanol Dehydrogenation. *Industrial & Engineering Chemistry Research* **1998**, *37* (7), 2618-2622.
40. Tu, Y.-J.; Chen, Y.-W.; Li, C., Characterization of unsupported copper—chromium catalysts for ethanol dehydrogenation. *Journal of Molecular Catalysis* **1994**, *89* (1), 179-189.
41. Tu, Y.-J.; Li, C.; Chen, Y.-W., Effect of chromium promoter on copper catalysts in ethanol dehydrogenation. *Journal of Chemical Technology & Biotechnology* **1994**, *59* (2), 141-147.
42. Mušič, A.; Batista, J.; Levec, J., Gas-phase catalytic dehydrogenation of methanol to formaldehyde over ZnO/SiO<sub>2</sub> based catalysts, zeolites, and phosphates. *Applied Catalysis A: General* **1997**, *165* (1), 115-131.
43. Carotenuto, G.; Kumar, A.; Miller, J.; Mukasyan, A.; Santacesaria, E.; Wolf, E. E., Hydrogen production by ethanol decomposition and partial oxidation over copper/copper-chromite based catalysts prepared by combustion synthesis. *Catalysis Today* **2013**, *203*, 163-175.
44. Carotenuto, G.; Tesser, R.; Di Serio, M.; Santacesaria, E., Kinetic study of ethanol dehydrogenation to ethyl acetate promoted by a copper/copper-chromite based catalyst. *Catalysis Today* **2013**, *203* (Supplement C), 202-210.
45. Santacesaria, E.; Carotenuto, G.; Tesser, R.; Di Serio, M., Ethanol dehydrogenation to ethyl acetate by using copper and copper chromite catalysts. *Chemical Engineering Journal* **2012**, *179* (Supplement C), 209-220.

46. Shiau, C.-Y.; Chen, S.; Tsai, J. C.; Lin, S. I., Effect of zinc addition on copper catalyst in isoamyl alcohol dehydrogenation. *Applied Catalysis A: General* **2000**, *198* (1), 95-102.
47. Guan, Y.; Hensen, E. J. M., Ethanol dehydrogenation by gold catalysts: The effect of the gold particle size and the presence of oxygen. *Applied Catalysis A: General* **2009**, *361* (1), 49-56.
48. Redina, E. A.; Greish, A. A.; Mishin, I. V.; Kapustin, G. I.; Tkachenko, O. P.; Kirichenko, O. A.; Kustov, L. M., Selective oxidation of ethanol to acetaldehyde over Au-Cu catalysts prepared by a redox method. *Catalysis Today* **2015**, *241*, 246-254.
49. Bauer, J. C.; Veith, G. M.; Allard, L. F.; Oyola, Y.; Overbury, S. H.; Dai, S., Silica-Supported Au-CuO<sub>x</sub> Hybrid Nanocrystals as Active and Selective Catalysts for the Formation of Acetaldehyde from the Oxidation of Ethanol. *ACS Catalysis* **2012**, *2* (12), 2537-2546.
50. Wang, Y.; Shi, L.; Lu, W.; Sun, Q.; Wang, Z.; Zhi, C.; Lu, A.-H., Spherical Boron Nitride Supported Gold-Copper Catalysts for the Low-Temperature Selective Oxidation of Ethanol. *ChemCatChem* **2017**, *9* (8), 1363-1367.
51. Homs, N.; Llorca, J.; de la Piscina, P. R., Low-temperature steam-reforming of ethanol over ZnO-supported Ni and Cu catalysts. *Catalysis Today* **2006**, *116* (3), 361-366.
52. Galetti, A. E.; Gomez, M. F.; Arrua, L. A.; Marchi, A. J.; Abello, M. C., Study of CuCoZnAl oxide as catalyst for the hydrogen production from ethanol reforming. *Catalysis Communications* **2008**, *9* (6), 1201-1208.
53. Resini, C.; Concepción Herrera Delgado, M.; Presto, S.; Alemany, L. J.; Riani, P.; Marazza, R.; Ramis, G.; Busca, G., Ytria-stabilized zirconia (YSZ) supported Ni-Co alloys (precursor of SOFC anodes) as catalysts for the steam reforming of ethanol. *International Journal of Hydrogen Energy* **2008**, *33* (14), 3728-3735.
54. He, L.; Berntsen, H.; Ochoa-Fernández, E.; Walmsley, J. C.; Blekkan, E. A.; Chen, D., Co-Ni Catalysts Derived from Hydrotalcite-Like Materials for Hydrogen Production by Ethanol Steam Reforming. *Topics in Catalysis* **2009**, *52* (3), 206-217.
55. Mariño, F.; Boveri, M.; Baronetti, G.; Laborde, M., Hydrogen production from steam reforming of bioethanol using Cu/Ni/K/γ-Al<sub>2</sub>O<sub>3</sub> catalysts. Effect of Ni. *International Journal of Hydrogen Energy* **2001**, *26* (7), 665-668.
56. Velu, S.; Suzuki, K.; Vijayaraj, M.; Barman, S.; Gopinath, C. S., In situ XPS investigations of Cu<sub>1-x</sub>Ni<sub>x</sub>ZnAl-mixed metal oxide catalysts used in the oxidative steam reforming of bio-ethanol. *Applied Catalysis B: Environmental* **2005**, *55* (4), 287-299.

57. Vizcaíno, A. J.; Carrero, A.; Calles, J. A., Hydrogen production by ethanol steam reforming over Cu–Ni supported catalysts. *International Journal of Hydrogen Energy* **2007**, *32* (10), 1450-1461.
58. Fierro, V.; Akdim, O.; Mirodatos, C., On-board hydrogen production in a hybrid electric vehicle by bio-ethanol oxidative steam reforming over Ni and noble metal based catalysts. *Green Chemistry* **2003**, *5* (1), 20-24.
59. Mariño, F. J.; Cerrella, E. G.; Duhalde, S.; Jobbagy, M.; Laborde, M. A., Hydrogen from steam reforming of ethanol. characterization and performance of copper-nickel supported catalysts. *International Journal of Hydrogen Energy* **1998**, *23* (12), 1095-1101.
60. Velu, S.; Satoh, N.; Gopinath, C. S.; Suzuki, K., Oxidative Reforming of Bio-Ethanol Over CuNiZnAl Mixed Oxide Catalysts for Hydrogen Production. *Catalysis Letters* **2002**, *82* (1), 145-152.
61. Anjaneyulu, C.; Costa, L. O. O. d.; Ribeiro, M. C.; Rabelo-Neto, R. C.; Mattos, L. V.; Venugopal, A.; Noronha, F. B., Effect of Zn addition on the performance of Ni/Al<sub>2</sub>O<sub>3</sub> catalyst for steam reforming of ethanol. *Applied Catalysis A: General* **2016**, *519*, 85-98.
62. Barroso, M. N.; Gomez, M. F.; Arrúa, L. A.; Abello, M. C., Hydrogen production by ethanol reforming over NiZnAl catalysts. *Applied Catalysis A: General* **2006**, *304*, 116-123.
63. Galetti, A. E.; Gomez, M. F.; Arrúa, L. A.; Abello, M. C., Hydrogen production by ethanol reforming over NiZnAl catalysts. *Applied Catalysis A: General* **2008**, *348* (1), 94-102.
64. Casanovas, A.; Llorca, J.; Homs, N.; Fierro, J. L. G.; Ramírez de la Piscina, P., Ethanol reforming processes over ZnO-supported palladium catalysts: Effect of alloy formation. *Journal of Molecular Catalysis A: Chemical* **2006**, *250* (1), 44-49.
65. Mironova, E. Y.; Lytkina, A. A.; Ermilova, M. M.; Efimov, M. N.; Zemtsov, L. M.; Orekhova, N. V.; Karpacheva, G. P.; Bondarenko, G. N.; Muraviev, D. N.; Yaroslavtsev, A. B., Ethanol and methanol steam reforming on transition metal catalysts supported on detonation synthesis nanodiamonds for hydrogen production. *International Journal of Hydrogen Energy* **2015**, *40* (8), 3557-3565.
66. Örucü, E.; Gökaliler, F.; Aksoylu, A. E.; Önsan, Z. I., Ethanol Steam Reforming for Hydrogen Production over Bimetallic Pt–Ni/Al<sub>2</sub>O<sub>3</sub>. *Catalysis Letters* **2008**, *120* (3), 198-203.
67. Sanchez-Sanchez, M. C.; Navarro Yerga, R. M.; Kondarides, D. I.; Verykios, X. E.; Fierro, J. L. G., Mechanistic Aspects of the Ethanol Steam Reforming Reaction for

Hydrogen Production on Pt, Ni, and PtNi Catalysts Supported on  $\gamma$ -Al<sub>2</sub>O<sub>3</sub>. *The Journal of Physical Chemistry A* **2010**, *114* (11), 3873-3882.

68. Bi, J.-L.; Hong, Y.-Y.; Lee, C.-C.; Yeh, C.-T.; Wang, C.-B., Novel zirconia-supported catalysts for low-temperature oxidative steam reforming of ethanol. *Catalysis Today* **2007**, *129* (3), 322-329.

69. Freitas, I. C.; Gallo, J. M. R.; Bueno, J. M. C.; Marques, C. M. P., The Effect of Ag in the Cu/ZrO<sub>2</sub> Performance for the Ethanol Conversion. *Topics in Catalysis* **2016**, *59* (2), 357-365.

70. Iwasa, N.; Yamamoto, O.; Tamura, R.; Nishikubo, M.; Takezawa, N., Difference in the reactivity of acetaldehyde intermediates in the dehydrogenation of ethanol over supported Pd catalysts. *Catalysis Letters* **1999**, *62* (2), 179-184.

71. Jeroro, E.; Vohs, J. M., Exploring the Role of Zn in PdZn Reforming Catalysts: Adsorption and Reaction of Ethanol and Acetaldehyde on Two-dimensional PdZn Alloys. *The Journal of Physical Chemistry C* **2009**, *113* (4), 1486-1494.

72. Sanchez, A. B.; Homs, N.; Miachon, S.; Dalmon, J.-A.; Fierro, J. L. G.; Ramirez de la Piscina, P., Direct transformation of ethanol into ethyl acetate through catalytic membranes containing Pd or Pd-Zn: comparison with conventional supported catalysts. *Green Chemistry* **2011**, *13* (9), 2569-2575.

73. Davies, E., Endangered Elements - As our supply of some essential elements dries up, it's time to start urban mining. *Chemistry World* **2011**, 50-54.

74. Personick, M. L.; Madix, R. J.; Friend, C. M., Selective Oxygen-Assisted Reactions of Alcohols and Amines Catalyzed by Metallic Gold: Paradigms for the Design of Catalytic Processes. *ACS Catalysis* **2017**, *7* (2), 965-985.

75. Zugic, B.; Karakalos, S.; Stowers, K. J.; Biener, M. M.; Biener, J.; Madix, R. J.; Friend, C. M., Continuous Catalytic Production of Methyl Acrylates from Unsaturated Alcohols by Gold: The Strong Effect of C=C Unsaturation on Reaction Selectivity. *ACS Catalysis* **2016**, *6* (3), 1833-1839.

76. Wang, L.-C.; Stowers, K. J.; Zugic, B.; Biener, M. M.; Biener, J.; Friend, C. M.; Madix, R. J., Methyl ester synthesis catalyzed by nanoporous gold: from 10<sup>-9</sup> Torr to 1 atm. *Catalysis Science & Technology* **2015**, *5* (2), 1299-1306.

77. Zugic, B.; Wang, L.; Heine, C.; Zakharov, D. N.; Lechner, B. A. J.; Stach, E. A.; Biener, J.; Salmeron, M.; Madix, R. J.; Friend, C. M., Dynamic restructuring drives catalytic activity on nanoporous gold-silver alloy catalysts. *Nat Mater* **2017**, *16* (5), 558-564.

78. Boucher, M. B.; Zugic, B.; Cladaras, G.; Kammert, J.; Marcinkowski, M. D.; Lawton, T. J.; Sykes, E. C. H.; Flytzani-Stephanopoulos, M., Single atom alloy surface analogs in Pd<sub>0.18</sub>Cu<sub>15</sub> nanoparticles for selective hydrogenation reactions. *Physical Chemistry Chemical Physics* **2013**, *15* (29), 12187-12196.
79. Lucci, F. R.; Liu, J.; Marcinkowski, M. D.; Yang, M.; Allard, L. F.; Flytzani-Stephanopoulos, M.; Sykes, E. C. H., Selective hydrogenation of 1,3-butadiene on platinum-copper alloys at the single-atom limit *Nat. Commun.* **2015**, *6*, 8550.
80. Shan, J.; Lucci, F. R.; Liu, J.; El-Soda, M.; Marcinkowski, M. D.; Allard, L. F.; Sykes, E. C. H.; Flytzani-Stephanopoulos, M., Water co-catalyzed selective dehydrogenation of methanol to formaldehyde and hydrogen. *Surface Science* **2016**, *650*, 121-129.
81. Marcinkowski, M. D.; Liu, J.; Murphy, C. J.; Liriano, M. L.; Wasio, N. A.; Lucci, F. R.; Flytzani-Stephanopoulos, M.; Sykes, E. C. H., Selective Formic Acid Dehydrogenation on Pt-Cu Single-Atom Alloys. *ACS Catalysis* **2017**, *7* (1), 413-420.
82. Kyriakou, G.; Boucher, M. B.; Jewell, A. D.; Lewis, E. A.; Lawton, T. J.; Baber, A. E.; Tierney, H. L.; Flytzani-Stephanopoulos, M.; Sykes, E. C. H., Isolated Metal Atom Geometries as a Strategy for Selective Heterogeneous Hydrogenations. *Science* **2012**, *335* (6073), 1209-1212.
83. Suelves, I.; Lázaro, M. J.; Moliner, R.; Corbella, B. M.; Palacios, J. M., Hydrogen production by thermo catalytic decomposition of methane on Ni-based catalysts: influence of operating conditions on catalyst deactivation and carbon characteristics. *International Journal of Hydrogen Energy* **2005**, *30* (15), 1555-1567.
84. Zeng, G.; Liu, Q.; Gu, R.; Zhang, L.; Li, Y., Synergy effect of MgO and ZnO in a Ni/Mg-Zn-Al catalyst during ethanol steam reforming for H<sub>2</sub>-rich gas production. *Catalysis Today* **2011**, *178* (1), 206-213.
85. Hughes, R., Deactivation of catalysts. Academic Press: London, 1984.
86. Spencer, M. S.; Twigg, M. V., Metal Catalyst Design and Preparation in Control of Deactivation. *Annual Review of Materials Research* **2005**, *35* (1), 427-464.
87. Shan, J.; Liu, J.; Li, M.; Lustig, S.; Lee, S.; Flytzani-Stephanopoulos, M., NiCu single atom alloys catalyze the CH bond activation in the selective non-oxidative ethanol dehydrogenation reaction. *Applied Catalysis B: Environmental* **2018**, *226*, 534-543.
88. Zielasek, V.; Jürgens, B.; Schulz, C.; Biener, J.; Biener, M. M.; Hamza, A. V.; Bäumer, M., Gold Catalysts: Nanoporous Gold Foams. *Angewandte Chemie International Edition* **2006**, *45* (48), 8241-8244.



*Chapter 1. Introduction - Sustainable Catalysis*

89. Personick, M. L.; Zugic, B.; Biener, M. M.; Biener, J.; Madix, R. J.; Friend, C. M., Ozone-Activated Nanoporous Gold: A Stable and Storable Material for Catalytic Oxidation. *ACS Catalysis* **2015**, 5 (7), 4237-4241.

90. Fujita, T.; Guan, P.; McKenna, K.; Lang, X.; Hirata, A.; Zhang, L.; Tokunaga, T.; Arai, S.; Yamamoto, Y.; Tanaka, N.; Ishikawa, Y.; Asao, N.; Yamamoto, Y.; Erlebacher, J.; Chen, M., Atomic origins of the high catalytic activity of nanoporous gold. *Nature Materials* **2012**, 11, 775.

## Chapter 2.

### Methods

#### **2.1 Abstract**

In this chapter, catalytic testing of materials and characterization techniques are described. All methods described here and summarized in their respective chapters were conducted by the author of this thesis. Experimental details of work performed by collaborators are described solely in their respective chapters.

#### **2.2 Catalyst Pretreatments**

##### **2.2.1 H<sub>2</sub> and O<sub>2</sub> Pretreatments of Cu-based Catalysts**

Hydrogen pretreatments were conducted on Cu-based catalysts to ensure a fully reduced sample was used for catalytic tests using a flow reactor. Hydrogen treatment was performed prior to catalytic testing by flowing 10% hydrogen at 20 ml/min at room temperature, followed by ramping the temperature to 350°C at 10°C/min and holding for 1 hr. The temperature was then lowered to 250°C for ethanol dehydrogenation reactions. Oxygen pretreatments were performed using 20% oxygen at a flow rate of 50 ml/min. The catalysts were held at room temperature and ramped to 250°C at 10°C/min and held there for 1 hr. The temperature was kept at 250°C for ethanol dehydrogenation reaction.

## **2.2.2 Pretreatments of Bulk Ag-Au Alloys**

For nanoporous Au catalysts and bulk AgAu systems, ozone pretreatment is used to activate the catalysts. Without ozone treating Au-based catalysts, these materials are not active for alcohol oxidation and coupling reactions. Ozone treatment was performed on Ag<sub>70</sub>Au<sub>30</sub> bulk alloy ingots at 150°C under a flow of 3% O<sub>3</sub> in O<sub>2</sub>/He at 100 ml/min for 1 h. The sample was then exposed to methanol oxidation reaction conditions of 6% methanol and 20% oxygen balanced in He using a flow rate of 50 ml/min at 150°C for 1 h.

## **2.3 Catalytic Activity Tests**

### **2.3.1 Steady-State Ethanol Dehydrogenation Reaction Tests**

Steady-state activity tests were performed using a flow reactor at atmospheric pressure housed in a temperature-controlled furnace (Figure 2.1). Ultrahigh-purity gases were supplied to the reactor by mass-flow controllers. In a typical experiment, ~30 mg of catalyst was diluted with sand, loaded into the reactor tube, and topped with quartz wool. The reactants flow through the catalyst bed, where the temperature and pressure are regulated, and exit with any products to be analyzed by either a mass spectrometer or a gas chromatograph-mass spectrometer. The gas composition for a typical activity test was 6% ethanol balanced in He using a typical flow rate of 50 ml/min. Ethanol was obtained by flowing a saturated He stream through a bubbler filled with liquid ethanol. For steady-state activity tests, the catalyst was maintained at 250°C. Reactant and product gases were analyzed using an online gas chromatograph-mass spectrometer (GC-MS, Agilent 5975C and Agilent

7890A) equipped with columns, HP-PLOT Q and CARBONLOT, and a thermal conductivity detector.

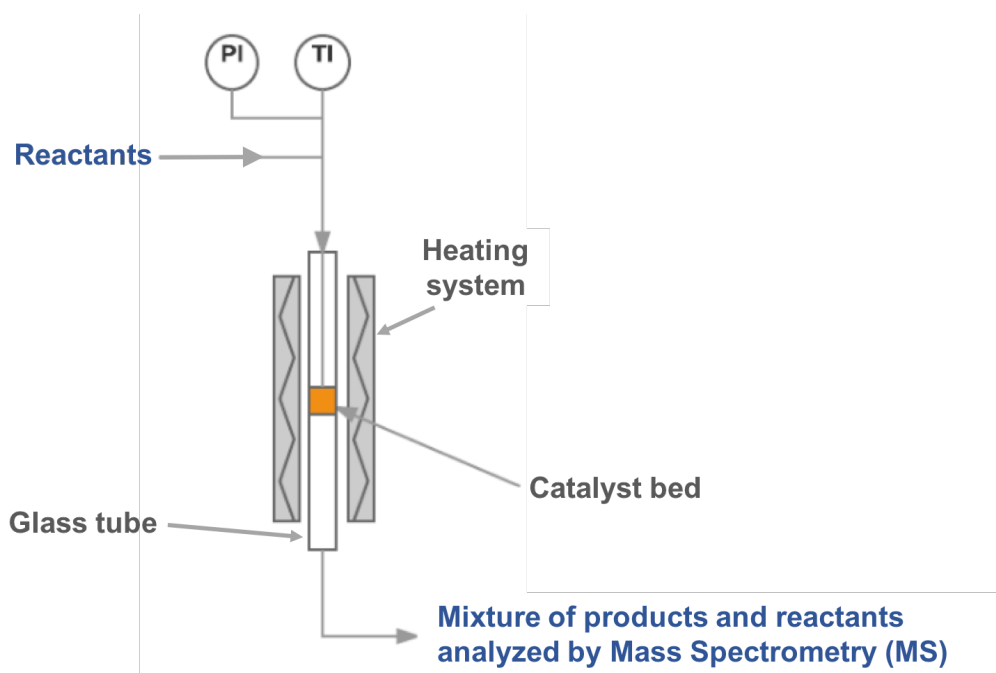


**Figure 2.1** Schematic of flow reactor system

Products detected by the GC-MS are quantified by their peak areas in the chromatograph. All product peak areas are corrected by their ionization cross sections (Table 2.1). Because only acetaldehyde is detected by the GC-MS, as hydrogen is light and travels too quickly through the column for detection, all conversion and kinetic analyses are conducted using acetaldehyde. Based on the reaction stoichiometry, an equal number of moles of acetaldehyde and hydrogen are produced by the reaction. Conversion to acetaldehyde was calculated based on the reaction stoichiometry using the expression:

$$X_{\text{acetaldehyde}}(\%) = 100 \cdot \frac{C_{\text{acetaldehyde}} + C_{\text{CO}} + C_{\text{methane}}}{C_{\text{acetaldehyde}} + C_{\text{CO}} + C_{\text{methane}} + C_{\text{ethanol}}}$$

where  $C_{\text{acetaldehyde}}$ ,  $C_{\text{CO}}$ ,  $C_{\text{methane}}$ , and  $C_{\text{ethanol}}$  are the concentrations of acetaldehyde, CO, methane, and ethanol in the gas stream, respectively. The mass-specific reaction rate of acetaldehyde ( $R_m$ ) was determined by:

$$R_m = \frac{F \cdot X_{\text{acetaldehyde}} \cdot \% \text{ethanol}}{60 \frac{\text{s}}{\text{min}} \cdot 22400 \frac{\text{ml}}{\text{mol}} \cdot m_{\text{catalyst}}}$$

where  $F$  is the total flow rate of the reaction mixture,  $\% \text{ethanol}$  is the percent of ethanol in the reactant gas composition, and  $m_{\text{catalyst}}$  is the weight of the catalyst.

The selectivity to acetaldehyde,  $S_{\text{acetaldehyde}}$ , is calculated using:

$$S_{\text{acetaldehyde}} = 100 \cdot \frac{C_{\text{acetaldehyde}}}{C_{\text{acetaldehyde}} + C_{\text{CO}} + C_{\text{methane}} + C_{\text{ethanol}}}$$

**Table 2.1** Ionization cross sections used in quantitative mass spectrometry

Molecule	$\sigma$
CO	2.63 <sup>1</sup>
CO <sub>2</sub>	3.74 <sup>1</sup>
Methane (CH <sub>4</sub> )	4.24 <sup>2</sup>
Acetaldehyde	7.25 <sup>3</sup>
Ethanol	7.68 <sup>4</sup>
Ethylacetate	12.69 <sup>3</sup>
2-butanone	12.69 <sup>3</sup>

<sup>1</sup>Adapted from *J. Phys. B: At. Mol. Opt. Phys.* 37 (2004) 445-455.

<sup>2</sup>Adapted from *J. Phys. B: At. Mol. Opt. Phys.* 30 (1997) 2465-2475.

<sup>3</sup>Calculated according to equation  $\sigma_m = 2.72n_c + 1.81$  ( $n_c$  = number of carbons) from *Int. J. Mass. Spectrum.* 273 (2008) 53-57.

<sup>4</sup>Calculated according to equation  $\sigma_m = 2.67n_c + 2.34$  ( $n_c$  = number of carbons) from *Int. J. Mass. Spectrum.* 248 (2006) 42-46.

### 2.3.2 Activation Energy Measurements

For activation energy measurements, the total conversion was kept below 15% to ensure differential reactor conditions. The catalyst was maintained at 250°C for at least 1 h in reaction conditions before lowering the temperature by 10°C. The temperature was lowered by 10°C increments until ~1% conversion was reached and then returned to 250°C in 10°C increments to ensure the catalyst recovered the same activity at each temperature. The catalyst was kept at each temperature for at least 30 min to reach steady-state. The activation energy is calculated by plotting the natural log of the reaction rate at each temperature in an Arrhenius plot versus 1/T, where T is temperature. A linear fit is added and the slope of the linear fit is used to obtain the activation energy in kJ mol<sup>-1</sup> using the equation:  $E_a = \text{slope} \cdot R$ , where R is the universal gas constant.

### 2.3.3 Temperature-Programmed Ethanol Dehydrogenation Reaction Tests

Temperature-programmed surface reaction (TPSR) tests were performed using the flow reactor system described previously (Figure 2.1). A typical amount of catalyst

## *Chapter 2. Methods*

was loaded and pretreated as needed. After cooling to room temperature, 6% Ethanol/He gas was flowed through the catalyst at 50 ml/min. The temperature was ramped linearly at 10 °C/min to the reaction temperature of 250 °C. The effluent gas was analyzed by a residual gas analyzer (Hiden HAL 3F RGA) operated at a pressure of  $\sim 1\text{e-}6$  Torr.

Ethanol, water, and H<sub>2</sub> were monitored by  $m/z = 31$ , 18, and 2, respectively. For acetaldehyde,  $m/z = 43$  and 29 were both monitored as  $m/z = 43$  is unique to acetaldehyde, however,  $m/z = 29$  provides better signal-to-noise, though it is not unique to acetaldehyde.

## **2.4 Catalyst Characterization**

### **2.4.1 X-ray Photoelectron Spectroscopy**

X-ray photoelectron spectroscopy (XPS) was conducted at the Center for Nanoscale Systems at Harvard University using a Thermo Scientific K-Alpha or K-Alpha + system. Both instruments utilize a monochromatic Al K $\alpha$  X-ray source with an energy  $\sim 1.4866$  keV and a 180° double focusing hemispherical analyzer and 128-channel detector. All XPS spectra were obtained with an X-ray spot size of 400  $\mu\text{m}$  and a flood gun to compensate any sample charging during a measurement. Survey scans were collected using a 1 eV step size, 100 eV pass energy, and 10 scans. High-resolution scans were obtained using a 0.05 eV step size, 40 eV pass energy, and 10 scans except for Ni where 40 scans were used for better signal-to-noise ratio. An argon sputter gun was used for depth profiling. All spectra were analyzed using the CasaXPS software and energy calibrated to the 1s carbon peak at 284.5 eV.

### **2.4.2 Ambient-Pressure X-ray Photoelectron Spectroscopy (AP-XPS)**

Ambient-pressure X-ray photoelectron spectroscopy (AP-XPS) experiments were conducted at Beamline 23-ID-2 at the National Synchrotron Light Source II at Brookhaven National Laboratory. Because the freeze-drying synthesis step results in a Ni and Zn enriched ingot surface and samples are crushed for reactivity testing, both the surface and the cross section of an ingot sample were studied. To do this, a npNiCu ingot (dimensions: ~12 mm x 3 mm x 1 mm) was halved into two pieces with lengths of 6 mm each. One of these pieces was cut lengthwise to expose the cross section and loaded with the cross section facing out. The other was loaded as is to expose the outer surface of the ingot. Both pieces were held onto a tantalum back-plate with tantalum foil that was spot welded on each side to keep in place. The whole contraption was then loaded on platinum button heater and mounted within the AP-XPS chamber. Both an as prepared ingot and a previously treated ingot in the flow reactor (10% H<sub>2</sub>, 1 atm, 1 h, 350°C) were used for the AP-XPS studies.

To ensure that the same depth was probed for each element and similar gas-phase attenuation, the X-ray photon energy was varied such that the kinetic energy of all photoelectrons was 200 eV. After every photon-energy change, the mirrors were adjusted to optimize the XPS counts. With each metal 2p or survey spectrum that was collected in each condition, a corresponding Fermi edge spectrum was collected and used to calibrate the energy of the respective spectrum. The sample was first analyzed in ultra-high vacuum (UHV) at room temperature (RT) (condition



0). Then it was exposed to 0.2 Torr ethanol for 6 h at 250 °C (condition 1), after which it was exposed to 1 Torr O<sub>2</sub> at 250 °C for 1 h (condition 2). The sample was exposed to each of these conditions and analyzed in vacuum after the reactant gas was completely pumped out of the chamber to limit beam effects. In the final condition, the spectra were taken while the sample was in 0.2 Torr ethanol after being exposed to the ethanol for 1 h at 250 °C (condition 3). During reactant exposures, the beam was blocked between spectra collection to limit beam damage.

### **2.4.3 AP-XPS Spectral Analysis**

All the C 1s and O 1s spectra were de-convoluted using Voigt-type line-shapes after subtracting a Shirley-type background. Ni 2p spectra were analyzed using least square fitting based on a linear combination of area normalized reference 2p<sub>3/2</sub> spectra of Ni<sup>0</sup>, Ni<sup>2+</sup>, and Ni(OH)<sub>2</sub> to extract the percentage of each specie present. Peak fitting with Gaussian-type fits was not appropriate to use as the Ni 2p spectra exhibited complicated line-shapes with characteristic satellites. Because the Cu 2p spectra exhibited pure Cu<sup>2+</sup> or Cu<sup>0</sup>/Cu<sup>+1</sup>, which are indistinguishable by XPS, no further fitting was conducted. Efforts to fit the Zn 2p spectra were not made as the Zn metal and oxide components overlap and thus quantification is difficult for mixed systems. Therefore, the LMM Auger parameter, as generally agreed in the literature<sup>1</sup>, was used to qualitatively demonstrate changes in the Zn/Zn<sup>2+</sup> ratio under different conditions. The Zn LMM Auger spectra were extrapolated from the survey spectra collected with a photon energy of 1221 eV. Due to the large step size in the survey spectra, no fitting was performed.

Atomic ratios were calculated using the peak area (PA) and ionization cross-

$$Ratio A/B = \frac{PA(A)}{PA(B)} \square \frac{ICS(B)}{ICS(A)} \square \frac{PF @ E_{hv,B}}{PF @ E_{hv,A}}$$

section (ICS) of each element and the photon flux (PF) at the corresponding photon energy using the following formula<sup>2</sup>:

#### 2.4.4 Near-Edge X-ray Absorption Fine Structure (NEXAFS)

NEXAFS spectra were acquired using the AP-XPS analyzer in partial electron yield (PEY) mode. For Cu L-edge spectra and Ni L-edge spectra, the kinetic energies of the emitted photoelectrons were selected to be 320 eV and 240 eV, respectively, as no XPS peaks appear at this kinetic energy within the energy range scanned, which would otherwise produce false NEXAFS peaks. Because most of the spectra showed prominent Cu<sup>0</sup> characteristics, the energy calibration was conducted by aligning the Cu<sup>0</sup> peaks and corresponding satellites to reported literature values. To extract Cu<sup>0</sup>/Cu<sup>1+</sup> ratios, least square fitting was performed based on the linear combination of Cu<sup>0</sup> and Cu<sup>1+</sup> area normalized reference spectra of the L<sub>3</sub> region.

#### 2.4.5 Raman Spectroscopy

Raman spectroscopy was performed using a Horiba LabRam HR Evolution Spectrometer using a 633 nm excitation wavelength and 100% laser power. Spectra were acquired from 65 cm<sup>-1</sup> to 3000 cm<sup>-1</sup>. Z-height profiling was conducted on each sample from -5 μm to +5 μm. The spectrum with the highest intensity among the Z

profile was chosen for comparison. Raman spectroscopy was conducted at the Center for Nanoscale Systems at Harvard University.

#### **2.4.6 Electron Microscopy – SEM and TEM**

All ex situ transmission electron microscopy (TEM) was performed at the Center for Nanoscale Systems at Harvard University. For TEM imaging, a JEOL 2100 instrument operated using a lanthanum hexaboride filament source at 200 kV was used. Selected area electron diffraction (SAED) was performed on the JEOL 2100 to obtain diffraction patterns of samples. High-resolution transmission electron microscopy (HR-TEM) was performed on a JEOL 2100 instrument with a field emission source operated at 200 kV.

Aberration-corrected scanning transmission electron microscopy (STEM) was performed using a JEOL ARM 200F microscope operated at 200 kV with a field emission gun. Energy dispersive X-ray spectroscopy (EDS) was performed on the JEOL ARM 200F microscope equipped with a two-quadrant EDS detector. EDS mapping was also performed at Brookhaven National Laboratory at the Center for Functional Nanomaterials using a FEI Talos F200X microscope operated at 200 kV equipped with a four-quadrant EDS detector and a high angle annular dark field (HAADF) detector.

TEM and STEM samples were prepared by dispersing the catalyst in deionized water and dropping onto 200 mesh copper grids coated with lacey carbon film. Gold grids coated with lacey carbon film were utilized instead of copper grids when EDS mapping was to be performed.

## *Chapter 2. Methods*

Scanning electron microscopy (SEM) was performed at the Center of Nanoscale Systems at Harvard University using field emissions microscopes, Zeiss Ultra 55 and Zeiss Supra 55VP. An accelerating voltage of 5 keV was used for imaging samples at working distances of 5 to 8.5 mm. EDS was also performed on the SEM where an accelerating voltage of 15 keV was used and a working distance of ~8.5 mm. SEM samples were prepared by loading pieces of catalyst sample onto double-sided carbon tape, which was pre-loaded on appropriate SEM stubs or silicon wafer pieces. For any measurements of size, the program ImageJ was used and at least 100 measurements were made for statistical accuracy.

Due to the low mass of nanoporous Cu (npCu) yielded by the synthesis and used for catalytic testing, Brunauer-Emmett-Teller (BET) surface area measurements could not be conducted after each treatment. One BET measurement was conducted using N<sub>2</sub> adsorption on an as prepared npCu sample to yield a surface area of 2.7 m<sup>2</sup>/g. For npCu after a specified treatment, the ligament size was used to estimate the surface area of the nanoporous structure following the published procedure<sup>1</sup>. The as prepared npCu sample was used as a reference to determine the dimensionless constant of the porous structure. To account for any spherical nanoparticles at the surface, the surface area per gram was calculated using the radius of the particle. The total surface area of the nanoporous structure and particles was then calculated by taking a weighted average with the number of particles and ligaments measured.

#### **2.4.7 Environmental Transmission Electron Microscopy (E-TEM)**

Environmental transmission electron microscopy (E-TEM) was performed at Brookhaven National Laboratory using a FEI Titan microscope operated at 300 kV equipped with an electron energy loss spectrometer (EELS). The instrument operates at a base pressure of  $3 - 4 \times 10^{-7}$  Torr. Powdered samples were dispersed in deionized water and drop-casted onto a DENS Solutions heated sample holder. Gases and vapors were introduced into the microscope using a gas-handling manifold equipped with dosing valves. EELS spectra were analyzed using FEI's TEM imaging and analysis (TIA) program.

#### **2.4.8 TEM Imaging of Twinned Pd Nanostructures**

The following are contributions made by the thesis author to the publication, "*Defects by design: synthesis of palladium nanoparticles with extended twin defects and corrugated surfaces*", for which the author is acknowledged<sup>3</sup>.

This paper was published in *Nanoscale*, **2017**, 9, 17914-17921.

The premise of the report is the synthesis of well-defined palladium nanoparticles with an increased density of surface defects as undercoordinated sites are catalytically more active. The ratio of chloride to bromide in the particle growth solutions was tuned to form multiply twinned palladium nanostructures with corrugated surface features and extended fin-like twin defects. This synthetic method produced complex nanostructures such as concave icosahedra, star-like

## Chapter 2. Methods

pentatwinned rods, and bipyramids, where the fin-like features are the result of outward growth at the twin defects along the [111] directions. Figures 2.2A and 2.3A illustrate a concave icosahedron and pentatwinned rod, respectively. Figures 2.2B and 2.2C show the presence of twin planes in the fins of the concave icosahedron, which the other two geometries also exhibit. The surfaces of each of the structures is also corrugated and not planar, highlighted in Figures 2.3B and 2.2C, which is related to the ratio of chloride and bromide ions in the growth solution along with the growth at the twin planes. The use of chloride and bromide ions in the growth medium to tailor nanoparticle structures can be extended to other noble metal systems to generate structures with a high density of defects, ideal for catalytic applications.

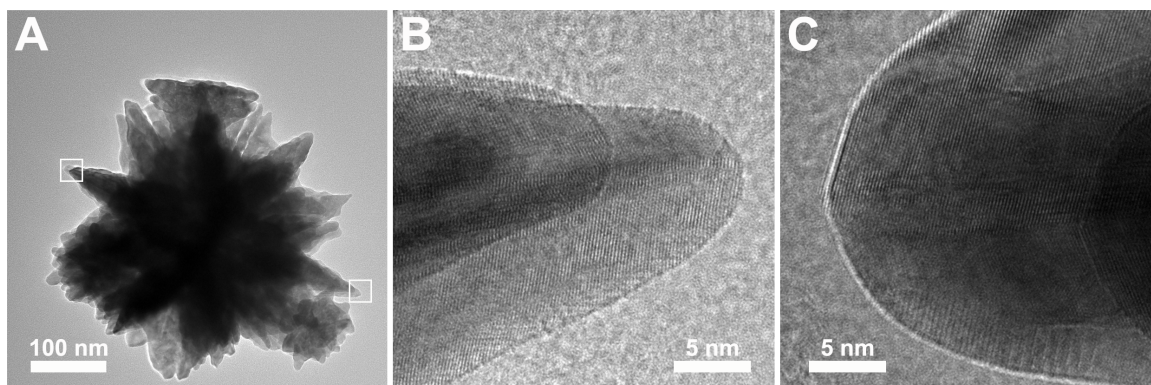


**Figure 2.2** A) High-resolution TEM images showing the presence of twin planes in the fins of a concave icosahedron. The areas highlighted by boxes in the low-magnification image in (A) are the sites of the high-magnification images in (B) and (C).

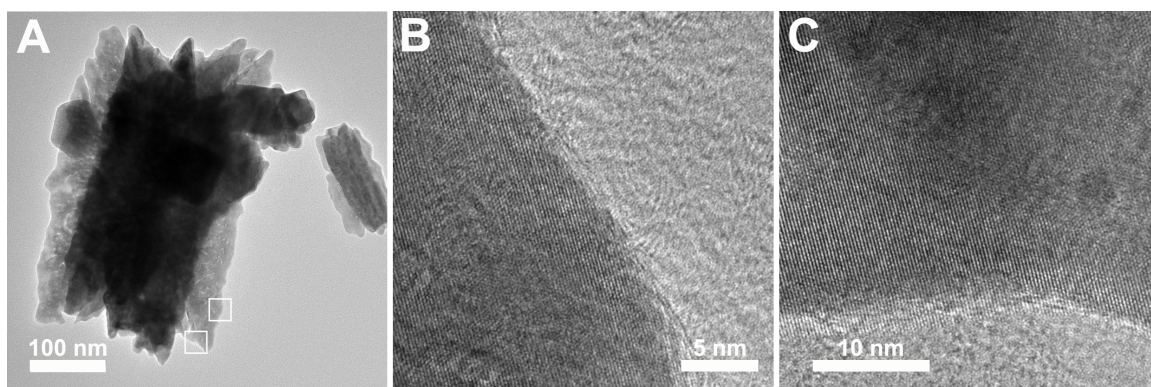


**Figure 2.3** A) High-resolution TEM images showing atomic scale roughness and undercoordination at the surface of the corrugated fins of a pentatwinned rod. The areas highlighted in the low magnification image in (A) are the sites of the high-magnification images in (B) and (C).

#### 2.4.9 TEM Imaging of AuPt Nanostructures

The following TEM images are contributions made by the thesis author to the publication, “*Synthetic Routes to Shaped AuPt Core-Shell Particles with Smooth Surfaces Based on Design Rules for Au Nanoparticle Growth*”, for which the author is acknowledged<sup>4</sup>.

This paper was published in *Part. Part. Syst. Charact.*, **2018**, 1700401.

In this work, AuPt core-shell particles were produced using a one-pot synthesis under mild reaction conditions. Core-shell particles were produced with various shapes and smooth, well-defined surfaces, a novel development, as previous studies observed Pt-islands covering the surface of AuPt core-shell particles. The

## *Chapter 2. Methods*

concentration of bromide ions in the growth solution determined the shape and facets of the AuPt nanoparticles leading to lower energy surfaces with the addition of bromide. When no bromide was present, {110}-faceted rhombic dodecahedra formed, the highest energy surface (Figure 2.4). When a small amount of bromide was added, {100}-faceted cubes and bipyramids formed (Figure 2.5). With a larger concentration of bromide in the growth solution, {111}-faceted octahedra, truncated triangular bipyramids, and decahedra form which have the lowest energy surfaces (Figure 2.6 and 2.7).

It is clear from Figures 2.4 to 2.7 that the Pt shell grows epitaxially on the Au core as the surfaces are smooth, contrary to previous studies which observed spherical Pt clusters or dendrites on the Au core. Figure 2.8 shows the formation of a {100}-faceted cube after Au reduction but prior to Pt deposition, illustrating that when the Pt layers deposit, they retain the structure of the Au core. Comparison of the Au cube with the AuPt cube, where multiple Pt layers have been deposited, show similar surface structures demonstrating that the Pt grows epitaxially on the Au nanoparticle (Figure 2.9).

When higher Pt contents are deposited by allowing the deposition to proceed for 48 h instead of 24 h, the beginning of dendritic growth can be observed on the {111}-faceted octahedra (Figure 2.10). The beginnings of dendritic growth are less apparent on the {111}-faceted truncated bipyramids that form in the same conditions (Figure 2.10). As determined by inductively coupled plasma atomic emission spectroscopy (ICP-AES), the {111}-faceted particles contained 9.4% Pt after 24 h of growth, whereas they contained 12.6% Pt after 48 h of growth.



## *Chapter 2. Methods*

Elemental mapping, ICP-AES, along with estimates of Pt percentage as a function of particle shape, size, and the number of Pt layers revealed that the Pt octahedra likely have ~3 layers of Pt after 24 h of growth, which increases to ~4 layers of Pt after 48 h growth. This suggests that around four layers of Pt is the maximum for epitaxial growth, after which Pt deposition continues by dendritic growth.

Fundamental experimental and theoretical studies on Pt single crystals can be readily applied to these nanoparticles because of their large, uniform facets. These particles are well-suited for facet-dependent catalytic activity studies as well as Pt coverage-dependent studies in heterogeneous catalysis. The use of Au particle growth chemistry to manipulate the resulting nanoparticles can also be extended to produce AuPt nanoparticles with high-index surface facets, which are favored for catalytic applications.

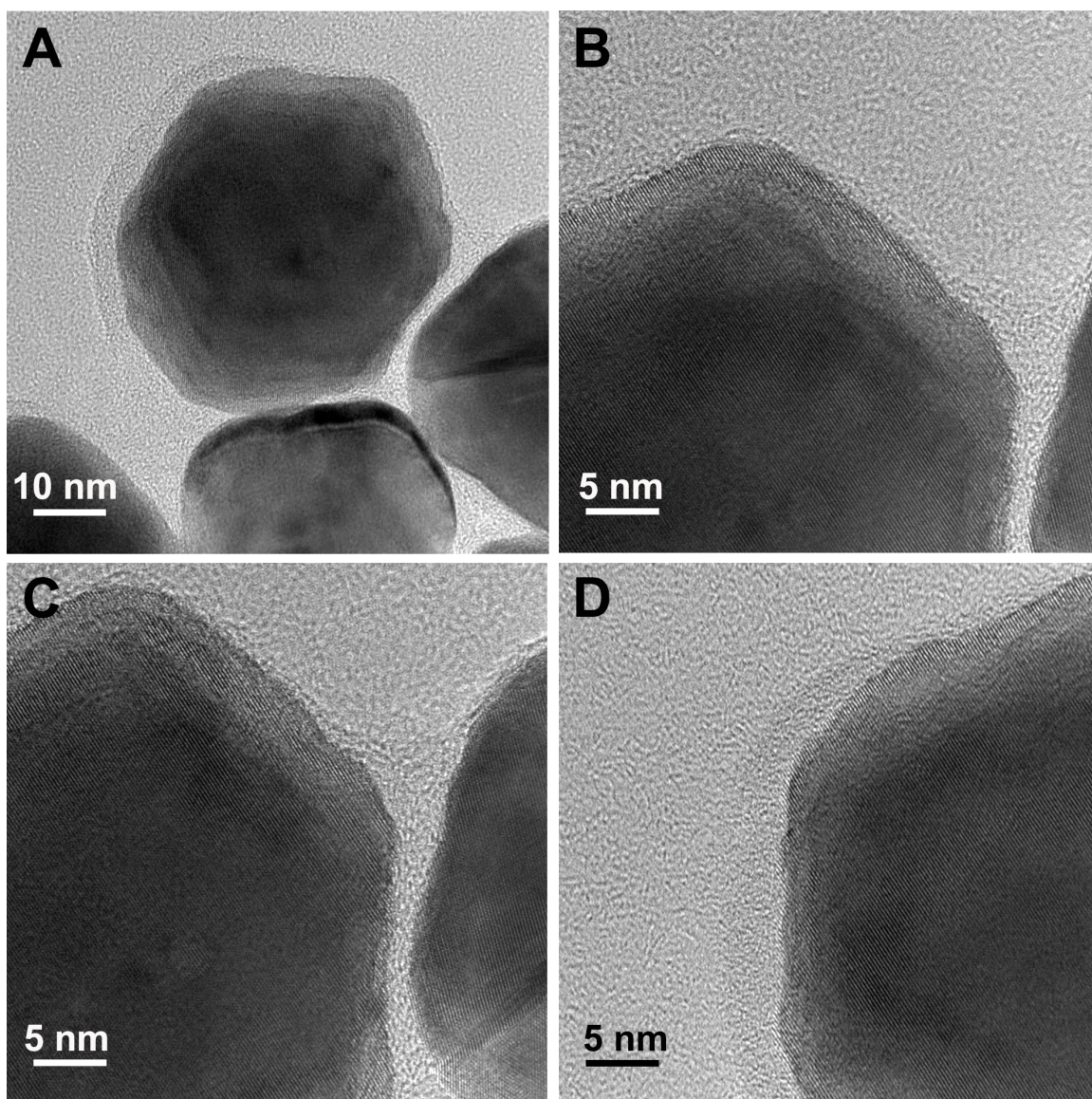


**Figure 2.4** (B-D) HRTEM images of the edges of the {110}-faceted AuPt rhombic dodecahedron in (A), showing epitaxial growth of Pt and the absence of spherical islands or dendrites. The particle was imaged after 24 hours of growth.

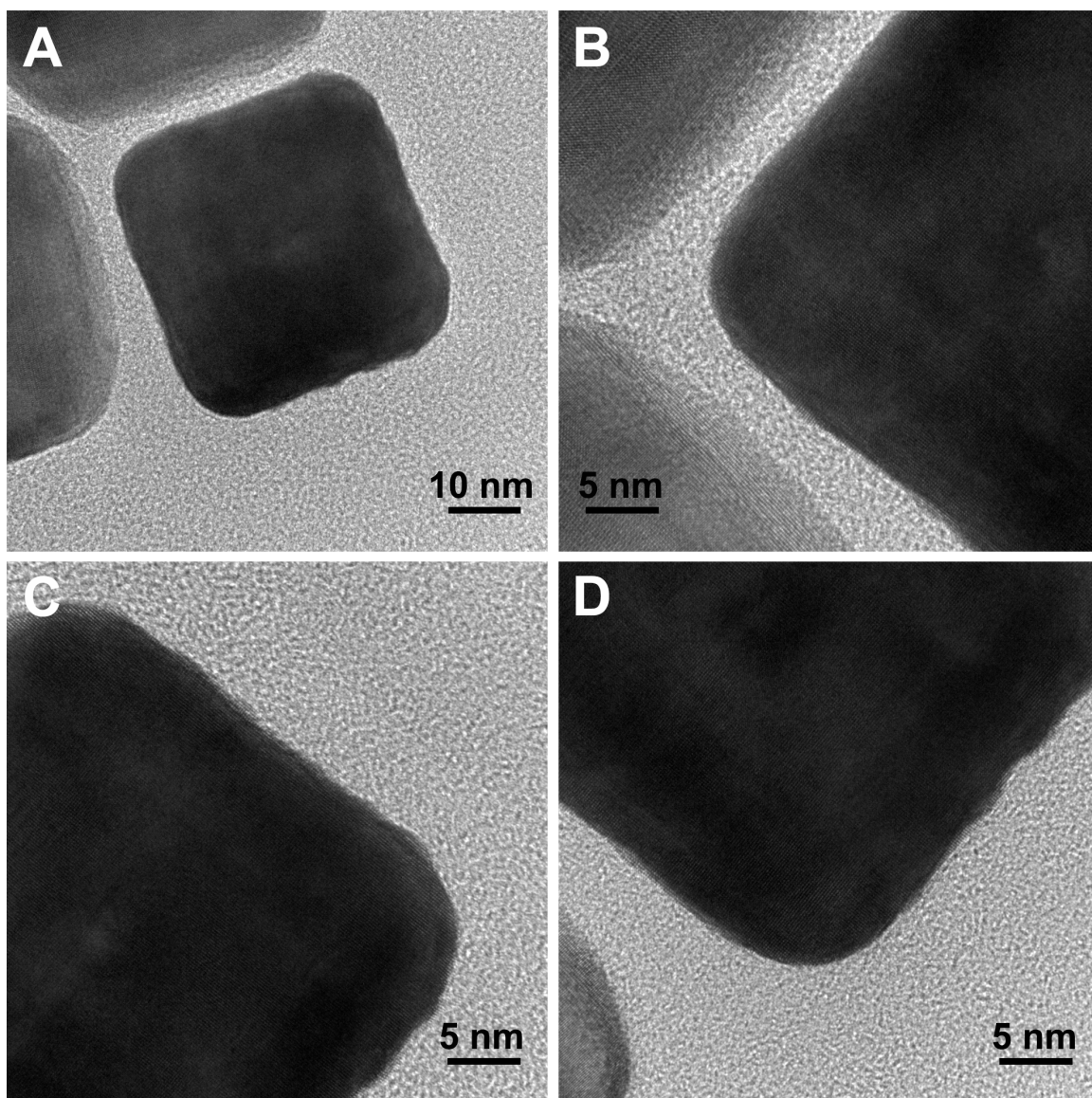


**Figure 2.5** (B-D) HRTEM images of the edges of the {100}-faceted AuPt cube in (A), showing epitaxial growth of Pt and the absence of spherical islands or dendrites. The particle was imaged after 24 hours of growth.



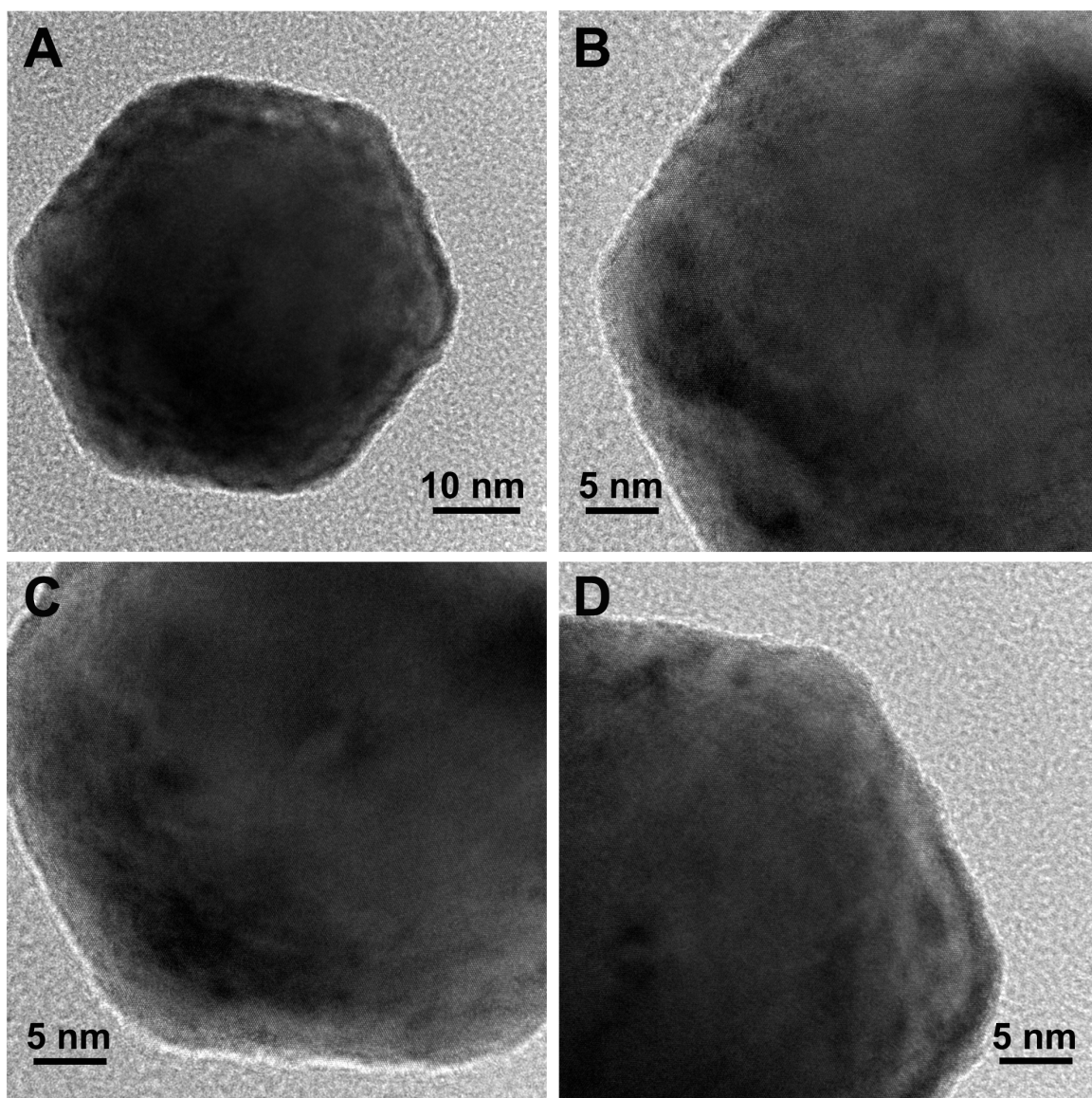


**Figure 2.6** (B-D) HRTEM images of the edges of the {111}-faceted AuPt octahedron in (A), showing epitaxial growth of Pt and the absence of spherical islands or dendrites. The particle was imaged after 24 hours of growth.

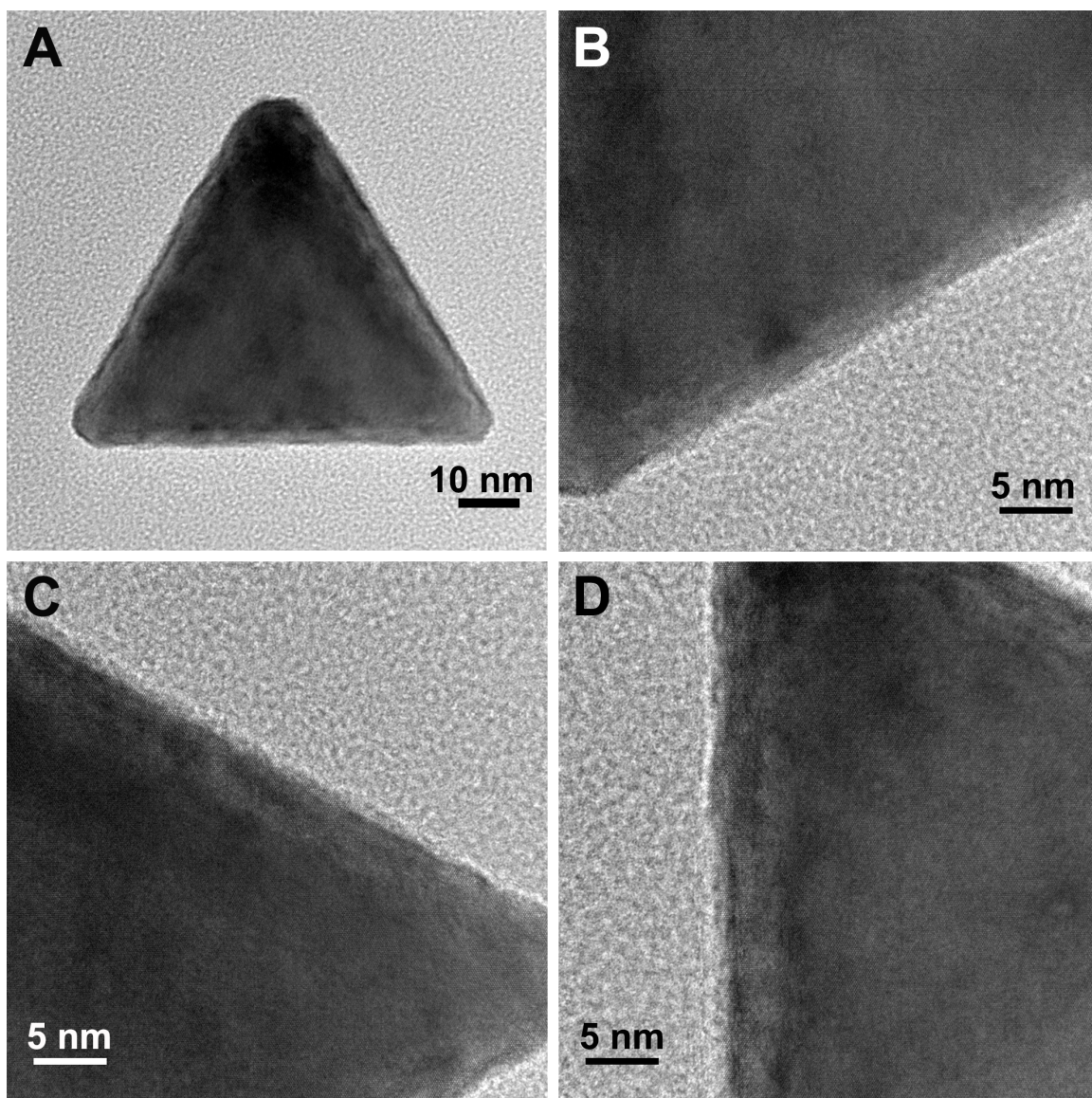


**Figure 2.7** (B-D) HRTEM images of the edges of the {111}-faceted AuPt truncated bipyramid in (A), showing epitaxial growth of Pt and the absence of spherical islands or dendrites. The particle was imaged after 24 hours of growth.



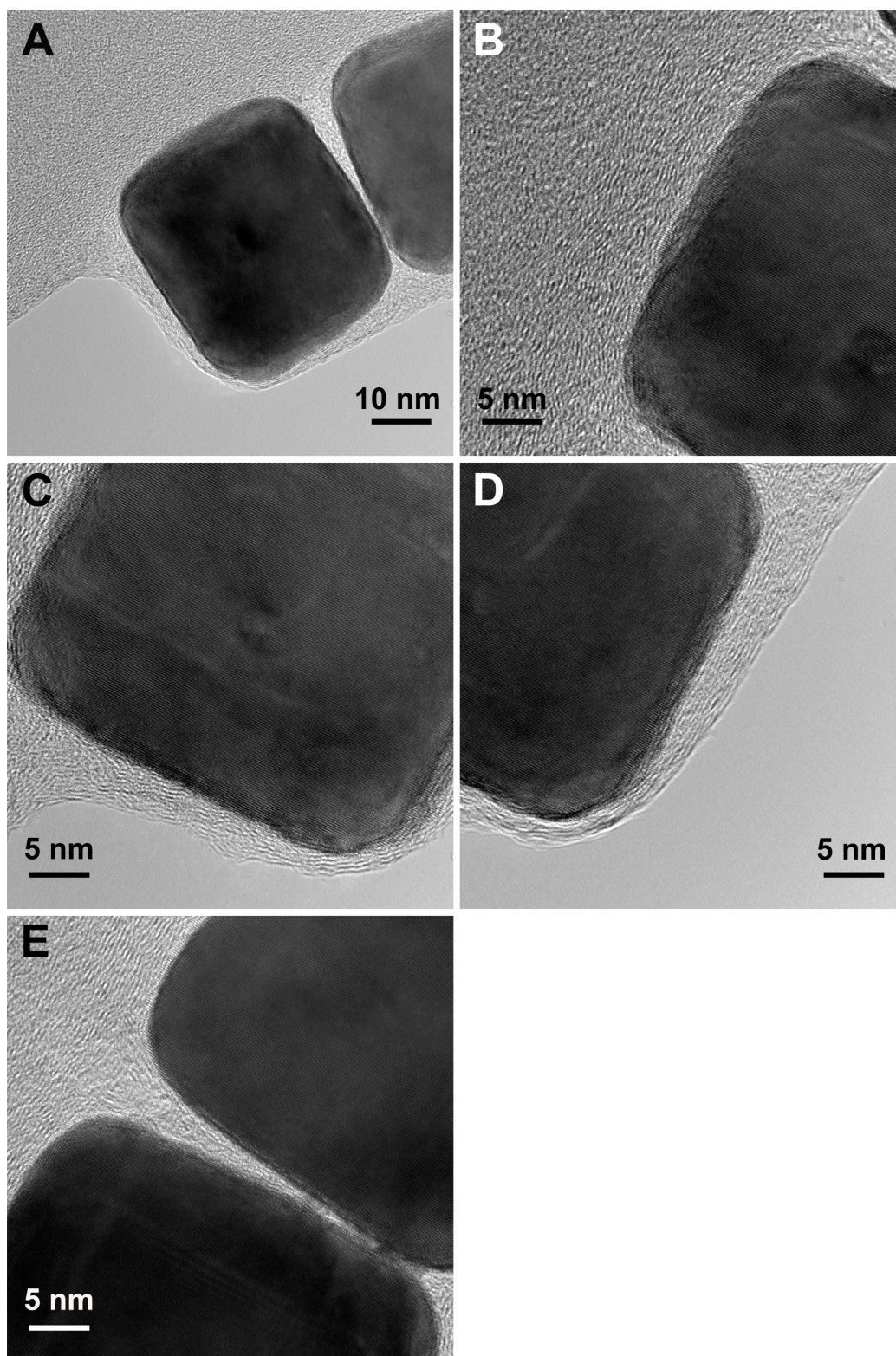


**Figure 2.8** (B-E) HRTEM images of the edges of the {100}-faceted AuPt cube in (A). The cube is representative of particles formed in a reaction that was quenched at 10

min of growth, which is after the reduction of Au but prior to the deposition of significant Pt. The particle has a similar surface structure to the particle in Figure 2.5, supporting the epitaxial growth of Pt.

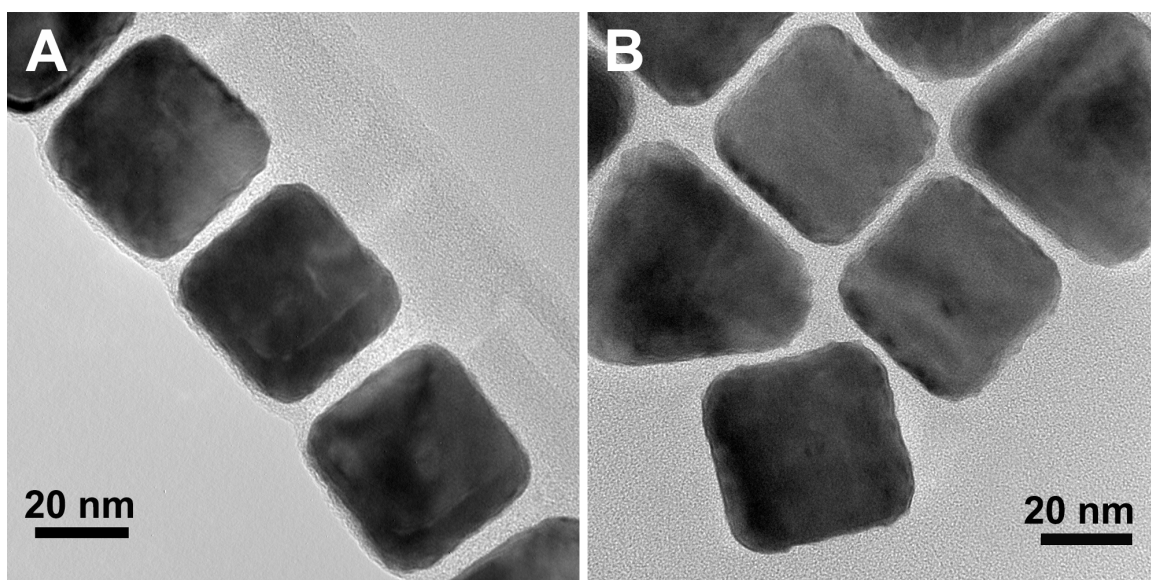


**Figure 2.9** High magnification TEM images of {100}-faceted AuPt cubes (A) after 10 min of growth (prior to the onset of significant Pt deposition); and (B) after 24 hours of growth (when multiple layers of Pt have been deposited). The similarity of the surface structure in the two samples indicates that Pt grows epitaxially on the Au core, rather than forming spherical islands or dendrites.

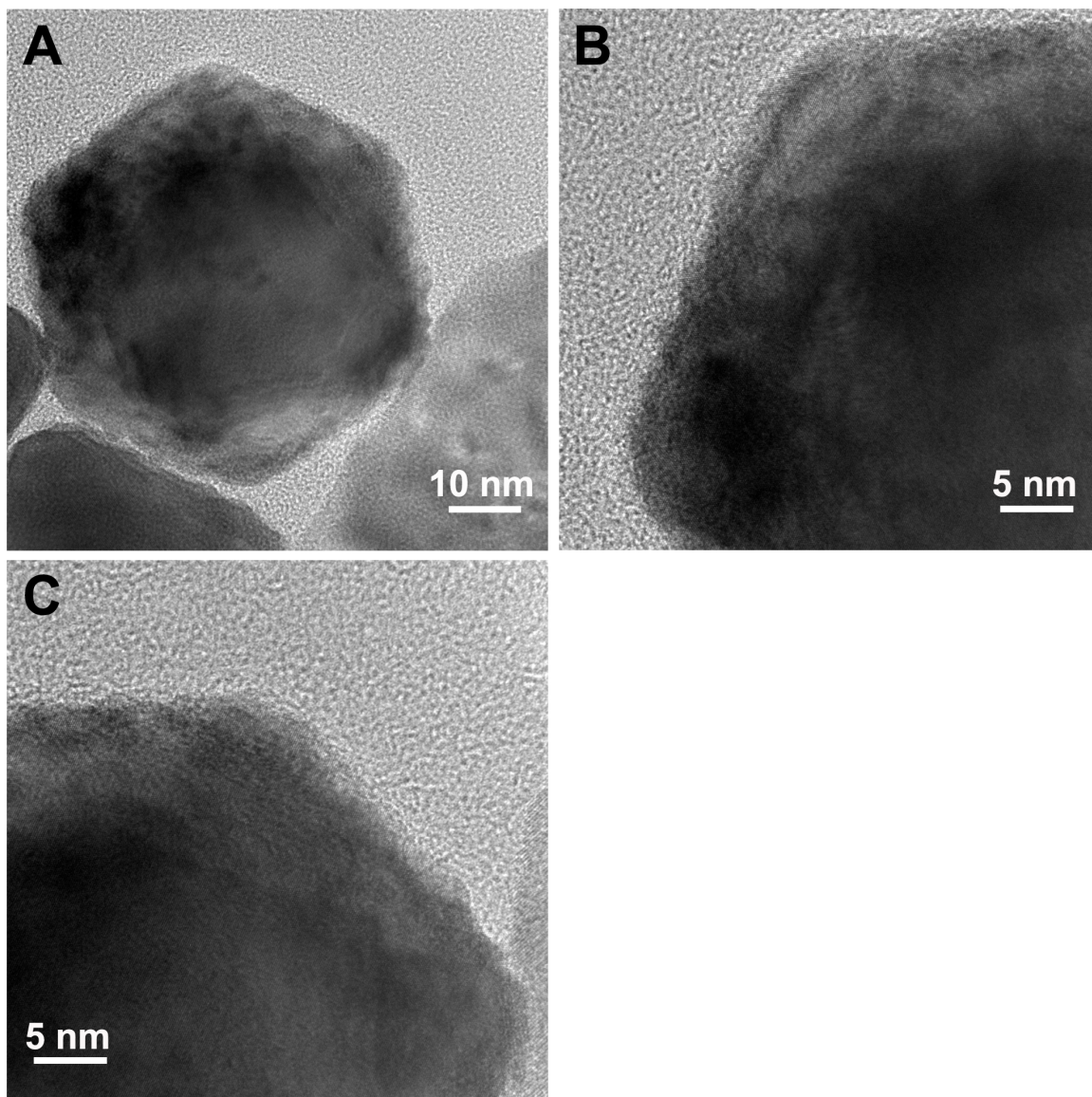


**Figure 2.10** (B-C) HRTEM images of the edges of the {111}-faceted AuPt octahedron in (A), showing the beginnings of some dendritic growth of Pt. The particle was imaged after 48 hours of growth.



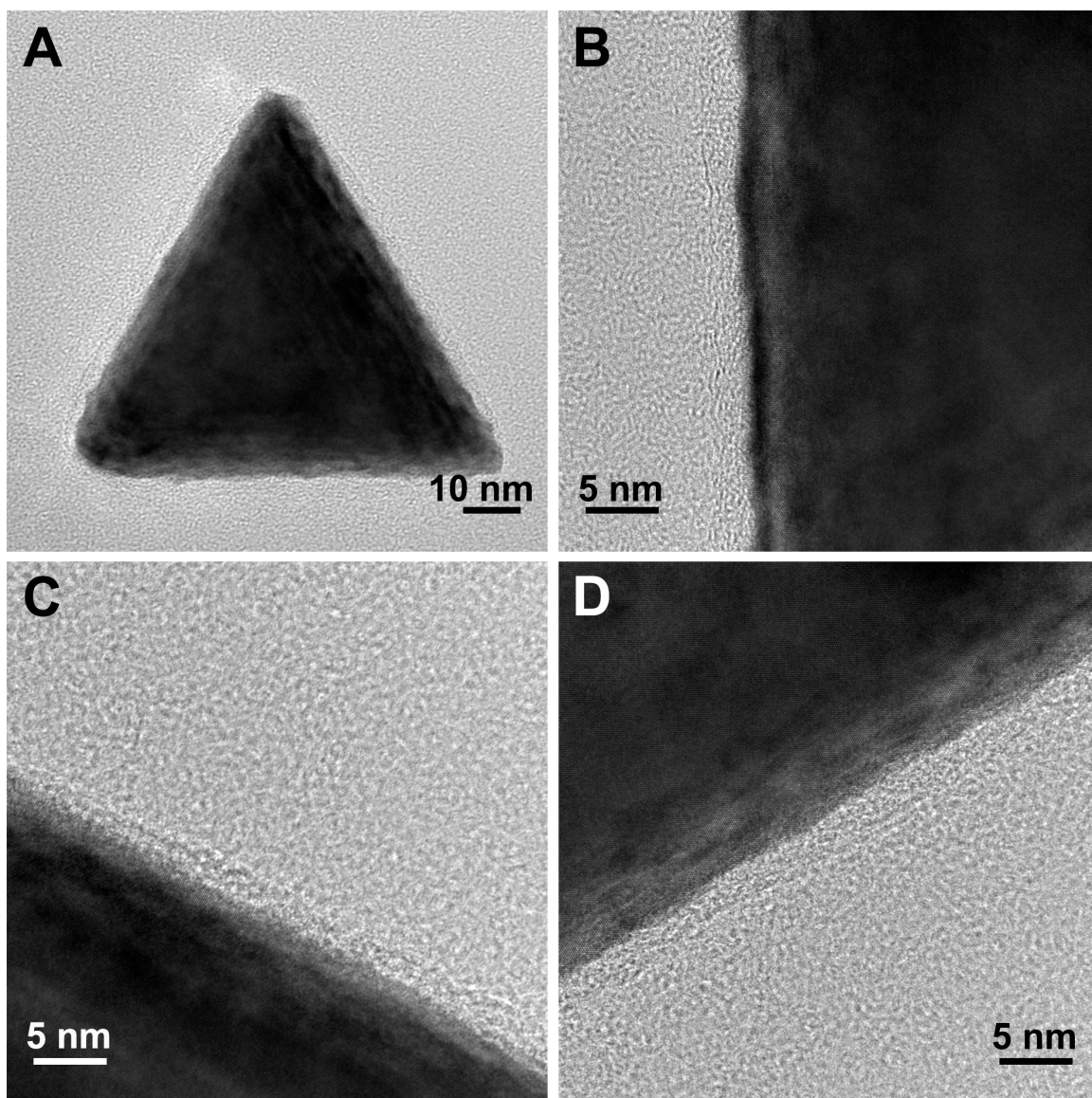


**Figure 2.11** (B-D) HRTEM images of the edges of the {111}-faceted AuPt truncated bipyramid in (A), showing largely epitaxial growth of Pt. The particle was imaged after 48 hours of growth.

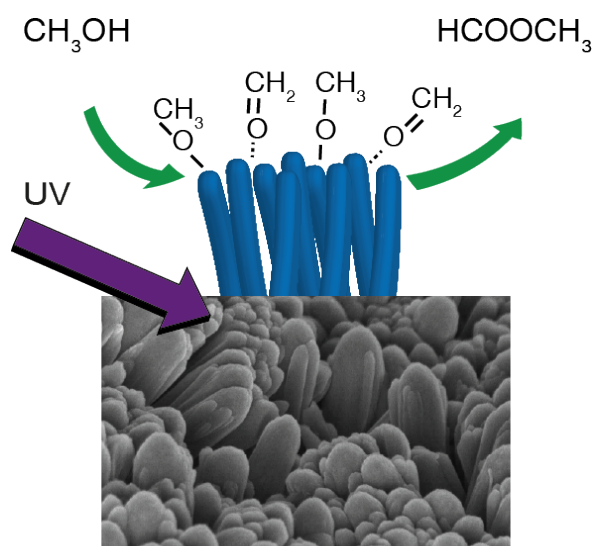
## 2.5 References

1. Biesinger, M. C.; Lau, L. W. M.; Gerson, A. R.; Smart, R. S. C., Resolving surface chemical states in XPS analysis of first row transition metals, oxides and hydroxides: Sc, Ti, V, Cu and Zn. *Applied Surface Science* **2010**, *257* (3), 887-898.
2. Yeh, J. J. L., I., Atomic Subshell Photoionization Cross Sections and Asymmetry Parameters:  $1 < Z < 103$ . *Atomic Data and Nuclear Data Tables* **1985**, *33*, 1-155.
3. King, M. E.; Personick, M. L., Defects by design: synthesis of palladium nanoparticles with extended twin defects and corrugated surfaces. *Nanoscale* **2017**, *9* (45), 17914-17921.
4. Stone, A. L.; King, M. E.; McDarby, S. P.; Robertson, D. D.; Personick, M. L., Synthetic Routes to Shaped AuPt Core-Shell Particles with Smooth Surfaces Based on Design Rules for Au Nanoparticle Growth. *Particle & Particle Systems Characterization* **2018**, 1700401.

## Chapter 3.

# Methanol Photo-Oxidation on Rutile TiO<sub>2</sub> Nanowires: Probing Reaction Pathways on Complex Materials

### 3.1 Abstract



Understanding photochemical processes on nanomaterials is key to developing effective photocatalysts. Herein, methanol oxidation and reduction is used to probe the thermal- and photo-chemical properties of rutile titania nanowires grown using a hydrothermal method. The presence of oxygen vacancy defects leads to methoxy formation and subsequent disproportionation to formaldehyde and methanol at 700 K. Methane and dimethyl ether are also produced in minor quantities. Oxygen adatoms enhance the formation of methoxy, which led to an increase in the disproportionation products and dimethyl ether at high

temperature, and a decreased amount of methane. The thermal reactivity of the nanowires parallels that of rutile TiO<sub>2</sub>(110) single crystals. Photo-oxidation of methoxy using UV light produced formaldehyde and methyl formate. These product yields were enhanced on nanowires with oxygen adatoms, but a majority of methoxy (~70%) is *not* photo-active. In contrast, all methoxy is photo-oxidized on rutile TiO<sub>2</sub>(110) when O-adatoms are present. This difference indicates that holes created in the nanowires during UV excitation do not migrate to most of the methoxy—a required step for methoxy photo-oxidation. This lack of activity could either be due to trapping of holes in the material or different binding of the inactive methoxy. These studies demonstrate that while charge carriers can be efficiently created in nanowires, differences in chemical properties can suppress photo-oxidation.

This paper was published in *J. Phys. Chem. C* **2017**, *121*, 9910-9919.

### **3.2 Introduction**

Transition metal oxide semiconductors, including TiO<sub>2</sub>, are an important class of materials for a wide variety of photocatalytic applications. In order to optimize their function as photocatalysts, an understanding of the critical reaction steps and the effect of materials properties, especially the presence of defects, is required. A major challenge is to develop insight into the fundamental behavior of nanomaterials. In recent years, there has been a revolution in the synthesis of nanostructured materials<sup>1</sup> so that controlled shapes and sizes are now routinely synthesized. Nanowires are particularly interesting as photocatalysts because they are designed to increase light absorption along their length while decreasing

the radial diffusion length to the surface of charge carriers (electrons and holes) created by light absorption (Fig. 1). At the same time, control of defects in these materials could prove to be challenging because defects can more readily be created through oxidation or reduction processes that occur via reaction at the surface because of the short radial length.

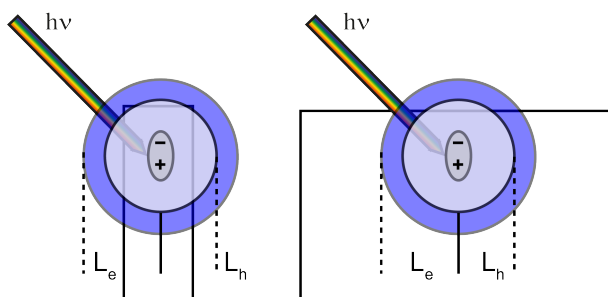


**Figure 3.1** Schematic depicting the advantage of nanostructuring a photocatalyst. On the left, the diffusion lengths for an electron ( $L_e$ ) and hole ( $L_h$ ) are now similar to the size of the material, meaning that the probability of an electron or hole to reach a surface site and initiate a reaction is enhanced. On the right, a single-crystal surface illustrates that there is a much higher probability of diffusion and recombination in the bulk. Additionally, the nanostructure has more exposed surface area which can absorb photons, thereby increasing the concentration of charge carriers.

Fundamental studies of metal-oxide single crystal surfaces provide a basis for understanding thermal and photochemical processes on a well-controlled material that can inform the design of nanomaterials.<sup>2-5</sup> A wide range of studies on rutile TiO<sub>2</sub>(110) single crystals have established a general framework for understanding photochemical transformations.<sup>6</sup> Various defects, including bridging oxygen vacancies ( $O_v$ ), O adatoms ( $O_{ad}$ ), and Ti interstitials, play a role in determining the selectivity and activity for

photochemical reactions on rutile TiO<sub>2</sub>(110).<sup>6-8</sup> Hence, titania is an excellent system for comparison of single crystals and nanomaterials.

The photo-oxidation of methanol has been extensively studied on TiO<sub>2</sub> single crystals and on high-surface-area materials, rendering it a good prototype for understanding both thermal and photocatalytic reactions.<sup>9-24</sup> The first step in methanol oxidation is the conversion to methoxy (CH<sub>3</sub>O<sub>ads</sub>).<sup>23</sup> Thermal reaction can occur at bridging oxygen vacancies, yielding methoxy bound to the vacancy site and bridging OH. Only a limited amount of methoxy is formed by this path because there are typically only a few vacancies (<10%) on the surface. Alternately, the O-H bond dissociation is enhanced by the presence of O<sub>ad</sub>. The alcoholic hydrogen is transferred to O<sub>ad</sub>, forming OH<sub>ads</sub> and CH<sub>3</sub>O adsorbed on a 5-coordinate Ti center; the formed OH<sub>ads</sub> reacts with a second methanol to yield another methoxy and water.<sup>9,16</sup> Methoxy can also form from photo-induced OH bond dissociation.<sup>10</sup>

Photo-oxidation of methoxy to formaldehyde occurs by hole-induced C-H bond transfer to a nearby bridging oxygen.<sup>10</sup> Time-dependent density functional theory studies show that the C-H bonds become acidic as the photo-generated hole migrates onto the methyl group.<sup>25</sup> While formaldehyde is the primary photo-product, secondary photochemical coupling with unreacted methoxy species can also occur to yield methyl formate.<sup>13,16,17</sup> The coupling depends on a relatively high density of methoxy species. The density of methoxy species in turn depends on the degree of reduction of the surface since formation of O<sub>ad</sub> is promoted by available charge from both surface and subsurface reduced species. Besides formaldehyde and methyl formate, dimethyl ether and methane are also produced thermo-chemically from methanol.<sup>19-22</sup>

Herein, we apply the tools of surface chemistry under ultra-high vacuum conditions to investigate the photo-oxidation of methanol induced by titania nanowires. Our objective is to build on the understanding of this model reaction as a means of probing the materials properties and photo-reaction efficiencies of the nanowires. Only one other study of the fundamental behavior of titania nanomaterials has been reported to date, in which methanol oxidation induced by anatase nanoparticles of varying size was investigated.<sup>22</sup> Reactivity similar to that of single crystals was observed; specifically, formaldehyde and methyl formate were produced after UV irradiation, as well as thermal reaction to form methane and dimethyl ether. These shape-controlled anatase particles contained mainly (101) facets and a minority of the (001) plane. On these particles, coupling of methoxy to form dimethyl ether was preferred on the minority (001) planes and attributed to four-fold Ti cation sites, defects or crystal edges. Methyl formate was posited to form from five-fold coordinated Ti sites on the (101) planes.

Our work shows that the thermal and photochemical reactions of methanol on rutile titania nanowires are qualitatively similar to the previously studied anatase particles and that these reactions can be understood from studies of the rutile single crystal. There are, however, differences compared to single crystals. Specifically, methyl formate evolved near room temperature (315 K) is produced at the expense of dimethyl ether, demonstrating that the key reactive site is one which facilitates bimolecular coupling on nanowires. Additionally, reactivity trends of the nanowires are used to sensitively gauge the defect density in the nanowires through chemical methods. This study demonstrates how understanding of key reactions on well-defined single crystals can be used to probe the properties of

nanomaterials so as to potentially optimize their properties for efficient and selective reactions.

### **3.3 Methods**

The rutile TiO<sub>2</sub> nanowire arrays were synthesized on Ti foil substrates (Goodfellow, >99.6 %) using the previously reported hydrothermal method with modification.<sup>26</sup> The Ti foils were first cleaned by sonication in acetone, methanol and isopropyl alcohol, and then rinsed in water, and finally dried in air. For a typical synthesis, 0.2 mL of titanium(IV) butoxide (Aldrich Chemicals, 97%) was added into 12 mL of an aqueous HCl solution (6 mL of deionized (DI) water + 6 mL of concentrated HCl (38%)) under magnetic stirring. After stirring for 10 min, the solution was poured into a Teflon-lined stainless steel autoclave (80 mL capacity), and pieces of the Ti foil substrates were immersed in the solution. The autoclave was sealed and heated to 135 °C in an oven, and it was held at 135 °C for 12 h and then cooled to room temperature naturally. The obtained samples were washed with ethanol and DI water, and finally annealed at 450 °C for 1 h in air.

The TiO<sub>2</sub> nanowires were characterized by scanning electron microscopy (SEM) (Zeiss Supra 55VP microscope) and X-ray photoelectron spectroscopy (XPS) (Thermo Scientific K-Alpha XPS system; monochromatic Al K $\alpha$  source). Raman spectra were measured with a Horiba LabRAM HR Evolution Spectrometer using the 532 emission of a Laser Quantum Ventus diode pumped solid state laser with a 10 % neutral density filter.

The reactivity measurements were performed in an ultrahigh vacuum (UHV) chamber with a base pressure of < 10<sup>-10</sup> Torr. Tungsten wires (0.125 mm dia., Goodfellow)



were affixed (Aremco, Ceramabond 569) directly on the back of the Ti-foil to mount on the sample holder and for heating and cooling with liquid nitrogen. The temperature was measured by a type-K thermocouple affixed to the back of the substrate. The sample was annealed for 10 minutes at 800 K for cleaning and for preparation of the vacuum annealed surface. No impurities other than adventitious carbon (see Figure 3.9 in the supporting information) were detected using *ex situ* XPS either before or after use in the UHV system. Methanol (Sigma Aldrich,  $\geq 99.98\%$  purity) was dosed at 300 K using a directional dosing apparatus attached to a leak valve after several freeze-pump-thaw cleaning cycles. Each dose was performed for 20 s; by changing the dosing time the coverage was estimated to be 0.7 times the saturation coverage at 300 K, where saturation is defined as the maximum methanol (31 m/z) signal achieved when dosing at 300 K. The sample was positioned < 5 mm from the doser during adsorption. Oxygen (Airgas, 4.4 purity) was dosed at 300 K in a similar fashion, but a background pressure of  $5 \times 10^{-7}$  Torr was established for 5 mins in order to ensure a saturation coverage. This preparation was performed after annealing at 800 K and generates the O<sub>ad</sub> surface.

The temperature programmed reaction (TPR) measurements were performed using a Hiden HAL 301 RGA quadrupole with the temperature ramp controlled by a Eurotherm 2404 PID controller. Quantitative analysis was performed by taking into consideration fragmentation pattern, transmission coefficients, and ionization cross section.<sup>27</sup> This allows for a complete quantitative analysis of the measured product signals. The methanol fragmentation pattern was measured using the methanol multilayer peak at 200 K. The source for UV-illumination was a 300 W Xe lamp with a 400 nm short pass filter (3.1 eV) purchased from Asahi Spectra to match the band gap of TiO<sub>2</sub>. The flux at the surface was

previously determined to be 92 mW/cm<sup>2</sup>, 14% of which is >400 nm.<sup>28</sup> The nanowires were held at 200 K using liquid nitrogen and irradiated for 5 minutes unless otherwise noted.

## 3.4 Results and Discussion

### 3.4.1 Nanowire Characterization

Previous characterization of the titania nanowires synthesized using this hydrothermal method determined that they have (110) facets exposed on their sidewalls and (100) planes comprising the tip.<sup>26,29</sup> The titania nanowires used for this study are several microns long with an average diameter of 169 ±23 nm. *Ex situ* analysis shows that they are not substantially altered following investigation under ultrahigh vacuum conditions (Figure 3.2). There is little change in their morphology after multiple reaction cycles (~ 150 methanol temperature programmed cycles involving heating to 800 K): the average wire diameter measured using SEM after prolonged investigation in UHV is 182 ±23 nm.

The titania nanowires are predominantly rutile based on the characteristic Raman peaks observed at 447 and 611 cm<sup>-1</sup> (Figure 3.2c).<sup>30</sup> No peaks characteristic of anatase, which would be signified as a very intense peak at 145 cm<sup>-1</sup> and others at 639, 515 and 396 cm<sup>-1</sup>, were detected.<sup>31</sup> X-ray photoelectron spectra indicate that there is no dramatic change in the overall Ti oxidation state based on the binding energies of the Ti 2p peaks (2p<sub>3/2</sub> =458.6 eV, 2p<sub>1/2</sub> =464.3 eV) which are the same before and after the extended studies of reactivity in the UHV chamber (Figure 3.2d). These peak positions and separation both correspond to literature values.<sup>32</sup> Because these measurements are made *ex situ*, reduced Ti

### Chapter 3. Methanol Photo-Oxidation on Rutile TiO<sub>2</sub> Nanowires: Probing Reaction Pathways on Complex Materials

at the surface could be healed by exposure to air, so that subtle changes in the surface due to reaction may not be detected. The electron mean free path at these kinetic energies is  $\sim 2$  nm, so that defects deeper in the material will not be detected.

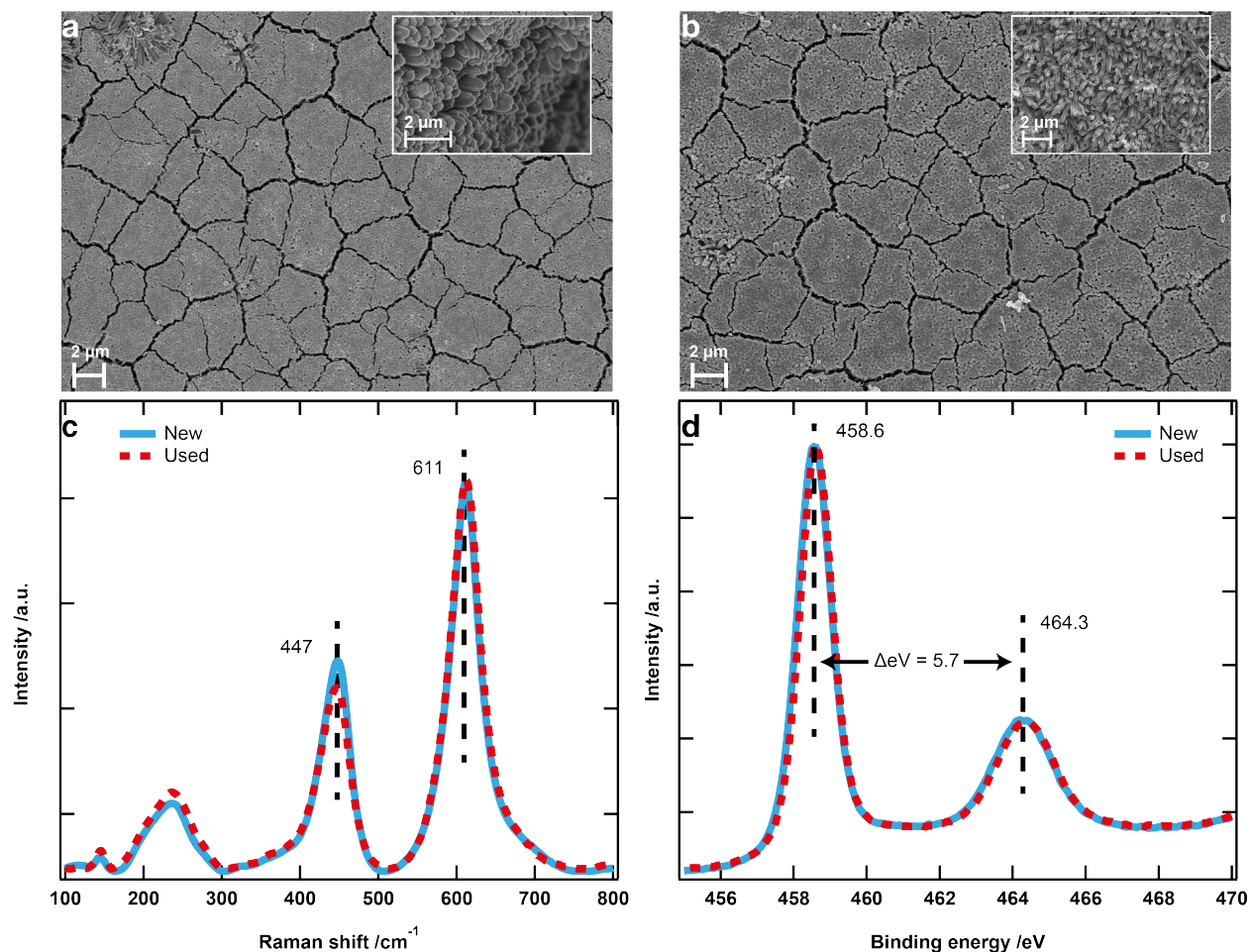


**Figure 3.2** Physical characterization of the titania nanowires shows that they are highly oriented and that the predominant phase is rutile. Exemplary SEM images of the nanowire films (a) before and (b) after use in the UHV chamber. Insets: magnified views of the nanowires show their orientation. (c) Raman spectra showing peaks at 444 ( $E_g$ ) and 611  $\text{cm}^{-1}$  ( $A_{1g}$ ), characteristic of rutile TiO<sub>2</sub>. The spectra are essentially the same before and after use. (d) X-ray photoelectron spectra for the Ti 2p region

manifest peaks at 458.6 and 464.3, characteristic of TiO<sub>2</sub>, with no shoulder at lower binding energy characteristic of Ti<sup>3+</sup> or other reduced states. There is no discernable change in the spectra before and after the reactive studies. All measurements were made *ex situ*.

### **3.4.2 Oxygen Adsorption and Photo-Desorption**

Oxygen adatom (O<sub>ad</sub>) formation is mediated through vacancies and interstitials on the titania nanowires either through thermal dissociation of O<sub>2</sub> at room temperature or via photodissociation at lower temperature. Molecular oxygen interaction with the vacuum-annealed nanowires is similar to TiO<sub>2</sub> single crystals which indicates the presence of oxygen vacancy defect sites. After exposure of the nanowires to O<sub>2</sub> below 200 K, an oxygen desorption feature at 435 K is observed (Figure 3.3, curve a). Previous studies on rutile TiO<sub>2</sub>(110) attributed this state to loss of one O<sub>2</sub> from a cluster of three chemisorbed O<sub>2</sub> adsorbed near an oxygen vacancy.<sup>33-35</sup> The remaining two oxygen molecules heal the surface defect, so that the molecular desorption state cannot be repopulated without annealing to 800 K in vacuum to reduce the material.<sup>34</sup> The conditions used for the desorption experiments were insufficient (T<sub>max</sub>= 700 K, dwell time of a few seconds) to regenerate the oxygen vacancies required for population of the “chemisorbed” O<sub>2</sub> state; thus, there is very little desorption in a sequential experiment in which O<sub>2</sub> was exposed to the surface under the same conditions (Figure 3.3, curve b).

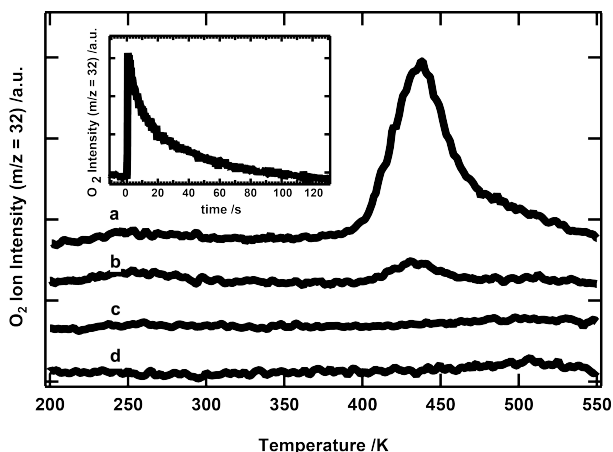


**Figure 3.3** Dioxygen temperature programmed desorption from the vacuum annealed nanowires is used to probe conditions for O<sub>2</sub> dissociation and photo-desorption (inset). The peak at 435 K is attributed to a strongly-bound state, (a) is observed when O<sub>2</sub> is exposed to the nanowires below 200 K. This peak is substantially reduced in intensity following a sequential exposure to O<sub>2</sub> under the same conditions (b), suggesting that the sites for O<sub>2</sub> binding were healed by the first exposure. Adsorption below 200 K followed by photo-stimulated desorption (inset), also leads to the disappearance of this chemisorbed state (c). There is very little O<sub>2</sub> desorption following exposure of dioxygen to the nanowires at 300 K, suggesting dissociation forming O<sub>ad</sub> species and no molecular chemisorbed species (d). The maximum temperature in the desorption experiments was 700 K and the dwell time at 700 K only a few seconds.

The “chemisorbed” O<sub>2</sub> created by exposure of dioxygen to the nanowires is not detected after exposure to ultraviolet (UV) photons, based on the depletion of the 435 K desorption state and the associated observation of O<sub>2</sub> in the gas phase when the material is irradiated (Figure 3.3 inset). Prior studies of single crystals attribute the photodesorbed O<sub>2</sub> to loss from five-fold coordinated Ti sites (Ti<sub>5c</sub>).<sup>36</sup> There is no detectable thermal desorption of O<sub>2</sub> after exposure to UV light (Figure 3.3, curve c), in agreement with previous work.<sup>37</sup>

This demonstrates that either the photoactive molecule is responsible for desorption feature at 435 K or some other photo-induced process has consumed the chemisorbed species. Currently, the interpretation is that either molecular O<sub>2</sub> bonded at an oxygen vacancy can photodissociate, or it is photoinactive<sup>36,38</sup>, with the photodissociation pathway, supported by our data, leading to the oxygen atoms healing the defect and bonding to a Ti<sub>5c</sub> site.

The O vacancies are also healed by exposure of the reduced nanowires to O<sub>2</sub> at 300 K. Dissociation of O<sub>2</sub> on single crystal TiO<sub>2</sub>(110) heals bridging oxygen vacancies at the surface; the second O forms an O<sub>ad</sub> on a neighboring Ti site.<sup>39</sup> There is no appreciable desorption of O<sub>2</sub> at 435 K after exposure of the nanowires to O<sub>2</sub> at 300 K (Figure 3.3, curve d). This result indicates that O<sub>ad</sub> are produced by exposure of the nanowires to dioxygen at 300 K, by analogy to single crystal studies.

Taken together, these results show that O adatoms are created on the nanowires either through thermal dissociation or via photodissociation of O<sub>2</sub>. The creation of O<sub>ad</sub> and chemisorbed O<sub>2</sub> is indicative of defects in the nanowire material that can be healed in the near-surface region by O<sub>2</sub> dissociation. These conclusions are based on the strong correspondence in the behavior of the nanowires to single crystal rutile TiO<sub>2</sub>(110). Creation of O<sub>ad</sub> is expected to alter the photochemical behavior of the nanowires and forms a basis for comparing reactivity based upon their presence.

### **3.4.3 Methanol Thermal and Photocatalysis on TiO<sub>2</sub> Nanowires**

Nanowires subjected to vacuum annealing are active for methanol photo-oxidation, yielding formaldehyde and methyl formate in temperature programmed reaction following exposure

to UV light (Figure 3.4a), indicating that defects are present. The behavior of the nanowires is similar to rutile TiO<sub>2</sub>(110).<sup>13,16</sup> The activity for photo-oxidation of methanol is evaluated based on the appearance of new peaks assigned to formaldehyde and methyl formate slightly above 300 K and the corresponding depletion of peaks at ~700 K that are characteristic of thermal decomposition of methoxy (Figures 3.4a and 3.4c). Methanol (green) is mainly evolved thermally in a peak at 365 K, with a small feature (~10 %) at ~700K (Figure 3.4a, solid). The methanol peak at ~700 K coincides with the production of formaldehyde (orange). These features are attributed to thermal disproportionation of methoxy in analogy to prior studies of single crystal rutile titania.<sup>9,16,40</sup> The disproportionation is a signature of defects, including bridging oxygen vacancies and Ti interstitials, in rutile TiO<sub>2</sub>(110). In the absence of illumination, there are no products detected below 350 K, the onset of methanol evolution.

Exposure to UV light lead to small amounts of formaldehyde and methyl formate production at ~300 K and 315 K, respectively (Figures 3.4a and 3.4c). There is minimal change in the higher temperature features characteristic of thermal chemistry ( $\leq 10\%$ ) compared to without irradiation. The data shown are corrected for mass spectrometer transmission, detector efficiency, ionization cross section and fragmentation,<sup>27</sup> (Figure 3.4c). These results are generally consistent with studies of single crystal rutile TiO<sub>2</sub>(110) in that there is limited photochemical reaction on defective, as-prepared material.

Chapter 3. Methanol Photo-Oxidation on Rutile TiO<sub>2</sub> Nanowires: Probing Reaction Pathways on Complex Materials

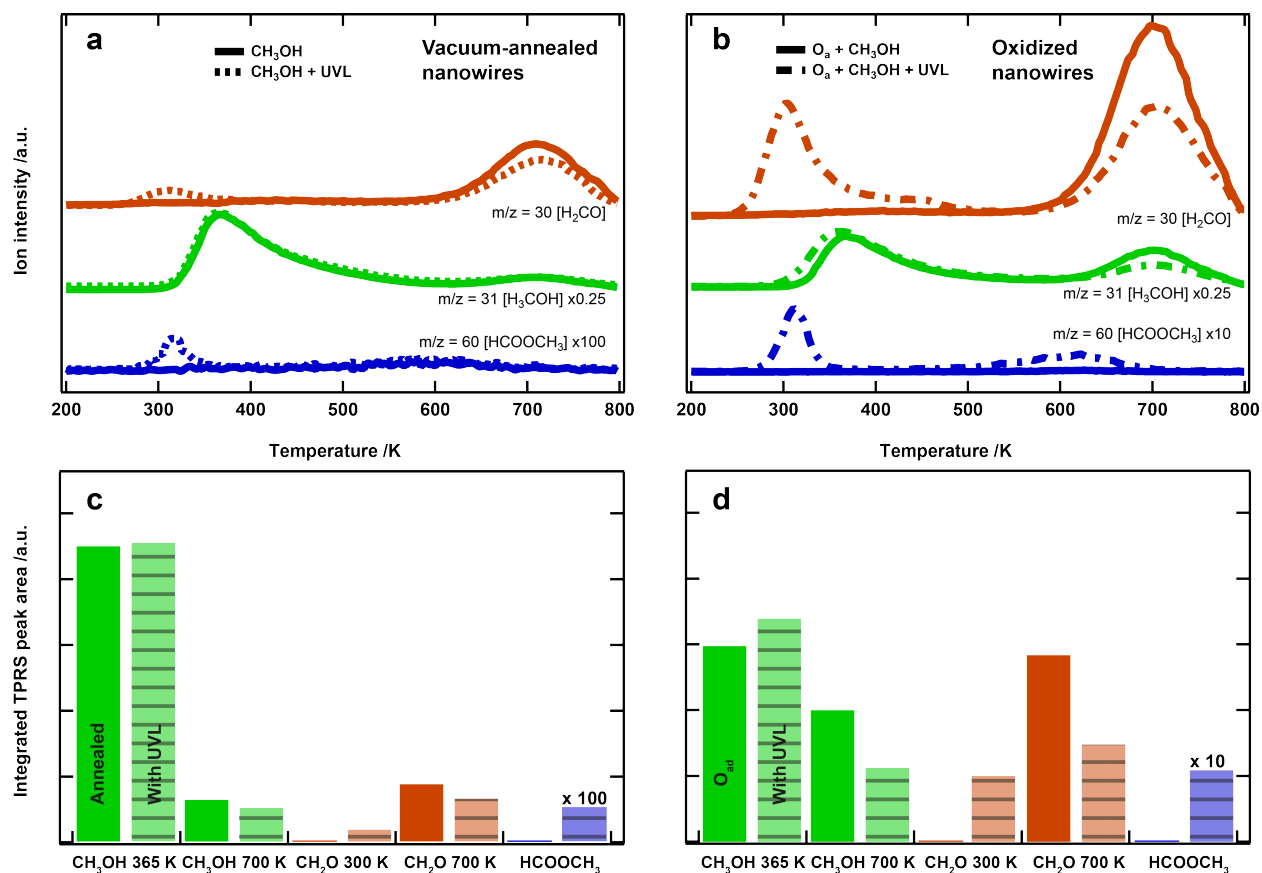


**Figure 3.4** Photo-oxidation of methanol is demonstrated by comparison of temperature programmed reaction spectra obtained either without exposure to light (solid curves) or after light exposure (dashed lines). (a) Vacuum annealed nanowires and (b) nanowires containing oxygen adatoms (O<sub>ad</sub>). The O adatoms were created by exposure of the nanowires to O<sub>2</sub> (150 L; 1L=10<sup>-6</sup> torr•s) at 300 K. Quantitative analysis of the temperature programmed reaction data in (a) and (b) are depicted in (c) and (d), respectively. The results are corrected for mass spectrometer transmission, detector efficiency, ionization cross section and fragmentation.<sup>27</sup> All graphs are plotted on the same y-axis scale for direct comparison; the baselines of the various products are offset for clarity. Exposure to UVL at 200 K for 5 minutes from a xenon lamp with a short pass 442 nm filter was used for both cases (92 mW/cm<sup>2</sup>). The formaldehyde traces, m/z = 30, have been corrected for methanol fragmentation (see Methods for detail). In all experiments, the same dose of methanol was



### *Chapter 3. Methanol Photo-Oxidation on Rutile TiO<sub>2</sub> Nanowires: Probing Reaction Pathways on Complex Materials*

used (0.7 saturation at 300 K) and the crystal was subsequently cooled to 200 K prior to the experiments. The protocols used for these experiments were selected based on prior studies of rutile TiO<sub>2</sub>(110).

The thermal and photo-oxidation of methanol are enhanced by the presence of O<sub>ad</sub> on the nanowires (Figures 3.4b and 3.4d). In the absence of light, the formaldehyde and methanol peaks, characteristic of methoxy disproportionation at ~700 K, all increase by a factor of three relative to the vacuum-annealed surface (Figures 3.4b and 3.4d). This indicates an increase in the formation of adsorbed methoxy which is similar to single crystal rutile titania.<sup>9,16,19</sup> There is also less methanol evolution at 365 K. When O adatoms react with methanol at 300 K on rutile TiO<sub>2</sub>(110), water is formed and evolved into the gas phase, creating two methoxy species for each O<sub>ad</sub> originally on the surface;<sup>16</sup> hence, the amount of molecular methanol that desorbs is depleted (see Table 3.2 for complete integration results of all products).

The yields of photoproducts, formaldehyde and methyl formate, evolved below 350 K after exposure to UV light, are increased when O<sub>ad</sub> are present (Figures 3.4b and 3.4d). The formaldehyde yield increased by a factor of ~5 and the methyl formate yield by more than an order of magnitude. A similar pattern of reactivity was observed on single crystal; however, the relative yields of methyl formate to formaldehyde generated photo-chemically is lower on the nanowires.<sup>13,16</sup>

There is also a new broad methyl formate feature at ~600 K that accounts for ~40% of its total yield (Figure 3.4b, blue, dash-dot). Formaldehyde and methyl formate evolved at

lower temperature are attributed to primary photoproducts formed during exposure to UVL. In contrast, the higher temperature methyl formate peak must be due to thermal reaction of a photoproduct formed at lower temperature.

Quantitative analysis clearly demonstrates that O<sub>ad</sub> enhances the formation of methoxy via thermal reaction, based on the yields of disproportionation products (formaldehyde and methanol) at higher temperature, analogous to single-crystal TiO<sub>2</sub>(110) where this reaction path was only observed in the presence of oxygen.<sup>9,40</sup> Our results differ in that the vacuum annealed sample shows appreciable high temperature disproportionation, in contrast to the single crystal where this reaction pathway was not observed.<sup>9,16</sup> This reaction path is likely due to reactive sites on the nanowires that remain active for methoxy formation.

The yields of the photoproducts formed at 300 K (formaldehyde and methyl formate) increase with the time of exposure to UV light with the largest change occurring in the first minute of exposure (Figure 3.5). Without any UV irradiation, there is no formaldehyde detected below 600 K and no detectable methyl formate (Figures 3.4 and 3.5). The yields of formaldehyde and methyl formate at 300 K grow quickly in the first minute of light exposure. The yields level off after 5 minutes of light exposure and the ratio between methyl formate and low temperature formaldehyde remains approximately 1:10. Additionally, the high-temperature formaldehyde peak decreases as a function of UV exposure, indicating that its precursor, methoxy, is converted to formaldehyde by a photon induced process.

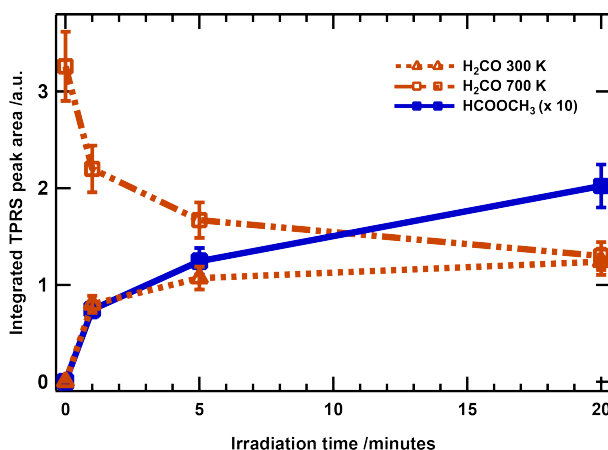


**Figure 3.5** The yields of photoproducts—formaldehyde (orange) and methyl formate (blue)—increase as a function of the time of UV irradiation following methanol dosing on titania nanowires containing O<sub>ad</sub>. The error bars represent an 11 % error based on the standard deviation of methyl formate yield from repeated experiments after 5 minutes of irradiation. The surface was prepared by vacuum annealed and subsequent exposure to O<sub>2</sub> at 300 K. Photolysis was carried out after cooling the sample to 200 K so that photoproducts are trapped on the surface. Exposure to UVL was performed with a xenon lamp with a short pass 442 nm filter was used for all experiments (92 mW/cm<sup>2</sup>). No temperature rise was observed during irradiation.

Methoxy, is only partially converted to formaldehyde by exposure to UV light indicating that some of the methoxy bound to the nanowires is not photo-active. In contrast, all methoxy can be photo-oxidized on single-crystal TiO<sub>2</sub>(110).<sup>16</sup> On the nanowires the majority of formaldehyde formed from exposure to UV light is observed within the first minute, and only increases by a factor of three after 20 minutes of irradiation. Thus, only a fraction (~30%) of the methoxy is efficiently photo-oxidized, indicating that there are at least two different methoxy binding environments. Methoxy on single-crystal TiO<sub>2</sub>(110) is

completely converted to photo-products after only five minutes of UV exposure under the same conditions.<sup>16</sup>

Aside from increasing the concentration of methoxy, the effect of oxygen on the photo-oxidation of methanol to methyl formate has also been previously rationalized as removing possible hole trap surface vacancies.<sup>16</sup> This behavior has been experimentally and theoretically demonstrated for trimethyl acetate on TiO<sub>2</sub>(001).<sup>41</sup> Our results could be influenced by this effect, but also show that, in the absence of O<sub>ad</sub>, nanostructuring the material does not lead to a quenching of the photo-oxidation reaction pathway. This could be attributed to the increase in the concentration of charge carriers reaching the surface which can drive the reaction, the attenuation of bulk recombination and the increase in the surface concentration of methoxy evidenced by the high temperature methoxy disproportionation products on the vacuum annealed nanowires.

Water, dimethyl ether and methane (Figure 3.6) are also produced from reaction of methoxy on the nanowires. These products are characteristic of {110} (methane and water) and (114) faceted TiO<sub>2</sub>(001) surfaces<sup>21</sup>, a TiO<sub>2</sub>(110) surface (methane and water)<sup>19</sup> and nanocatalysts/powders.<sup>20,22</sup> Dimethyl ether was identified by the m/z 45:46 ratio measured in the fragmentation pattern of the product during reaction (see Figure 3.10). Methane was identified based on the m/z 16:15 ratio and on the basis of the isotopic shift to m/z 20 under identical reaction conditions for d<sub>3</sub>-methanol. Isotopic labeling excludes the m/z 16 peak as being due to methyl radical desorption followed by reaction with background hydrogen.<sup>42</sup>

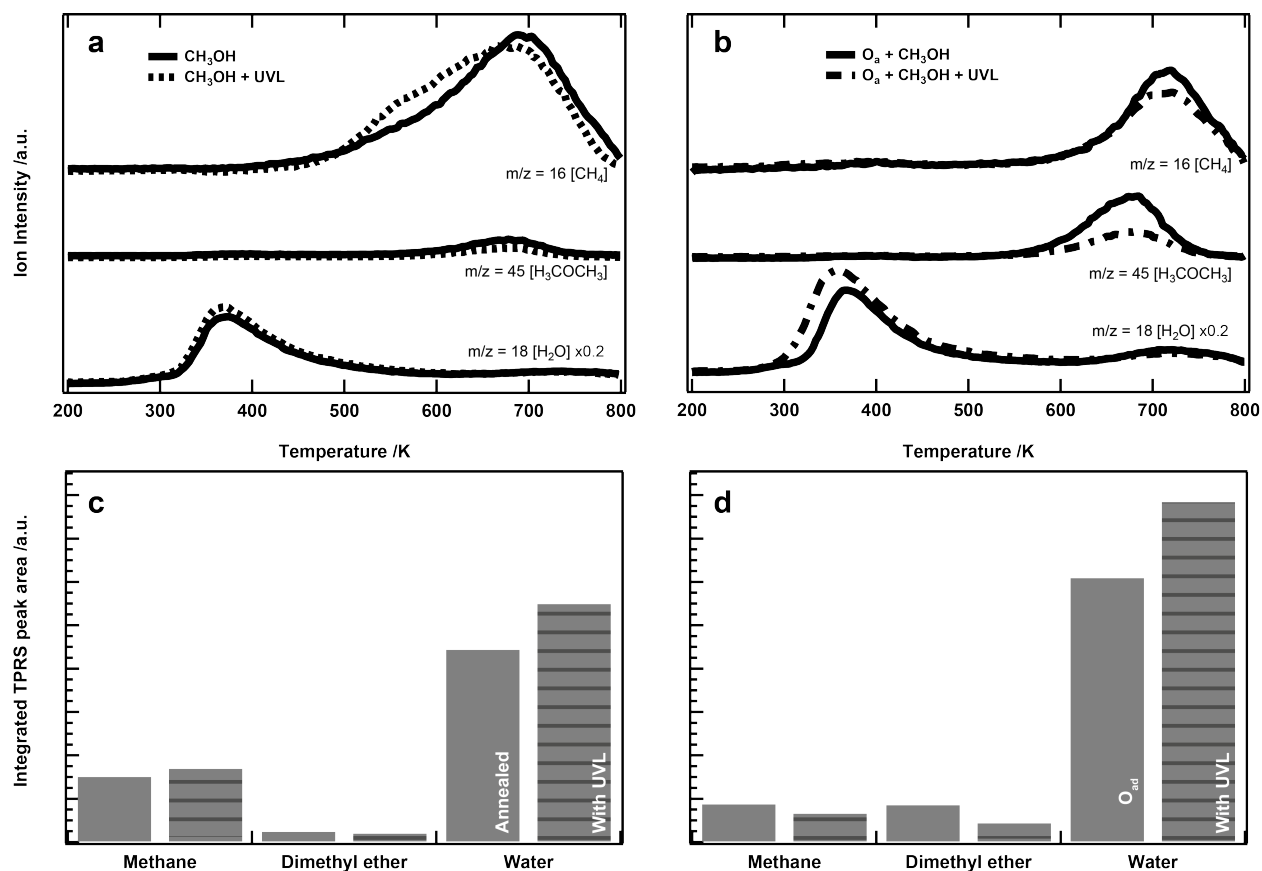


**Figure 3.6** Methane, dimethyl ether and water are all evolved during temperature programmed reaction both from (a) vacuum annealed nanowires and (b) nanowires containing O<sub>ad</sub>. The yield of water increases by exposure to UV light as is apparent from comparison of the data without (solid curves) and subsequent to exposure to UVL at 200 K for 5 minutes (dashed lines) from a xenon lamp with a short pass 442 nm filter (92 mW/cm<sup>2</sup>). Methane and dimethyl ether both decrease on the O<sub>ad</sub> surface due to UV light exposure, but methane increases and dimethyl ether decreases on the vacuum annealed surface. The baselines for the various products are offset for clarity.

Water evolution peaks at a temperature of 370 K (Figures 3.6a and 3.6b) which is attributed to recombination of adsorbed OH species produced from methoxy formation based on previous studies.<sup>19,40</sup> There is also a small water peak at ~715 K for the surface

containing O<sub>ad</sub> (Figure 3.6b). Quantitative analysis of the amount of water generated from the vacuum annealed surface is in good agreement with the total amount of water formation expected (Table 3.1). The amount of water formation is predicted by quantifying the reaction products that have lost hydrogen atoms, presumably by transfer to O or OH.<sup>10,16,19</sup> This corroborates the assertion that methoxy leads to all thermal reaction products on the vacuum annealed surface in the absence of UV light.

In contrast, there is significant loss of water formed on the surface containing O<sub>ad</sub> during dosing at 300 K. The measured amount of water from the surface containing O<sub>ad</sub> is 1.22 compared to a predicted amount of ~3, indicating that water desorbs during methoxy formation from methanol at 300 K. This explanation is based on prior studies of rutile TiO<sub>2</sub>(110)<sup>16</sup> and is also supported by an observed shift in the water desorption peak with increasing water coverage (Figure 3.11). As we expect close to three times the amount of water to be evolved from the O<sub>ad</sub> surface, OH recombination already at 300 K is likely great enough to induce this discrepancy.

**Table 3.1** Quantitative analysis of the predicted and measured amount of water formed using data in Figures 2 and 3. All values represent absolute number densities of molecules.

surface	species	dark integral	UV integral
	Methoxy <sup>a</sup>	1.73	1.34
	300 K H <sub>2</sub> CO	-	0.21
Vacuum Annealed	Dimethyl ether	0.04	0.03

Chapter 3. Methanol Photo-Oxidation on Rutile TiO<sub>2</sub> Nanowires: Probing Reaction Pathways on Complex Materials

	<b>Expected H<sub>2</sub>O<sup>b</sup></b>	0.95	0.91
	Actual H <sub>2</sub> O	0.89	1.10
	Methoxy <sup>a</sup>	5.56	2.99
	300 K H <sub>2</sub> CO	-	1.15
O <sub>ad</sub>	Dimethyl ether	0.17	0.07
	<b>Expected H<sub>2</sub>O<sup>b</sup></b>	2.95	2.97
	Actual H <sub>2</sub> O	1.22	1.57

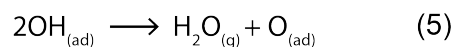
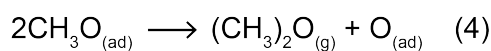
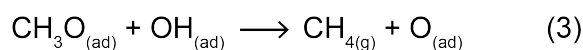
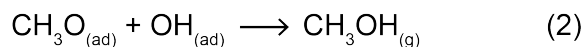
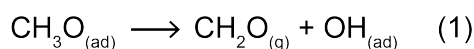
<sup>a</sup>The sum of the methanol and formaldehyde peak integrals at ~700 K.

<sup>b</sup>The sum takes into consideration the stoichiometry of each species, methoxy:H<sub>2</sub>O = 2:1; 300 K H<sub>2</sub>CO: H<sub>2</sub>O = 1:1; dimethyl ether: H<sub>2</sub>O = 1:1. In the case of the O<sub>ad</sub> surface, the contribution of methyl formate was included for the UV exposed surface (1:2 H<sub>2</sub>O).

The low-temperature water peak increases upon exposure of the two different surfaces to UV light following exposure to methanol at 300 K, indicating that OH is formed during photolysis (Figure 3.6). On the vacuum annealed surface, the amount of water produced is increased by ~24% after light exposure; from 0.89 to 1.10 (Table 3.1). On the surface containing O<sub>ad</sub>, an increase of ~29% is measured after photolysis of methanol. We attribute this increase in water formation primarily to production of formaldehyde through transfer of H to a bridging O.<sup>25</sup> Note also that the onset of water evolution is somewhat lower after photolysis of CH<sub>3</sub>OH on the surface containing O<sub>ad</sub>, which is consistent with the shift in water desorption to lower temperature with coverage.

The minority reaction products, methane and dimethyl ether, are part of a reaction network available to methoxy at high-temperature (Scheme 3.1). Reaction 1 and 2 represent the well-known disproportionation pathway to form formaldehyde and methanol, respectively. These reactions do not produce any hydrogen or healing of defects. Methane formation, reaction 3, results in the healing of a defect site while also consuming a hydrogen. Dimethyl ether, reaction 4, entails the healing of a defect site and is hydrogen neutral.

**Scheme 3.1** Methoxy reaction pathways at high-temperature.



Our data demonstrate a preference for methane formation on the vacuum-annealed nanowires. Methane production has been attributed to the presence of methoxy decomposition at defects on rutile TiO<sub>2</sub>(110).<sup>19</sup> This points to defect concentration being an essential factor regarding methane formation as the process results in the healing of O<sub>v</sub>. In the same study, co-adsorbed oxygen (dosed after methanol) led to an increase in the temperature for methane evolution and a smaller yield indicating that the removal of surface defects inhibits this reaction pathway.<sup>19</sup>



Stoichiometric methoxy disproportionation would yield a 1:1 correlation between methanol and formaldehyde at high-temperature, which was not observed. However, the amount of methane and methanol produced on the vacuum-annealed nanowires at high-temperature does have a 1:1 correspondence with the amount of formaldehyde in the same temperature range. This demonstrates that reactions 1, 2 and 3 are coupled through the common methoxy intermediate on the vacuum-annealed nanowires, with hydrogen production from formaldehyde producing both methanol and methane, and methane healing a  $O_v$  defect site. On the  $O_{ad}$  surface the correlation is 0.92:1 (taking into consideration high-temperature water, and methyl formate, evolution), still indicating a strong correlation (See Table 3.2 for complete integration results of all products).

Without UV exposure, methoxy on the  $O_{ad}$  nanowires shows a higher propensity to form dimethyl ether compared to the vacuum-annealed nanowires. This increase in the amount of methoxy converted to dimethyl ether matches the decrease in methane observed (1.2:1), demonstrating that the precursor for dimethyl ether,  $CH_3O_{(ad)}$ , on the  $O_{ad}$  surface preferentially forms methane on the vacuum-annealed surface in the presence of  $O_v$ .

The analysis of the minority products demonstrates that higher concentrations of  $O_v$  defect sites lead to methoxy disproportion to form formaldehyde, methanol and methane (reaction 1,2 and 3) with a small amount of dimethyl ether on the vacuum-annealed surface. With  $O_{ad}$ , methoxy prefers reaction 1,2 and 4, i.e. more methanol and dimethyl ether, but less methane, and the increase in dimethyl ether corresponds directly to the decrease in methane. These trends demonstrate again the essential role which  $O_v$  defects play on the chemistry of TiO<sub>2</sub> nanowires.

UV exposure on the vacuum-annealed surface leads to a minor decrease in the amount of dimethyl ether produced; increasing the amount methane. These results are qualitatively similar to Bennett *et al.* in their study on anatase TiO<sub>2</sub> nanocrystals, albeit our differences are close to negligible.<sup>22</sup> On the O<sub>ad</sub> surface we observe a clear decrease in dimethyl ether after UV exposure, and a small decrease in methane. The decrease in dimethyl ether production on the O<sub>ad</sub> surface signifies that its precursor is photo-activated to form another species.

The depletion of dimethyl ether upon exposure to UV light on *both* surfaces is similar to the amount of methyl formate evolved (excluding the high temperature feature on the O<sub>ad</sub> surface): 1.25:1 and 1.38:1 for the vacuum annealed and O<sub>ad</sub> surface, respectively. Varying the UV exposure time on the O<sub>ad</sub> surface supports the correlation between dimethyl ether and methyl formate evolved at 300 K. The quantitative integrals of these two species on the O<sub>ad</sub> surface (Table 3.3), reveals that the sum of dimethyl ether and methyl formate at 300 K remains approximately equal, irrespective of UV exposure time.

This quantitative treatment is strong evidence that the adsorbed state of methoxy on the nanowire surface which forms dimethyl ether without UV exposure, forms methyl formate upon UV exposure. As these both represent bimolecular reactions, it is logical to assume the adsorption site must be one which facilitates coupling reactions, in particular between formaldehyde and methoxy. This was also postulated in the work of Bennett *et al.* where the dimethyl ether yield was observed to decrease with increasing UV exposure time and that the magnitude of the attenuation was correlated with the photo-activity reported for methyl formate, i.e. the dimethyl ether yield decreased fastest on larger particles, which

also showed the highest methyl formate yield. As previously mentioned, they tentatively attributed dimethyl ether production to 4-fold coordinated Ti cation sites on minority (001) planes, but not without reservations. In order to account for the 4-fold coordinated sites (which would not be present on an ideal TiO<sub>2</sub>(001) plane) they employed a well-known (1 x 4) surface reconstruction which should produce the required 4-fold coordinated sites. However, a study of carboxylic acids on (1 x 4) anatase TiO<sub>2</sub>(001) raised doubts about the concentration of 4-fold coordinated Ti cations being high enough to observe bimolecular coupling.<sup>43</sup> Clearly, the adsorption details of methoxy intermediates which can undergo bimolecular coupling reactions are still uncertain. As mentioned by Bennett, different reconstructions could be present on nanostructured materials which provide the active sites for bimolecular coupling. This would also explain the lack of dimethyl ether on single crystal TiO<sub>2</sub>(110).<sup>19</sup> An additional factor which must be taken into consideration is the concentration of O<sub>v</sub>, which we have shown have a detrimental impact on dimethyl ether production and subsequently methyl formate after UV exposure. This again indicates that healed O<sub>v</sub> sites at least play a role in the formation of these reaction products.

### **3.5 Conclusions**

Titania nanowires exhibit primary thermal- and photochemical reactions of methanol which have been well documented on single crystal surfaces. The presence of O<sub>ad</sub> greatly enhances production of methoxy species on the nanowires, similar to single crystal studies on rutile TiO<sub>2</sub>(110). This enhancement works in concert with the photon-induced generation of formaldehyde, which participates in the production of the coupling product, methyl formate,

and substantially increases the product yield. One significant difference in the nanowire behavior is that a significant fraction (~70%) is not photo-oxidized. In contrast, methoxy bound to rutile TiO<sub>2</sub>(110) is completely photo-oxidized under similar conditions.<sup>16</sup>

This lack of activity could either be due to trapping of holes in the material or different binding of the inactive methoxy to the nanowires. These studies demonstrate that while charge carriers can be efficiently created in nanowires, differences in chemical properties can suppress photo-oxidation.

The near unity correlation between the decrease in dimethyl ether production and methyl formate yield at 300 K on both the vacuum annealed and O<sub>ad</sub> surfaces after UV exposure suggests an identical precursor adsorption site conducive for bimolecular coupling. It is, however, unclear whether or not these adsorption sites are the same as those on single crystals responsible for methyl formate production.

The correlation between nanowire and single crystal TiO<sub>2</sub> is a testament to the value of model systems for understanding the chemical behavior of complex materials. The ability to study these systems under well-controlled environments allows for targeted studies of individual factors governing reactivity, which has been shown in this case for the positive influence of O<sub>ad</sub> on formation of methyl formate. Further studies of such correlations promises to lead to a complete understanding of how changing specific experimental parameters can lead to different reaction outcomes and catalyst behavior. We hope that our work provides the impetus for future studies in this direction.

## 3.6 Supporting Information

### 3.6.1 Characterization

SEM measurements of the nanowire samples were performed at the Center for Nanoscale Systems (CNS) at Harvard University. A selection of images is displayed in Figure 3.1.

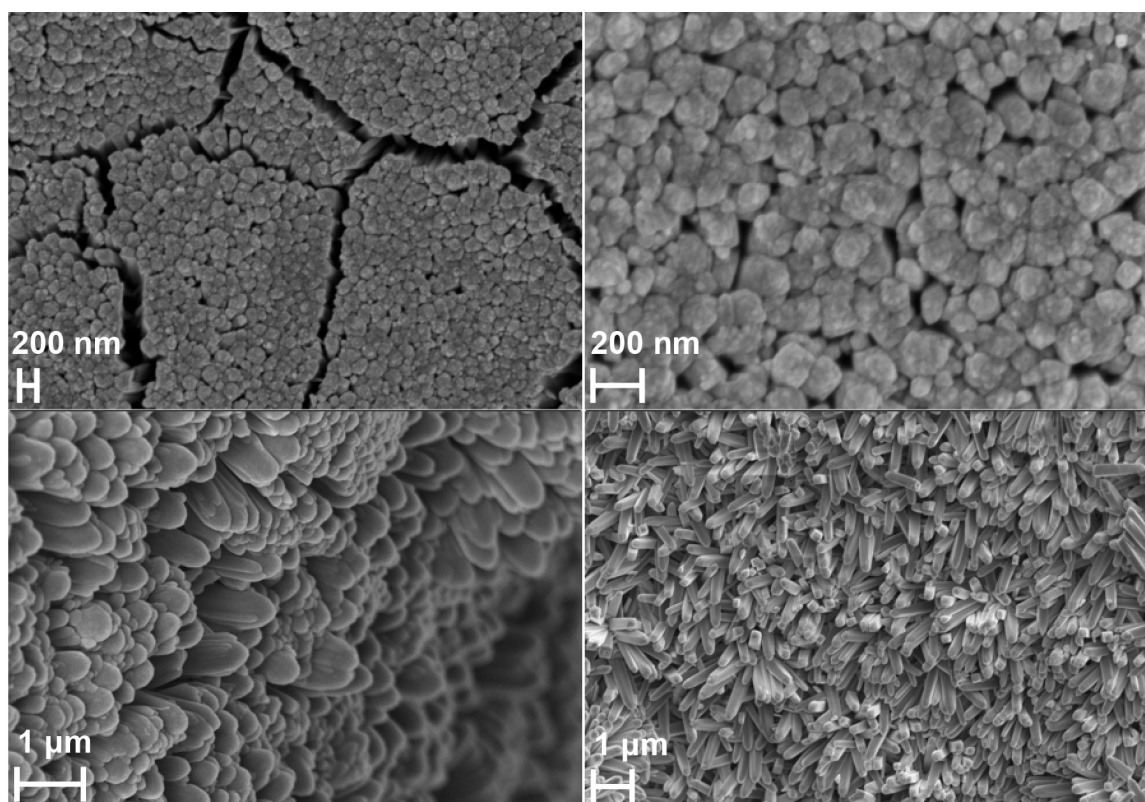


**Figure 3.7** SEM images of TiO<sub>2</sub> nanowire samples before introduction into the UHV chamber.

XPS spectra of the O1s region, Figure 3.8, demonstrates the same behavior as seen for the Ti 2p peaks in manuscript Figure 3.1.

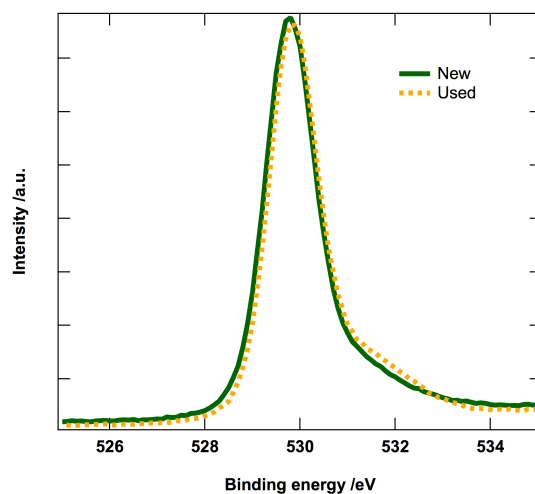


**Figure 3.8** X-ray photoelectron spectra of the nanowires showing the O1s region. The main peak shape remains the same for both samples (peak maximum within 0.1 eV).

A depth profile analysis of the nanowires after reaction cycles using x-ray photoelectron spectroscopy (XPS) with argon ion sputtering shows that carbon is primarily found on the surface of the nanowires, and decreases considerably after etching for 150 s, which we estimate to be ~ 24 nm. We attribute this to adventitious carbon formed by exposure after removal from the ultra-high vacuum system and transferring into the XPS instrument at the CNS facilities. Note that the oxygen and titanium peak areas increase slightly, but then remain relatively constant as the etching time increases.

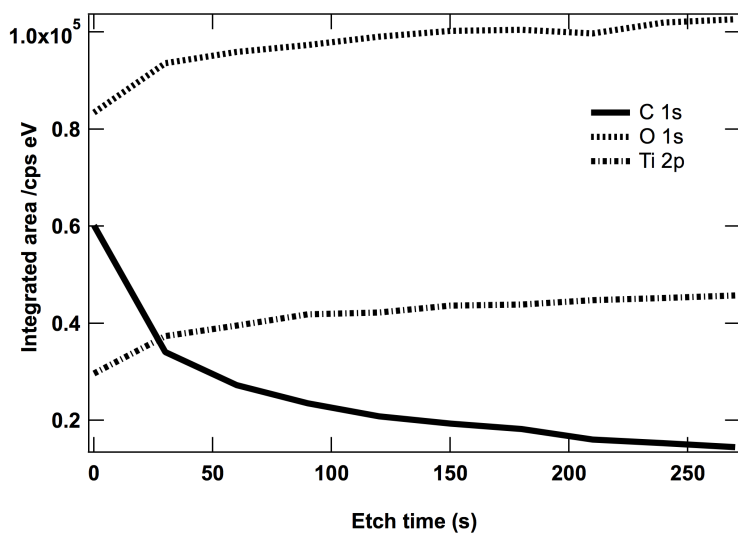


**Figure 3.9** Depth profile analysis of the C 1s, O 1s and Ti 2p, x-ray photoelectron peaks. The etch time on the x-axis corresponds to a depth of  $\sim 0.16$  nm/s.

### 3.6.2 Reactivity

Dimethyl ether was confirmed to be the  $m/z = 45$  species desorbing at 675 K, from its symmetrical correlation with  $m/z = 46$ , and the NIST reported fragmentation pattern ratio of  $\sim 0.6 = 46:45$ . Note that formic acid would yield a higher intensity for the  $m/z = 46$  trace.

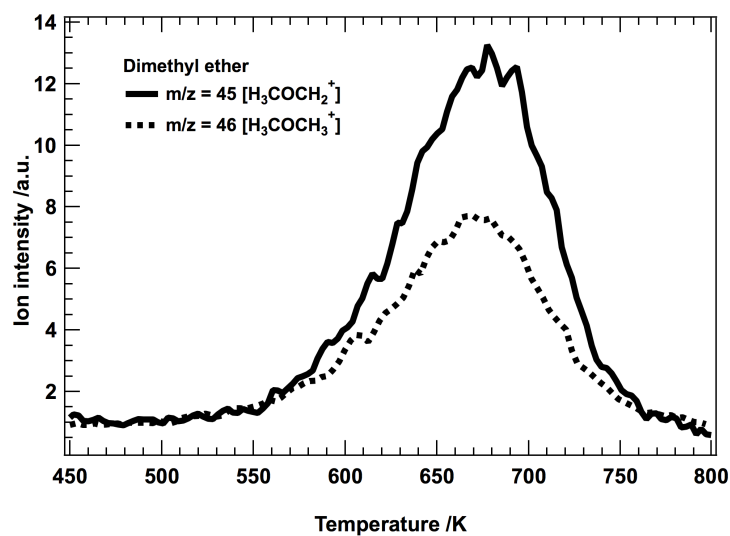


**Figure 3.10** Temperature programmed reaction traces of m/z = 45 and 46 used to identify dimethyl ether.

Temperature programmed desorption of water at different coverages demonstrates that increased coverages lead to a decrease in desorption temperature.

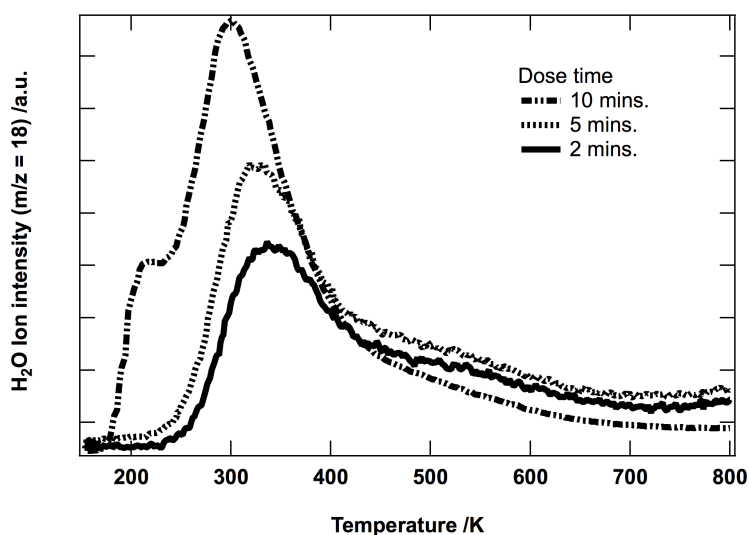




**Figure 3.11** Temperature programmed desorption of water ( $m/z = 18$ ) from vacuum annealed titania nanowires as a function of water coverage. The water coverage was controlled by variation in the time of exposure to water at 500 mTorr gas line pressure and 150 K.

**Table 3.2** Number density of desorbed molecules from integration of TiO<sub>2</sub> nanowire TPRs.

Molecule	Vac. <sup>a</sup> dark	Vac. with UV	O <sub>ad</sub> <sup>a</sup> dark	O <sub>ad</sub> with UV
Methanol 300 K	5.16	5.22	3.42	3.89
Methanol 700 K	0.73	0.59	2.29	1.29
Formaldehyde 300 K	0.00	0.21	0.00	1.15
Formaldehyde 700 K	1.00	0.75	3.26	1.70
Methyl formate	0.00	0.01	0.00	0.13
Methane	0.28	0.33	0.08	0.06
Dimethyl ether	0.04	0.03	0.17	0.07
Water	0.89	1.10	1.22	1.57

<sup>a</sup>Vac. = vacuum annealed, O<sub>ad</sub> = treated with oxygen at 300 K.

**Table 3.3** Quantitative analysis of the amount of dimethyl ether and methyl formate at 300 K on the O<sub>ad</sub> surface, along with the sum of these two values. All values represent absolute number densities of molecules.

UV exposure time	methyl formate (300 K)	dimethyl ether	sum
0	0	0.17	0.17
1	0.04	0.10	0.14
5	0.07	0.07	0.14
20	0.10	0.06	0.16

### 3.7 References

1. Parak, W. J.; Nel, A. E.; Weiss, P. S. Grand Challenges for Nanoscience and Nanotechnology. *ACS Nano* **2015**.
2. Sauer, J.; Freund, H.-J. Models in Catalysis. *Catalysis Letters* **2014**, *145* (1), 109–125.
3. Boudart, M. Model Catalysts: Reductionism for Understanding. *Top. Catal.* **2000**, *13*, 147–149.
4. Goodman, D. W. Correlations Between Surface Science Models and "Real-World" Catalysts. *J. Phys. Chem.* **1996**, *100* (31), 13090–13102.
5. Xu, B.; Madix, R. J.; Friend, C. M. Predicting Gold-Mediated Catalytic Oxidative-Coupling Reactions From Single Crystal Studies. *Acc. Chem. Res.* **2014**, *47* (3), 761–772.
6. Henderson, M. A. A Surface Science Perspective on Photocatalysis. *Surf. Sci. Rep.* **2011**, *66* (6-7), 185–297.
7. Vohs, J. M. Site Requirements for the Adsorption and Reaction of Oxygenates on Metal Oxide Surfaces. *Chem. Rev.* **2013**, *113* (6), 4136–4163.

8. Diebold, U. The Surface Science of Titanium Dioxide. *Surf. Sci. Rep.* **2003**, *48* (5-8), 53–229.
9. Henderson, M. A.; Otero-Tapia, S.; Castro, M. E. The Chemistry of Methanol on the TiO<sub>2</sub>(110) Surface: the Influence of Vacancies and Coadsorbed Species. *Faraday Discussions* **1999**, *114* (0), 313–329.
10. Shen, M.; Henderson, M. A. Identification of the Active Species in Photochemical Hole Scavenging Reactions of Methanol on TiO<sub>2</sub>. *J. Phys. Chem. Lett.* **2011**, *2* (21), 2707–2710.
11. Shen, M.; Acharya, D. P.; Dohnálek, Z.; Henderson, M. A. Importance of Diffusion in Methanol Photochemistry on TiO<sub>2</sub>(110). *J. Phys. Chem. C* **2012**, *116* (48), 25465–25469.
12. Wei, D.; Jin, X.; Huang, C.; Dai, D.; Ma, Z.; Li, W.-X.; Yang, X. Direct Imaging Single Methanol Molecule Photocatalysis on Titania. *J. Phys. Chem. C* **2015**, *119* (31), 17748–17754.
13. Guo, Q.; Xu, C.; Yang, W.; Ren, Z.; Ma, Z.; Dai, D.; Minton, T. K.; Yang, X. Methyl Formate Production on TiO<sub>2</sub>(110), Initiated by Methanol Photocatalysis at 400 Nm. *J. Phys. Chem. C* **2013**, *117* (10), 5293–5300.
14. Guo, Q.; Zhou, C.; Ma, Z.; Ren, Z.; Fan, H.; Yang, X. Elementary Photocatalytic Chemistry on TiO<sub>2</sub> Surfaces. *Chem. Soc. Rev.* **2016**, *45* (13), 3701–3730.
15. El-Roz, M.; Bazin, P.; Daturi, M.; Thibault-Starzyk, F. On the Mechanism of Methanol Photooxidation to Methylformate and Carbon Dioxide on TiO<sub>2</sub>: an Operando-FTIR Study. *Phys. Chem. Chem. Phys.* **2015**, *17* (17), 11277–11283.
16. Phillips, K. R.; Jensen, S. C.; Baron, M.; Li, S.-C.; Friend, C. M. Sequential Photo-Oxidation of Methanol to Methyl Formate on TiO<sub>2</sub>(110). *J. Am. Chem. Soc.* **2013**, *135* (2), 574–577.
17. Yuan, Q.; Wu, Z.; Jin, Y.; Xu, L.; Xiong, F.; Ma, Y.; Huang, W. Photocatalytic Cross-Coupling of Methanol and Formaldehyde on a Rutile TiO<sub>2</sub>(110) Surface. *J. Am. Chem. Soc.* **2013**, *135* (13), 5212–5219.
18. Feng, H.; Tan, S.; Tang, H.; Zheng, Q.; Shi, Y.; Cui, X.; Shao, X.; Zhao, A.; Zhao, J.; Wang, B. Temperature- and Coverage-Dependent Kinetics of Photocatalytic Reaction of Methanol on TiO<sub>2</sub>(110)-(1 × 1) Surface. *J. Phys. Chem. C* **2016**, *120* (10), 5503–5514.
19. Farfan-Arribas, E.; Madix, R. J. Different Binding Sites for Methanol Dehydrogenation and Deoxygenation on Stoichiometric and Defective TiO<sub>2</sub>(110) Surfaces. *Surf. Sci.* **2003**, *544* (2-3), 241–260.
20. Taylor, E. A.; Griffin, G. L. Product Selectivity During Methanol Decomposition on

Titania Powders. *J. Phys. Chem.* **1988**, 92 (2), 477–481.

21. Kim, K. S.; Barteau, M. A.; Farneth, W. E. Adsorption and Decomposition of Aliphatic Alcohols on Titania. *Langmuir* **1988**, 4 (3), 533–543.
22. Bennett, D. A.; Cargnello, M.; Gordon, T. R.; Murray, C. B.; Vohs, J. M. Thermal and Photochemical Reactions of Methanol on Nanocrystalline Anatase TiO<sub>2</sub> Thin Films. *Phys. Chem. Chem. Phys.* **2015**, 17 (26), 17190–17201.
23. Zhang, Z.; Bondarchuk, O.; White, J. M.; Kay, B. D.; Dohnálek, Z. Imaging Adsorbate O–H Bond Cleavage: Methanol on TiO<sub>2</sub>(110). *J. Am. Chem. Soc.* **2006**, 128 (13), 4198–4199.
24. Shen, M.; Henderson, M. A. Role of Water in Methanol Photochemistry on Rutile TiO<sub>2</sub>(110). *J. Phys. Chem. C* **2012**, 116 (35), 18788–18795.
25. Kolesov, G.; Vinichenko, D.; Tritsarlis, G. A.; Friend, C. M.; Kaxiras, E. Anatomy of the Photochemical Reaction: Excited-State Dynamics Reveals the C-H Acidity Mechanism of Methoxy Photo-Oxidation on Titania. *J. Phys. Chem. Lett.* **2015**, 6 (9), 1624–1627.
26. Cai, L.; Cho, I. S.; Logar, M.; Mehta, A.; He, J.; Lee, C. H.; Rao, P. M.; Feng, Y.; Wilcox, J.; Prinz, F. B.; et al. Sol-Flame Synthesis of Cobalt-Doped TiO<sub>2</sub> Nanowires with Enhanced Electrocatalytic Activity for Oxygen Evolution Reaction. *Phys. Chem. Chem. Phys.* **2014**, 16 (24), 12299–12306.
27. Xu, B.; Madix, R. J.; Friend, C. M. Achieving Optimum Selectivity in Oxygen Assisted Alcohol Cross-Coupling on Gold. *J. Am. Chem. Soc.* **2010**, 132 (46), 16571–16580.
28. Cremer, T.; Jensen, S. C.; Friend, C. M. Enhanced Photo-Oxidation of Formaldehyde on Highly Reduced O-TiO<sub>2</sub>(110). *J. Phys. Chem. C* **2014**, 118 (50), 29242–29251.
29. Cho, I. S.; Chen, Z.; Forman, A. J.; Kim, D. R.; Rao, P. M.; Jaramillo, T. F.; Zheng, X. Branched TiO<sub>2</sub> Nanorods for Photoelectrochemical Hydrogen Production. *Nano Letters* **2011**, 11 (11), 4978–4984.
30. Mazza, T.; Barborini, E.; Piseri, P.; Milani, P.; Cattaneo, D.; Li Bassi, A.; Bottani, C. E.; Ducati, C. Raman Spectroscopy Characterization of TiO<sub>2</sub> Rutile Nanocrystals. *Phys. Rev. B* **2007**, 75 (4), 045416.
31. Sekiya, T.; Ohta, S.; Kamei, S.; Hanakawa, M.; Kurita, S. Raman Spectroscopy and Phase Transition of Anatase TiO<sub>2</sub> Under High Pressure. *J. Phys. Chem.* **2001**, 62 (4), 717–721.
32. Mayer, J. T.; Diebold, U.; Madey, T. E.; Garfunkel, E. Titanium and Reduced Titania Overlayers on Titanium Dioxide(110). *J. Electron. Spectrosc. Relat. Phenom.* **1995**, 73 (1), 1–11.

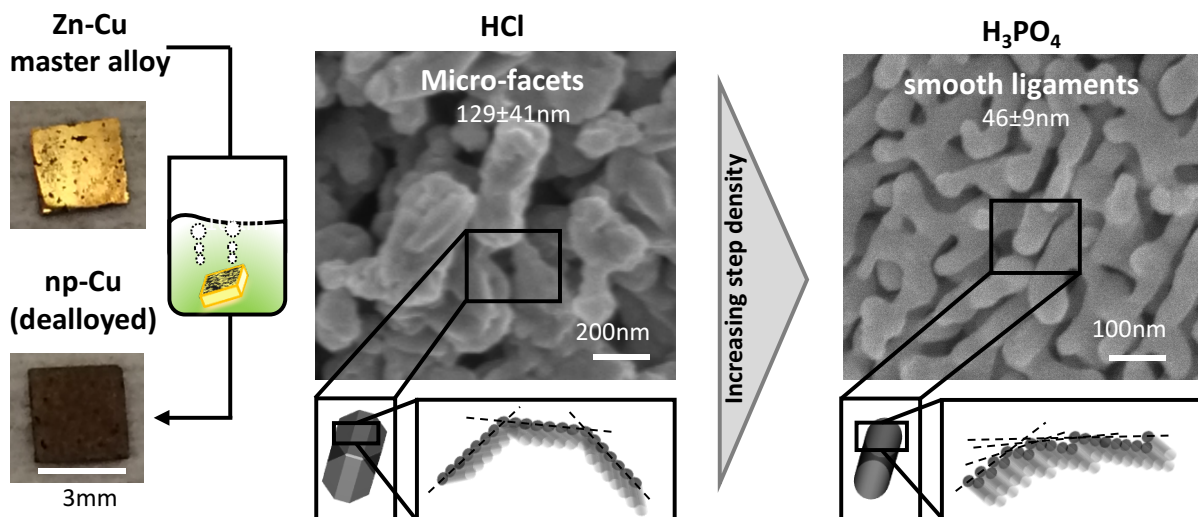
*Chapter 3. Methanol Photo-Oxidation on Rutile TiO<sub>2</sub> Nanowires: Probing Reaction Pathways on Complex Materials*

33. Kimmel, G. A.; Petrik, N. G. Tetraoxygen on Reduced TiO<sub>2</sub>(110): Oxygen Adsorption and Reactions with Bridging Oxygen Vacancies. *Phys. Rev. Lett.* **2008**, *100* (19), 196102.
34. Henderson, M. A.; Epling, W. S.; Perkins, C. L.; Peden, C. H. F.; Diebold, U. Interaction of Molecular Oxygen with the Vacuum-Annealed TiO<sub>2</sub>(110) Surface: Molecular and Dissociative Channels. *J. Phys. Chem. B* **1999**, *103* (25), 5328–5337.
35. Petrik, N. G.; Zhang, Z.; Du, Y.; Dohnálek, Z.; Lyubinetsky, I.; Kimmel, G. A. Chemical Reactivity of Reduced TiO<sub>2</sub>(110): the Dominant Role of Surface Defects in Oxygen Chemisorption. *J. Phys. Chem. C* **2009**, *113* (28), 12407–12411.
36. Wang, Z.-T.; Aaron Deskins, N.; Lyubinetsky, I. Direct Imaging of Site-Specific Photocatalytical Reactions of O<sub>2</sub> On TiO<sub>2</sub>(110). *J. Phys. Chem. Lett.* **2012**, *3* (1), 102–106.
37. Perkins, C. L.; Henderson, M. A. Photodesorption and Trapping of Molecular Oxygen at the TiO<sub>2</sub>(110)–Water Ice Interface. *J. Phys. Chem. B* **2001**, *105* (18), 3856–3863.
38. Petrik, N. G.; Kimmel, G. A. Photoinduced Dissociation of O<sub>2</sub> on Rutile TiO<sub>2</sub>(110). *J. Phys. Chem. Lett.* **2010**, *1* (12), 1758–1762.
39. Du, Y.; Dohnálek, Z.; Lyubinetsky, I. Transient Mobility of Oxygen Adatoms Upon O<sub>2</sub> Dissociation on Reduced TiO<sub>2</sub>(110). *J. Phys. Chem. C* **2008**, *112* (7), 2649–2653.
40. Kim, K. S.; Barteau, M. A. Reactions of Methanol on TiO<sub>2</sub>(001) Single Crystal Surfaces. *Surf. Sci.* **1989**, *223* (1), 13–32.
41. Wang, Z.-T.; Deskins, N. A.; Henderson, M. A.; Lyubinetsky, I. Inhibitive Influence of Oxygen Vacancies for Photoactivity on TiO<sub>2</sub>(110). *Phys. Rev. Lett.* **2012**, *109* (26), 266103.
42. Serafin, J. G.; Friend, C. M. Evidence for Formation of Gaseous Methyl Radicals in the Decomposition of Methoxide on Oxygen-Precovered Molybdenum(110). *J. Am. Chem. Soc.* **1989**, *111* (24), 8967–8969.
43. Tanner, R. E.; Liang, Y.; Altman, E. I. Structure and Chemical Reactivity of Adsorbed Carboxylic Acids on Anatase TiO<sub>2</sub>(001). *Surf. Sci.* **2002**, *506* (3), 251–271.

## Chapter 4.

# Multiscale Morphology of Nanoporous Copper made from Intermetallic Phases

### 4.1 Abstract



Many application relevant properties of nanoporous metals critically depend on their multiscale architecture. For example, the intrinsically high step-edge density of curved surfaces at the nanoscale provides highly reactive sites for catalysis while the macroscale pore and grain morphology determines macroscopic properties such as mass transport, electrical conductivity, or mechanical properties. In this work, we systematically study the effects of alloy composition and dealloying conditions on the multi-scale morphology of nanoporous copper (np-Cu) made from various commercial Zn-Cu precursor alloys. Using a

combination of x-ray diffraction (XRD), electron backscatter diffraction (EBSD), and focused ion beam cross-sectional analysis (FIB-xSEM), our results reveal that the macroscopic grain structure of the starting alloy surprisingly survives the dealloying process despite a change in crystal structure from body centered cubic (Zn-Cu starting alloy) to face centered cubic (Cu). The nanoscale structure can be controlled by the acid used for dealloying, with HCl leading to a larger and more faceted ligament morphology as compared to H<sub>3</sub>PO<sub>4</sub>. Anhydrous ethanol dehydrogenation was used as a probe reaction to test the effect of the nanoscale ligament morphology on the apparent activation energy of the reaction.

This paper was published in *ACS Appl. Mater. Interfaces* **2017**, 9, 25615-25622.

## **4.2 Introduction**

Nanoporous metals have many promising applications including, catalysis,<sup>1-2</sup> batteries,<sup>3</sup> actuators,<sup>4-6</sup> and electrochemical sensors.<sup>7-8</sup> The performance of nanoporous metals in all these applications critically depends on their multiscale architecture that determines macroscale properties such as materials strength, electrical conductivity, and mass transport, all the way to atomistic properties such as reactive sites for catalysis. In recent years, dealloying has been established as a versatile synthesis route towards high-quality monolithic nanoporous metals providing both compositional flexibility and a high level of morphological control.<sup>7, 9</sup> During dealloying, the less noble component of an alloy is selectively removed by a corrosive environment while the more noble component

spontaneously forms a characteristic bicontinuous open-pore structure via surface diffusion assisted self-assembly of vacancies and noble metal atoms.<sup>8, 10</sup> The mechanism of morphology evolution has been studied in detail for single-phase solid solution precursor alloys such as Ag-Au<sup>9-12</sup>, Cu-Au, and Mn-Cu<sup>13</sup>. These systems have in common that both the starting alloy and the resulting nanoporous metal have the same crystal structure and similar lattice constants. For the case of a single-phase alloy, porosity formation can be explained by coherent surface diffusion of the more noble metal adatoms and vacancies on a rigid lattice.<sup>14</sup> This leads to a coherent crystallographic transformation, for example from face centered cubic (*fcc*) Ag-Au to *fcc* nanoporous gold (np-Au) that preserves the macroscopic crystal grain structure of the starting alloy.<sup>14</sup> However, the dealloying mechanism is much less understood for more complex intermetallic starting alloys where both crystal structure and lattice constant change dramatically during dealloying.

Next to np-Au, nanoporous copper (np-Cu) is one of the most studied nanoporous metals made by dealloying. Cu is not only less expensive than Au and Ag, but Cu-based catalysts are used in several important industrial fuel and chemical production processes, including the water-gas shift reaction, dehydrogenation of alcohols, and production of methanol.<sup>15</sup> The first example of np-Cu made by dealloying is Raney Cu which is prepared by dealloying a Al-Cu alloy in sodium hydroxide solution<sup>16</sup> and is a widely used catalyst for gas-phase and liquid-phase dehydrogenation and hydrogenation reactions<sup>15</sup>. Later, np-Cu was made from single-phase solid solution starting alloys such as Ni-Cu<sup>17</sup> and Mn-Cu<sup>8, 13, 17</sup>. In 2006, Hayes and co-workers<sup>13</sup> first synthesized monolithic np-Cu by dealloying a Mn<sub>0.7</sub>Cu<sub>0.3</sub> starting alloy. Recently, np-Cu was fabricated by dealloying intermetallic or multiple-phase alloy precursors including Mg-Cu<sup>18</sup>, Al-Cu<sup>19</sup> and Zn-Cu<sup>17</sup> alloys. Other Zn-based alloys like



Zn-Ag<sup>20-21</sup> have been studied to fabricate porous Ag nanostructures. The effects of temperature, time, and precursor alloy on the structure of the material have been successfully discussed for many nanoporous metals, including np-Cu.<sup>9, 11, 13, 22</sup> However, for the technologically relevant system of Zn-Cu alloys, several important questions related to dealloying have not yet been addressed. These include questions such as what happens to the crystal structure as the body centered cubic (*bcc*) structure of the Zn-Cu starting alloy undergoes a phase transformation to face centered cubic (*fcc*) np-Cu, and what is the effect of the etching solution on the ligament morphology.

Here, we revisit the synthesis of np-Cu from various Zn-Cu alloys. Specifically, we selected a Zn-rich (Zn<sub>80</sub>Cu<sub>20</sub>) and a Cu-rich (Zn<sub>50</sub>Cu<sub>50</sub>) starting alloy that are both aligned with single phase regions of the Cu-Zn phase diagram (Figure 4.1a). Dealloying of the Zn-rich Zn<sub>80</sub>Cu<sub>20</sub> alloy is expected to generate high porosity np-Cu (~80% porosity not accounting for potential sample shrinkage) ideally suited for applications that require fast mass transport; dealloying of the Cu-rich Zn<sub>50</sub>Cu<sub>50</sub> alloy is expected to generate a low porosity and thus mechanically very robust np-Cu that undergoes little mechanical deformation during dealloying. We also fabricated a crack-free 3-inch diameter np-Cu wafer with a relative density of 50% for gas gun high pressure experiments at LLNL.<sup>23</sup> Using the Zn and Cu-rich alloys, we systematically studied the effect of the Zn-Cu starting alloy composition and dealloying conditions on both the macroscale grain structure and the nanoscale ligament surface morphology. Our results show that the crystal grain structure of a Zn<sub>50</sub>Cu<sub>50</sub> starting alloy is surprisingly preserved during dealloying despite the *bcc* Zn<sub>50</sub>Cu<sub>50</sub> to *fcc* np-Cu phase transformation. We also observed that the nanoscale ligament morphology can be controlled by the nature of the acid used for dealloying, with HCl leading to a larger and more faceted

ligament morphology as compared to  $\text{H}_3\text{PO}_4$ . This is important as the curvature of the ligaments determines the density of catalytically more reactive under-coordinated step edge sites. Control over the multiscale morphology of np-Cu, from the macroscopic grain structure to the nanoscale ligament morphology, thus potentially opens the door to engineered np-Cu catalysts with tailored reactivity and selectivity.

### **4.3 Methods**

Custom-made  $\text{Zn}_{50}\text{Cu}_{50}$  3-inch diameter disks (*Plasmaterials*) and  $\text{Zn}_{80}\text{Cu}_{20}$  (*Goodfellow*) alloy cubes ( $2 \times 2 \times 2 \text{ cm}^3$ ) were cut into  $3 \times 3 \times 0.3 \text{ mm}^3$  pieces using a low-speed diamond saw and cleaned in an ultrasonic bath with acetone for 15 minutes. Samples for dealloying were polished with 1200 grit SiC paper. The samples for electron backscatter diffraction (EBSD) experiments were polished to a  $0.05 \mu\text{m}$  finish using a colloidal silica suspension. The effect of electrolyte composition on morphology was systematically studied using various non-oxidizing acids including 15M  $\text{H}_3\text{PO}_4$  (pH 0.48), 5M  $\text{H}_3\text{PO}_4$  (pH 0.72), 5M  $\text{H}_3\text{PO}_4$  + 0.25mol NaCl (pH 0.72), 2.5M  $\text{H}_3\text{PO}_4$  + 2.5M HCl (pH -0.42), 5M HCl (pH -0.70) and 5M HCl + 0.25mol NaCl (pH -0.70). Both HCl and  $\text{H}_3\text{PO}_4$  have negative oxidation potentials and thus are expected to selectively dissolve Zn (standard potentials in Table 4.2) while forming highly soluble Zn salts. Sulfuric acid, on the other hand, forms a thick  $\text{ZnSO}_4$  surface layer that prevents further reaction. The oxidation potential of nitric acid is too positive (+0.96V vs. SHE) to allow for selective dissolution of Zn.

All electrolytes were made with 18.2 M $\Omega$ -cm deionized (DI) water and reagent grade chemicals (*SigmaAldrich*). Alloy samples were placed in an electrolyte solution of 50 mL and dealloyed for 1 to 6 days, depending on alloy composition, electrolyte composition and concentration, and sample thickness. The dealloying process is accompanied by hydrogen formation, and the cessation of hydrogen bubble formation at the alloy surface was used as a qualitative indicator for the completion of the dealloying process. The samples were then rinsed three times with DI water and kept in a DI water bath to displace the electrolyte completely from the internal pores. The samples were then dried overnight in a vacuum desiccator and subsequently stored in a glovebox until further characterization.

The multiscale morphology of np-Cu was studied by scanning electron microscopy (SEM, field emission *JEOL SEM JSM-7401F* equipped with an EDS detector, *Oxford Instruments*). Surface grain orientation maps were obtained by EBSD (*FEI Helios Nanolab 660* system equipped with *EDAX* and *Texture & Elemental Analytical Microscopy* software). The electron beam was set to 30 kV and 13 nA with a working distance of approximately 11.5 mm. Fiducials (50x5x5  $\mu\text{m}$ ) were prepared by ion milling to allow for spatial matching of the EBSD grain orientation maps before and after dealloying. X-ray diffraction (XRD) data were collected using a *Bruker D8 Advance*. The parameters were:  $2\theta$ : 10° - 90°; step size: 0.03°/step; number of steps: 2691; time per step: 1 second. The *TOPAS* program was used for Rietveld refinement. The lattice and final structure parameters for  $\text{Zn}_{50}\text{Cu}_{50}$  can be found in Table 4.3, 4.4 and 4.5. The refinement pattern is shown in Figure 4.6. Parameters and the pattern for  $\text{Cu}_{20}\text{Zn}_{80}$  are listed in Table 4.6 and Figure 4.7. Weight measurements were done on a lab scale (*Mettler Toledo*, Model XP204). Ligament size distributions were obtained by

SEM image analysis (*ImageJ*) using 200 ligament diameter measurements per histogram (Figures 4.8 and 4.9).

Apparent activation energies of various np-Cu samples for ethanol dehydrogenation to acetaldehyde and hydrogen were measured at atmospheric pressure using a quartz tube continuous flow-reactor housed in a tubular furnace. The reaction rate of acetaldehyde production was measured at 180 – 230 °C under steady-state conditions going from high to low then high temperatures again to exclude coarsening induced artifacts. For catalytic tests, the samples were crushed and mixed with sand with a 1 to 5 ratio. Prior to testing, all samples were reduced in 10% H<sub>2</sub> with a flow rate of 20 mL/min for 1 h at 250 °C. The samples were subsequently exposed to reaction conditions of 6% ethanol balanced in Helium using a flow rate of 25 mL/min and kept at 250 °C for 1 h in ethanol. The activation barriers were measured at different flow rates, ranging from 7.5 mL/min to 50 mL/min (Table 4.7), to identify conditions that minimize external mass transport limitations. Conversion values measured at the different flow rates as a function of temperature are shown in Table 4.8, illustrating that conversion decreases with increasing flow rate, as expected if mass transport effects are not dominating. The measured activation energies for 25 and 50 mL/min are the same and are hence characteristic of the reaction itself. Gas phase ethanol was obtained by flowing He gas through liquid ethanol at room temperature. The effluent gas was continuously analyzed by a GC-MS (*Agilent 5975C* and *Agilent 7890A*) equipped with *HP-PLOT Q* and *CARBONPLOT* columns. To test for the presence of a concentration gradient or internal diffusion limitation, different size distributions of np-Cu particles were tested at 250°C at 50 mL/min with 6% ethanol to obtain the dependence of the mass-averaged conversion on particle size (Table 4.9). Different particle size distributions were obtained by

sieving with 106, 212, and 425  $\mu\text{m}$  sized meshes. Particles larger than 425 $\mu\text{m}$  were disregarded.

#### **4.4 Results and Discussion**

The XRD data and the corresponding crystallographic phase composition of the  $\text{Zn}_{50}\text{Cu}_{50}$  and  $\text{Zn}_{80}\text{Cu}_{20}$  master alloys are summarized in Figures 4.1b and 4.1c. For the  $\text{Zn}_{50}\text{Cu}_{50}$  precursor alloy, XRD revealed the coexistence of several Zn-Cu phases, a Zn-rich ( $\text{Cu}_5\text{Zn}_8$ ) and a Cu-rich ( $\text{Cu}_3\text{Zn}_1$ ) phase in addition to the expected  $\text{Cu}_1\text{Zn}_1$  phase (Figure 4.1b). Quantitative Rietveld analysis yielded: 23.6%  $\text{Cu}_3\text{Zn}_1$ , 55.9%  $\text{Cu}_1\text{Zn}_1$  and 20.5%  $\text{Cu}_5\text{Zn}_8$ . By contrast, only the  $\text{Cu}_1\text{Zn}_4$  phase was detected in the  $\text{Zn}_{80}\text{Cu}_{20}$  alloy sample (Figure 4.1c).

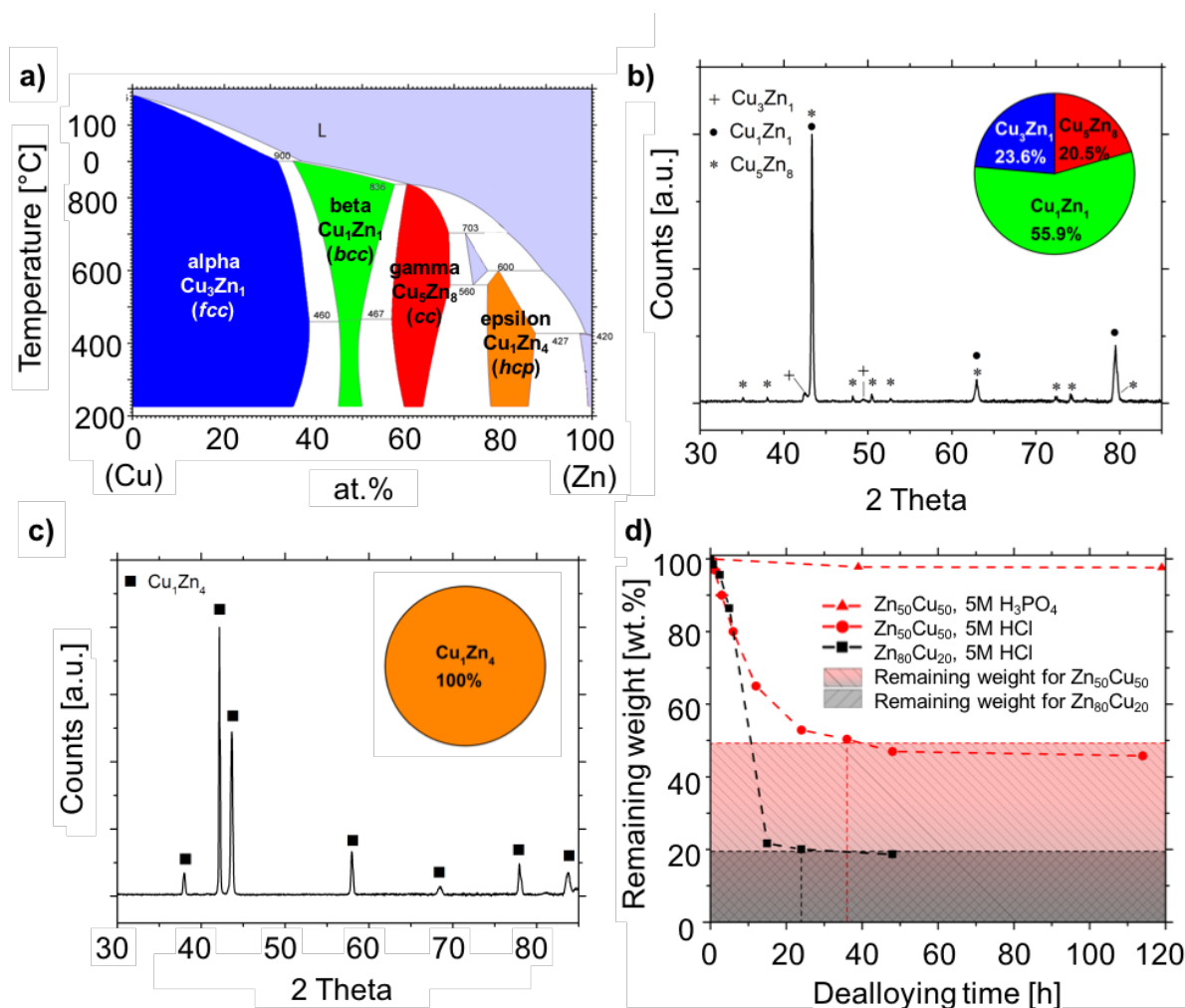


**Figure 4.1** Characterization of Zn-Cu samples **(a)** Copper-Zinc phase diagram; XRD analysis of commercially obtained  $\text{Zn}_{50}\text{Cu}_{50}$  **(b)** and  $\text{Zn}_{80}\text{Cu}_{20}$  **(c)** alloys; insets reflect the phase distribution of the alloys obtained by Rietveld analysis; **(d)** Remaining weight over dealloying time:  $\text{Zn}_{50}\text{Cu}_{50}$  with 5M HCl,  $\text{Zn}_{80}\text{Cu}_{20}$  with 5M HCl and  $\text{Zn}_{50}\text{Cu}_{50}$  with 5M  $\text{H}_3\text{PO}_4$ .

For dealloying, alloy samples ( $3 \times 3 \times 0.3 \text{ mm}^3$ ) were submerged in HCl,  $\text{H}_3\text{PO}_4$ , or mixtures thereof (with and without NaCl addition) until hydrogen bubble formation ceased indicating the completion of the dealloying process. Dissolution of Zn almost immediately

changed the color of the samples, from brass-like ( $\text{Zn}_{50}\text{Cu}_{50}$ ) or silver ( $\text{Zn}_{80}\text{Cu}_{20}$ ) to dark brown (Figures 4.2 and 4.3, center). The bulk morphology of both master alloys, before and after dealloying, was studied by FIB-xSEM (Figures 4.2 and 4.3). The cross-section of the  $\text{Zn}_{50}\text{Cu}_{50}$  starting alloy (Figure 4.2b) reveals an inhomogeneous particle-like morphology with voids that seem to be remnants of the particle sintering manufacturing method (*Plasmaterials*). Due to its significantly lower melting point, zinc tends to solidify later during the manufacturing process thus accumulating near the surface of the particle-like structures found in the  $\text{Zn}_{50}\text{Cu}_{50}$  alloy as confirmed by EDAX on FIB cross-sections (Figure 4.10 and Table 4.10). The Zn enrichment near the surface of the particles leads to the formation of a hierarchical porosity during dealloying: Pores formed in the Zn-rich shell of the particles are with 1-10 $\mu\text{m}$  diameter significantly larger than those formed in the more Cu-rich core of the particles. The large pores formed in the Zn-rich shell together with the pre-existing intrinsic voids of the precursor alloy (Figure 4.2b) form a mass transport facilitating macroporous network structure. Indeed, control experiments using a non-porous  $\text{Zn}_{44}\text{Cu}_{56}$  master alloy (*Plasmaterials*) showed impractically slow Zn removal rates for 5M HCl whereas 7M HCl started to dissolve Cu (Figures 4.11 and 4.12). By contrast, the  $\text{Zn}_{80}\text{Cu}_{20}$  starting alloy is homogeneous in composition and free of intrinsic voids (Figure 4.3a), and dealloying in 5M HCl results in the formation of a uniform nanoporous structure (Figure 4.3b).

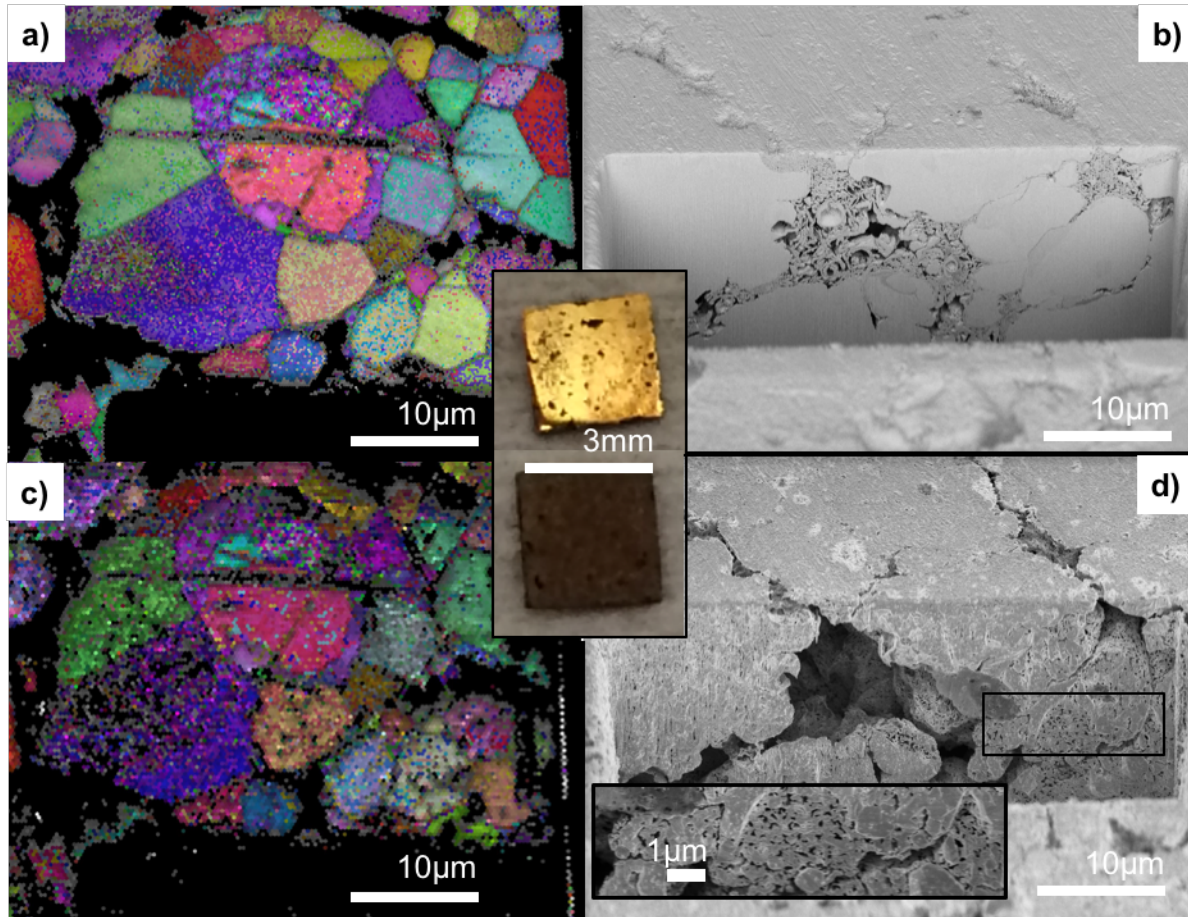


**Figure 4.2** Characterization of the macrostructure of Zn-Cu samples. EBSD grain orientation maps (superposition of EBSD image quality and inverse pole figure (IQ + IPF)) before **(a)** and after **(c)** dealloying in 5M HCl for 36h. Cross-sectional SEM of the  $Zn_{50}Cu_{50}$  master alloy before **(b)** and after **(d)** dealloying the same sample. This reveals the retention of the grain structure and orientation as well as the presence of macropores in the structure - due to the fabrication - initially accelerating the dealloying process by increasing mass transport properties. Centered image represents the  $3 \times 3 \times 0.3 \text{ mm}^3$  sample before and after dealloying.



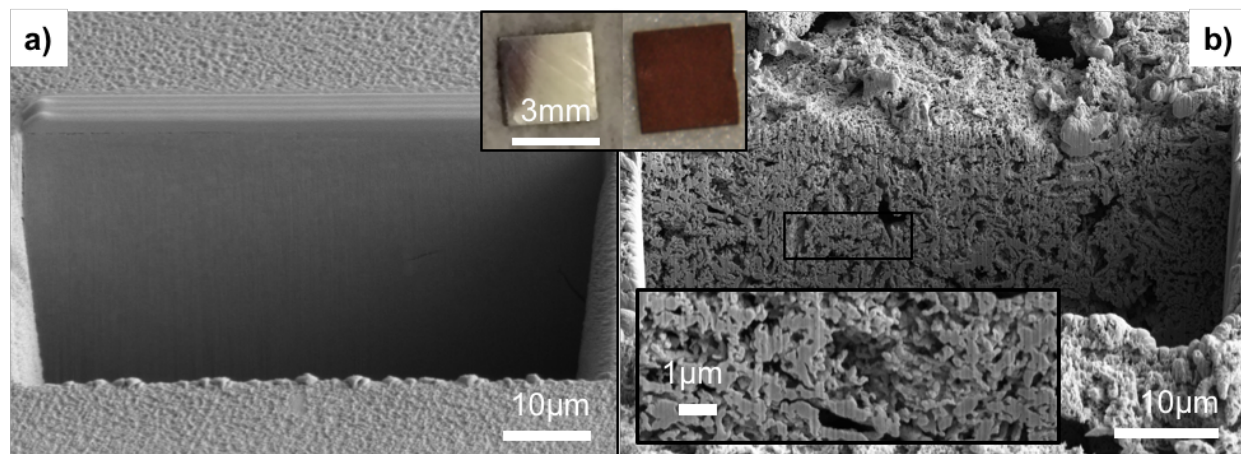


**Figure 4.3** Cross-sectional SEM of the Zn<sub>80</sub>Cu<sub>20</sub> master alloy before **(a)** and after **(b)** dealloying for 24h in 5M HCl. Centered image represents the 3x3x0.3mm<sup>3</sup> sample before and after dealloying. This represents the formation of a uniform nanoporous structure from a homogeneous starting alloy and highlights extensive stress-induced deformation of the surface.

As expected, the dealloying kinetics depends on both the alloy composition and its morphology. For Zn<sub>50</sub>Cu<sub>50</sub> in 5M HCl (Figure 4.1d, red circles), the sample weight decreases exponentially with the dealloying time; the anticipated weight loss of 49.5% (complete Zn removal) is reached after about 36h. For dealloying times in excess of 36h, slow weight loss over time indicates Cu dissolution consistent with the electrolyte becoming faint green in color. By contrast, the Zn<sub>80</sub>Cu<sub>20</sub> alloy does not show an exponential decay in the dealloying rate as observed for the Zn<sub>50</sub>Cu<sub>50</sub> alloy (Figure 4.1d, black squares). Only after most of the Zn has been removed does the weight loss start to slow down. The fast dealloying kinetics of the Zn<sub>80</sub>Cu<sub>20</sub> alloy is a consequence of the lower critical potential (onset of selective Zn

dissolution) of Zn-rich brasses<sup>24</sup>. The initial fast weight loss of the Zn<sub>50</sub>Cu<sub>50</sub> alloy (initially the weight loss appears to be even faster than that of Zn<sub>80</sub>Cu<sub>20</sub>) can be attributed to the formation of the macroporous network and the presence of the Zn-rich shell of the particles found in this alloy. However, its more noble character makes the Zn<sub>50</sub>Cu<sub>50</sub> alloy inert against corrosion by phosphoric acid (H<sub>3</sub>PO<sub>4</sub>) whereas Zn<sub>80</sub>Cu<sub>20</sub> is readily attacked. H<sub>3</sub>PO<sub>4</sub> is a weaker acid, so the critical potential is still reached for Zn<sub>80</sub>Cu<sub>20</sub> but not for Zn<sub>50</sub>Cu<sub>50</sub>. Additional data on the dealloying kinetics for different acid strengths and sample thicknesses are provided in the supporting information (Figure 4.12).

A comparison of the grain orientation maps obtained by EBSD from a Zn<sub>50</sub>Cu<sub>50</sub> alloy sample before and after dealloying clearly demonstrates that the grain structure as well as the orientation of the Zn<sub>50</sub>Cu<sub>50</sub> starting alloy are preserved during dealloying (Figures 4.2a and 4.2c). Although the crystal structures of both the starting alloy (mostly *bcc* type) and np-Cu (*fcc*) are cubic, the transformations involve considerable changes in the lattice constants. The change from the *bcc* related intermetallic structures of Zn<sub>50</sub>Cu<sub>50</sub> to *fcc* Cu is 22.7% (from 2.95 Å to 3.62 Å) for the Cu<sub>1</sub>Zn<sub>1</sub> phase, 1.4% (from 3.67 Å to 3.62 Å) for the Cu-rich (Cu<sub>3</sub>Zn<sub>1</sub>), and 22.3% (from 2.96 Å to 3.62 Å) for the Zn-rich phase (Cu<sub>5</sub>Zn<sub>8</sub>). The minuscule changes in the lattice constant from Cu<sub>3</sub>Zn<sub>1</sub> to Cu are difficult to monitor confidently since they are close to the measurement error of the EBSD, and because Cu<sub>3</sub>Zn<sub>1</sub> is a non-stoichiometric intermetallic compound which impedes proper identification of the Kikuchi bands. The lattice constants, space group, and crystallographic motif of all occurring phases that were entered in the EBSD acquisition software are summarized in Table 4.11. We could not obtain reliable EBSD data from the dealloyed Zn<sub>80</sub>Cu<sub>20</sub> structure which we attribute to substantial stress-induced deformation and tilting of the lattice planes during dealloying.

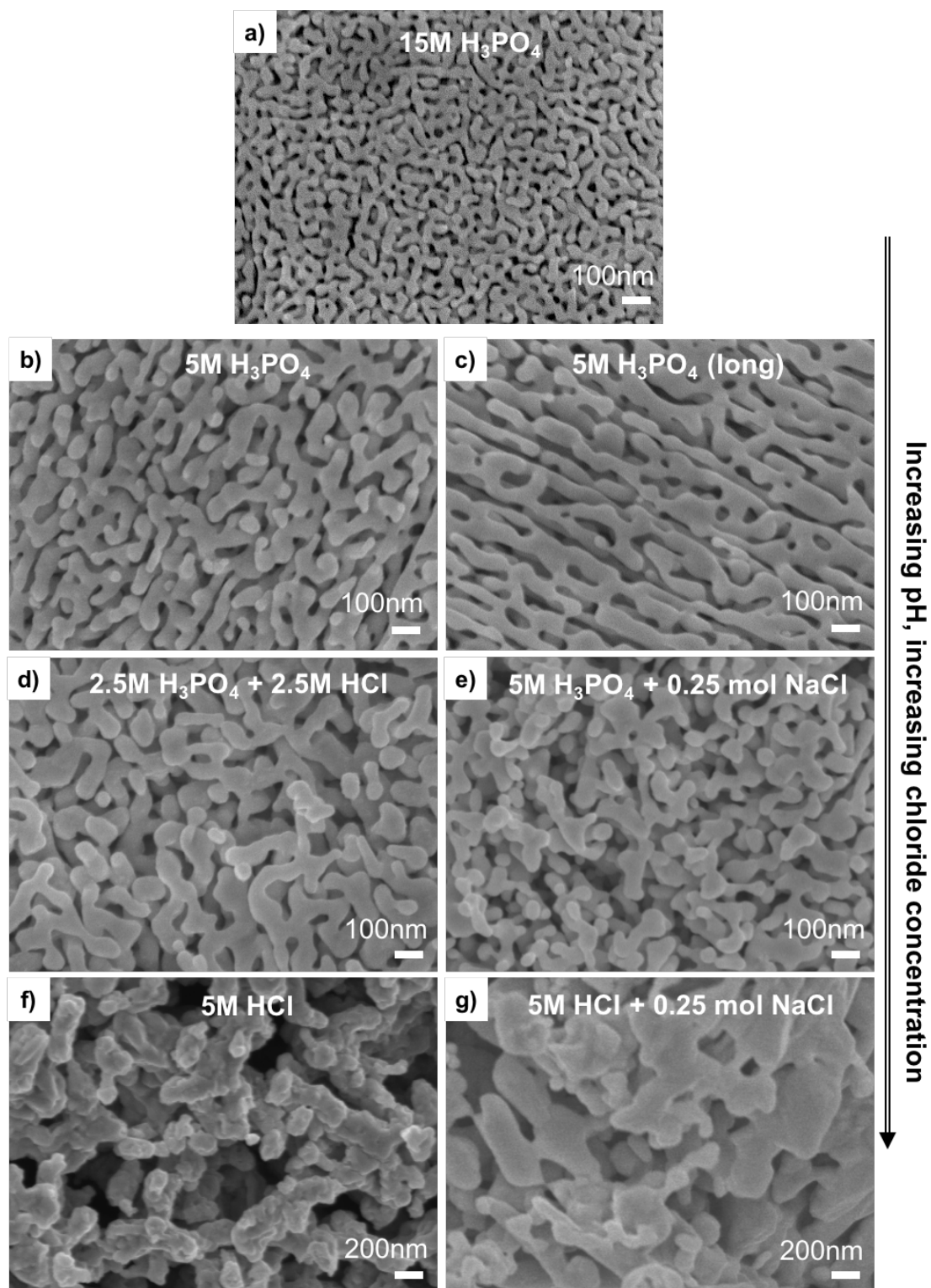


**Figure 4.4 (a) - (g)** SEM micrographs for Zn<sub>80</sub>Cu<sub>20</sub> dealloyed in various electrolytic solutions showing the evolution of the ligament morphology as a function of the electrolyte

composition used for the dealloying process. Chloride anions promote Cu surface diffusion whereas phosphate or its combination with chloride inhibits diffusivity. Further increasing the amount of chloride by adding NaCl pronounces effects of surface rearrangement even more and is independent of the pH level.

Generally, the accepted mechanism for dealloying of single-phase solid solution alloys is based on coherent surface diffusion<sup>10, 22, 25</sup>, a mechanism which preserves the grain structure and orientation of the starting alloy<sup>14, 25</sup>. This, however, requires that both the starting alloy and the dealloyed material have the same crystal structure and similar lattice constants. By contrast, excessive stress at the dealloying front caused by a change in crystal structure or in the lattice constant (like in the Zn-Cu system discussed here) is expected to change the grain structure by triggering nucleation events. Dealloying induced nucleation has indeed been confirmed for amorphous multicomponent starting alloys as demonstrated by the observation of the *fcc* Cu<sup>26</sup> / Pt<sup>27</sup> / Au<sup>27</sup> structure after dealloying. In view of the change in crystal structure from *bcc* to *fcc* and the change in lattice constants, the preservation of the grain structure of the Zn<sub>50</sub>Cu<sub>50</sub> alloy during dealloying clearly is an unexpected result.

The effect of pH and anion species on the nanoscale morphology of np-Cu was studied on the Zn<sub>80</sub>Cu<sub>20</sub> alloy as this alloy composition allowed us to use both H<sub>3</sub>PO<sub>4</sub> and HCl as etchants. The SEM micrographs shown in Figure 4.4 reveal that the microstructures formed by dealloying Zn<sub>80</sub>Cu<sub>20</sub> in diluted 5M H<sub>3</sub>PO<sub>4</sub> (pH 0.72) and 5M HCl (pH -0.70) are very different (see also the size histograms in Figures 4.8 and 4.9). Small (46 ± 9 nm) ligaments with smoothly curved surfaces are observed after dealloying for 24 h in H<sub>3</sub>PO<sub>4</sub> (Figure 4.4b)

while large  $129 \pm 41$  nm micro-faceted ligaments are formed in HCl after 36 h of dealloying (Figure 4.4f). To determine whether the difference in the ligament nanostructure originates from differences in pH value, dealloying time or anion specific interactions, we systematically studied the effect of dealloying time, pH, and anion composition. Adding HCl to  $\text{H}_3\text{PO}_4$  (by mixing equal amounts of 5M  $\text{H}_3\text{PO}_4$  and 5M HCl) slightly increased the ligament size ( $51 \pm 12$  nm) with respect to 5M  $\text{H}_3\text{PO}_4$  ( $46 \pm 9$  nm) (Figure 4.4d). Addition of chloride anions to 5M  $\text{H}_3\text{PO}_4$  (by adding 0.25 moles NaCl to the 50 mL solution) again slightly increased the ligament size to  $57 \pm 16$  nm (Figure 4.4e). Prolonged six-day etching in 5M  $\text{H}_3\text{PO}_4$  (Figure 4.4c) also only slightly increased the ligament size to  $53 \pm 14$  nm (compared to  $46 \pm 9$  nm after 24 h dealloying in  $\text{H}_3\text{PO}_4$ ). Increasing the concentration of  $\text{H}_3\text{PO}_4$ , from 5M to 15M (pH 0.48), however, resulted in the formation of smaller ligaments ( $35 \pm 8$  nm), (Figure 4.4a). Thus, these conditions resulted in the formation of similar sized ligaments with smoothly curved surfaces despite large differences in the pH value, composition, and dealloying time. On the other hand, addition of NaCl to 5M HCl also led to the formation of micro-faceted ligaments and further increased the feature size ( $156 \pm 76$  nm) relative to the micro-faceted ligaments obtained by 5M HCl ( $129 \pm 41$  nm) (Figure 4.4g).

The experiments reported upon above indicate that the large differences in ligament size and morphology between  $\text{H}_3\text{PO}_4$  and HCl dealloyed np-Cu samples are caused by the effect of the acid anions on the Cu surface diffusivity<sup>28</sup>. The presence of chloride anions increases the surface diffusion of Cu while the presence of phosphate suppresses the surface diffusion. In the presence of both phosphate and chloride anions, the suppressing effect of phosphate dominates over the promoting effect of chloride anions. The increase in surface diffusivity in the presence of chloride anions is consistent with previous reports. For

example, the presence of chloride anions decreases the corrosion potential for Al-Cu<sup>19</sup>. Delamare and Rhead<sup>29</sup> were first to report that the surface self-diffusion of Cu in the presence of adsorbed chlorine is enhanced by  $\sim 4$  orders of magnitude. Hayes et al.<sup>13</sup> reported that the size of Cu ligaments in np-Cu obtained from Mn-Cu increases from 16nm for sulfuric acid to 125 nm for HCl which is similar to the ligament size observed in the current study for HCl (Figure 4.4f). Similarly, the ligament size of nanoporous silver is associated with the diffusivity of Ag adatoms during dealloying in different acidic solutions<sup>30</sup>. Martin et al.<sup>28</sup> experimentally determined the activation energy of Cu surface diffusion in the presence of a NaCl solution to be  $12 \pm 4$  kJ/mol, compared to 58.6 kJ/mol for Cu diffusion at the vacuum / Cu interface (estimated as  $0.2 \Delta H_s$ , where  $\Delta H_s$  is the molar enthalpy of sublimation at standard temperature and pressure). Thus, the presence of chloride anions can increase the surface diffusivity coefficient by 5 orders of magnitude compared to a chloride-free electrolyte which is consistent with the earlier work of Delamare and Rhead. By contrast, phosphate was found to passivate the Cu surface<sup>31</sup>.

In good agreement with literature, the pH value does not have a dominating effect because the experiments involving  $H_3PO_4$  exhibited similar morphology despite large differences in the pH value, composition, and dealloying time. In contrast, the addition of NaCl to 5M HCl and prolonged etching led to micro-faceted ligaments and further increased the feature size relative to 5M HCl which indicates accelerated Cu surface diffusion. As observed in our study, the passivating/stabilizing effect of phosphate anions dominates over the mobilizing effect of chloride anions and inhibits the anodic dissolution of Cu if phosphate forms a compact film on the copper surface.<sup>31</sup>

The capability to control both ligament size and shape opens up an exciting opportunity in catalysis, namely to tailor the reactivity of Cu catalysts by controlling the step edge densities (Figure 4.5a). Our measurement of the apparent activation energies ( $E_a$ ) of three np-Cu materials for anhydrous ethanol dehydrogenation to acetaldehyde showed that the  $E_a$  for this reaction is relatively insensitive to the nanoscale structure over the temperature range of 180 – 230 °C under steady-state conditions. The calculated apparent activation energies from the Arrhenius plot (Figure 4.5b) are summarized in Table 4.1, and are in good agreement with recently synthesized Zn-free Cu catalysts<sup>32-33</sup>. Therefore, we conclude that the residual Zn from dealloying has no significant impact on the ethanol dehydrogenation reaction. Although the 5M H<sub>3</sub>PO<sub>4</sub> np-Cu material has a higher ligament curvature and thus a higher step edge density than the micro-faceted 5M HCl np-Cu material, within the margin of error, both materials have the same apparent activation energy.

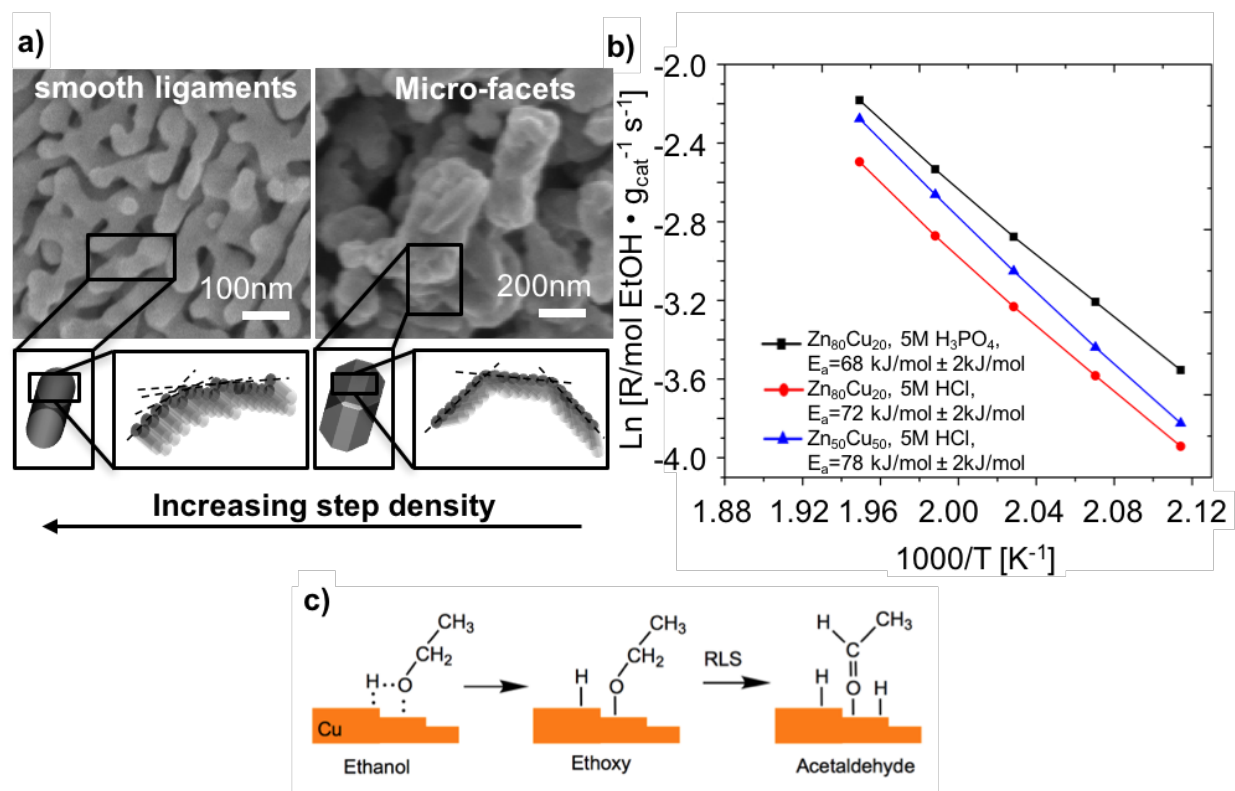


**Figure 4.5 (a)** Influence of surface structure and curvature on the step edge density which affects catalytic reactivity. **(b)** Arrhenius plot of the various np-Cu materials made with different precursor alloys ( $\text{Zn}_{50}\text{Cu}_{50}$  or  $\text{Zn}_{80}\text{Cu}_{20}$ ) and dealloyed in the various electrolytic solutions (5M HCl or 5M  $\text{H}_3\text{PO}_4$ ). **(c)** Reaction scheme for the anhydrous ethanol dehydrogenation on Cu highlighting that the cleavage of the O-H bond to form adsorbed ethoxy is *not* rate limiting. Thus, the rate of reaction does not depend on morphology.

**Table 4.1** Apparent activation energies ( $E_a$ ) for ethanol dehydrogenation on np-Cu from the Arrhenius plot (measured at 180 – 230 °C under steady-state conditions)

Electrolyte	from $\text{Zn}_{80}\text{Cu}_{20}$ Precursor Alloy	from $\text{Zn}_{50}\text{Cu}_{50}$ Precursor Alloy
-------------	--	--



5M HCl	72 kJ/mol $\pm$ 2 kJ/mol	78 kJ/mol $\pm$ 2 kJ/mol
5M H <sub>3</sub> PO <sub>4</sub>	68 kJ/mol $\pm$ 2 kJ/mol	-

To ensure that our reaction conditions were far from equilibrium conversion, a requirement for probing external mass transport limitations, the gas phase equilibrium constant at 500 K (227°C) was calculated from thermodynamic data ( $K_{eq} = 14.5$ ) and used to calculate the equilibrium conversion. As illustrated in Table 4.12, the equilibrium conversion is much higher than the measured conversions of the tested samples thus demonstrating that the measurements were conducted far from equilibrium conversion. In addition, to illustrate that our measurements were not strongly affected by concentration gradients due to internal mass transport limitations, catalytic tests were performed with size-selected np-Cu particles (Table 4.9). The mass-averaged conversion of different size distributions of 5M HCl etched Zn<sub>80</sub>Cu<sub>20</sub> as well as that of a heterogeneous size distribution of a 5M H<sub>3</sub>PO<sub>4</sub> etched sample were all within 0.365 to 0.417 %/mg. Given that the mass-averaged conversion did not depend on particle size, distribution, or sample, we conclude that particle size does not play a critical role in our activation energy measurements.

Through a combination of photoelectron spectroscopy and temperature programmed experiments, previous studies under UHV on Cu(110) and Cu(210) demonstrated that the first step in alcohol dehydrogenation at low conversions and oxygen-free surfaces is the cleavage of the O-H bond to form adsorbed alkoxy and hydrogen on the surface.<sup>34-37</sup> At higher temperatures, the C-H bond in ethoxy is broken to form aldehyde and recombinative hydrogen by further dehydrogenation<sup>34-36</sup>. Wachs *et al.*<sup>35</sup> found that C-H bond

activation is the rate determining step in ethanol dehydrogenation. In a recent study, Sykes and co-workers<sup>38</sup> used a combination of temperature programmed experiments and scanning tunneling microscopy on Cu(111) and Cu(110) model surfaces to verify the two-step dehydrogenation of alcohols. Furthermore, they confirm that dehydrogenation occurs at defect sites. The relative insensitivity of the apparent activation energy for acetaldehyde formation on the ligament curvature in our study is consistent with the C-H bond activation in ethoxy being the rate determining step. Since ethoxy forms preferentially at step edges on Cu(111) and Cu(110)<sup>38</sup>, the step density will be a factor in determining the amount of the ethoxy intermediate formed. However, due to the rate-limiting nature of the first step, the rate of reaction is only weakly dependent on morphology. The different morphologies can potentially be used to manipulate the rates of other reactions that have structure sensitive rate-determining steps. For example, Cu(100) facets seem to be favorable for synthesizing ethylene from CO<sub>2</sub>, whereas Cu(111) facets are more selective for methylene production.<sup>39</sup>

## **4.5 Conclusions**

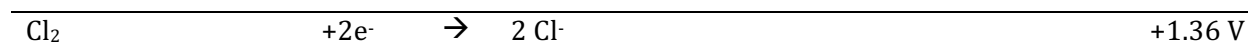
On the macroscale, our EBSD study revealed the retention of grain structure and orientation despite phase transformation for the intermetallic phases in the Zn<sub>50</sub>Cu<sub>50</sub> starting alloy during dealloying. This result provides new insights into dealloying of complex alloy systems that undergo crystallographic phase changes during dealloying. Concerning the structure at the ligament level, the morphology of np-Cu prepared by dealloying Zn<sub>80</sub>Cu<sub>20</sub> precursors fundamentally differs when using 5M HCl or 5M H<sub>3</sub>PO<sub>4</sub> as the etching solution. Chloride anions facilitate Cu surface diffusion and result in larger and micro-faceted ligaments with

129 ± 41 nm in the case of 5M HCl and 156 ± 76 nm for 5M HCl + 0.25 mol NaCl. The presence of phosphate anions suppresses surface diffusion and leads to the formation of np-Cu with smaller and smoothly curved ligaments (50 nm). The morphology control at the nanoscale opens up an opportunity to design more effective Cu catalysts for various reactions. Testing this idea on selective ethanol dehydrogenation, however, we found that the apparent activation energy was relatively insensitive to ligament feature size and curvature which both control the step edge density. Nonetheless, this result is coherent because the C-H bond cleavage of ethoxy is the rate-determining step in the reaction mechanism. Since ethoxy formation, which is more facile on step edges, is not rate determining, an augmented presence of step edge sites does not facilitate the overall reaction. Future work includes the development of methodologies to further tune the np-Cu surface to achieve homogeneous and well-defined facets by using surfactants or electrochemically supported redox reactions. Upon micro and macro-structural optimization, np-Cu could provide a tunable 3D structure with high surface area and an abundance of active sites while reducing mass flow limitations of the reactants.

## 4.6 Supporting Information

### 4.6.1 Standard potentials

**Table 4.2** Reduction half-cell reactions with reference to SHE at 25°C of selected species to illustrate possible combinations of etchants.<sup>40</sup>



HNO <sub>3</sub>	+3H <sup>+</sup>	+3e <sup>-</sup>	→	NO	+2H <sub>2</sub> O	+0.96 V
Cu <sup>2+</sup>		+2e <sup>-</sup>	→	Cu		+0.34 V
SO <sub>4</sub> <sup>2-</sup>	+4H <sup>+</sup>	+2e <sup>-</sup>	→	SO <sub>2</sub>	+2H <sub>2</sub> O	+0.16 V
2 H <sup>+</sup>		+2e <sup>-</sup>	→	H <sub>2</sub>		0.00 V
H <sub>3</sub> PO <sub>4</sub>	+2H <sup>+</sup>	+2e <sup>-</sup>	→	H <sub>3</sub> PO <sub>3</sub>	+H <sub>2</sub> O	-0.28 V
Zn <sup>2+</sup>		+2e <sup>-</sup>	→	Zn		-0.79 V

#### 4.6.2 Crystallographic parameters for Rietveld refinement and the EBSD study

**Table 4.3** Lattice parameters and the final structure parameters determined for Cu<sub>5</sub>Zn<sub>8</sub> in

Zn<sub>50</sub>Cu<sub>50</sub>

Atom	Site	x	y	z	Occ	B <sub>iso</sub>
Zn (1)	8	0.10890	0.10890	0.10890	1	1.12
Cu (1)	8	-0.172000	-0.172000	-0.172000	1	0.88
Cu (2)	12	0.35580	0.00000	0.00000	1	0.71
Zn (2)	24	0.31280	0.31280	0.03660	1	1.32

Unit cell: cubic *I-43m*,  $a = 8.88655(52) \text{ \AA}$ ,  $V = 701.78(12) \text{ \AA}^3$ ; wt% Rietveld: 20.5(37)

**Table 4.4** Lattice parameters and the final structure parameters determined for Cu<sub>1</sub>Zn<sub>1</sub> in

Zn<sub>50</sub>Cu<sub>50</sub>

Atom	Site	x	y	z	Occ	B <sub>iso</sub>
Zn (1)	1	0.50000	0.50000	0.50000	1	1
Cu (1)	1	0.00000	0.00000	0.00000	1	1

Unit cell: cubic *Pm-3m*,  $a = 3.6886(17) \text{ \AA}$ ,  $V = 50.188(68) \text{ \AA}^3$ ; wt% Rietveld: 55.9(86)

**Table 4.5** Lattice parameters and the final structure parameters determined for  $\text{Cu}_3\text{Zn}_1$  in  $\text{Zn}_{50}\text{Cu}_{50}$

Atom	Site	x	y	z	Occ	$B_{iso}$
Zn (1)	4	0.00000	0.00000	0.00000	0.25	1
Cu (1)	4	0.00000	0.00000	0.00000	0.75	1

Unit cell: cubic  $Fm-3m$ ,  $a = 2.95783(11)\text{\AA}$ ,  $V = 25.8773(28)\text{\AA}^3$ ; wt% Rietveld: 24(12)

**Table 4.6** Lattice parameters and the final structure parameters determined for  $\text{Cu}_1\text{Zn}_4$  in  $\text{Zn}_{80}\text{Cu}_{20}$

Atom	Site	x	y	z	Occ	$B_{iso}$
Zn (1)	6	0.33330	0.66660	0.25000	0.2	1
Cu (1)	6	0.33330	0.66660	0.25000	0.8	1

Unit cell: hexagonal  $P63/mmc$ ,  $a = 2.7419842\text{\AA}$ ,  $c = 4.2912936\text{\AA}$ ,  $V = 27.94144\text{\AA}^3$ ; wt% Rietveld: 100

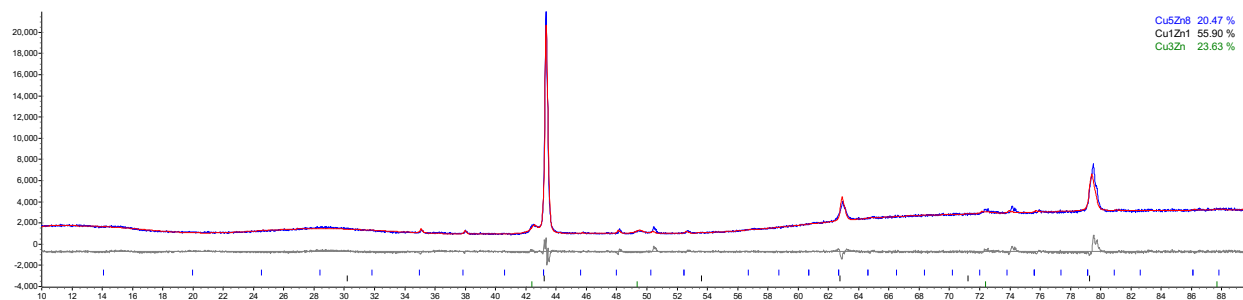


**Figure 4.6** Rietveld refinement patterns of  $Zn_{50}Cu_{50}$ ;  $R_{exp} = 2.24$ ,  $R_{wp} = 4.63$ ,  $R_p = 3.15$ , Goodness of fit  $S = R_{wp} / R_{exp} = 2.06$ .

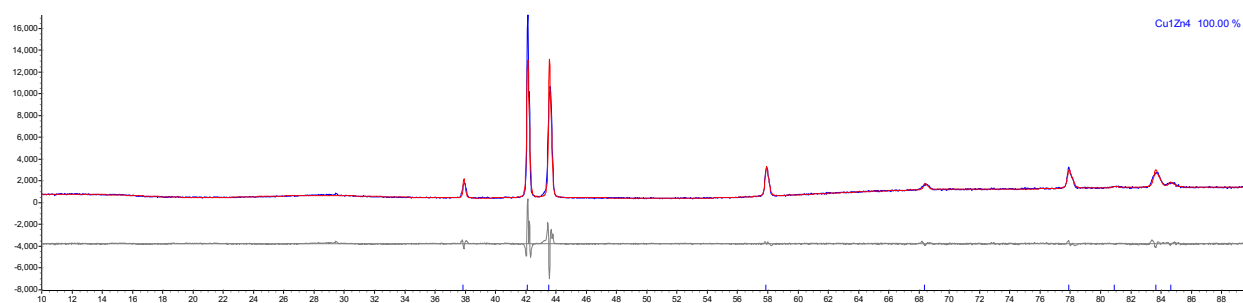


**Figure 4.7** Rietveld refinement patterns of  $Zn_{80}Cu_{20}$ ;  $R_{exp} = 3.27$ ,  $R_{wp} = 8.42$ ,  $R_p = 5.15$ , Goodness of fit  $S = R_{wp} / R_{exp} = 2.58$ .

### 4.6.3 Ligament size distribution/ Histograms

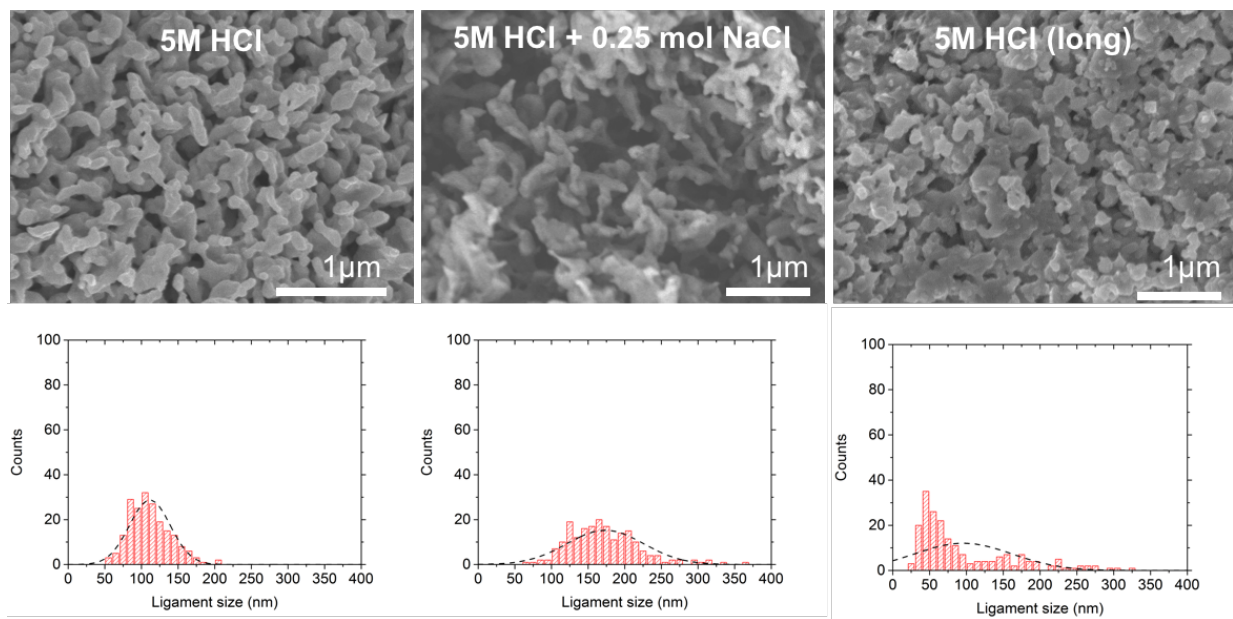


**Figure 4.8.** SEM micrographs for Zn<sub>50</sub>Cu<sub>50</sub> dealloyed in various HCl electrolytic solutions and corresponding histograms showing the ligament size distribution

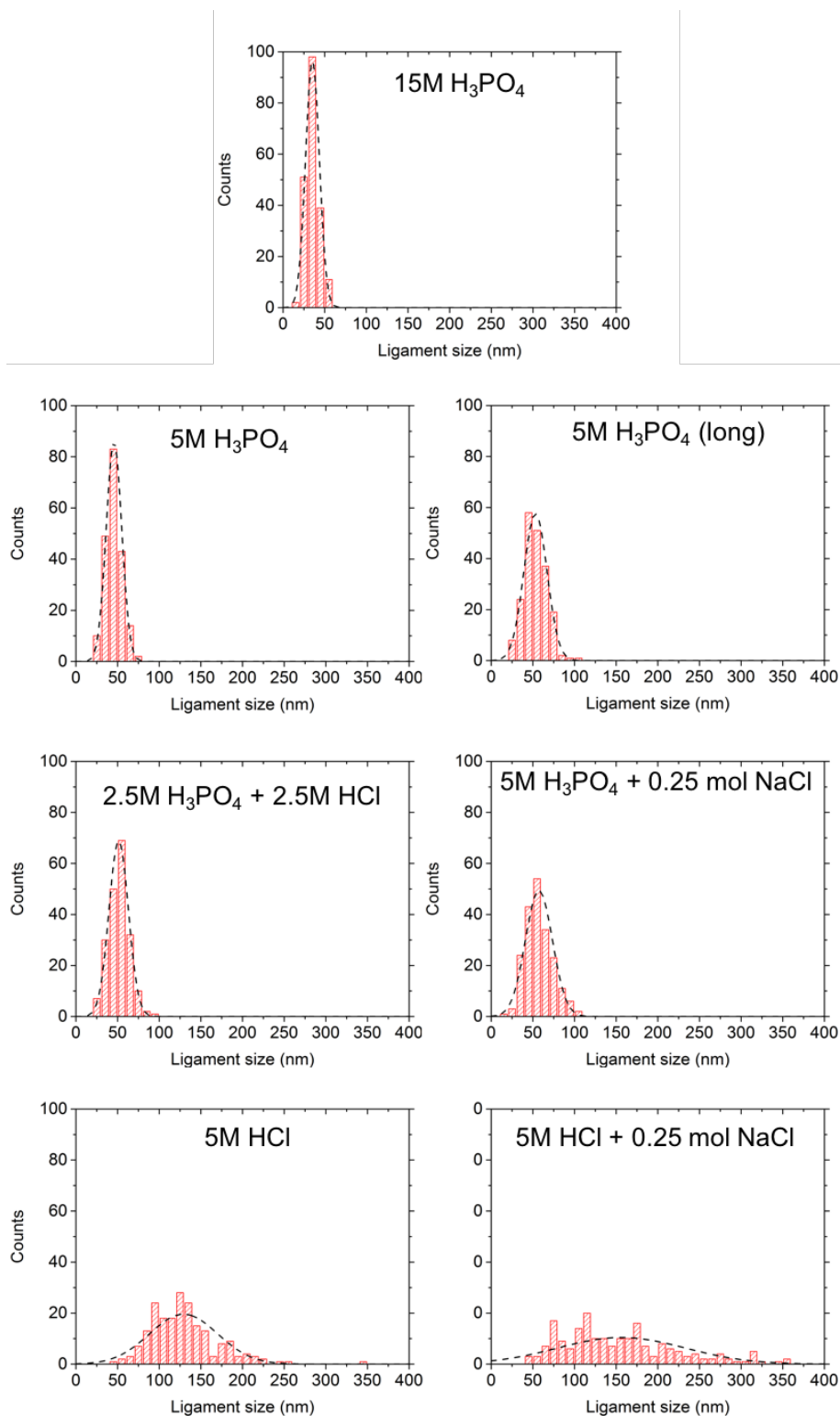


**Figure 4.9.** Ligament size distributions corresponding to Figure 4 (SEM micrographs for  $Zn_{80}Cu_{20}$  dealloyed in various electrolytic solutions).



#### 4.6.4 Structural and compositional changes during dealloying of Zn<sub>50</sub>Cu<sub>50</sub>

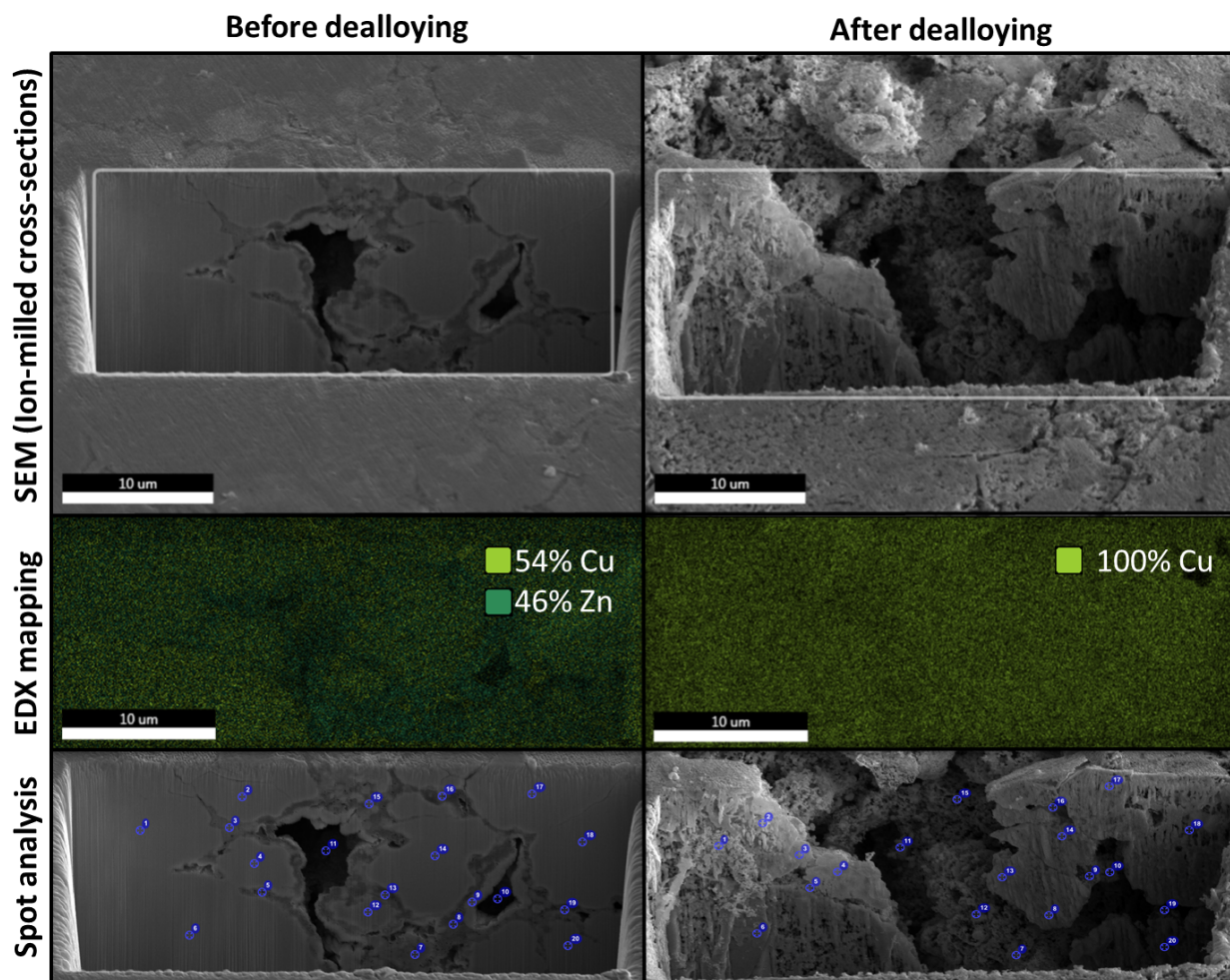


**Figure 4.10.** SEM cross-sections together with EDX analysis (elemental map and spot analysis) for the Zn<sub>50</sub>Cu<sub>50</sub> alloy before and after dealloying. Cu:Zn ratios for spot analysis are listed in Table 4.10

## 4.6.5 Ethanol dehydrogenation

**Table 4.7** Apparent activation energies ( $E_a$ ) for ethanol dehydrogenation on np-Cu from the Arrhenius plot (measured at 180 – 230 °C under steady-state conditions) under different flow rates (7.5, 25 and 50 mL/min).

Electrolyte	Precursor Alloy	Flow Rate (ml/min)	Apparent Activation Energy $E_a$ (kJ/mol)
5M HCl	Zn <sub>80</sub> Cu <sub>20</sub>	25	72 ± 2
5M HCl	Zn <sub>50</sub> Cu <sub>50</sub>	25	78 ± 2
<b>5M H<sub>3</sub>PO<sub>4</sub></b>	<b>Zn<sub>80</sub>Cu<sub>20</sub></b>	<b>25</b>	<b>68 ± 2</b>
<b>5M H<sub>3</sub>PO<sub>4</sub></b>	<b>Zn<sub>80</sub>Cu<sub>20</sub></b>	<b>50</b>	<b>69 ± 2</b>
5M H <sub>3</sub> PO <sub>4</sub>	Zn <sub>80</sub> Cu <sub>20</sub>	7.5	57 ± 2
5M HCl	Zn <sub>80</sub> Cu <sub>20</sub>	7.5	55 ± 3
5M HCl	Zn <sub>50</sub> Cu <sub>50</sub>	7.5	57 ± 2

**Table 4.8** Ethanol conversion of np-Cu prepared from Zn<sub>80</sub>Cu<sub>20</sub> with 5M H<sub>3</sub>PO<sub>4</sub> etchant at different flow rates (7.5, 25 and 50 mL/min) as a function of temperature.

Zn <sub>80</sub> Cu <sub>20</sub> , 5M H <sub>3</sub> PO <sub>4</sub> Sample			
Temperature (°C)	Conversion at 7.5 mL/min Flow Rate	Conversion at 25 mL/min Flow Rate	Conversion at 50 mL/min Flow Rate
250		16.4	13.5
240		11.3	9.4
230		7.9	6.7
220	10.9	5.6	4.8
210	8.1	4.0	3.4
200	6.0	2.9	2.4

190	4.4	2.1	1.7
200		3.0	2.5
210	9.0	4.3	3.6
220	12.2	6.1	5.1
230	15.9	8.4	7.0
240		11.5	9.7
250		15.5	13.0

**Table 4.9** Mass-averaged conversion at 250°C and 50 mL/min flow rate of particle size-selected 5M HCl etched samples and a mixed particle size 5M H<sub>3</sub>PO<sub>4</sub> etched sample tested twice on separate occasions. Particle sizes were selected by sieving with 106, 212, and 425 μm sized meshes. Particles larger than 425 μm were disregarded.

Sample	Particle Sizes (μm)	Mass-averaged Conversion at 250°C and 50 mL/min Flow Rate (%/mg)
Zn <sub>80</sub> Cu <sub>20</sub> , 5M HCl	0 - 106	0.417
Zn <sub>80</sub> Cu <sub>20</sub> , 5M HCl	106 - 212	0.411
Zn <sub>80</sub> Cu <sub>20</sub> , 5M HCl	212 - 425	0.380
Zn <sub>80</sub> Cu <sub>20</sub> , 5M H <sub>3</sub> PO <sub>4</sub>	Mixed	0.365, 0.403 (same sample)

#### 4.6.6 Cu/Zn ratios

**Table 4.10** Atomic ratios for Cu:Zn acquired by EDX spot measurements before and after dealloying in Zn<sub>50</sub>Cu<sub>50</sub> cross-section

Spot#	Before: Cu/Zn (at.%)	After: Cu/Zn (at.%)
1	43.72/56.28	100/0

2	42.95/57.05	100/0
3	<b>20.37/79.63</b>	100/0
4	43.42/56.58	100/0
5	<b>38.00/62.00</b>	96.67/3.33
6	52.02/47.98	100/0
7	<b>24.12/75.88</b>	96.42/3.58
8	46.79/53.21	100/0
9	<b>29.83/70.17</b>	97.22/2.78
10	<b>22.96/77.04</b>	97.05/2.95
11	<b>31.97/68.03</b>	97.55/2.45
12	41.67/58.33	96.22/3.78
13	53.40/46.60	96.95/3.05
14	42.73/57.27	100/0
15	49.74/50.26	96.91/3.09
16	47.55/52.45	100/0
17	42.49/57.51	100/0
18	41.60/58.40	97.52/2.48
19	<b>23.69/76.31</b>	95.14/4.86
20	46.59/53.41	93.51/6.49

#### 4.6.7 Electron backscatter diffraction

**Table 4.11** Crystallographic parameters for EBSD, detailed structure parameters can be found in Table 4.3-4.6

	Lattice parameter	Space group	Bravais lattice
Cu	3.615 Å	Fm-3m (#225)	face-centered cubic
Cu <sub>3</sub> Zn <sub>1</sub>	3.6669 Å	Fm-3m (#225)	face-centered cubic
Cu <sub>1</sub> Zn <sub>1</sub>	2.950 Å	Pm-3m (#221)	Simple cubic
Cu <sub>5</sub> Zn <sub>8</sub>	8.878 Å	I-43m (#217)	Complex cubic
Cu <sub>1</sub> Zn <sub>4</sub>	2.7418 Å, 4.2939 Å	P63/mmc (#194)	Simple hexagonal

#### 4.6.8 Effects of sample geometry and concentration of etching solution

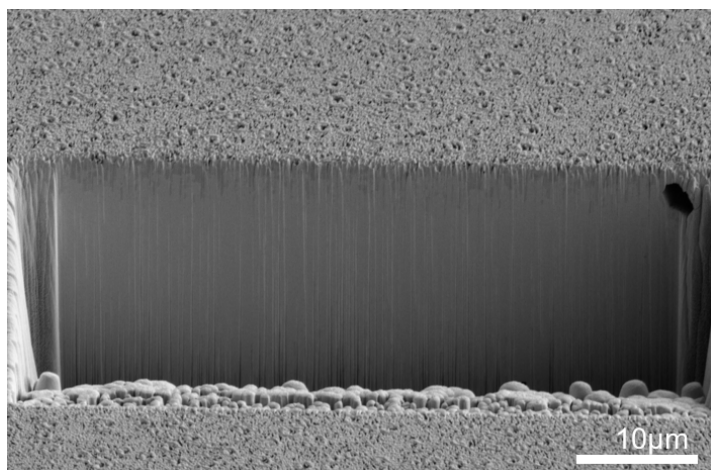


**Figure 4.11.** Cross-sectional SEM of Zn<sub>44</sub>Cu<sub>56</sub> master alloy.

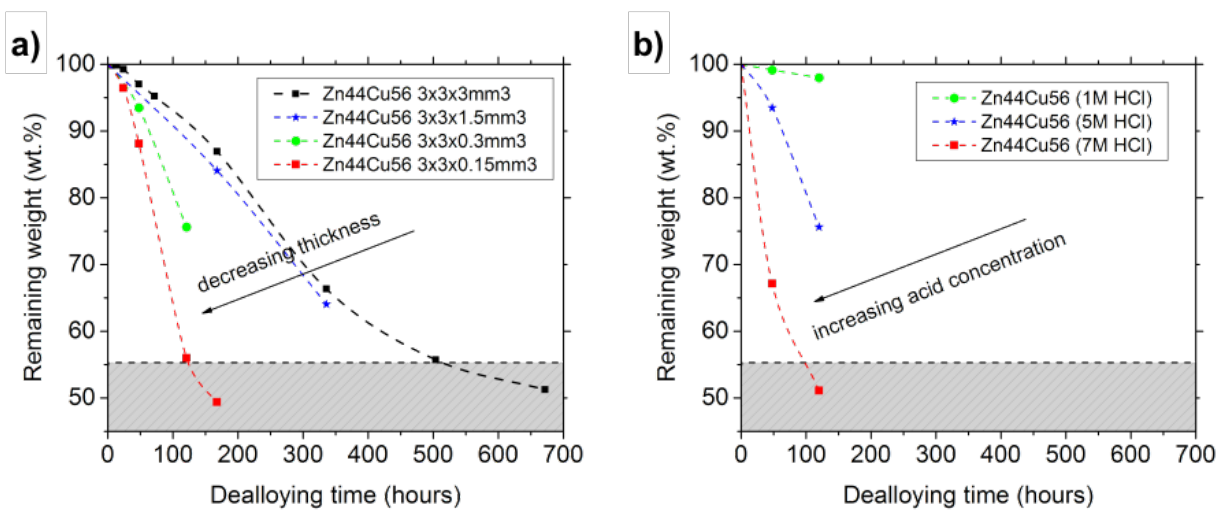


**Figure 4.12.** (a) Influence of sample thickness on the dealloying time for dealloying of Zn<sub>44</sub>Cu<sub>56</sub> in 5M HCl; (b) Influence of the electrolyte concentration on the dealloying time for dealloying of Zn<sub>44</sub>Cu<sub>56</sub> with a sample size of 3x3x0.3mm<sup>3</sup>.

#### 4.6. 9 Conversion of our samples compared to equilibrium conversion

**Table 4.12** The gas phase equilibrium constant was calculated from thermodynamic data at 500K (227°C) (Free energy values from: Haynes, W. M.; Lide, D. R., Handbook of chemistry and physics. *National Institute for Standards and Technology, CRC Press, New York, NY 2010.*) To make the closest comparison, the equilibrium conversion calculated at 500K (227°C) is compared to conversion values measured at 503K (230°C) of the various samples tested.

Sample	Temperature (Kelvin)	Flow Rate (mL/min)	Conversion (%)
Thermodynamic gas phase	500	/	93.6
Zn <sub>80</sub> Cu <sub>20</sub> , 5M H <sub>3</sub> PO <sub>4</sub>	503	50	6.7
Zn <sub>80</sub> Cu <sub>20</sub> , 5M H <sub>3</sub> PO <sub>4</sub>	503	25	7.9
Zn <sub>80</sub> Cu <sub>20</sub> , 5M HCl	503	25	5.7
Zn <sub>50</sub> Cu <sub>50</sub> , 5M HCl	503	25	7.0

#### 4.7 References

1. Ding, Y.; Chen, M. W.; Erlebacher, J., Metallic Mesoporous Nanocomposites for Electrocatalysis. *J. Am. Chem. Soc.* **2004**, *126*, 6876-6877.
2. Wittstock, A.; Zielasek, V.; Biener, J.; Friend, C. M.; Baumer, M., Nanoporous Gold Catalysts for Selective Gas-Phase Oxidative Coupling of Methanol at Low Temperature. *Science* **2010**, *327*, 319-322.
3. Lang, X.; Hirata, A.; Fujita, T.; Chen, M., Nanoporous Metal/Oxide Hybrid Electrodes for Electrochemical Supercapacitors. *Nat. Nanotechnol.* **2011**, *6*, 232-236.

Chapter 4. Multiscale Morphology of Nanoporous Copper made from Intermetallic Phases

4. Biener, J.; Wittstock, A.; Baumann, T. F.; Weissmüller, J.; Bäumer, M.; Hamza, A. V., Surface Chemistry in Nanoscale Materials. *Materials* **2009**, *2*, 2404-2428.
5. Biener, J.; Wittstock, A.; Zepeda-Ruiz, L. A.; Biener, M. M.; Zielasek, V.; Kramer, D.; Viswanath, R. N.; Weissmüller, J.; Bäumer, M.; Hamza, A. V., Surface-Chemistry-Driven Actuation in Nanoporous Gold. *Nat. Mater.* **2009**, *8*, 47-51.
6. Weissmüller, J.; Viswanath, R.; Kramer, D.; Zimmer, P.; Würschum, R.; Gleiter, H., Charge-Induced Reversible Strain in a Metal. *Science* **2003**, *300*, 312-315.
7. Wittstock, A.; Biener, J.; Bäumer, M., Nanoporous Gold: a New Material for Catalytic and Sensor Applications. *Phys. Chem. Chem. Phys.* **2010**, *12*, 12919-12930.
8. Chen, L.-Y.; Yu, J.-S.; Fujita, T.; Chen, M.-W., Nanoporous Copper with Tunable Nanoporosity for SERS Applications. *Adv. Funct. Mater.* **2009**, *19*, 1221-1226.
9. Zhang, Z. H.; Wang, Y.; Qi, Z.; Zhang, W. H.; Qin, J. Y.; Frenzel, J., Generalized Fabrication of Nanoporous Metals (Au, Pd, Pt, Ag, and Cu) through Chemical Dealloying. *J. Phys. Chem. C* **2009**, *113*, 12629-12636.
10. Erlebacher, J.; Aziz, M. J.; Karma, A.; Dimitrov, N.; Sieradzki, K., Evolution of Nanoporosity in Dealloying. *Nature* **2001**, *410*, 450-453.
11. Erlebacher, J., An Atomistic Description of Dealloying - Porosity Evolution, the Critical Potential, and Rate-Limiting Behavior. *J. Electrochem. Soc.* **2004**, *151*, C614-C626.
12. Barroo, C.; Montemore, M. M.; Janvelyan, N.; Zugic, B.; Akey, A. J.; Magyar, A. P.; Ye, J.; Kaxiras, E.; Biener, J.; Bell, D. C., Macroscopic 3D Nanoporosity Formation by Dry Oxidation of AgAu Alloys. *J. Phys. Chem. C* **2017**, *121* (9), 5115-5122.
13. Hayes, J. R.; Hodge, A. M.; Biener, J.; Hamza, A. V.; Sieradzki, K., Monolithic Nanoporous Copper by Dealloying Mn-Cu. *J. Mater. Res.* **2006**, *21*, 2611-2616.
14. Van Petegem, S.; Brandstetter, S.; Maass, R.; Hodge, A. M.; El-Dasher, B. S.; Biener, J.; Schmitt, B.; Borca, C.; Van Swygenhoven, H., On the Microstructure of Nanoporous Gold: An X-ray Diffraction Study. *Nano Lett.* **2009**, *9*, 1158-1163.
15. Ertl, G.; Knözinger, H.; Weitkamp, J., Handbook of Heterogeneous Catalysis. **1997**, 2910-2914.
16. Smith, A. J.; Tran, T.; Wainwright, M. S., Kinetics and Mechanism of the Preparation of Raney (R) Copper. *J. Appl. Electrochem.* **1999**, *29*, 1085-1094.
17. Pryor, M. J.; Fister, J. C., The Mechanism of Dealloying of Copper Solid-Solutions and Intermetallic Phases. *J. Electrochem. Soc.* **1984**, *131*, 1230-1235.

18. Liu, W.; Zhang, S.; Li, N.; Zheng, J.; Xing, Y., Monolithic Nanoporous Copper Ribbons from Mg-Cu Alloys with Copper Contents below 33 at.%. Fabrication, Structure Evolution and Coarsening Behavior along the Thickness Direction. *Int. J. Electrochem. Sci.* **2011**, *6*, 5445-5461.
19. Zhang, Q.; Zhang, Z. H., On the Electrochemical Dealloying of Al-Based Alloys in a NaCl Aqueous Solution. *Phys. Chem. Chem. Phys.* **2010**, *12*, 1453-1472.
20. Zhang, C.; Sun, J.; Xu, J.; Wang, X.; Ji, H.; Zhao, C.; Zhang, Z., Formation and Microstructure of Nanoporous Silver by Dealloying Rapidly Solidified Zn-Ag Alloys. *Electrochim. Acta* **2012**, *63*, 302-311.
21. Li, Z. Q.; Li, B. Q.; Qin, Z. X.; Lu, X., Fabrication of Porous Ag by Dealloying of Ag-Zn Alloys in H<sub>2</sub>SO<sub>4</sub> Solution. *J. Mater. Sci.* **2010**, *45*, 6494-6497.
22. Ding, Y.; Kim, Y. J.; Erlebacher, J., Nanoporous Gold Leaf: "Ancient technology"/Advanced Material. *Adv. Mater.* **2004**, *16*, 1897-1901.
23. Duchaineau, M.; Hamza, A. V.; La Rubia, D.; Diaz, T.; Abraham, F. F., Atomistic Simulation of Compression Wave Propagation in Nanoporous Materials. *arXiv preprint arXiv:0807.1332* **2008**.
24. Sieradzki, K.; Dimitrov, N.; Movrin, D.; McCall, C.; Vasiljevic, N.; Erlebacher, J., The Dealloying Critical Potential. *J. Electrochem. Soc.* **2002**, *149*, B370-B377.
25. Parida, S.; Kramer, D.; Volkert, C. A.; Rosner, H.; Erlebacher, J.; Weissmuller, J., Volume Change During the Formation of Nanoporous Gold by Dealloying. *Phys. Rev. Lett.* **2006**, *97*, 35504-1 - 35504-4.
26. Luo, X. K.; Li, R.; Liu, Z. Q.; Huang, L.; Shi, M. J.; Xu, T.; Zhang, T., Three-Dimensional Nanoporous Copper with high Surface Area by Dealloying Mg-Cu-Y Metallic Glasses. *Mater. Lett.* **2012**, *76*, 96-99.
27. Yu, J. S.; Ding, Y.; Xu, C. X.; Inoue, A.; Sakurai, T.; Chen, M. W., Nanoporous Metals by Dealloying Multicomponent Metallic Glasses. *Chem. Mater.* **2008**, *20*, 4548-4550.
28. Martin, H.; Carro, P.; Creus, A. H.; Morales, J.; Fernandez, G.; Esparza, P.; Gonzalez, S.; Salvarezza, R. C.; Arvia, A. J., Interplay of Surface Diffusion and Surface Tension in the Evolution of Solid/Liquid Interfaces. Dealloying of Beta-Brass in Aqueous Sodium Chloride. *J. Phys. Chem. B* **2000**, *104*, 8229-8237.
29. Delamare, F.; Rhead, G., Increase in the Surface Self-Diffusion of Copper due to the Chemisorption of Halogens. *Surf. Sci.* **1971**, *28*, 267-284.



30. Ji, H.; Wang, X.; Zhao, C.; Zhang, C.; Xu, J.; Zhang, Z., Formation, Control and Functionalization of Nanoporous Silver through Changing Dealloying Media and Elemental Doping. *Crystengcomm* **2011**, *13* (7), 2617-2628.
31. Drogowska, M.; Brossard, L.; Ménard, H., Influence of Anions on the Passivity Behavior of Copper in Alkaline Solutions. *Surf. Coat. Technol.* **1988**, *34*, 383-400.
32. Shan, J.; Janvelyan, N.; Li, H.; Liu, J.; Egle, T. M.; Ye, J.; Biener, M. M.; Biener, J.; Friend, C. M.; Flytzani-Stephanopoulos, M., Selective Non-Oxidative Dehydrogenation of Ethanol to Acetaldehyde and Hydrogen on Highly Dilute NiCu Alloys. *Appl. Catal., B* **2017**, *205*, 541-550.
33. Cassinelli, W. H.; Martins, L.; Passos, A. R.; Pulcinelli, S. H.; Rochet, A.; Briois, V.; Santilli, C. V., Correlation between Structural and Catalytic Properties of Copper supported on Porous Alumina for the Ethanol Dehydrogenation Reaction. *ChemCatChem* **2015**, *7* (11), 1668-1677.
34. Bowker, M.; Madix, R., XPS, UPS and Thermal Desorption Studies of Alcohol Adsorption on Cu(110): II. Higher Alcohols. *Surf. Sci.* **1982**, *116* (3), 549-572.
35. Wachs, I. E.; Madix, R. J., The Selective Oxidation of CH<sub>3</sub>OH to H<sub>2</sub>CO on a Copper (110) Catalyst. *J. Catal.* **1978**, *53* (2), 208-227.
36. Sexton, B.; Hughes, A.; Avery, N., Surface Intermediates in the Reaction of Methanol, Formaldehyde and Methyl Formate on Copper (110). *Appl. Surf. Sci.* **1985**, *22*, 404-414.
37. Chen, A.; Masel, R., Direct Conversion of Methanol to Formaldehyde in the Absence of Oxygen on Cu(210). *Surf. Sci.* **1995**, *343*, 17-23.
38. Wang, Z.-T.; Xu, Y.-F.; El-Soda, M.; Lucci, F. R.; Madix, R. J.; Friend, C. M.; Sykes, E. C. H., Surface Structure Dependence of the Dry Dehydrogenation of Alcohols on Cu (111) and Cu (110). *The Journal of Physical Chemistry C* **2017**.
39. Schouten, K.; Kwon, Y.; Van der Ham, C.; Qin, Z.; Koper, M., A New Mechanism for the Selectivity to C1 and C2 Species in the Electrochemical Reduction of Carbon Dioxide on Copper Electrodes. *Chem. Sci.* **2011**, *2*, 1902-1909.
40. Bard, A. J.; Parsons, R.; Jordan, J., *Standard Potentials in Aqueous Solution*. CRC press: **1985**; Vol. 6.

## Chapter 5.

# Selective Non-Oxidative Dehydrogenation of Ethanol to Acetaldehyde and Hydrogen on Highly Dilute NiCu Alloys

### 5.1 Abstract

The non-oxidative dehydrogenation of ethanol to acetaldehyde has long been considered as an important method to produce acetaldehyde and clean hydrogen gas. Although monometallic Cu nanoparticles have high activity in the non-oxidative dehydrogenation of ethanol, they quickly deactivate due to sintering of Cu. Herein, we show that adding a small amount of Ni ( $\text{Ni}_{0.01}\text{Cu}$  -  $\text{Ni}_{0.001}\text{Cu}$ ) into Cu to form highly dilute NiCu alloys dramatically increases the catalytic activity and increases their long-term stability. The kinetic studies show that the apparent activation energy decreases from  $\sim 70$  kJ/mol over Cu to  $\sim 45$  kJ/mol over the dilute NiCu alloys. The improved performance is observed both for nanoparticles and nanoporous NiCu alloys. The improvement in the long-term stability of the catalysts is attributed to the stabilization of Cu against sintering. Our characterization data show that Ni is atomically dispersed in Cu. The comparison of the catalytic performance of highly dilute alloy nanoparticles with nanoporous materials is useful to guide the design of novel mesoporous catalyst architectures for selective dehydrogenation reactions.

This paper was published in *Applied Catalysis B: Environmental* **2017**, *205*, 541-550.

## 5.2 Introduction

Acetaldehyde ( $\text{CH}_3\text{CHO}$ ) is an important commodity chemical and is widely used as the starting material for the synthesis of a large number of industrial chemicals such as acetic acid, acetate esters, and pentaerythritol.<sup>1, 2</sup> The selective non-oxidative dehydrogenation (DH) of ethanol to acetaldehyde and hydrogen is an important industrial reaction to produce acetaldehyde.<sup>3, 4</sup> It is also an essential first step in ethanol steam reforming and ethanol partial oxidation reactions.<sup>5, 6</sup> Monometallic Cu-based catalysts are widely used for this reaction; however, quick deactivation of copper takes place, attributed to copper particle sintering.<sup>4, 7</sup> On the other hand, the oxidative dehydrogenation (ODH) of ethanol to acetaldehyde and water is the oldest laboratory method to produce acetaldehyde. Commercially, ODH is typically catalyzed by copper, silver, and their oxides or alloys with air in the vapor phase.<sup>1</sup> Similar to the case of DH, the fast deactivation of the catalysts remains a challenging problem.<sup>8, 9</sup> Since DH also produces hydrogen, another valuable product, it is attractive to develop new catalysts that are highly active and selective, with improved catalyst stability during the ethanol dehydrogenation reaction. Naturally, the first consideration is the development of Cu-based alloys possessing these properties.

Although supported Cu based catalysts have been extensively studied for the ethanol dehydrogenation reaction, there is still disagreement on the chemical state of the active Cu species during the reaction. Several groups have reported that  $\text{Cu}^+$  is the

most active species,<sup>10-12</sup> while other studies find that high dehydrogenation activity is associated with the presence of metallic Cu.<sup>13, 14</sup> On the other hand, as mentioned above, the catalytic activity of Cu has been found to decrease rapidly even in the first hour of the reaction, where the deactivation has been attributed to the sintering of metallic Cu at the high dehydrogenation temperature.<sup>7, 14</sup> In searching for a promoter to inhibit the sintering of Cu, it has been reported that the incorporation of chromium oxide into Cu improves the catalyst stability.<sup>13, 15, 16</sup> However, the adverse environmental issues associated with the use of chromium have discouraged the application of this approach. The addition of alkali metal oxides has also been reported to improve the stability of Cu, although the effect is less significant than chromium oxide.<sup>7</sup>

Alternatively, the dehydrogenation of ethanol on Au NPs supported on reducible oxides has also been explored.<sup>3, 17-19</sup> Supported Au NPs with certain particle sizes have been demonstrated to have high activity and selectivity for the reaction.<sup>3</sup> An exception is Au/Al<sub>2</sub>O<sub>3</sub>, where the dehydration of ethanol to ethylene and dimethyl ether dominates the reaction.<sup>18</sup> Recently, Wang *et al.* have reported that isolated Au species supported on nanoscale ZnZrO<sub>x</sub> composite oxides catalyze the dehydrogenation of ethanol to acetaldehyde and hydrogen with 100% selectivity at low temperatures (~200 °C), even in the presence of water, in a well-separated temperature window from the dehydration and steam reforming reactions that take place on the support.<sup>17</sup> The presence of atomically dispersed Au species seems to play an essential role in the activation of ethanol and its subsequent dehydrogenation reaction.

In recent years, development of catalysts with atomic dispersions of an active metal on various supports has attracted considerable attention.<sup>20</sup> In the case of bimetallic catalysts, various highly dispersed alloys or even single atom alloy (SAA) catalysts containing atomically dispersed active species have been reported to be highly active and selective for many catalytic reactions. For example, atomically dispersed Au species supported on ZnZrO<sub>x</sub> oxides catalyze the ethanol dehydrogenation reaction, as discussed above.<sup>17</sup> Isolated Pt and Au cations stabilized by -O bonds on various supports supplying vicinal -OH groups have been found to be highly active for the water-gas shift reaction.<sup>21-24</sup> PdAu bimetallics have been reported as selective hydrogenation catalysts in both gas-phase<sup>25-27</sup> and liquid-phase reactions.<sup>28, 29</sup> These studies have focused on bimetallic nanoparticles supported on carbon, oxides or other supports. It has also reported that unsupported gold, prepared in nanoporous form from AuAg alloys after leaching out most (~97%) of the silver, is an effective catalyst for the selective oxidation of methanol, and other alcohols.<sup>30, 31</sup> Since unsupported gold is inert, it was apparent that the active sites must be at the interface of silver domains and gold. These sites also catalyze the oxidative self-coupling of methanol to methyl formate<sup>32</sup> and the cross coupling of methanol with higher alcohols or aldehydes to form esters.<sup>33</sup> The interaction of gold with nickel in Au@NiO<sub>x</sub> core-shell particles rather than silver has been exploited by Asahi Chemicals recently to selectively oxidize methacrolein with methanol to produce methyl methacrylate (MMA) in industrial volumes.<sup>34</sup>

Similar to gold, copper is a highly selective hydrogenation metal, but it has negligible activity for the hydrogenation of alkadienes or alkynes, limited by a large

activation energy barrier for dissociative adsorption of hydrogen.<sup>35</sup> However, it was recently shown that adding Pd or Pt atoms to metallic Cu hosts forming PdCu or PtCu SAAs is a good strategy to produce truly bi-functional catalysts, whereby the Pd or Pt atom dissociates H<sub>2</sub> and spills over H atoms to the Cu surface, rendering the latter active for alkyne and alkadiene hydrogenation reactions.<sup>36-38</sup> The SAAs have superior selectivity to the Pt or Pd monometallics. Excellent selectivity for dehydrogenation of methanol has also been demonstrated on PdCu and PtCu SAAs, the Pd or Pt atoms serve as exit points for the association of H atoms and desorption of H<sub>2</sub>.<sup>39, 40</sup>

In the present study, we have investigated the addition of Ni in Cu as a novel catalyst for the selective dehydrogenation of ethanol to acetaldehyde and hydrogen. Ni-containing Cu nanoparticles (NiCu NPs) and nanoporous Cu (np-NiCu) materials were prepared with high dispersions of Ni in Cu and found to be very active and selective for this reaction. The presence of highly dispersed Ni in Cu dramatically decreases the apparent activation energy from ~70 kJ/mol over Cu to ~45 kJ/mol over NiCu alloys. Moreover, as an additional beneficial effect, Ni efficiently suppresses the coarsening of Cu nanostructures during the dehydrogenation reaction, thus increasing the long-term stability of these catalysts.

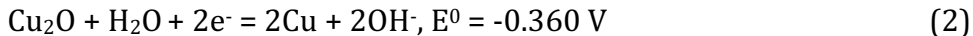
## **5.3 Methods**

### **5.3.1 Catalyst preparation**

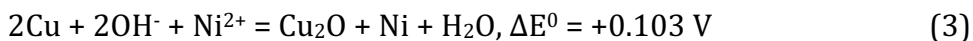
In this work, several types of highly dilute NiCu alloys were prepared as supported nanoparticles and unsupported nanoporous alloys. These were silica supported NiCu NPs, unsupported nanoporous NiCu prepared through a sacrificial support method labeled np-NiCu (SSM), and nanoporous NiCu prepared through a dealloying technique labeled np-NiCu (DL). Silica supported NiCu NPs with various Ni concentrations were synthesized through a wet chemistry method followed by a modified electroless galvanic deposition method. In the first step, metallic Cu nanoparticles were prepared as colloids in solution as described in detail in our recent publications.<sup>38, 40</sup> Briefly, under nitrogen protection, a 0.1 M solution of ascorbic acid was added to a mixed aqueous solution of  $\text{Cu}(\text{NO}_3)_2$  and polyvinylpyrrolidone (PVP) (200:1 molar ratio of Cu to PVP), followed by drop-wise addition of  $\text{NaBH}_4$  (0.1 M), upon which the solution turned to an opaque brown suspension. Fumed silica, with a surface area of  $200 \text{ m}^2/\text{g}$  (as received), was pre-activated by heating in air at  $650 \text{ }^\circ\text{C}$  for 12 h, suspended in deionized water under constant stirring, and added drop-wise to the colloidal solution. The solution was kept under nitrogen protection and constant stirring for 30 min, followed by filtering and washing with deionized water several times. The collected solid was dried in vacuum for 12 h and calcined in air to  $350 \text{ }^\circ\text{C}$  for 4 h. The product was subsequently reduced in pure hydrogen at  $350 \text{ }^\circ\text{C}$  for 3h to obtain supported metallic Cu NPs. The typical Cu

loading is 8wt% as determined by inductively coupled plasma (ICP) elemental analysis.

In our previous studies, galvanic replacement (GR) has been successfully used to prepare PdCu and PtCu single atom alloys.<sup>37, 38</sup> However, GR is not an applicable method to deposit Ni to Cu surface, since Ni has a lower reduction potential ( $\text{Ni}^{2+}/\text{Ni}$ ,  $E^0 = -0.257 \text{ V}$ ) than Cu ( $\text{Cu}^{2+}/\text{Cu}$ ,  $E^0 = +0.340$ ).<sup>41</sup> Therefore, a novel modified electroless galvanic deposition method was developed to deposit highly dispersed Ni to the Cu NPs. The following redox reactions show the principle of this method:



Combination of (1) and (2) gives:



Reaction (3) is spontaneous; accordingly, Ni atoms are deposited on the surface of  $\text{Cu}_2\text{O}$ , which is formed by the oxidation of the Cu metal in the presence of  $\text{OH}^-$  (alkaline solution). The deposition was as follows: first, a certain amount of  $\text{Ni}(\text{NO}_3)_2 \cdot 6\text{H}_2\text{O}$  was completely dissolved in deionized water under nitrogen bubbling and continuous stirring. Then, 0.01M NaOH was added drop-wise to the solution to



reach a pH value of 10.83. The desired amount of pre-reduced silica-supported Cu NPs was then added into the solution. The reaction was held for 1 h under nitrogen protection and continuous stirring. The typical atomic ratio of Ni to Cu ranged from 1:100 to 1:1000. Subsequently, the suspension was filtered and washed with deionized water several times, followed by vacuum drying at 70 °C for 12 h. The obtained solid was further reduced in pure hydrogen at 400 °C for 3h. The Ni loading was measured by ICP.

We also prepared np-NiCu (SSM) catalysts through the sacrificial support method.<sup>42</sup> To do this, pre-reduced Cu/SiO<sub>2</sub> powder was dispersed in an 8M KOH solution under continuous stirring at room temperature. This leaching process continued for 36 h to ensure that the majority of the silica support was leached away. In this process, the color of the solution changed from dark-brown initially to red-brown at the end. The solid was filtered and washed with deionized water until the pH value of the filtrate was neutral, followed by vacuum drying at 70 °C for 12 h. The obtained materials were then reduced in pure hydrogen at 350 °C for 3h to obtain np-Cu (SSM). Ni was introduced to the surface of np-Cu (SSM) using the galvanic deposition method discussed above. After Ni deposition, the solid was reduced in pure hydrogen at 400 °C for 3h to obtain the final product np-NiCu (SSM). The atomic ratio of Ni to Cu in np-NiCu (SSM) catalysts was determined by ICP measurements.

Alternatively, np-NiCu (DL) was prepared through dealloying of Cu-Zn alloys followed by a liquid salt impregnation/freeze drying Ni addition process. Firstly, np-Cu (DL) ingots were prepared by the selective etching the Zn from Cu<sub>50</sub>Zn<sub>50</sub> bimetallic

alloy disks in 5M hydrochloric acid for 36 h. The resulting nanoporous Cu sample was rinsed with deionized water and dried in a vacuum oven, labeled as np-Cu (DL). To prepare np-NiCu (DL), part of np-Cu (DL) was immersed in nickel(II) nitrate solution with a nickel concentration of 0.3M. To guarantee full penetration of solution into the pores of np-Cu (DL), vacuum was applied for 2 h to remove air bubbles trapped inside the core of np-Cu (DL). The sample was then kept under atmospheric conditions in solution overnight, followed by a freeze-drying precursor method, in which the sample was immersed into liquid nitrogen for 10 min and subsequently kept in a freeze-drying system at 0.012 mbar and -106 °C (Labconco, FreeZone 4.5 Liter Benchtop Freeze Dry System) for 2 days. Freeze drying helps to keep the homogeneous distribution of Ni precursors while removing water,<sup>43</sup> therefore, it allows a high dispersion of Ni in Cu after drying. In the final step, the sample was reduced in hydrogen (4% H<sub>2</sub> balanced in Ar) at 500°C for 1 h. The atomic ratio of Ni to Cu in the np-NiCu (DL) material was determined as approximately 0.03:1 through ICP measurements. ICP also found approximately 4% Zn residue in the np-Cu (DL) and np-NiCu (DL) materials.

### **5.3.2 Characterization techniques**

X-ray powder diffraction (XRD) patterns were collected on a PANalytical X'Pert Pro instrument using nickel-filtered Cu K $\alpha$  radiation ( $\lambda = 1.54056 \text{ \AA}$ ). The measurements were taken at 45 kV and 40 mA in a continuous mode. Data was collected for  $2\theta$  between 25° and 80°. High-resolution transmission electron microscope (HRTEM)

images of highly dilute NiCu alloys were obtained with a JEOL 2100 TEM system. All samples for HRTEM characterization were prepared by dropping the corresponding colloidal solutions onto lacey carbon TEM grids. Scanning electron microscope (SEM) images were taken using a Zeiss Supra 55VP microscope.

X-ray photoelectron spectroscopy (XPS) characterization was performed with a PHI VersaProbe II system equipped with a monochromatic Al K $\alpha$  source and a double focusing hemispherical analyzer. The XPS system is also equipped with an argon ion sputter gun for depth-profile analysis. XPS samples were prepared by loading the catalyst powder onto a Cu foil. XPS data were analyzed using the Casa XPS software. Diffuse reflectance infrared Fourier transform spectroscopy (DRIFTS) measurements were performed on a Thermo Scientific Nicolet iS50 FTIR Spectrometer and a Praying Mantis high temperature reaction chamber. NiCu alloys were reduced *in situ* with 10% H<sub>2</sub>/He at a flow rate of 10 mL/min at 350°C for 1 h. CO adsorption on the NiCu samples was performed at room temperature. Pure CO was introduced into the DRIFTS cell at a flow rate of 10 mL/min. This was followed by a He purge at a flow rate of 20 mL/min to remove gas phase CO in the cell prior to DRIFTS measurements.

The ethanol dehydrogenation activity of the NiCu alloys was evaluated in a fixed-bed flow reactor at atmospheric pressure. Typically 100 mg sample was loaded into a U-shaped quartz reactor tube between two layers of quartz sand and packed in between two quartz wool plugs. The reactor was heated in a furnace equipped with a temperature controller. The temperature of the catalyst was measured with a K-type

thermocouple reaching the top of the catalyst bed. Prior to testing, all catalysts were reduced under a flow of H<sub>2</sub> (10% in argon) with a flow rate of 10 mL/min at 350 °C for 1 h. The typical reaction gas composition was 5.6 % ethanol balanced in He, through a bubbler system, using a flow rate of 10 mL/min. The effluent gas was monitored online by a residual gas analyzer (SRS RGA 200). Ethanol, acetaldehyde, ethyl acetate, H<sub>2</sub>, CO, CO<sub>2</sub>, and C<sub>2</sub>H<sub>4</sub> were monitored by  $m/z = 31, 29, 61, 2, 28, 44,$  and 27, respectively. In addition, in the case of acetaldehyde, the contribution from the ethanol fragment was subtracted from the original  $m/z = 29$  signal prior to further processing.

Long-term ethanol dehydrogenation activity was tested in a quartz tube reactor operated at atmospheric pressure and housed in a tubular furnace. Hydrogen treatment was performed in 20% H<sub>2</sub> with a flow rate of 20 mL/min. The temperature was ramped to 250 °C for Cu catalysts and 350 °C for NiCu catalysts at a rate of 10 °C/min and held for 1 h. The sample was held or cooled to 250°C after hydrogen treatment and then exposed to reaction conditions of 5.6 % ethanol using a flow rate of 7.5 mL/min. To provide ethanol, He gas was flowed through a bubbler filled with liquid ethanol held at room temperature. The effluent gas was continuously analyzed by a GC-MS (Agilent 5975C and Agilent 7890A) equipped with HP-PLOT Q and CARBONPLOT columns.

## **5.4 Results and Discussion**

Inspired by our recent findings of methanol dehydrogenation on PtCu single atom alloy catalysts,<sup>40</sup> we prepared highly dilute NiCu alloy catalysts and examined their catalytic performance in the selective ethanol dehydrogenation reaction under realistic reaction conditions. As discussed below, Ni is atomically dispersed in Cu in the selective catalysts. Our work demonstrates that such Ni species play a key role in the dehydrogenation of ethanol.

XRD patterns of silica supported Cu NPs, silica supported Ni<sub>0.01</sub>Cu NPs before reduction, silica supported Ni<sub>0.01</sub>Cu NPs after reduction, and silica supported Ni<sub>0.01</sub>Cu NPs after use in ethanol dehydrogenation at 250 °C for 8 h are shown in Figure 5.1. The XRD pattern of Cu NPs is dominated by diffraction peaks that are attributed to the (111), (200) and (220) lattice planes of metallic Cu.<sup>44</sup> A rather broad peak centered at 37° can be attributed to the (111) diffraction of Cu<sub>2</sub>O.<sup>44</sup> The appearance of a small Cu<sub>2</sub>O diffraction peak is due to the formation of a thin Cu<sub>2</sub>O surface layer after the exposure of metallic Cu NPs to air.<sup>44, 45</sup> For Ni<sub>0.01</sub>Cu before reduction, the XRD pattern clearly shows that Cu<sub>2</sub>O is the majority phase, which is expected because of the oxidation of Cu to Cu<sub>2</sub>O by OH<sup>-</sup> during the Ni deposition step. After reduction, Cu<sub>2</sub>O was reduced and metallic Cu peaks are dominant. Moreover, XRD patterns of Ni<sub>0.01</sub>Cu NPs after reduction show no observable difference compared to Cu NPs, as expected if Ni is atomically dispersed, and mostly on the near surface layer of Cu (see XPS data below). No Ni NPs related XRD peaks are observed, although the Ni concentration in Ni<sub>0.01</sub>Cu NPs is probably too low to exclude the formation of Ni NPs based on the XRD

data alone. Similarly, the XRD patterns of Ni<sub>0.01</sub>Cu after the reaction were preserved, and no separate Ni phases were formed, at least not detectable by XRD at these small Ni content. In all samples, the estimated average crystallite size of Cu is ~14 nm, as calculated by the Scherrer equation.

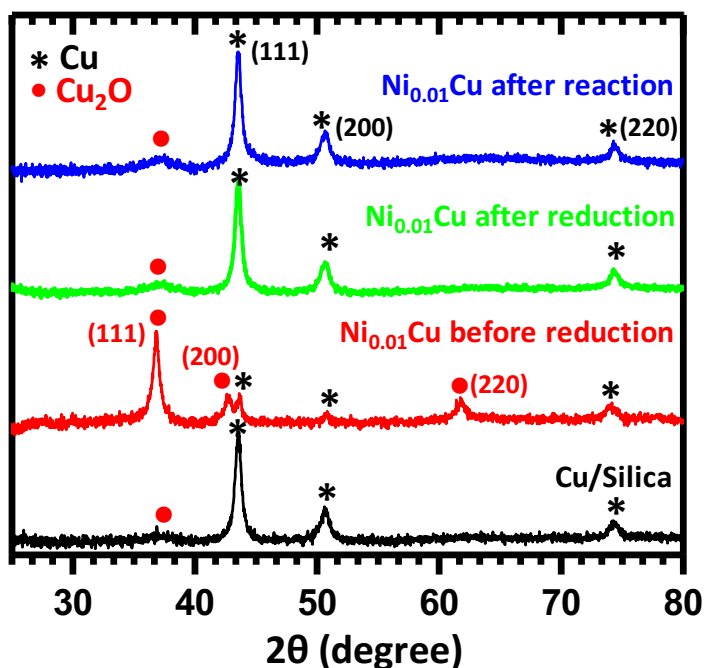


**Figure 5.1** XRD patterns of silica supported Cu NPs and silica supported Ni<sub>0.01</sub>Cu NPs before reduction, after reduction, and after the ethanol dehydrogenation reaction at 250 °C for 8 h.

Figure 5.2 shows the HRTEM images of NiCu alloys. Figure 5.2a shows the image of silica supported Ni<sub>0.01</sub>Cu NPs. The lattice fringes of Ni<sub>0.01</sub>Cu NPs show a spacing of 0.2 nm, in good agreement with the (111) lattice planes of Cu.<sup>46</sup> Moreover, the measured nanoparticle size is ~13-14 nm, in good agreement with the XRD

analysis of Figure 5.1. The HRTEM images in Fig 2b, 2c and 2d clearly exhibit the crystalline nature of nanoporous materials, indicating that the nanoporous NiCu alloys prepared by either the sacrificial support method or the dealloying method are not amorphous but are well-crystallized. Furthermore, the HRTEM images collected from np-Ni<sub>0.01</sub>Cu (SSM), np-Cu (DL), and np-Ni<sub>0.003</sub>Cu (DL) samples all show the (110) lattice fringes of metallic Cu (lattice spacing 0.25 nm).<sup>47</sup> Unfortunately, due to the similar atomic number of Ni and Cu, it is impossible to distinguish Ni from Cu through Z-contrast imaging in scanning TEM measurements.<sup>48</sup> Indeed, Ni species cannot be distinguished by TEM in the highly dilute NiCu alloys of Figure 5.2.

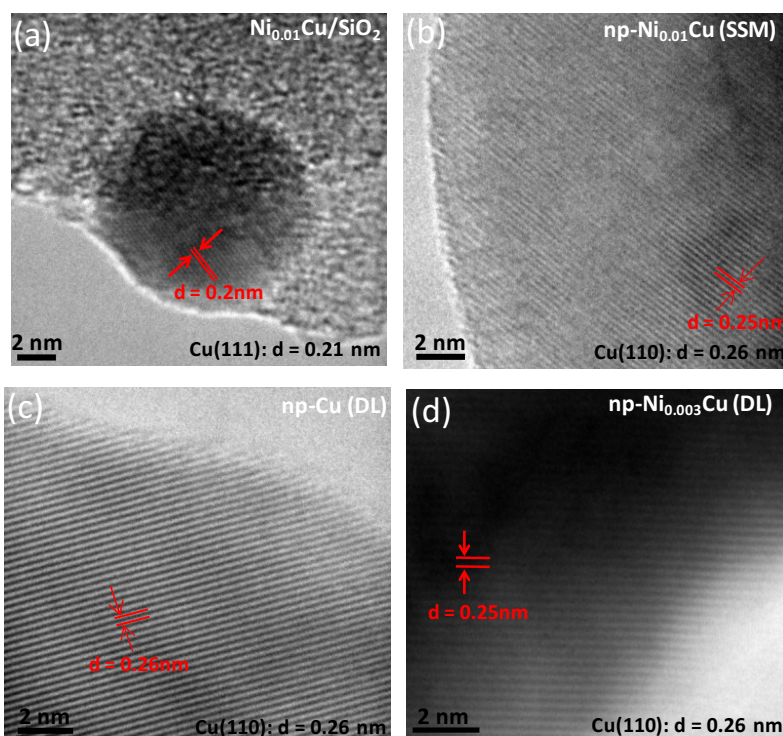


**Figure 5.2** a) HRTEM image of a silica supported Ni<sub>0.01</sub>Cu nanoparticle; b) HRTEM image of a typical region of the np-Ni<sub>0.01</sub>Cu (SSM) catalyst; c) HRTEM image of np-Cu

(DL); d) HRTEM image of np-Ni<sub>0.003</sub>Cu (DL). All samples were imaged in their prepared form.

SEM images of np-Ni<sub>0.01</sub>Cu (SSM) and np-Ni<sub>0.003</sub>Cu (DL), after reduction in hydrogen (10% balanced in Ar) at 350 °C for 1 h, as well as np-Cu (DL) after reduction in hydrogen (10% balanced in Ar) at 250 °C for 1 h, are shown in Figure 5.3. They illustrate the porous structure of these nanoporous materials. Clearly, these highly dilute NiCu alloys prepared by the sacrificial support method or by dealloying are porous materials with well-crystallized nanostructure. The average feature size of np-Ni<sub>0.01</sub>Cu (SSM) is  $395 \pm 99$  nm, whereas for np-Cu (DL) and np-Ni<sub>0.003</sub>Cu (DL) they are  $150 \pm 35$  and  $209 \pm 41$  nm, respectively. The average feature size of np-Ni<sub>0.003</sub>Cu is larger than that of np-Cu, which we attribute to the additional reduction step at 500 °C for np-Ni<sub>0.003</sub>Cu during the step of synthesis.

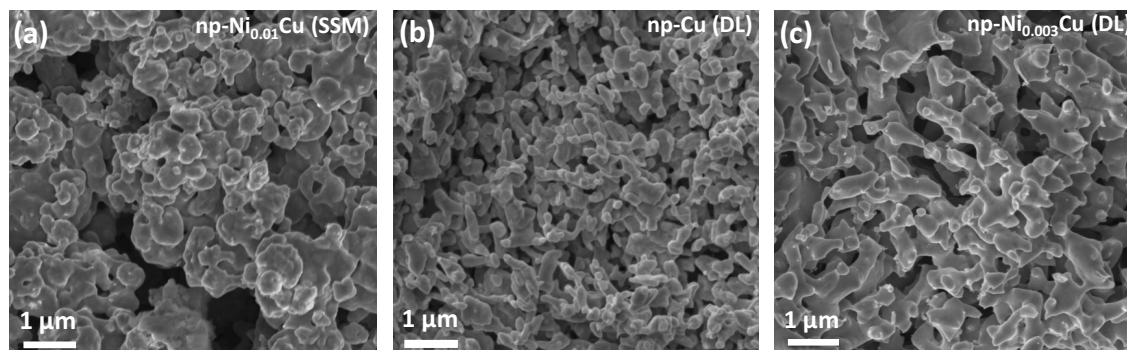


**Figure 5.3** a) SEM image of np-Ni<sub>0.01</sub>Cu (SSM); b) SEM image of np-Cu (DL); c) SEM image of np-Ni<sub>0.003</sub>Cu (DL). np-Ni<sub>0.01</sub>Cu (SSM) and np-Ni<sub>0.003</sub>Cu (DL) were pre-reduced



in hydrogen (10% balanced in Ar) at 350 °C for 1h prior to SEM imaging, while np-Cu (DL) was pre-reduced at 250 °C for 1h prior to SEM imaging.

Table 5.1 lists the surface areas (per gram of Cu) of silica supported Ni<sub>0.01</sub>Cu NPs, np-Ni<sub>0.01</sub>Cu (SSM), and np-Ni<sub>0.003</sub>Cu (DL). The surface area of silica supported Ni<sub>0.01</sub>Cu NPs was calculated based on following equations, assuming the spherical shape of particles: <sup>7, 49</sup>

$$S_{Cu}(m^2/g) = 6.73 \times 10^{11} / d_{Cu}(nm) \quad (4)$$

where  $S_{Cu}$  is the specific surface area of Cu ( $m^2/g$ ), while  $d_{Cu}$  stands for the average particle size of Cu (nm), here ~14 nm as determined from XRD and TEM. The surface areas of np-Ni<sub>0.01</sub>Cu (SSM) and np-Ni<sub>0.003</sub>Cu (DL) were determined from BET measurements, listed in Table 5.1. The silica supported nanoparticles, Ni<sub>0.01</sub>Cu NPs, have the largest specific copper surface area among these catalysts.

**Table 5.1** Cu surface area of silica supported Ni<sub>0.01</sub>Cu NPs, np-Ni<sub>0.01</sub>Cu (SSM), and np-Ni<sub>0.003</sub>Cu (DL).

<b>Samples</b>	<b>Surface area of Cu (<math>m^2/g</math>)</b>
Ni <sub>0.01</sub> Cu NPs	48
np-Ni <sub>0.01</sub> Cu (SSM)	8.7
np-Ni <sub>0.003</sub> Cu (DL)	2.7

Figures 5.4a and 5.4b show the photoemission features of Ni 2p and Cu 2p of np-Ni<sub>0.01</sub>Cu (SSM) before reduction, after reduction, and after the ethanol dehydrogenation reaction at 250 °C for 8 h. Table 5.2 lists the surface atomic ratio of Ni/Cu estimated from XPS. The surface Ni/Cu atomic ratio before reduction is 0.12 and decreases to 0.06 after reduction, a value that persists after the ethanol dehydrogenation reaction, suggesting that after reduction in hydrogen atmosphere part of Ni atoms diffuse to the subsurface, and remain in the subsurface during the ethanol dehydrogenation reaction. Furthermore, Ni 2p photoemission spectra also indicate that before reduction Ni<sup>2+</sup> is the dominant species.<sup>50, 51</sup> It has been reported that highly dispersed metallic Ni can be easily oxidized to NiO under atmospheric conditions.<sup>52, 53</sup> Whilst after reduction, the peak related to the metallic Ni significantly grows.<sup>50, 51</sup> The remaining of Ni<sup>2+</sup> after reduction is possibly due to the fact that NiO was not fully reduced at 400 °C, while it could also result from the re-oxidation of Ni<sup>0</sup> after exposing the sample to air after the reduction. On the other hand, Cu 2p photoemission spectra show that before reduction the features centered at 940 and 962 eV are present, while they disappear after reduction and after reaction; these features are assigned to the satellite peaks of CuO.<sup>54</sup> Clearly, Cu<sup>2+</sup> is only present in np-Ni<sub>0.01</sub>Cu (SSM) before reduction, not in np-Ni<sub>0.01</sub>Cu (SSM) after reduction and after reaction. On the other hand, Cu<sub>2</sub>O does not have satellite peaks in XPS, and also the main peak of Cu<sup>1+</sup> is overlapped with metallic Cu. Therefore, XPS data in Figure 5.4 cannot distinguish Cu<sub>2</sub>O from metallic Cu. Furthermore, we also tried to obtain Ni 2p photoemission features of silica supported Ni<sub>0.01</sub>Cu NPs, however the low Ni

concentration in the supported catalyst does not yield a measurable signal of Ni. Moreover, we also took the Ni 2p photoemission spectra of np-Ni<sub>0.003</sub>Cu (DL) (not shown here); the spectra are similar to np-Ni<sub>0.01</sub>Cu (SSM), and the surface atomic ratio of Ni/Cu is shown in Table 5.2. Similar to np-Ni<sub>0.01</sub>Cu (SSM), the surface Ni/Cu ratio of np-Ni<sub>0.003</sub>Cu (DL) suggests that after reduction, part of Ni atoms diffuse to the subsurface, and remain there during the reaction.

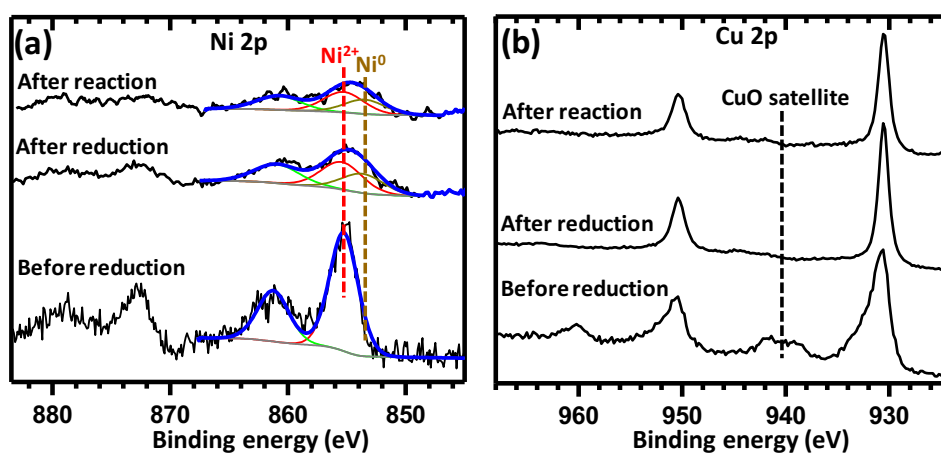


**Figure 5.4** The photoemission feature of Ni 2p (a) and Cu 2p (b) of np-Ni<sub>0.01</sub>Cu (SSM) before reduction, after reduction, and after the ethanol dehydrogenation reaction at 250 °C for 8 h. Approximately 10 consecutive scans were collected for the sample before reaction, and approximately 40 consecutive scans were collected for the samples after reduction and after reaction.

**Table 5.2** The surface atomic ratio of Ni/Cu of np-Ni<sub>0.01</sub>Cu (SSM) and np-Ni<sub>0.003</sub>Cu (DL) under various conditions.

Sample conditions	Surface Ni/Cu ratio of np-Ni <sub>0.01</sub> Cu (SSM)	Surface Ni/Cu ratio of np-Ni <sub>0.003</sub> Cu (DL)
Before reduction	0.12	0.035
After reduction at 400 °C	0.06	0.013
After reaction at 250 °C	0.06	0.013

Using CO as a probe molecule, DRIFTS measurements were performed on silica supported Cu NPs, Figure 5.5a, and silica supported Ni<sub>0.01</sub>Cu NPs, Figure 5.5b, at various temperatures. All samples were reduced *in situ* in 10% H<sub>2</sub> (balanced in Ar) at 350 °C for 1h prior to the introduction of CO. The adsorption of CO was performed at room temperature with a flow rate of 10 mL/min followed by a He purge at a flow rate of 20 mL/min for 10 min. Prior to acquiring the DRIFTS data, samples were heated to the desired temperature in He for 10 min and maintained at this temperature during the data acquisition. CO-DRIFT spectra in Fig 5a show a single peak centered at approximately 2128 cm<sup>-1</sup>, which may be attributed to either the Cu<sup>+</sup>-CO carbonyl species or the atop binding of CO on Cu NPs.<sup>36, 55</sup> With increasing temperatures, the peak area continuously decreases, indicating desorption of CO from the Cu surface. Clearly, at 100 °C, this peak disappears completely, suggesting that all the CO species had desorbed.

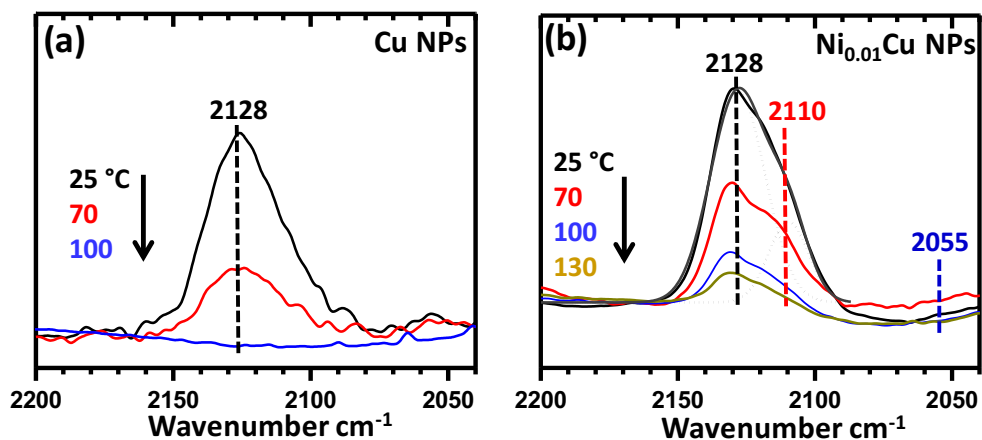


**Figure 5.5** CO-DRIFTS spectra of silica supported Cu NPs (a), and silica supported Ni<sub>0.01</sub>Cu NPs (b), at various temperatures. All samples were reduced *in situ* at 350 °C in hydrogen (10% balanced in Ar) for 1h. The CO adsorption was performed at room temperature with a flow rate of 10 mL/min followed by a He purge with a flow rate of 20 mL/min for 10 min prior to DRIFTS measurements.

On the other hand, DRIFT spectra on the supported Ni<sub>0.01</sub>Cu NPs, Fig 5b, show an additional shoulder at 2110 cm<sup>-1</sup> besides the 2128 cm<sup>-1</sup> peak. Similar to Figure 5.5a, the 2128 cm<sup>-1</sup> peak is assigned to CO binding to Cu surface atoms, while the additional 2110 cm<sup>-1</sup> peak must be related to the presence of Ni surface atoms. Indeed, the 2110 cm<sup>-1</sup> peak can be attributed to Ni(CO)<sub>x</sub> sub-carbonyl species with x = 2 or 3.<sup>56</sup> The formation of such sub-carbonyl species indicates a high dispersion of Ni species.<sup>56, 57</sup> Furthermore, the linear CO absorption band on Ni NPs is reported at 2055 cm<sup>-1</sup>,<sup>56</sup> which is completely absent in Figure 5.5b, indicating that the presence of metallic nickel nanoparticles can be excluded. Moreover, the adsorption bands related to CO

on  $\text{Ni}^{2+}/\text{Ni}^{1+}$  species are usually reported in the region of 2190 to 2200  $\text{cm}^{-1}$ ,<sup>58</sup> which are not present in the spectra of  $\text{Ni}_{0.01}\text{Cu}$  NPs. Therefore, the DRIFTS measurements suggest the presence of neutral atomic Ni species in  $\text{Ni}_{0.01}\text{Cu}$  NPs. In addition, the Ni related signal at 2110  $\text{cm}^{-1}$  is relatively strong given the low Ni surface concentration determined by XPS, thus indicating preferential CO adsorption at Ni sites. On the other hand, the relatively small concentration of Ni in  $\text{Ni}_{0.001}\text{Cu}$  NPs does not allow us to obtain reasonable Ni sub-carbonyl signal at 2110  $\text{cm}^{-1}$  in DRIFTS measurements; however, it is expected that Ni is atomically dispersed in Cu in the case of  $\text{Ni}_{0.001}\text{Cu}$  NPs.

Interestingly, Figure 5.5b also shows that although the peak area of 2128  $\text{cm}^{-1}$  feature decreases with increasing temperatures, the decreasing rate is much smaller than the rate on the bare Cu NPs. For example, at 100 °C, Figure 5.5a shows that all the CO species were desorbed from the Cu NPs, whereas Figure 5.5b shows that even at 130 °C, the CO species adsorbed on Cu are still clearly present. Therefore, surprisingly, addition of a small amount of Ni to Cu can strengthen the binding of CO on the Cu surface.

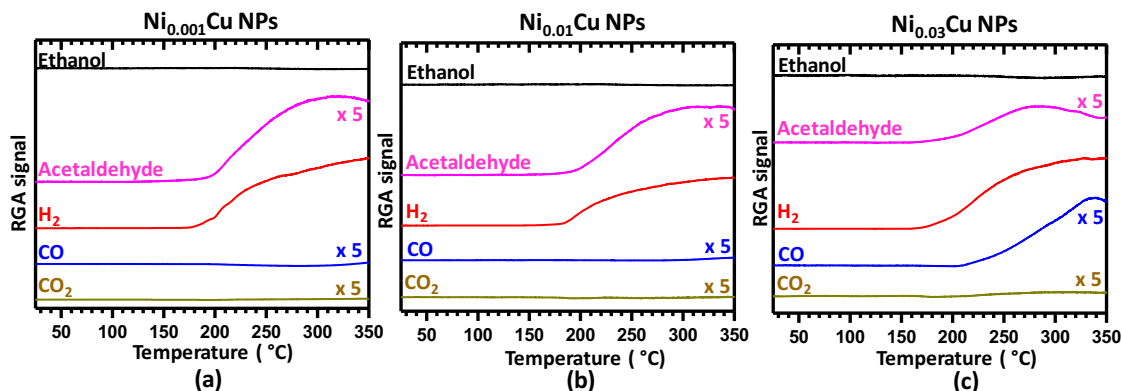


**Figure 5.6** TPSR of ethanol on (a) silica supported Ni<sub>0.001</sub>Cu NPs, (b) silica supported Ni<sub>0.01</sub>Cu NPs, and (c) silica supported Ni<sub>0.03</sub>Cu NPs. Reaction conditions: 100mg catalyst, 6% ethanol balanced in He, He flow rate 10mL/min.

The catalysis tests were first performed over silica supported NiCu NPs with different Ni concentrations. Figure 5.6 shows the temperature-programmed surface reaction (TPSR) of ethanol (6% balanced in He) on silica supported Ni<sub>0.001</sub>Cu NPs, Ni<sub>0.01</sub>Cu NPs, and Ni<sub>0.03</sub>Cu NPs with a heating rate of 10 °C/min. In all cases, formation of hydrogen and acetaldehyde is clearly observed, indicating the occurrence of ethanol dehydrogenation reaction. Because our mass spectrometer is connected to the reaction cell through a relatively long cold stainless steel tube, the signal of ethanol is delayed compared to the signals of other gaseous products. Therefore, the drop of ethanol signal is out of the temperature windows shown in Figure 5.6. Note that, the expected drop in the ethanol signal is observed when a lower heating rate is used. However, the ratio of acetaldehyde to H<sub>2</sub> is 1:1 when no CO or CO<sub>2</sub> is produced, and mass balance calculations in all cases show carbon closure close to 100%. For

Ni<sub>0.001</sub>Cu NPs and Ni<sub>0.01</sub>Cu NPs, the formation of CO and CO<sub>2</sub> is negligible up to 350 °C, indicating a nearly 100% selectivity to acetaldehyde, which is similar to the observation on Cu NPs (not shown here).

On Ni<sub>0.03</sub>Cu NPs, formation of CO is observed even at a low temperature, thus indicating to the partial decomposition of ethanol to H<sub>2</sub> and CO along with the dehydrogenation reaction. It has been reported that Ni NPs are active for the ethanol dehydrogenation reaction with CO and H<sub>2</sub> being the dominant products, particularly at temperatures >300 °C.<sup>59</sup> Therefore, the TPSR data suggests that for the case of Ni<sub>0.03</sub>Cu NPs, the formation of CO is likely resulting from the presence of relatively large Ni clusters, such as linear chains of Ni. The formation of Pt linear chains on Cu(111) surface has been observed and found to be active for C-C bond scission.<sup>37</sup> Similar to Pt, the larger Ni ensembles within the Cu matrix are likely capable of breaking C-C bonds leading to the formation of CO. While for Ni<sub>0.001</sub>Cu and Ni<sub>0.01</sub>Cu NPs, the presence of large Ni clusters seem to be negligible, in other words, Ni is highly or even atomically dispersed in Cu. This observation is consistent with the DRIFTS data discussed above. Furthermore, ethanol TPSR measurements on np-Ni<sub>0.003</sub>Cu (DL) and np-Ni<sub>0.01</sub>Cu (SSM) catalysts were also performed (not shown here). TPSR data show that these nanoporous catalysts exhibit a similar selectivity as supported Ni<sub>0.001</sub>Cu and Ni<sub>0.01</sub>Cu NPs, i.e. the only products are acetaldehyde and H<sub>2</sub>.

Kinetic studies of the ethanol dehydrogenation reaction on various NiCu alloys were performed by measuring the reaction rate at various temperatures under steady-state conditions. In all measurements, the conversion of ethanol was kept



below 15%. Figure 5.7 shows an Arrhenius-type plot of the H<sub>2</sub> formation rate on the silica supported monometallic Cu NPs, Ni<sub>0.001</sub>Cu NPs, Ni<sub>0.01</sub>Cu NPs, np-Cu (SSM), np-Ni<sub>0.01</sub>Cu (SSM), as well as np-Ni<sub>0.003</sub>Cu (DL). The H<sub>2</sub> formation rates are normalized by the Cu surface area of each catalyst. The calculated apparent activation energies from the Arrhenius-type plots in Figure 5.7 are shown in Table 5.3. The apparent activation energy determined for monometallic Cu NPs is  $70 \pm 5$  kJ/mol and for np-Cu (SSM) it is  $73 \pm 6$  kJ/mol, while for Ni<sub>0.001</sub>Cu NPs, Ni<sub>0.01</sub>Cu NPs, np-Ni<sub>0.003</sub>Cu (DL), and np-Ni<sub>0.01</sub>Cu (SSM) it is  $49 \pm 4$  kJ/mol,  $47 \pm 2$  kJ/mol,  $53 \pm 5$  kJ/mol, and  $45 \pm 4$  kJ/mol, respectively. Clearly, adding a small amount of Ni to Cu significantly decreases the apparent activation energy of the reaction, or in other words improves the reactivity of Cu. On the other hand, np-Cu (SSM) has similar apparent activation energy as supported Cu NPs. Furthermore, the apparent activation energy of np-Cu (DL) is also  $70 \pm 3$  kJ/mol (not shown here), indicating similar catalytic activity of np-Cu with supported monometallic Cu NPs.

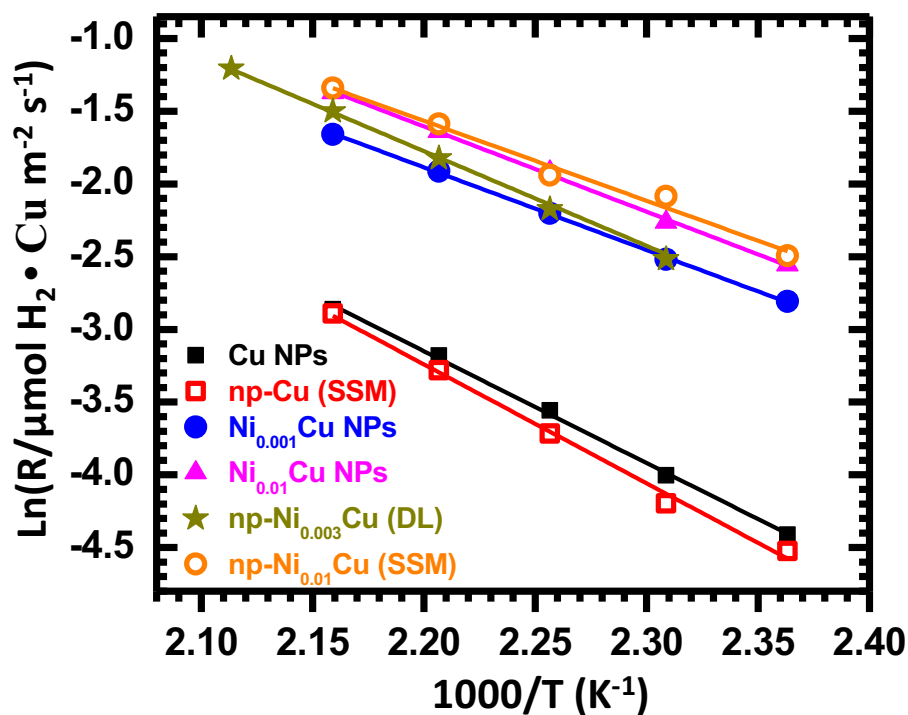


**Figure 5.7** Arrhenius-type plots of the reaction rate normalized by the surface area of Cu over monometallic Cu NPs and various highly dilute NiCu alloys used in the selective dehydrogenation of ethanol.

**Table 5.3** List of the apparent activation energy of various highly dilute NiCu alloys determined from Figure 5.7.

Samples	$E_a$ (kJ/mol)
Cu NPs	$70 \pm 5$
np-Cu (SSM)	$73 \pm 6$
$Ni_{0.001}Cu$ NPs	$49 \pm 4$

Ni <sub>0.01</sub> Cu NPs	47 ± 2
np-Ni <sub>0.003</sub> Cu (DL)	53 ± 6
np-Ni <sub>0.01</sub> Cu (SSM)	45 ± 4

Figure 5.8 shows stability tests of the silica supported monometallic Cu NPs, Ni<sub>0.001</sub>Cu NPs, and Ni<sub>0.01</sub>Cu NPs, and the unsupported np-Ni<sub>0.01</sub>Cu (SSM) in ethanol dehydrogenation reaction at 250 °C (a); stability tests of the silica supported monometallic Cu NPs, and Ni<sub>0.01</sub>Cu NPs at 300 °C (b). Clearly, for the supported monometallic Cu NPs a quick deactivation is observed at the reaction temperature of 250 °C and 300 °C. The activity decreases approximately 25% after 8 h of reaction at 250 °C, while it decreases approximately 50% after 12 h of reaction at 300 °C. Note that no residual carbon was found in temperature programmed oxidation (TPO) measurements on the used Cu catalysts, indicating that carbon deposition is not the reason for the deactivation. Previous studies have reported that sintering of Cu causes the observed deactivation.<sup>1, 7, 14</sup> Interestingly, the Ni-containing supported NiCu NPs and unsupported np-NiCu (SSM) do not exhibit significant deactivation after 8 h in ethanol dehydrogenation reaction at 250 °C. Whereas, after 12 h reaction at 300 °C, the Ni<sub>0.01</sub>Cu NP shows only a very small drop of activity. Since the main cause of deactivation of Cu catalysts is reported to be sintering, it is likely that adding Ni to Cu can prevent the sintering of Cu at elevated temperatures. Furthermore, after normalized by the copper surface area, the H<sub>2</sub> formation rates on NiCu highly dilute

alloys are significantly higher than that on monometallic Cu, showing the higher reactivity of NiCu alloy catalysts than Cu, which is in agreement with the apparent activation energies obtained from Figure 5.7. Interestingly, the areal activities of Ni<sub>0.001</sub>Cu NPs and the nanoporous np-Ni<sub>0.01</sub>Cu (SSM) are similar, as shown in Figure 5.8a. In our previous studies, we found that the Cu NPs prepared with the same protocol are single crystal NPs with a (111) surface,<sup>38</sup> whereas, np-Cu based NiCu alloys have other crystal orientations presented, for example (110). Thus, the non-oxidative ethanol dehydrogenation reaction over NiCu highly dilute alloys appears to be surface-insensitive. However, since the surface concentration of Ni differs among the samples, additional mechanistic work is needed to determine the TOFs of the reaction over the NiCu catalysts.

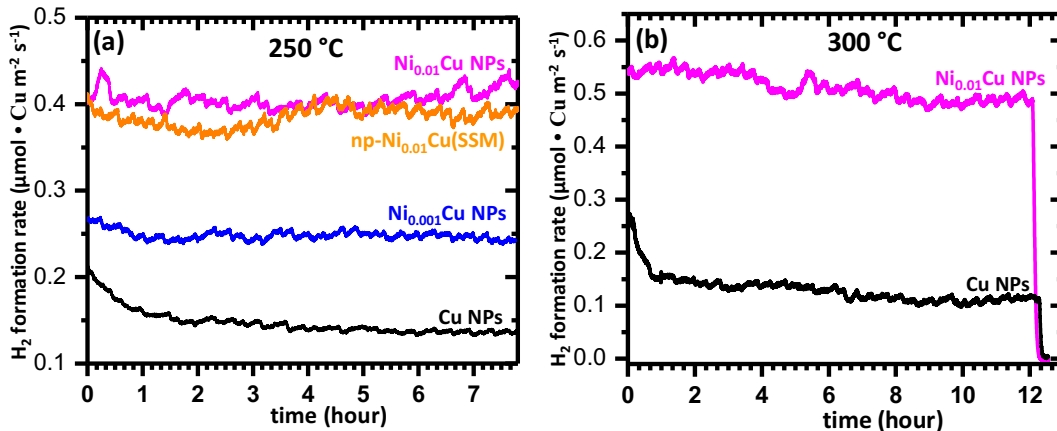


**Figure 5.8** Stability tests of silica supported monometallic Cu NPs, silica supported Ni<sub>0.001</sub>Cu NPs, silica supported Ni<sub>0.01</sub>Cu NPs, and np-Ni<sub>0.01</sub>Cu (SSM) in ethanol dehydrogenation reaction at 250 °C (a); stability tests of silica supported monometallic Cu NPs, and silica supported Ni<sub>0.01</sub>Cu NPs at 300 °C. The reaction rates are normalized by the surface area of Cu in each catalyst.

Figure 5.9 shows long-term stability tests of np-Cu (DL) and np-Ni<sub>0.003</sub>Cu (DL) in the ethanol dehydrogenation reaction at 250 °C for approximately 43 h. The ethanol conversion over np-Cu (DL) drops by ~ 8% after the reaction for 43 h. Clearly, the stability of np-Cu (DL) is much better than the supported Cu NPs in Figure 5.8. This could be due to the presence of Zn in the nanoporous Cu sample, which may improve the stability of Cu by preventing its sintering; or it may be due to the nanoporous structure of np-Cu (DL), which may have better structural stability against sintering. On the other hand, the ethanol conversion over np-Ni<sub>0.003</sub>Cu (DL) only decreases approximately 2% after the reaction for 43 h. Clearly, adding Ni to np-Cu (DL) can further improve the stability. Furthermore, although the same amounts of np-Cu (DL) and np-Ni<sub>0.003</sub>Cu (DL) were used, as well as identical reaction parameters were employed in the long-term stability tests, the ethanol conversion is much higher in the case of np-Ni<sub>0.003</sub>Cu (DL), indicating that adding a small amount of Ni improves the activity of np-Cu (DL), similar to the case of Cu NPs.

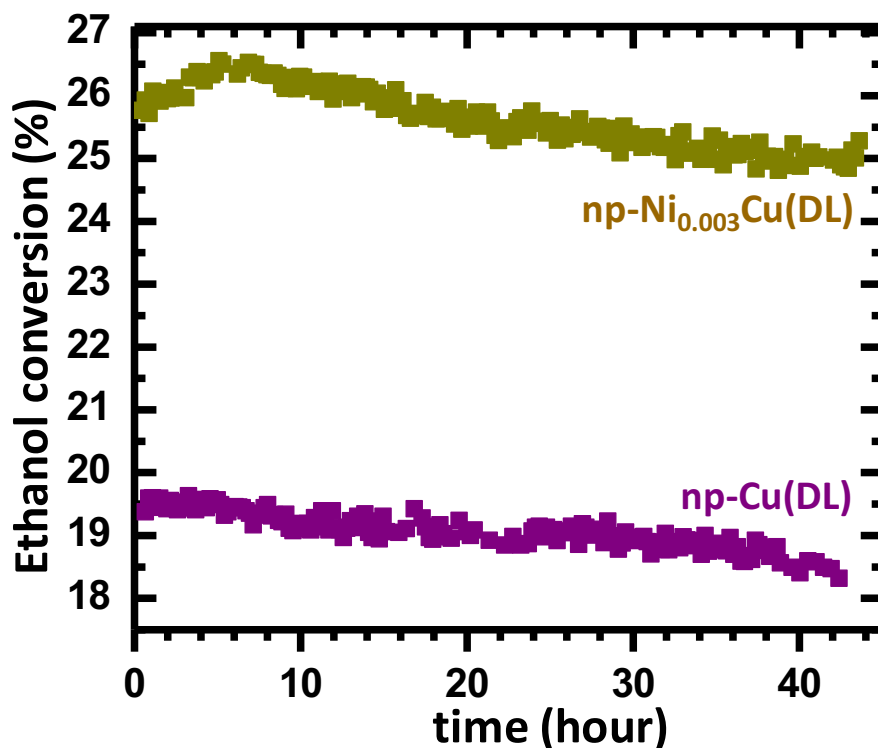


**Figure 5.9** Long-term stability tests of np-Cu (DL) and np-Ni<sub>0.003</sub>Cu (DL) in the ethanol dehydrogenation reaction at 250 °C for approximately 43 h. The same amount of catalysts (30 mg) was used.

Figure 5.10 shows SEM images of np-Cu (DL) before and after ethanol dehydrogenation reaction at 250 °C for 46 h, (a) and (b); as well as SEM images of np-Ni<sub>0.003</sub>Cu (DL) before and after ethanol dehydrogenation reaction at 250 °C for 60 h, (c) and (d). The average ligament size of np-Cu (DL) before reaction is  $165 \pm 35$  nm, whereas after reaction it is  $335 \pm 84$  nm. Therefore, the ethanol dehydrogenation reaction leads to coarsening of np-Cu. On the other hand, the average ligament size of np-Ni<sub>0.003</sub>Cu (DL) before reaction is  $192 \pm 46$  nm, and after reaction it is  $198 \pm 50$  nm.

Clearly, there is no coarsening of np-NiCu after the reaction, which is consistent with the stability tests shown in Figure 5.9.

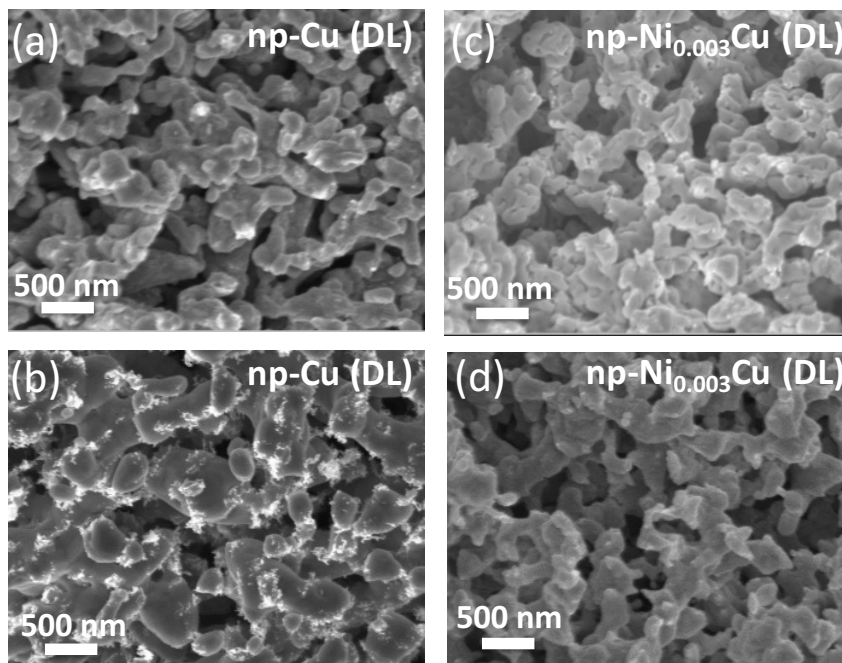


**Figure 5.10** a) SEM images of np-Cu (DL) before reaction; b) np-Cu (DL) after ethanol dehydrogenation reaction at 250 °C for 60 h; c) np-Ni<sub>0.003</sub>Cu (DL) before reaction; d) np-Ni<sub>0.003</sub>Cu (DL) after ethanol dehydrogenation reaction at 250 °C for 60 h.

As discussed above, these novel highly dilute NiCu alloys are very active for the non-oxidative ethanol dehydrogenation reaction, with nearly 100% selectivity to acetaldehyde. The sample characterizations show that Ni atoms are highly dispersed in Cu. During the ethanol dehydrogenation reaction, part of Ni moves into the sub-surface region. Although Cu NPs have been reported to be active for this reaction, the quick deactivation of the catalyst remains an unresolved issue. As for supported

monometallic Ni catalysts, a worse selectivity to acetaldehyde and a much quicker deactivation of the catalyst has been reported.<sup>59</sup> We found that adding a small amount of Ni to Cu, forming atomically dilute NiCu alloys, significantly improves the catalyst stability at 250 °C. Furthermore, adding a small amount of Ni to Cu can also dramatically enhance the activity of the catalysts. The apparent activation energy decreases from ~70 kJ/mol over Cu to ~45 kJ/mol over the NiCu alloys. Thus, addition of Ni has also an electronic effect on Cu, which warrants further investigation.

Of note, the obtained apparent activation energy, ~70 kJ/mol over Cu/SiO<sub>2</sub> NPs and np-Cu are in good agreement with values that have been reported on non-reducible oxides supported Cu NPs;<sup>11</sup> whereas, for Cu NPs supported on reducible oxides, the apparent activation energy is much smaller. Such differences could result from the different oxidation state of Cu, the different Cu dispersion, and the different metal-support interaction.<sup>11, 60, 61</sup> In the present study, by comparison of the apparent activation energy of the same type of catalysts with and without Ni, we show that the presence of a small amount of Ni in Cu can also significantly change the reactivity of the catalyst.

Bimetallic NiCu catalysts have been found to be active for the ethanol steam reforming reaction.<sup>62, 63</sup> The reactivity and stability of bimetallic NiCu are much better than monometallic Cu catalysts. However, the presence of Ni islands causes the decomposition of ethanol, leading to the formation of CO, which is an undesired product.<sup>62, 63</sup> A similar effect of Ni may be expected in the ethanol dehydrogenation reaction. However, we found that highly dispersed Ni in Cu does not cause the



decomposition of ethanol to CO (except for higher Ni concentrations like the one shown in Figure 5.6c. At the compositions employed here, Ni may be in the form of isolated atoms or atomically dispersed nanoclusters. Further work is warranted to discriminate between these structures, as they were shown to play a key role in improving both the activity and the stability of Cu in the ethanol dehydrogenation reaction.

## **5.5 Conclusions**

In this work, we demonstrated that highly dilute NiCu alloys are very active for the non-oxidative dehydrogenation of ethanol to acetaldehyde and hydrogen under realistic conditions with nearly 100% selectivity. Adding a small amount of Ni to the Cu surface does not only significantly increase the reactivity of copper, but also greatly improves its stability. Our data show that the presence of Ni atoms in the Cu surface may not only stabilize the morphology of Cu catalysts but also have a direct effect on the reaction mechanism. This work opens a new route for the use of highly dilute alloys for alcohol dehydrogenation reactions. Furthermore, the comparison of the catalytic performance of highly dilute alloy NPs with nanoporous materials is useful to guide the design of the novel mesoporous catalyst architectures for selective dehydrogenation or oxidation reactions.

## 5.6 References

1. Eckert, M.; Fleischmann, G.; Jira, R.; Bolt, H. M.; Golka, K., Acetaldehyde. In *Ullmann's Encyclopedia of Industrial Chemistry*, Wiley-VCH Verlag GmbH & Co. KGaA: 2000.
2. Hagemeyer, H. J.; Staff, U. b., Acetaldehyde. In *Kirk-Othmer Encyclopedia of Chemical Technology*, John Wiley & Sons, Inc.: 2000.
3. Guan, Y.; Hensen, E. J. M., Ethanol dehydrogenation by gold catalysts: The effect of the gold particle size and the presence of oxygen. *Applied Catalysis A: General* **2009**, *361* (1), 49-56.
4. Chang, F. W.; Yang, H. C.; Roselin, L. S.; Kuo, W. Y. *Applied Catalysis A: General* **2006**, *304*, 30-39.
5. Sanchez-Sanchez, M. C.; Navarro Yerga, R. M.; Kondarides, D. I.; Verykios, X. E.; Fierro, J. L. G., Mechanistic Aspects of the Ethanol Steam Reforming Reaction for Hydrogen Production on Pt, Ni, and PtNi Catalysts Supported on  $\gamma$ -Al<sub>2</sub>O<sub>3</sub>. *The Journal of Physical Chemistry A* **2010**, *114* (11), 3873-3882.
6. Sun, J. M.; Karim, A. M.; Mei, D. H.; Engelhard, M.; Bao, X. H.; Wang, Y. *Applied Catalysis B: Environmental* **2015**, *162*, 141-148.
7. Tu, Y.-J.; Chen, Y.-W., Effects of Alkali Metal Oxide Additives on Cu/SiO<sub>2</sub> Catalyst in the Dehydrogenation of Ethanol. *Industrial & Engineering Chemistry Research* **2001**, *40* (25), 5889-5893.
8. Besson, M.; Gallezot, P. *Catalysis Today* **2000**, *57*, 127-141.
9. Redina, E. A.; Greish, A. A.; Mishin, I. V.; Kapustin, G. I.; Tkachenko, O. P.; Kirichenko, O. A.; Kustov, L. M., Selective oxidation of ethanol to acetaldehyde over Au-Cu catalysts prepared by a redox method. *Catalysis Today* **2015**, *241*, 246-254.
10. Freitas, I. C.; Damyanova, S.; Oliveira, D. C.; Marques, C. M. P.; Bueno, J. M. C., Effect of Cu content on the surface and catalytic properties of Cu/ZrO<sub>2</sub> catalyst for ethanol dehydrogenation. *Journal of Molecular Catalysis A: Chemical* **2014**, *381*, 26-37.
11. Cassinelli, W. H.; Martins, L.; Passos, A. R.; Pulcinelli, S. H.; Rochet, A.; Briois, V.; Santilli, C. V., Correlation between Structural and Catalytic Properties of Copper Supported on Porous Alumina for the Ethanol Dehydrogenation Reaction. *ChemCatChem* **2015**, *7* (11), 1668-1677.

12. Cassinelli, W. H.; Martins, L.; Magnani, M.; Pulcinelli, S. H.; Briois, V.; Santilli, C. V., Time-resolved XAS/MS/Raman monitoring of mutual copper self-reduction and ethanol dehydrogenation reactions. *RSC Advances* **2016**, *6* (25), 20453-20457.
13. Colley, S. W.; Tabatabaei, J.; Waugh, K. C.; Wood, M. A., The detailed kinetics and mechanism of ethyl ethanoate synthesis over a Cu/Cr<sub>2</sub>O<sub>3</sub> catalyst. *Journal of Catalysis* **2005**, *236* (1), 21-33.
14. Chang, F. W.; Kuo, W. Y.; Lee, K. C. *Applied Catalysis A: General* **2003**, *246*, 253-264.
15. Tu, Y.-J.; Chen, Y.-W.; Li, C., Characterization of unsupported copper—chromium catalysts for ethanol dehydrogenation. *Journal of Molecular Catalysis* **1994**, *89* (1), 179-189.
16. Santacesaria, E.; Carotenuto, G.; Tesser, R.; Di Serio, M., Ethanol dehydrogenation to ethyl acetate by using copper and copper chromite catalysts. *Chemical Engineering Journal* **2012**, *179* (Supplement C), 209-220.
17. Wang, C. Y.; Garbarino, G.; Allard, L. F.; Wilson, F.; Busca, G.; Flytzani-Stephanopoulos, M. *ACS Catalysis* **2016**, *6*, 210-218.
18. Gazsi, A.; Koos, A.; Bansagi, T.; Solymosi, F. *Catalysis Today* **2011**, *160*, 70-78.
19. Ciftci, A.; Ligthart, D. A. J. M.; Pastorino, P.; Hensen, E. J. M. *Applied Catalysis B: Environmental* **2013**, *130*, 325-335.
20. Flytzani-Stephanopoulos, M.; Gates, B. C. *Annual review of chemical and biomolecular engineering* **2012**, *3*, 545-574.
21. Wang, C. Y.; Yang, M.; Flytzani-Stephanopoulos, M. *AiChE J.* **2016**, *62*, 429-439.
22. Yang, M.; Liu, J. L.; Lee, S.; Zugic, B.; Huang, J.; Allard, L. F.; Flytzani-Stephanopoulos, M. *J. Am. Chem. Soc.* **2015**, *137*, 3470-3473.
23. Yang, M.; Li, S.; Wang, Y.; Herron, J. A.; Xu, Y.; Allard, L. F.; Lee, S.; Huang, J.; Mavrikakis, M.; Flytzani-Stephanopoulos, M. *Science* **2014**, *346*, 1498-1501.
24. Zhai, Y. P.; Pierre, D.; Si, R.; Deng, W. L.; Ferrin, P.; Nilekar, A. U.; Peng, G. W.; Herron, J. A.; Bell, D. C.; Saltsburg, H.; Mavrikakis, M.; Flytzani-Stephanopoulos, M. *Science* **2010**, *329*, 1633-1636.
25. El Kolli, N.; Delannoy, L.; Louis, C. *Journal of Catalysis* **2013**, *297*, 79-92.

26. Pei, G. X.; Liu, X. Y.; Wang, A. Q.; Li, L.; Huang, Y. Q.; Zhang, T.; Lee, J. W.; Jang, B. W. L.; Mou, C. Y. *New J. Chem.* **2014**, *38*, 2043-2051.
27. McCue, A. J.; Baker, R. T.; Anderson, J. A. *Faraday Discuss.* **2016**, *188*, 499-523.
28. Pongthawornsakun, B.; Fujita, S.; Arai, M.; Mekasuwandumrong, O.; Panpranot, J. *Applied Catalysis A: General* **2013**, *467*, 132-141.
29. Dash, P.; Dehm, N. A.; Scott, R. W. *J. Mol. Catal. A-Chem.* **2008**, *286*, 114-119.
30. Zugic, B.; Karakalos, S.; Stowers, K. J.; Biener, M. M.; Biener, J.; Madix, R. J.; Friend, C. M., Continuous Catalytic Production of Methyl Acrylates from Unsaturated Alcohols by Gold: The Strong Effect of C=C Unsaturation on Reaction Selectivity. *ACS Catalysis* **2016**, *6* (3), 1833-1839.
31. Wittstock, A.; Zielasek, V.; Biener, J.; Friend, C. M.; Baumer, M. *Science* **2010**, *327*, 319-322.
32. Xu, B. J.; Siler, C. G. F.; Madix, R. J.; Friend, C. M. *Chem. Eur. J.* **2014**, *20*, 4646-4652.
33. Wang, L. C.; Stowers, K. J.; Zugic, B.; Personick, M. L.; Biener, M. M.; Biener, J.; Friend, C. M.; Madix, R. J. *Journal of Catalysis* **2015**, *329*, 78-86.
34. Suzuki, K.; Yamaguchi, T.; Matsushita, K.; Iitsuka, C.; Miura, J.; Akaogi, T.; Ishida, H. *ACS Catalysis* **2013**, *3*, 1845-1849.
35. Greeley, J.; Mavrikakis, M. *J. Phys. Chem. B* **2005**, *109*, 3460-3471.
36. Liu, J. L.; Lucci, F. R.; Yang, M.; Lee, S.; Marcinkowski, M. D.; Therrien, A. J.; Williams, C. T.; Sykes, E. C. H.; Flytzani-Stephanopoulos, M. *J. Am. Chem. Soc.* **2016**, *138*, 6396-6399.
37. Lucci, F. R.; Liu, J.; Marcinkowski, M. D.; Yang, M.; Allard, L. F.; Flytzani-Stephanopoulos, M.; Sykes, E. C. H., Selective hydrogenation of 1,3-butadiene on platinum-copper alloys at the single-atom limit *Nat. Commun.* **2015**, *6*, 8550.
38. Boucher, M. B.; Zugic, B.; Cladaras, G.; Kammert, J.; Marcinkowski, M. D.; Lawton, T. J.; Sykes, E. C. H.; Flytzani-Stephanopoulos, M., Single atom alloy surface analogs in Pd<sub>0.18</sub>Cu<sub>15</sub> nanoparticles for selective hydrogenation reactions. *Physical Chemistry Chemical Physics* **2013**, *15* (29), 12187-12196.

39. Boucher, M.B.; Marcinkowski, M. D.; Liriano, M. L.; Murphy, C. J.; Lewis, E. A.; Jewell, A. D.; Mattera, M. F. G.; Kyriakou, G.; Flytzani-Stephanopoulos, M.; Sykes, E. C. H. *ACS Nano* **2013**, *7*, 6181-6187.
40. Shan, J.; Lucci, F. R.; Liu, J.; El-Soda, M.; Marcinkowski, M. D.; Allard, L. F.; Sykes, E. C. H.; Flytzani-Stephanopoulos, M., Water co-catalyzed selective dehydrogenation of methanol to formaldehyde and hydrogen. *Surface Science* **2016**, *650*, 121-129.
41. Li, Z. Y.; Han, C. H.; Shen, J. Y. *J. Mater. Sci.* **2006**, *41*, 3473-3480.
42. Serov, A.; Artyushkova, K.; Niangar, E.; Wang, C. M.; Dale, N.; Jaouen, F.; Sougrati, M. T.; Jia, Q. Y.; Mukerjee, S.; Atanassov, P. *Nano Energy* **2015**, *16*, 293-300.
43. Tachiwaki, T.; Suzuki, M.; Okajima, H.; Koizumi, S.; Ito, T.; Hiraki, A. *Applied Surface Science* **1993**, *70*, 751-754.
44. Dhas, N. A.; Raj, C. P.; Gedanken, A. *Chem. Mater.* **1998**, *10*, 1446-1452.
45. Jeong, S.; Woo, K.; Kim, D.; Lim, S.; Kim, J. S.; Shin, H.; Xia, Y. N.; Moon, J. *Adv. Funct. Mater.* **2008** *18*, 679-686.
46. Zhang, Z. L.; Ji, Y. J.; Li, J.; Zhong, Z. Y.; Su, F. B. *RSC Advances* **2015**, *5*, 54364-54371.
47. Yoshida, Y.; Uto, K.; Hattori, M.; Tsuji, M. *CrystEngComm* **2014**, *16*, 5672-5680.
48. Pennycook, S. J. *Adv. Imag. Elect. Phys.* **2002**, *123*, 173-206.
49. Bond, G. C. Namijo, S. N. *Journal of Catalysis* **1989**, *118*, 507-510.
50. Grosvenor, A. P.; Biesinger, M. C.; Smart, R. S.; McIntyre, N. S. *Surface Science* **2006**, *600*, 1771-1779.
51. Shan, J. J.; Huang, W. X.; Nguyen, L.; Yu, Y.; Zhang, S. R.; Li, Y. Y.; Frenkel, A. I.; Tao, F. *Langmuir* **2014**, *30*, 8558-8569.
52. D'Addato, S.; Grillo, V.; Altieri, S.; Tondi, R.; Valeri, S.; Frabboni, S., Structure and stability of nickel/nickel oxide core-shell nanoparticles. *Journal of Physics: Condensed Matter* **2011**, *23* (17), 175003.
53. Prieto, P.; Nistor, V.; Nouneh, K.; Oyama, M.; Abd-Lefdil, M.; Díaz, R., XPS study of silver, nickel and bimetallic silver-nickel nanoparticles prepared by seed-mediated growth. *Applied Surface Science* **2012**, *258* (22), 8807-8813.
54. Komarneni, M.; Shan, J.; Burghaus, U. *J. Phys. Chem. C* **2011**, *115*, 16590-16597.

55. Subramanian, N. D.; Kumar, C. S. S. R.; Watanabe, K.; Fischer, P.; Tanaka, R.; Spivey, J. J. *Catalysis Science & Technology* **2012**, *2*, 621-631.
56. Moya, S. F.; Martins, R. L.; Schmal, M. *Applied Catalysis A: General* **2011**, *396*, 159-169.
57. Poncelet, G.; Centeno, M. A.; Molina, R. *Applied Catalysis A: General* **2005** *288*, 232-242.
58. Anderson, J. A.; Rodrigo, M. T.; Daza, L.; Mendioroz, S. *Langmuir* **1993**, *9*, 2485-2490.
59. Neramittagapong, A.; Attaphaiboon, W.; Neramittagapong, S. *Chiang Mai J. Sci.* **2008**, *35*, 171-177.
60. Sato, A. G.; Volanti, D. P.; Meira, D. M.; Damyanova, S.; Longo, E.; Bueno, J. M. C. *Journal of Catalysis* **2013**, *307*, 1-17.
61. Sun, K.; Zhang, M. H.; Wang, L. C. *Chem. Phys. Lett.* **2013**, *585*, 89-94.
62. Chen, L. C.; Lin, S. D. *Applied Catalysis A: Environmental* **2014** *148*, 509-519.
63. Wang, F.; Li, Y.; Cai, W. J.; Zhan, E. S.; Mu, X. L.; Shen, W. J. *Catalysis Today* **2009**, *146*, 31-36.

## Chapter 6.

# Surface Compositional Evolution of Nanoporous NiCu

### **6.1 Abstract**

In this investigation, we use Ni-doped nanoporous Cu to demonstrate activating and deactivating surface compositional changes the system undergoes during different pretreatments. Although Ni-doping nanoporous Cu enhances the activity, it lowers the stability of the catalyst compared to nanoporous Cu, which is stable for the reaction regardless of pretreatment. In situ and ex situ X-ray photoelectron spectroscopy is used to demonstrate the compositional and oxidation states changes that occur towards stable catalytic activity or deactivation for selective ethanol dehydrogenation. XPS and characterization measurements identify metallic Ni, created by hydrogen treatment, as the deactivating agent promoting carbon deposition. Oxidation induces Ni<sup>2+</sup> at the surface, which does not deposit carbon, and thus leads to a functioning catalyst. Due to the chosen reaction conditions, Ni<sup>2+</sup> is kinetically trapped at the surface in a metastable state demonstrating a classic example of stunted kinetics overruling thermodynamics.

This paper is under preparation for publication.

## **6.2 Introduction**

Ethanol dehydrogenation is a resourceful, attractive reaction producing acetaldehyde, an important industrial chemical, and hydrogen, a clean fuel. Acetaldehyde is widely found in nature and produced on the industrial scale as a starting material for acetic acid, acetate esters, pentaerythritol, pyridine, and other pyridine based compounds<sup>1-2</sup>. Although ethanol dehydrogenation is an attractive process, it is not currently economically viable due to the lack of a robust catalyst. Currently, acetaldehyde is mainly produced via the Wacker process using a homogenous palladium-copper chloride catalyst in the oxidation of ethylene or by the oxidative dehydrogenation of ethanol over silver catalysts at high temperatures<sup>1-2</sup>. However, these methods have drawbacks, as they require high temperatures, corrosive catalysts, or separation from by-products, a substantial energy consumer. Therefore, there is a significant need to develop a working catalyst for the ethanol dehydrogenation reaction to take full advantage of the valuable H<sub>2</sub> by-product.

Cu-based catalysts were widely studied for ethanol and alcohol dehydrogenation reactions<sup>3-9</sup> due to their high selectivity for dehydrogenating the C-O bond without cleaving the C-C bond, although their active site remains disputed. Some studies report metallic Cu to be the most active species<sup>10-12</sup>, whereas others cite Cu<sup>+</sup> or a mixture of Cu<sup>0</sup>/Cu<sup>+</sup> as the most active species for the dehydrogenation of ethanol<sup>13-16</sup> as well as for cyclohexanol<sup>9</sup>. Recently, non-oxidative methanol and ethanol dehydrogenation was shown to occur at step and kink sites on Cu (111) and Cu (110) single crystals<sup>17</sup> providing an explanation for the long-lasting observed low conversions on Cu single crystals<sup>18-21</sup>.



Cu catalysts generally deactivate in ethanol<sup>22-23</sup> and methanol<sup>5-6</sup> dehydrogenation conditions due to sintering. To improve the stability of Cu catalysts, the addition of chromium<sup>7, 12</sup>, magnesium<sup>9</sup>, aluminum<sup>3, 8-9</sup>, and alkali metals<sup>23</sup> as promoters have been investigated among others<sup>24</sup>. Metal alloys demonstrate excellent activity, selectivity, and stability compared to their individual components for many reactions. Bimetallic catalysts with more noble components have been extensively studied for ethanol steam reforming and oxidation reactions including Au-Cu<sup>25-27</sup>, Co-Cu<sup>28-29</sup>, Co-Ni<sup>28, 30-31</sup>, Cu-Ni<sup>32-37</sup>, Ni-Zn<sup>38-40</sup>, Pd-Zn<sup>41</sup>, Pt-Cu<sup>42</sup>, Pt-Ni<sup>42-44</sup>, and Pt-Ru<sup>42, 45</sup>. However, their use for non-oxidative selective alcohol dehydrogenation reactions has been limited to Ag-Cu<sup>46</sup>, Au-Cu<sup>26</sup>, and Pd-Zn<sup>47-49</sup>.

Dilute metal alloys, where a minority component drives the reaction on a majority host component, have also displayed remarkable cases of improved performance compared to their monometallic counterparts. Nanoporous Au, for example, is a dilute Ag-Au alloy with ~3% Ag that can catalyze numerous complex oxygen-assisted coupling reactions with high reactivity, selectivity, and long-term stability<sup>50-52</sup>. On their own, Au is inert for these reactions and Ag promotes combustion of the alcohol reactants. Additional studies demonstrated that a mixed Ag-Au oxide is key to the high performance of nanoporous Au by facilitating O<sub>2</sub> dissociation<sup>53</sup>.

Further dilution of bimetallic catalysts still results in highly active catalysts. Studies of Pd-Cu and Pt-Cu single atom alloys demonstrated that these catalysts are capable of dissociating H<sub>2</sub> and catalyzing alkyne and alkadiene hydrogenation reactions with higher activity and selectivity compared to their Cu and Pd/Pt

counterparts, respectively<sup>54-55</sup>. Single atom alloys have atomically dispersed active species, Pd or Pt, supported on a host metal, Cu, which is in the form of a single crystal or nanoparticle. Pt-Cu single atom alloys are also capable of associating H atoms and assisting in dehydrogenation reactions of methanol<sup>56</sup> and formic acid<sup>57</sup>.

Recently, dilute Ni-Cu alloys in the form of nanoparticles and nanoporous materials were shown to be active and selective for ethanol dehydrogenation to acetaldehyde and hydrogen<sup>58</sup>. The study found that small amounts of nickel in Cu based materials, regardless of form, lower the activation barrier for the ethanol dehydrogenation reaction and thus, have higher activity while maintaining high selectivity for acetaldehyde and hydrogen. Ni-Cu alloys were widely studied for the oxidative steam reforming of ethanol<sup>32-37</sup>. Overall, these studies demonstrated that Cu rich alloys preferentially dehydrogenate ethanol to acetaldehyde, whereas Ni promotes C-C bond scission reactions to H<sub>2</sub>, CO<sub>2</sub>, CO, and CH<sub>4</sub><sup>33, 36-37</sup>. The amount of coke deposition also decreased with NiCu catalysts compared to pure Ni catalysts<sup>32, 35</sup>.

In this investigation, O<sub>2</sub> pretreatment is used to create an active and metastable nanoporous NiCu material for the ethanol dehydrogenation reaction by the creation of Ni<sup>2+</sup> species. H<sub>2</sub> pretreatment of the same material led to deactivation of the catalyst attributed to metallic Ni. The catalyst is compared to its non-Ni doped counterpart to elucidate the role of Ni in the catalyst. Ambient-pressure X-ray photoelectron spectroscopy (AP-XPS) is used to study npNiCu with various reactive environments with the goal of correlating composition and oxidation states changes to catalytic activity of the ethanol dehydrogenation reaction. To study long-term

changes of the catalyst, ex situ XPS was also used after various treatments to demonstrate the deactivating effect of Ni<sup>0</sup> by carbon deposition and the enhancing effect of Ni<sup>2+</sup> on the catalyst activity.

## **6.3 Methods**

### **6.3.1 Catalyst Preparation**

Nanoporous Cu (npCu) samples were first prepared by selectively etching Zn from a Zn<sub>80</sub>Cu<sub>20</sub> alloy ingot in 5 M hydrochloric acid for 36 hours at room temperature. After etching, the sample was rinsed with deionized water and dried in a vacuum oven. To dope the npCu ingot with Ni, the ingot was placed in a 0.3 M nickel (II) nitrate solution. The sample was placed under vacuum for 2 h in order to ensure full penetration of the pores with solution. The ingot was then immersed in liquid nitrogen for 10 min and then placed in a freeze-drying system at 0.012 mbar and -106 °C (Labconco, FreeZone 4.51 Benchtop Freeze Dry System) for 2 days. Finally, the resulting npNiCu ingot was reduced in 4% H<sub>2</sub> in Ar at 1 atm for 1 h at 500 °C. This reduction step is considered part of the synthesis procedure and is not considered a “pretreatment” as discussed later.

Crushed samples, revealing the cross section of the ingot, had Ni and Zn concentrations of ~3 at% and ~5 at%, respectively, as determined by energy-dispersive spectroscopy analysis (EDS) with ligament sizes of 200 ± 50 nm (Figure 6.1). Ingot surfaces had ~10 at% Ni and ~6 at% Zn by EDS analysis with a characteristic depth ~2 μm, revealing an inhomogeneous distribution of Ni, a result of the freeze-drying impregnation technique. Prepared npNiCu ingots were used as is

for ambient-pressure X-ray photoelectron spectroscopy (AP-XPS) studies. For all other techniques, npNiCu or npCu ingots were crushed into a powder for testing or characterization.

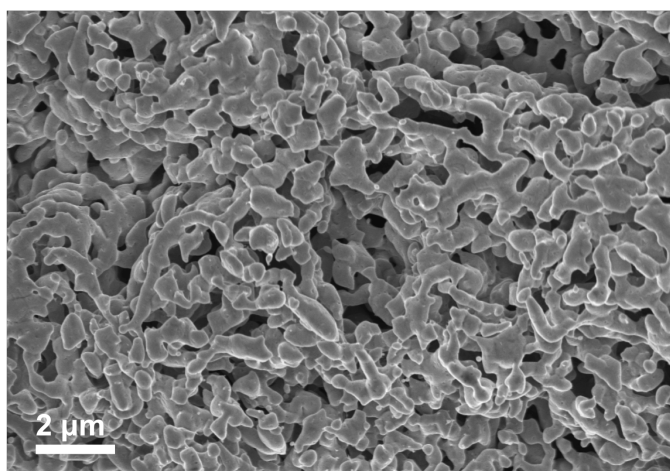


**Figure 6.1** Scanning electron microscopy (SEM) image of as prepared npNiCu.

### **6.3.2 Catalytic Activity**

Catalyst samples were tested in a quartz reactor tube reactor housed in a temperature-controlled furnace operated at atmospheric pressure. Ultrahigh-purity gases were supplied to the reactor by mass-flow controllers. Hydrogen treatment was performed by flowing 10% hydrogen at 20 mL/min at room temperature, followed by ramping the temperature to 350 °C at 10 °C/min and holding for 1 hr. Oxygen treatments were performed at 250 °C using 20% O<sub>2</sub>/He at a flow rate of 50 mL/min for 1 hr. Ethanol dehydrogenation reaction was performed using 6% ethanol/He with a 50 mL/min total flow at 250 °C by flowing a He stream through a bubbler filled with ethanol at room temperature. The effluent gas was monitored by an online GC-MS

(Agilent 5975C and Agilent 7890A) equipped with HP-PLOT Q and CARBONPLOT columns. The effluent gas was also monitored by an online residual gas analyzer (Hiden HAL 3F RGA). Ethanol, acetaldehyde, water, and H<sub>2</sub> were monitored by m/z = 31, 43 and 29, 18, and 2, respectively.

### **6.3.3 Ex situ Characterization Techniques**

Scanning electron microscopy (SEM) was performed using a Zeiss Supra55VP field-emission SEM equipped with an energy-dispersive X-ray spectroscopy (EDS) detector at the Center for Nanoscale Systems (CNS) at Harvard University. Scanning and transmission electron microscopy (STEM and TEM) along with EDS mapping was performed using an aberration-corrected JEOL ARM 200F STEM at CNS as well as a FEI Talos F200X at the CFN at BNL. To prepare TEM and STEM samples, powder samples were dispersed in deionized water and drop-casted onto lacey C/Au mesh grids from Ted Pella. Ex situ X-ray photoelectron spectroscopy (XPS) was also performed at CNS using a Thermo Scientific K-Alpha XPS with a monochromatic Al K $\alpha$  source. XPS samples of the crushed ingots to expose their interior were prepared by loading the catalyst particles onto carbon tape. Temperature-programmed oxidation (TPO) experiments were conducted using 20% O<sub>2</sub>/He and a temperature ramp of 10 °C/min from room temperature to 430 °C. The effluent gases were monitored using a residual gas analyzer (SRS RGA 200). Raman spectroscopy was performed in a Horiba LabRam Evolution microscope using a 633 nm excitation wavelength.

### **6.3.4 Environmental Transmission Electron Microscopy (E-TEM)**

Environmental-TEM (E-TEM) studies were conducted at the Center for Functional Nanomaterials (CFN) at Brookhaven National Laboratory (BNL) using a FEI Titan aberration-corrected TEM operating at 300 kV equipped with an electron energy loss spectrometer (EELS). The instrument has a base pressure of  $3\text{-}4 \cdot 10^{-7}$  Torr. As prepared npNiCu powder was dispersed in deionized water and drop-casted onto a DENS Solutions sample holder. After drying, the holder was inserted in the microscope. Gases and vapors were introduced into the microscope using a gas-handling manifold equipped with dosing valves. Gases were introduced into the sample stage area with the beam blanked. The sample was then heated to the specified temperatures and held for the treatment duration. After cooling, the gases were evacuated to vacuum pressure for imaging and EELS analysis. EELS spectra were analyzed using TEM Imaging and Analysis (TIA) software.

### **6.3.5 Ambient-Pressure XPS (AP-XPS)**

Ambient-pressure X-ray photoelectron spectroscopy (AP-XPS) experiments were conducted at Beamline 23-ID-2 at the National Synchrotron Light Source II at Brookhaven National Laboratory. Because the freeze-drying synthesis step results in a Ni and Zn enriched ingot surface and samples are crushed for reactivity testing, both the surface and the cross section of an ingot sample were studied. To do this, a npNiCu ingot with dimensions, 12 mm x 3 mm x 1 mm (length x width x height), was halved into two pieces with lengths of 6 mm each. One of these pieces was cut lengthwise to expose the cross section and loaded with the cross section facing out

(left, Figure 6.13). The other was loaded as is to expose the outer surface of the ingot (right, Figure 6.13). Both pieces were held onto a tantalum back-plate with tantalum foil that was spot welded on each side to keep in place. The whole contraption was then loaded on platinum button heater and mounted within the AP-XPS chamber. Both an as prepared ingot and a previously treated ingot in the flow reactor (10% H<sub>2</sub>, 1 atm, 1 h, 350 °C) were used for the AP-XPS studies.

To ensure that the same depth was probed for each element and similar gas-phase attenuation, the X-ray photon energy was varied such that the kinetic energy of all photoelectrons was 200 eV. After every photon-energy change, the mirrors were adjusted to optimize the XPS counts. With each metal 2p or survey spectrum that was collected in each condition, a corresponding Fermi edge spectrum was collected and used to calibrate the energy of the respective spectrum. The sample was first analyzed in ultra-high vacuum (UHV) at room temperature (RT) (condition 0). Then it was exposed to 0.2 Torr ethanol for 6 h at 250 °C (condition 1), after which it was exposed to 1 Torr O<sub>2</sub> at 250 °C for 1 h (condition 2). The sample was exposed to each of these conditions and analyzed in vacuum after the reactant gas was completely pumped out of the chamber to limit beam effects. In the final condition, the spectra were taken while the sample was in 0.2 Torr ethanol after being exposed to the ethanol for 1 h at 250 °C (condition 3). During reactant exposures, the beam was blocked between spectra collection to limit beam damage.

### 6.3.6 XPS Spectral Analysis

Both ex situ and in situ XPS spectra were analyzed using Casa XPS software. All spectra were de-convoluted using Voigt line-shapes after subtracting a Shirley background. Peak fitting using Gaussian-Lorentzian peaks was not appropriate for Ni 2p spectra as the Ni 2p spectrum of each Ni species exhibits complicated line-shapes with characteristic satellites. Instead, Ni 2p spectra were analyzed using least square fitting based on a linear combination of area normalized reference 2p<sub>3/2</sub> spectra of Ni<sup>0</sup>, Ni<sup>2+</sup>, and Ni(OH)<sub>2</sub> to extract the percentage of each specie present (Figure 6.14). Because the Cu 2p spectra exhibited pure Cu<sup>2+</sup> or Cu<sup>0</sup>/Cu<sup>+1</sup>, which are indistinguishable by XPS, no further fitting was conducted. Efforts to fit the Zn 2p spectra were not made as the Zn metal and oxide components overlap and thus quantification is difficult for mixed systems. Therefore, the LMM Auger parameter, as generally agreed in the literature<sup>59</sup>, was used to qualitatively demonstrate changes in the Zn/Zn<sup>2+</sup> ratio under different conditions. The Zn LMM Auger spectra were extrapolated from the survey spectra collected with a photon energy of 1221 eV. Due to the large step size in the survey spectra, no fitting was performed.

Atomic ratios were calculated using the peak area (PA) and ionization cross-section (ICS) of each element and the photon flux (PF) at the corresponding photon

$$Ratio A/B = \frac{PA(A)}{PA(B)} \square \frac{ICS(B)}{ICS(A)} \square \frac{PF @ E_{hv,B}}{PF @ E_{hv,A}}$$

energy using the following formula<sup>60</sup>:



### **6.3.7 Near-Edge X-ray Absorption Fine Structure (NEXAFS)**

NEXAFS spectra were acquired using the XPS analyzer in partial electron yield (PEY) mode. For Cu L-edge spectra and Ni L-edge spectra, the kinetic energies of the emitted photoelectrons were selected to be 320 eV and 240 eV, respectively, such that no XPS peaks appear at this kinetic energy within the energy range scanned, which would otherwise produce false NEXAFS peaks. Because most of the spectra showed prominent Cu<sup>0</sup> characteristics, the energy calibration was conducted by aligning the Cu<sup>0</sup> peaks and corresponding satellites to reported literature values. To extract Cu<sup>0</sup>/Cu<sup>1+</sup> ratios, least square fitting was performed based on the linear combination of Cu<sup>0</sup> and Cu<sup>1+</sup> area normalized reference spectra of the L<sub>3</sub> region.

### **6.3.8 Density Functional Theory (DFT)**

DFT calculations were performed with the VASP code<sup>61-62</sup>, the PBE exchange-correlation functional<sup>63</sup>, and the projector-augmented wave method<sup>64-65</sup>. The Tkatchenko-Scheffler method<sup>66</sup> was used for dispersion corrections. A 400 eV planewave cutoff was used in all cases. A Cu (110) surface was used to model the reduced catalyst surface and CuO (111) was used to model the oxidized surface. For Cu (110), the surface was modelled using a 3x2 surface cell, and the Brillouin zone was sampled with a 7x7x1 k-point mesh. For CuO (111), a 2x2 surface cell was used, with a 4x4x1 k-point mesh. U values were taken from previous work<sup>67</sup> (4 eV for Cu, 6 eV for Ni), as was the antiferromagnetic structure<sup>68</sup>. Spin polarization was employed in all calculations. An isolated Ni atom was placed in each unit cell. Energies were calculated with the Ni atom in each of the first three layers of the Cu surface as a

function of hydrogen and oxygen coverage to see which layer had the lowest energy at each coverage. The energies are referenced to Ni in the 4<sup>th</sup> layer per unit cell to reflect Ni in the bulk.

## 6.4 Results and Discussion

### 6.4.1 Reactivity of npCu for Ethanol Dehydrogenation Reaction

Exposure of hydrogen-treated nanoporous Cu (npCu) to a reactant stream of 6% ethanol under non-oxidative ethanol dehydrogenation conditions results in stable, anhydrous production of acetaldehyde for 40 h (black, Figure 6.2a). The catalyst reaches its peak activity around the 15<sup>th</sup> h of reaction with an average rate of production of  $7.6 \times 10^{-6} \text{ mol s}^{-1} \text{ g}^{-1}$ . Acetaldehyde is produced with 100% selectivity over the period of time tested. The catalyst loses a negligible amount of activity over the 40 h reaction period. Even up to 60 h of reaction, the loss in activity is still negligible.

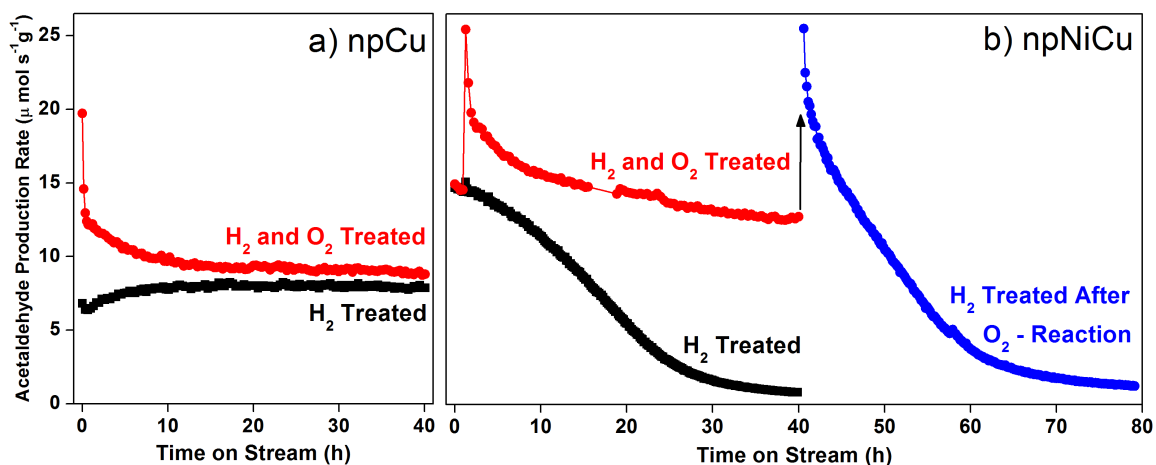


**Figure 6.2** Activity of a) npCu and b) npNiCu catalysts for ethanol dehydrogenation as a function of time on stream after hydrogen (black) and oxygen (red)

pretreatments. npCu displays stable production over time regardless of pretreatment, whereas npNiCu deactivates after H<sub>2</sub> and is more stable after O<sub>2</sub> treatment. After the O<sub>2</sub>-treated npNiCu is exposed to reaction for 40 h, it is H<sub>2</sub> treated again and returned to reaction, where it deactivates (blue). Reaction conditions: 250 °C, 50 mL min<sup>-1</sup>, 6 vol.% ethanol. H<sub>2</sub> pretreatment: 350 °C, 20 mL min<sup>-1</sup>, 10 vol.% hydrogen. O<sub>2</sub> pretreatment: 250 °C, 50 mL min<sup>-1</sup>, 20 vol.% oxygen.

Pretreating the catalyst with H<sub>2</sub> followed by O<sub>2</sub> increases its initial activity for acetaldehyde production. After npCu is hydrogen and oxygen treated (denoted O<sub>2</sub>-treated), its activity immediately spikes when returned to reaction conditions, exhibiting an acetaldehyde production rate that is approximately 2.5 times the peak activity of the H<sub>2</sub>-treated npCu (red, Figure 6.2a). The majority of the initial activation declines within the first two hours, attributed to the reduction of Cu oxides<sup>22</sup>. After the short enhancement in activity, the O<sub>2</sub>-treated npCu is 15% more active than its H<sub>2</sub>-treated counterpart, a slight increase compared to the 5% error margin (Figure 6.2a). A previous study on a Cu/SiO<sub>2</sub> catalyst suggested that an oxidation treatment re-dispersed Cu leading to increased activity for isopropyl alcohol dehydrogenation<sup>69</sup>. This suggests that the modest increase may stem from having a higher surface area when the Cu is re-dispersed by the oxidation treatment. The O<sub>2</sub>-treated npCu is also 100% selective to acetaldehyde and after the activity stabilizes around the 15<sup>th</sup> h, the activity loss is also negligible over the 40 h period and even up to 60 h on stream. Studies showed that oxidation-reduction cycling of CuZn

nanoparticles is structurally and compositionally reversible suggesting that the Zn component does not contribute to the increased activity<sup>70</sup>.

Previous studies of alcohol dehydrogenation reactions on Cu materials observed deactivation using temperatures of 160 – 300 °C<sup>5, 22-23, 69</sup>, whereas the npCu catalyst used in this study is stable at 250 °C. The difference observed may be due to the nanoporous morphology<sup>58</sup> or the Zn component<sup>24</sup>, either of which may provide better structural stability against sintering at this temperature. With the use of a higher temperature, 300 °C, deactivation is also observed on npCu. Thus, the reaction temperature was carefully chosen at 250 °C to minimize deactivation of Cu to better assess the use of Ni to increase the reactivity and decouple the simultaneous effects.

#### **6.4.2 Reactivity of npNiCu for Ethanol Dehydrogenation Reaction**

While Ni doping the npCu catalyst increases the initial activity, it degrades the longevity of the catalyst. When nanoporous NiCu (npNiCu) is reduced and exposed to reaction conditions, the initial rate of acetaldehyde production is twice the peak rate of production of npCu (black, Figure 6.2b). However, the activity quickly declines with the catalyst losing 95% of its initial activity in 40 h of reaction, whereas npCu is still active at this point. The selectivity of the reduced npNiCu catalyst is 99.2% to acetaldehyde with by-products being CO and CH<sub>4</sub> during the reaction period, whereas the npCu catalyst does not produce CO or CH<sub>4</sub> (Figure 6.15). The production of CO and CH<sub>4</sub> indicates ethanol or acetaldehyde are decomposing<sup>71</sup>. However, more CO is produced than CH<sub>4</sub>. This may indicate that methane is also decomposing to C and H<sub>2</sub> or that carbon on the surface is being hydrogenated by hydrogen produced by the

reaction to CH<sub>4</sub><sup>71-72</sup>. The decomposition reactions involving C-C bond scission suggest coke formation may be occurring<sup>38, 71-72</sup>.

Unlike the npCu system, the npNiCu catalyst exhibits a significant change after oxygen treatment resulting in an active and more stable catalyst (red, Figure 6.2b). npNiCu also exhibits a spike in activity when returned to reaction conditions after the additional oxidation pretreatment (red, Figure 6.2b). The initial activity is almost twice the initial activity of the H<sub>2</sub>-treated npNiCu. After 15 h of reaction, in which the rise in activity attributed to the oxygen pretreatment has declined, the catalyst exhibits a similar reaction rate as initially exhibited by the H<sub>2</sub>-treated npNiCu catalyst. However, unlike the H<sub>2</sub>-treated npNiCu catalyst that quickly deactivated, the oxidized npNiCu catalyst is relatively stable for the period of time tested with 99.0% selectivity to acetaldehyde. By the 40<sup>th</sup> hour, the O<sub>2</sub>-treated catalyst only lost 15% of its activity since the 15<sup>th</sup> h, whereas its H<sub>2</sub>-treated counterpart lost 95% of its activity.

Because this behavior was only observed in the Ni-doped system, the source of the enhanced activity must be due to the Ni dopant and not, for example, the presence of Zn. Regardless of H<sub>2</sub> or O<sub>2</sub> treatment, npNiCu is initially more active for the reaction than npCu. This is due to the Ni doping as both catalysts contain the same amount of residual Zn from the synthesis. Additionally, previous studies on npCu and npNiCu catalysts demonstrated that the residual Zn content does not affect the activation energy for the reaction compared to non-Zn containing Cu and NiCu catalysts<sup>58, 73</sup>. The addition of Ni in Cu-based materials did however lower the activation energy for the ethanol dehydrogenation reaction by facilitating cleavage of the C-H bond, the rate-determining step in the reaction mechanism, leading to higher

activity<sup>58, 74</sup>. Furthermore, the difference between this investigation and previous work is the use of a higher flow rate for the reaction, which accelerates the deactivation mechanism<sup>58</sup>.

The difference in stability is also linked to the Ni dopant and the pretreatment as npCu is stable for the reaction regardless of pretreatment. Clearly, H<sub>2</sub> treatment induces a change in the npNiCu catalyst that leads to deactivation in reaction, whereas O<sub>2</sub> treatment induces a change to a more stable and active form of the catalyst. To further illustrate the adverse effect of hydrogen, after 40 h of being active and stable in reaction, the O<sub>2</sub>-treated npNiCu was hydrogen treated again and returned to reaction where it deactivated over time (blue, Figure 6.2b). The activity immediately following the H<sub>2</sub> treatment exhibited a high reaction rate, though it was short-lived, likely due to cleaning of the surface by hydrogen<sup>75</sup>, as the GC-MS chromatograph showed a large signal for CO and CH<sub>4</sub> during hydrogen treatment. With subsequent time on stream, the catalyst quickly deactivated, losing 95% of its initial activity by the 40<sup>th</sup> h, same as the H<sub>2</sub>-treated npNiCu. Because the second hydrogen treatment caused an otherwise active sample to deactivate, it supports the notion that hydrogen treatment induces a change in the material that deactivates over time in reaction.

These findings demonstrate an important principle: that different pretreatments can be used to manipulate the activity of a catalyst. Hydrogen can deactivate the npNiCu catalyst for ethanol dehydrogenation, whereas oxygen can activate the catalyst. However, it is important to note that it is not inherently the hydrogen treatment that deactivates the catalyst as it is initially active after the pretreatment. Rather, it is the evolution of the H<sub>2</sub>-treated catalyst in reaction

conditions that leads to deactivation. In addition, the O<sub>2</sub>-treated catalyst is not perfectly stable in reaction conditions. It exhibits a slow deactivation in reaction suggesting this “active” form is metastable that retains the activity for a longer period of time than the H<sub>2</sub>-treated catalyst. Thus, the different pretreatments initiate distinct structural or surface compositional changes in the catalyst that evolve differently in reaction. To understand the changes the catalyst undergoes with the different reactive environments and the role of Ni, in situ and ex situ XPS were conducted to correlate changes in the surface composition to the reactivity.

#### **6.4.3 Compositional and Chemical State Changes of the npNiCu Surface**

Ambient-pressure XPS (AP-XPS) was performed to monitor changes in the surface composition and chemical states with different pretreatments. Because of the enrichment of Ni and Zn at the surface of the ingot, both the ingot surface and cross section were studied by AP-XPS. Reactivity studies are generally conducted on crushed samples with the cross sections exposed, revealing the most prevalent surface. No differences in activity are observed between when an ingot is used instead indicating the reaction is relatively insensitive to catalyst architecture and that there is no mass-transport limitation. AP-XPS studies of the ingot and cross section reveal similar trends with various exposures thus, mostly the cross section is discussed as it is the most prevalent surface in the reactivity studies, though quantification of both are available in Table 6.1.

Analysis of As Prepared npNiCu

Initial XPS analysis of the as prepared npNiCu sample under UHV and room temperature (RT) revealed that the surface of the cross section consisted of 91.4% Cu, 3.0% Ni, and 5.6% Zn (Table 6.1), reflecting the bulk composition as determined by EDS (see experimental). In the Cu 2p spectrum of the as prepared sample (0, Figure 6.3a), the  $2p_{3/2}$  peak is centered around 932.6 eV which corresponds to  $\text{Cu}^0$  or  $\text{Cu}^{1+}$ , as they overlap and cannot be distinguished. The other Cu oxidation state,  $\text{Cu}^{2+}$ , is centered around 933.6 eV. The weak satellite feature centered around 945 eV also indicates that  $\text{Cu}^{1+}$  is present. Partial electron yield (PEY)-NEXAFS spectra of the Cu L-edge indicates that a mixture of  $\text{Cu}^0$ ,  $\text{Cu}^{1+}$ , and  $\text{Cu}^{2+}$  species is present at the surface (0, Figure 6.4a). The small peak at  $\sim 932$  eV indicates  $\text{Cu}^{2+}$  and the satellite features around 938 and 941 eV indicate  $\text{Cu}^0$  species are present. From the ratio of the  $2p_{3/2}$  peak centered at 933.5 to the satellite features, in addition to the line-shape and sharpness, it can be inferred that there is a mixture of  $\text{Cu}^{1+}$  and  $\text{Cu}^0$  species.



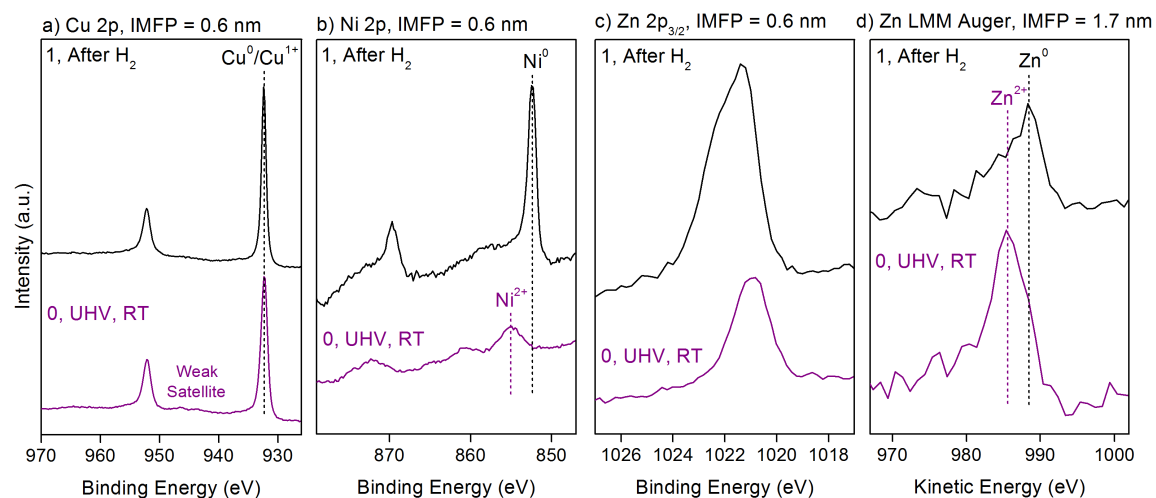


**Figure 6.3** AP-XPS of as prepared npNiCu in (0) UHV at RT and (1) after H<sub>2</sub> treatment (1h, 350 °C, 1 Torr) showing the complete reduction of Cu and Ni and the partial reduction of Zn. Spectra displayed are a) Cu 2p, b) Ni 2p, c) Zn 2p, and d) Zn LMM Auger parameter. Initial analysis (0) of the as prepared sample reveals a mixture of metallic and oxidized Cu, Ni, and Zn species.

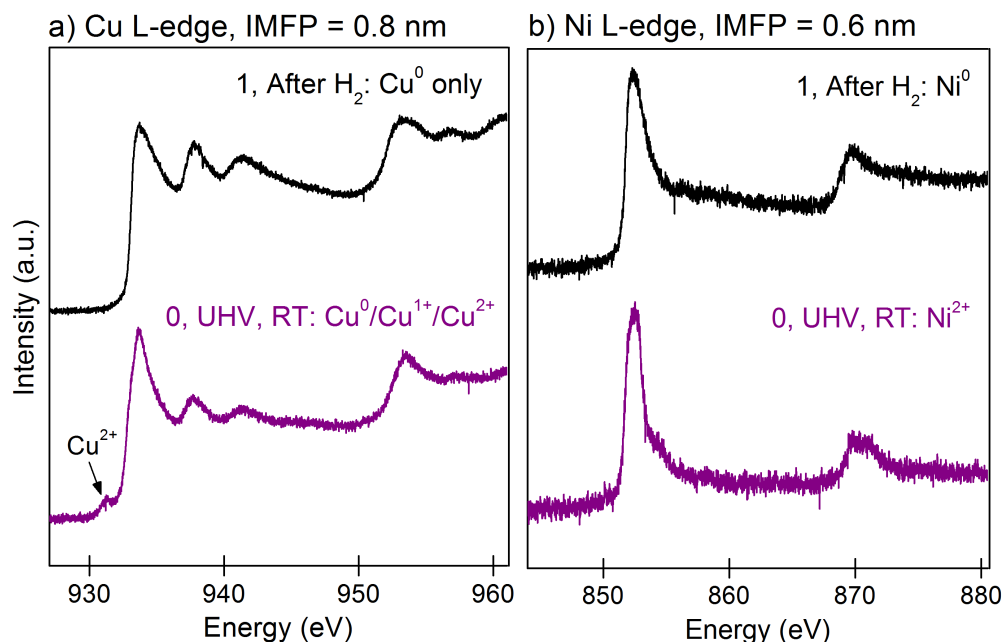


**Figure 6.4** NEXAFS analysis of as prepared npNiCu in (0) UHV at RT and (1) after H<sub>2</sub> treatment (1h, 350 °C, 1 Torr) showing the complete reduction of (a) Cu and (b) Ni. Initial analysis (0) of the as prepared sample reveals a mixture of metallic and oxidized Cu and Ni species.

A Cu 2p spectrum was also taken with a higher photon energy (1600 eV) to provide a depth profile of the surface and exhibits a mixture of Cu species as well. The spectrum displays a satellite feature ~945 eV and a shoulder feature in the Cu 2p<sub>3/2</sub> peak at higher binding energy, an indicator of Cu<sup>2+</sup> (0, Figure 6.16a). The probing depth of this depth profile is 1.2 nm, whereas NEXAFS and XPS are 0.8 nm and 0.6 nm, respectively. Thus, XPS and NEXAFS are more surface sensitive, while the depth profile XPS provides information about the near-surface region.

Ni XPS of the as prepared sample taken at RT in UHV show that Ni oxide is initially at the surface. The Ni 2p spectrum shows mostly NiO and Ni(OH)<sub>2</sub> at the

surface from the broad peak centered around 855 eV (1, Figure 6.3b). The depth profile XPS spectrum shows a mixture of oxidized and metallic species as there is a shoulder at lower energy in the  $2p_{3/2}$  peak, a contribution of metallic Ni species (0, Figure 6.16b).

Unfortunately, the oxidation state of the Zn cannot be inferred or quantified from its XPS spectrum<sup>59</sup> (0, Figure 6.3c). Using the Zn LMM Auger parameter, extracted from the survey spectrum, a mixture of  $Zn^{2+}$  and  $Zn^0$  can be identified (0, Figure 6.3d). The main peak located at a kinetic energy of 986.6 eV suggests a majority of oxidized Zn, while the shoulder feature located at a kinetic energy of 989.6 eV indicates some metallic Zn is also present. The Auger feature provides deeper information compared to XPS due to the difference in probing depth. Due to air exposure, the oxide is likely at the surface and the metallic component is located more in the sub-surface region.

Due to the noise level in the Ni NEXAFS, it is difficult to use the spectrum to identify the Ni oxidation state. However, the XPS spectrum already shows oxidized Ni at the surface. The two techniques probe a similar depth for Ni thus, either one may be used to identify the Ni oxidation state. In conclusion, the as prepared surface and sub-surface regions consist of a mixture of metallic and oxidized Cu, Ni, and Zn species.

### H<sub>2</sub> Treatment

To understand the effect of hydrogen treatment on the catalyst, the as prepared npNiCu ingot was hydrogen treated in situ and studied by AP-XPS and NEXAFS to show that both Cu and Ni are fully reduced by the treatment (Figures 6.3 and 6.4).

After in situ hydrogen treatment at 350 °C with 1 Torr H<sub>2</sub>, Cu is completely reduced to Cu<sup>0</sup> in the surface and sub-surface as satellite features of oxidized Cu species can no longer be observed in the XPS spectra (1, Figures 6.3a and 6.16). Cu NEXAFS analysis also confirms that only metallic Cu is present (1, Figure 6.4a), as the ratio of satellite peaks to the main 2p<sub>3/2</sub> peak has reduced and agree with reference spectra. The sharp main 2p<sub>3/2</sub> and 2p<sub>1/2</sub> peaks also became less sharp reflecting the reduction of Cu<sup>1+</sup> species to Cu<sup>0</sup>. The peak ~932 eV has also disappeared indicating reduction of Cu<sup>2+</sup> species.

After hydrogen treatment, Ni in the surface and sub-surface is completely reduced. The 2p spectra reveal a sharp 2p<sub>3/2</sub> peak centered around a lower binding energy of 852.6 eV than Ni<sup>2+</sup>. In addition, with the broad satellite feature around 855 eV, the spectra reflect perfect metallic Ni spectra both in the surface (1, Figure 6.3b) and in sub-surface (1, Figure 6.16b). After hydrogen treatment, NEXAFS analysis reflects pure Ni<sup>0</sup>, in agreement with the XPS spectra. The 2p<sub>3/2</sub> and 2p<sub>1/2</sub> peaks have tails that progressively increase compared to the background region before 850 eV, a clear indicator of Ni<sup>0</sup> (1, Figure 6.4b). In a Ni<sup>2+</sup> NEXAFS spectrum, the background level throughout the whole spectrum would be flat and the 2p<sub>3/2</sub> and 2p<sub>1/2</sub> peaks would also exhibit peak-splitting. Neither of these features are evident in the NEXAFS, suggesting full Ni<sup>0</sup> at the surface in agreement with the XPS.

Upon reduction, Zn is partially reduced. The Zn 2p<sub>3/2</sub> peak broadens and splits indicating a second Zn specie is present (1, Figure 6.3c). The second Zn 2p<sub>3/2</sub> feature appears at higher binding energy, possibly indicating more reduced Zn. The Auger parameter confirms that more Zn<sup>0</sup> is present at the surface as the Zn<sup>0</sup> peak located at

kinetic energy of 989.6 eV increases (1, Figure 6.3d). A contribution from oxidized Zn located around a kinetic energy 986.6 eV is still present. This suggests that Zn is partially reduced as it had a majority of oxidized species in the as prepared surface, that is now mostly metallic species.

Thus, we can conclude that hydrogen treatment at 350 °C for 1 h at 1 Torr completely reduces Cu and Ni at the surface and sub-surface regions and partially reduces Zn at the surface. It is important to note the difference in pressures between the AP-XPS and flow reactor. In the AP-XPS, 1 Torr of hydrogen was sufficient to reduce both metals therefore, when the catalyst is reduced using the flow reactor at a higher pressure of 76 Torr (10% H<sub>2</sub> at 760 Torr) and subsequently exposed to reaction, the exposed surface that conducts the reaction is metallic Cu and Ni and partially reduced Zn. As seen in the reactivity data in Figure 6.2b, this reduced surface results in deactivation of the npNiCu catalyst, whereas the reduced npCu catalyst is active and stable for a prolonged period of time. Therefore, it can be concluded that metallic Ni plays a role in the deactivation mechanism.

#### Analysis of H<sub>2</sub>-pretreated npNiCu

In the following AP-XPS experiments, a npNiCu catalyst was studied that was pretreated with H<sub>2</sub> in the flow reactor prior to being introduced into the XPS analysis chamber as complete reduction in situ was not expected and to eliminate pressure effects. Initial XPS analysis under UHV and RT revealed that H<sub>2</sub> treated cross section consisted of ~75% Cu, ~7% Ni, and ~18% Zn (Figure 6.5 and Table 6.1). Compared to the as prepared sample, the H<sub>2</sub> pretreated surface was Ni and Zn enriched on the

surface. Quantification of the as prepared sample after in situ hydrogen treatment is not used as a lower quantity of Zn (7%) was brought to the surface attributed to the lower H<sub>2</sub> pressure used in the AP-XPS (1 Torr) than in the flow reactor (76 Torr). This observation is consistent with studies of Cu/ZnO nanoparticles which demonstrated that Zn coverage of the surface increases with increasing H<sub>2</sub> partial pressure using a constant temperature and pretreatment duration<sup>76-77</sup>.

Although surface segregation of Ni by CO is well-documented in Cu-Ni systems, segregation by H<sub>2</sub> is limited<sup>78-79</sup>. To understand the enrichment of Ni at the surface, density functional theory (DFT) calculations were performed that support the observation that Ni does indeed prefer being at the surface in a hydrogen-rich environment (Figure 6.17a). With 0 to 0.5 monolayers (ML) of hydrogen on the surface, the lowest energy configuration is of Ni in the second layer. With 0.5 to 1 ML, Ni prefers to be in the first layer (Figure 6.17a). Qualitatively, the DFT calculation supports the observation of Ni segregating to the surface as the 1 ML H-coverage best reflects the high pressure and hour long H<sub>2</sub> exposure in the flow reactor.

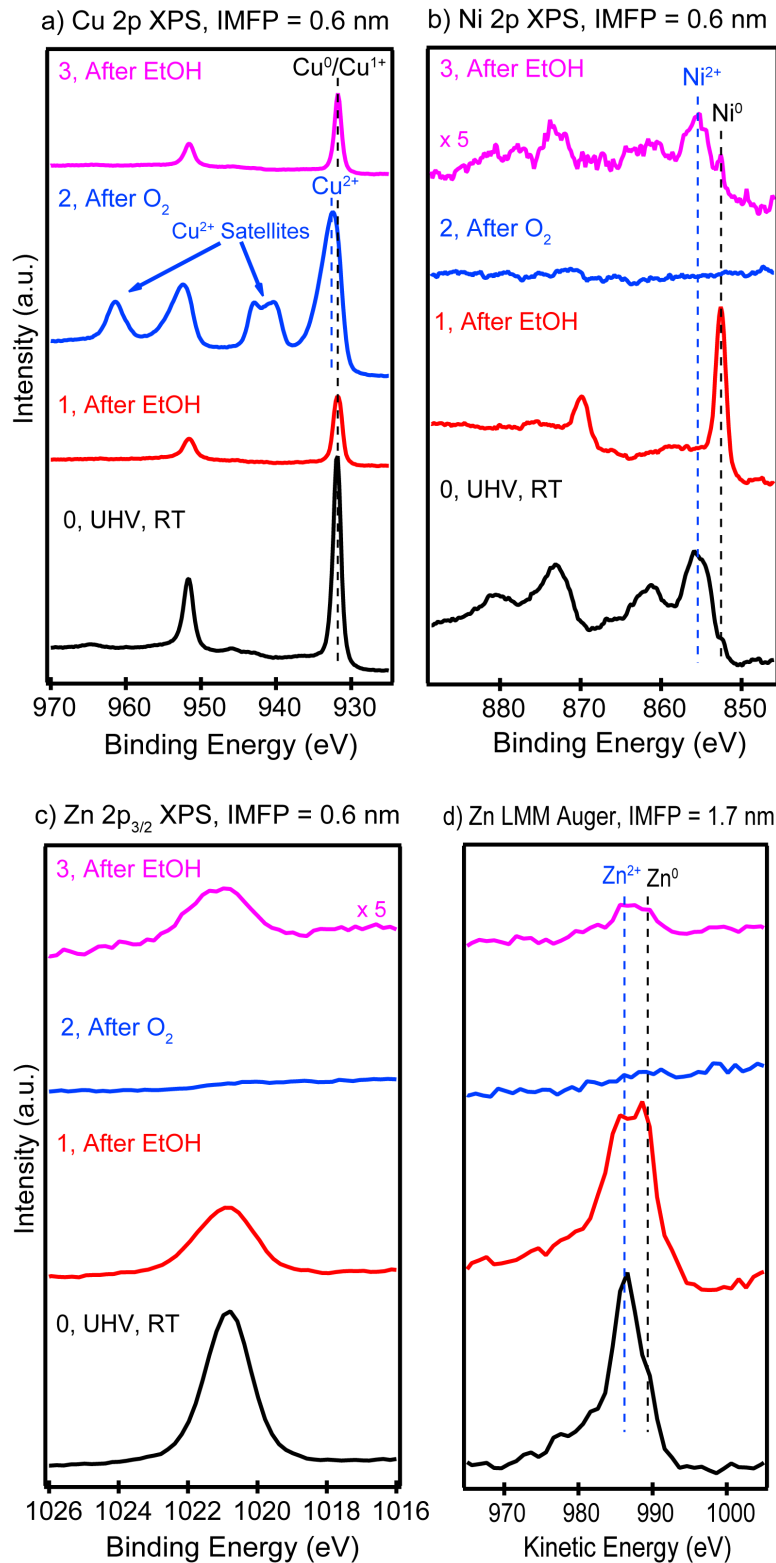


**Figure 6.5** AP-XPS analysis of ex situ H<sub>2</sub> treated npNiCu in (0) ultrahigh vacuum (UHV) at room temperature (RT), and after sequential exposures of (1) ethanol

(EtOH) (6h, 250 °C, 0.2 Torr), (2) O<sub>2</sub> (1hr, 250 °C, 1 Torr), and in ethanol after (3) ethanol (1h, 250 °C, 0.2 Torr). Spectra were taken of a) Cu 2p, b) Ni 2p, c) Zn 2p, and d) the Zn LMM Auger parameters were extrapolated from survey spectra. Initial analysis (0) of the as loaded H<sub>2</sub> pretreated sample reveals a mixture of metallic and oxidized Cu, Ni, and Zn species. After ethanol (1), Cu is reduced to Cu<sup>1+</sup>/Cu<sup>0</sup> (indistinguishable by XPS), Ni is fully reduced, and Zn is partially reduced. After oxidation (2), Cu is completely oxidized to Cu<sup>2+</sup>, whereas no Ni or Zn remain at the surface. After ethanol exposure again (3), Cu is reduced to Cu<sup>1+</sup>/Cu<sup>0</sup>, Ni reappears as Ni<sup>0</sup>/NiO/Ni(OH)<sub>2</sub>, and Zn reappears as Zn<sup>2+</sup>/Zn<sup>0</sup>.

Even though the H<sub>2</sub>-treated sample had been stored in air for a few days before the measurements, the Cu 2p XPS spectrum (0, Figure 6.5a) showed no sign of Cu<sup>2+</sup> (933.5 eV). However, the weak satellite feature between 940 and 950 eV suggests the existence of a small amount Cu<sub>2</sub>O. Quantification of the oxide is difficult due to the strong resemblance between Cu and Cu<sup>1+</sup> XPS spectra. The NEXAFS spectrum of the Cu L-edge suggests almost 100% Cu<sup>0</sup> was present at the surface (0, Figure 6.6a). The disagreement may arise from the difference in the probing depth, though it may suggest the presence of a very thin surface oxide.

Ni 2p spectrum of the as loaded sample exhibited features related to multiple Ni components, including metallic Ni and oxidized Ni species (0, Figure 6.5b). Because the XPS signatures of all the potential Ni species exhibit complicated line-shapes with prominent satellite features, conventional peak deconvolution is not possible. Instead, a least square fitting based on a linear combination of reference spectra (Figure 6.14)



of standard Ni species including Ni<sup>0</sup>, NiO, and Ni(OH)<sub>2</sub> was performed revealing a mixture of ~10% Ni<sup>0</sup>, 54% NiO, and 36% Ni(OH)<sub>2</sub> (Table 6.2). Similar to the Cu NEXAFS and XPS, the Ni L-edge NEXAFS of the surface also shows mostly metallic components, although it is difficult to distinguish small contributions of Ni<sup>2+</sup> in the spectrum due to the noisiness (0, Figure 6.6c). The differences in the NEXAFS and XPS spectra of Cu and Ni may also indicate that only a surface oxide exists from the exposure to air after hydrogen treatment that does not penetrate to the sub-surface region.

The broad Zn 2p peak centered around a binding energy of 1021 eV (0, Figure 6.5c) is not sufficient for reliable identification and quantification of the oxidized and metallic Zn. The Zn LMM Auger spectrum (0, Figure 6.5d) indicates a majority of oxidized Zn components from the main peak located at a kinetic energy of 986.6 eV. The shoulder feature located at a kinetic energy of 989.6 eV corresponds to metallic Zn, suggesting mostly ZnO is present at the surface with a small amount of metallic Zn.

To summarize the effect of hydrogen, in situ reduction revealed complete reduction of Cu and Ni at the surface and sub-surface regions and partial reduction of Zn at the surface. Therefore, the surface oxide composed of Cu, Ni, and Zn present on the as loaded H<sub>2</sub>-pretreated sample is due to air exposure. The sub-surface region was still composed of metallic Cu and Ni and a mixture of metallic and oxidized Zn, consistent with the in situ reduction. Hydrogen treatment also brought Zn and Ni to the surface compared to the as prepared sample.

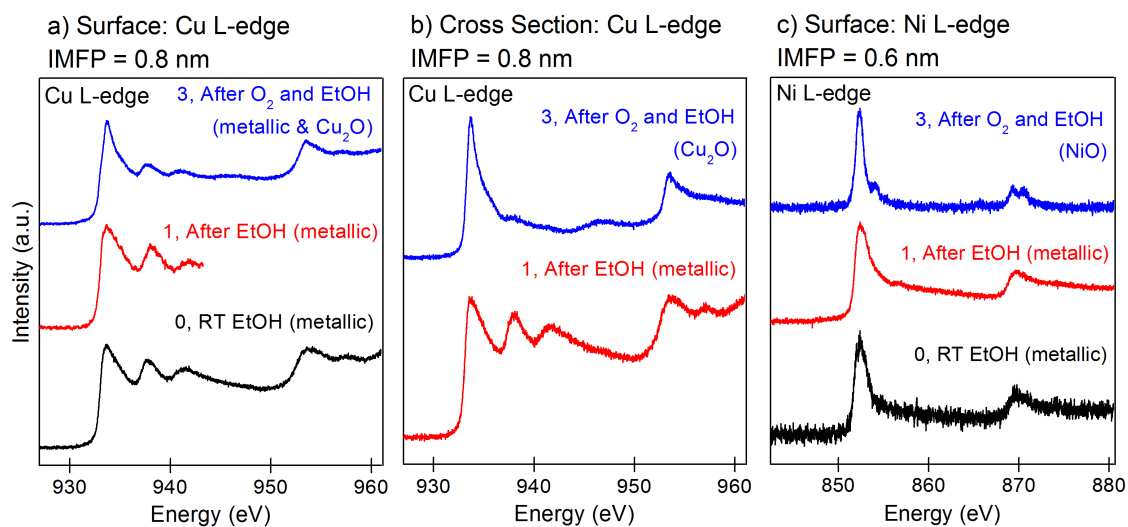


**Figure 6.6** NEXAFS analysis of H<sub>2</sub> pretreated npNiCu in (0) 0.2 Torr ethanol at RT, (1) after ethanol exposure (6 h, 250 °C, 0.2 Torr), and (3) after O<sub>2</sub> (1hr, 250 °C, 1 Torr) and taken in ethanol after ethanol exposure (1h, 250 °C, 0.2 Torr). Cu L-edge spectra of the a) ingot surface and b) cross section were taken and c) Ni L-edge spectra of the surface. Initial analysis (0) of the as loaded H<sub>2</sub> pretreated sample reveals metallic Cu on the surface and a mixture of Ni<sup>2+</sup> and Ni<sup>0</sup>. After ethanol (1), metallic Cu is on the surface and cross section, and metallic Ni is also at the surface. After oxidation and reaction (3), the ingot surface is a mixture of Cu<sup>1+</sup> (Cu<sub>2</sub>O) and Cu<sup>0</sup> and Ni<sup>2+</sup> (NiO), and the Cu on the cross section is completely Cu<sup>1+</sup>.

### Reaction After H<sub>2</sub> Treatment

After initial analysis of the loaded sample, the npNiCu catalyst was exposed to 0.2 Torr ethanol and heated to 250 °C to simulate non-oxidative ethanol dehydrogenation reaction conditions used in the flow reactor to measure the reactivity of the catalyst. During this time, the sample performance was monitored

using a mass spectrometer in the AP-XPS chamber with the inlet aimed at the sample to demonstrate that the catalyst was active (Figure 6.8). Illustrated in Figure 6.8a, as the temperature is increased and reaches 250 °C, hydrogen (mass 2) and acetaldehyde (masses 29 and 43) production peaks and begins to decline in the half hour monitored during which steady production is not yet reached. Correspondingly, the amount of ethanol (mass 31) plummets as the reaction takes off. No water (mass 18) production is observed. After sustaining the sample in reaction conditions for about 6 hours during which steady production of products was achieved, the temperature is gradually decreased (Figure 6.8b). Acetaldehyde and hydrogen production decrease, while ethanol increases. Though the water signal seems to decline, this is likely due to the overall pressure in the chamber decreasing with no reaction as flow reactor studies monitored by MS are consistent with the dry production of acetaldehyde and hydrogen. The MS data demonstrate the hydrogen production along with the acetaldehyde that is not detected by the GC-MS.

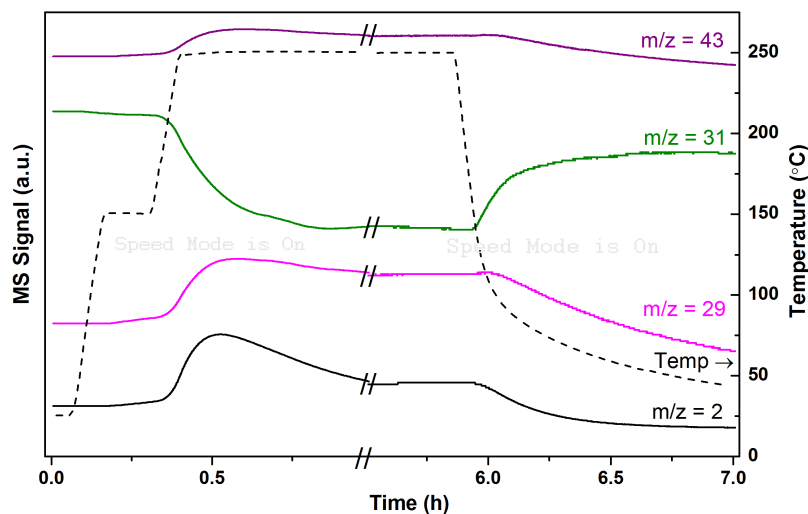


**Figure 6.8** Operando mass spectrometry (MS) during AP-XPS measurements of the  $\text{H}_2$  pretreated npNiCu ingot as the temperature is increased and decreased in 0.2 Torr ethanol showing the production of acetaldehyde and the hydrogen co-product (not detected by GC-MS). The sample was held in 0.2 Torr ethanol at 250 °C for 6 h before decreasing the temperature.

XPS spectra were collected after reaction took place for 6 h and the gas-phase ethanol was evacuated from the chamber and the catalyst cooled to room temperature to ensure high resolution spectra (1, Figure 6.5). After reaction, the surface composition of Ni decreased to 2% and Zn increased to 24% (Table 6.1). DFT calculations were performed with 0 to 0.3 ML of methoxy coverage of Cu (110) (Figure 6.17b). Methoxy was used instead of ethoxy for ease of calculations as the formation of either is the first step in the reaction mechanism of ethanol and methanol dehydrogenation reactions. The results reveal that Ni prefers to be in the third layer of the Cu (110) structure regardless of methoxy coverage (Figure 6.17b),

supporting the migration of Ni from the surface to the bulk observed in the XPS after ethanol exposure.

Cu and Ni 2p spectra almost exclusively showed metallic components (1, Figures 6.5a and 6.5b). NEXAFS spectra of Cu on the ingot surface and cross section confer that only metallic Cu species are present at the sample surface (1, Figures 6.6a and 6.6b). Analysis of the Ni NEXAFS spectrum of the surface illustrates a clear metallic Ni component (1, Figure 6.6c). The readily reduced nickel species reflect the existence of a surface oxide as nickel oxide would otherwise not be reduced by ethanol at such a low temperature<sup>80-82</sup>. Due to the small amount of Ni dopant in the cross section, NEXAFS spectra of the cross section yielded peaks that were too small for identification of the Ni<sup>0</sup> or Ni<sup>2+</sup> species and thus are not included. The Zn LMM Auger spectrum exhibited an increased Zn<sup>0</sup> feature located around a kinetic energy of 990 eV, indicating oxidized Zn species on the surface were partially reduced to metallic Zn during the reaction or that metallic Zn species migrated to the surface from the bulk as the amount of Zn at the surface also increased (1, Figure 6.5d).

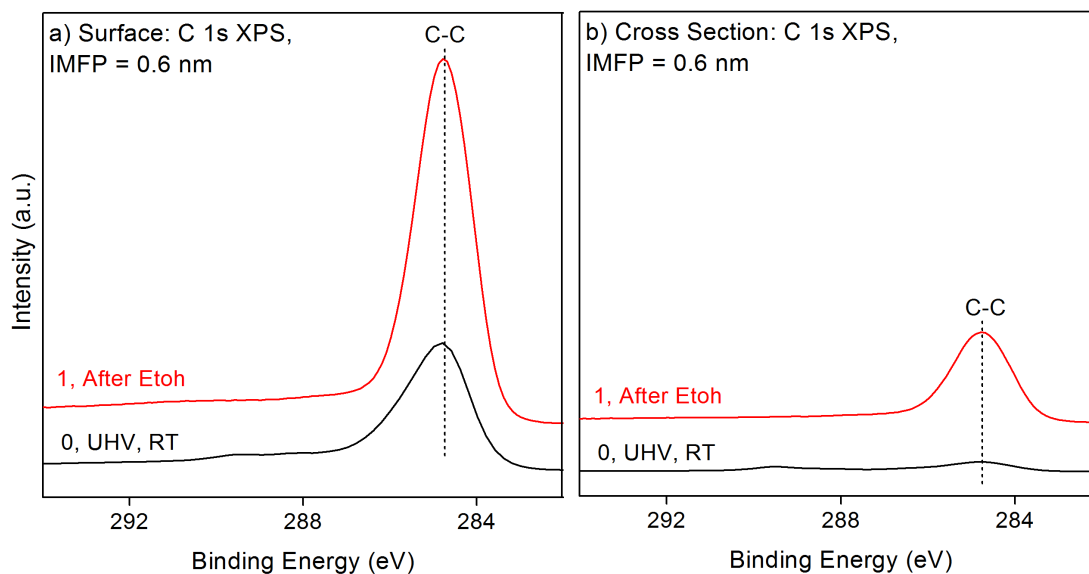


**Figure 6.8** C 1s XPS spectra of the H<sub>2</sub> pretreated npNiCu a) ingot surface and b) cross section analyzed in (0) UHV at RT and (1) after ethanol exposure (6 h, 250 °C, 0.2 Torr) showing an increase in C content at the surface.

After 6 h in reaction conditions, the C 1s XPS spectra of the ingot surface and cross section showed an increase in carbon at the surface compared to the as loaded sample (Figure 6.8). Initial analysis of the as loaded H<sub>2</sub> pretreated sample in UHV and RT revealed some adventitious carbon at the surface to expected from air exposure. The C to total metal (Cu+Ni+Zn) percentage was 120.7 at% on the surface and 34.6 at% on the cross section (Table 6.3). This percentage reveals that there is approximately a 1:1 ratio of C to metal atoms on the ingot surface and 1:3 C to metal atoms on the cross section. The primary C specie at the surface is C-C (sp<sup>3</sup> hybridized C) located at a binding energy of 284.8 eV. After reaction, the C content on the surface increased as the intensity of the C-C peak increased. The C to total metal percentage

increased to 988.7 at% on the ingot surface and 270.9 at% on the cross section, ratios of approximately 10:1 and 3:1 C to metal atoms on the surface and cross section, respectively (Table 6.3). This reflects a 10-fold and 9-fold increase of C on the surface and cross section, respectively, after ethanol exposure. Carbon deposition by the X-ray beam was found to be insignificant thus the increase in C must be due to the reaction. The ~10-fold increase of C at the surface after just 6 h of reaction agrees with the reactivity studies that carbon deposition is occurring (Figures 6.2b and 6.15).

### O<sub>2</sub> Treatment

After 6 h of ethanol exposure, the catalyst was exposed to 1 Torr of O<sub>2</sub> at 250 °C for 1 h to mimic the oxygen pretreatment used for the reactivity measurements. After the oxidation treatment, Cu is completely oxidized as the Cu 2p XPS spectrum exclusively exhibits Cu<sup>2+</sup> features (2, Figure 6.5a), whereas Ni and Zn were below the XPS detection limit on the surface and in the surface, given the flat lines in their spectra (2, Figures 6.5b and 6.5c), either segregating into the bulk or being fully covered by the newly formed CuO. Supporting the latter, the phenomenon of copper oxide overgrowing nickel in CuNi alloys has been previously observed by XPS studies<sup>83-84</sup> and X-ray diffraction (XRD) combined with infrared spectroscopy<sup>85</sup> even with the use of 30-40% Ni containing alloys. These detailed studies not only documented the overgrowth of copper oxide, but they also revealed the mechanism by which oxidation proceeds at low and high temperatures including 250 °C, the oxidation temperature used in this study.

To summarize, nickel oxide is initially formed from the exposure of oxygen, after which, cupric oxide ( $\text{Cu}_2\text{O}$ ) forms and overgrows the nickel oxide, initiating a duplex structure. With additional time, cuprous oxide ( $\text{CuO}$ ) develops from the cupric oxide and results in a more pronounced duplex structure, with an outer-rich cuprous oxide layer and an inner-rich nickel oxide layer<sup>83, 85-86</sup>. One study observed complete overgrowth of the initially formed nickel oxide by  $\text{CuO}$  in a  $\text{Cu}_{60}\text{Ni}_{40}$  alloy after 30 minutes in 0.4 Torr  $\text{O}_2$  at 250 °C<sup>83</sup>. The duplex structure was observed even at oxidation temperatures below 200 °C<sup>83, 85-86</sup>. Therefore, it is not surprising that with ~11% Ni on the ingot surface and ~2% Ni in the cross section, that a copper oxide overlayer was observed after exposure to 1 Torr  $\text{O}_2$  (a higher pressure than the studies) for 1 h at 250 °C. Similarly, in situ TEM and XPS studies demonstrated that oxidation of CuZn alloy nanoparticles leads to encapsulation of zinc oxide by copper oxide, attributed to the volume expansion of copper oxide<sup>70</sup>.



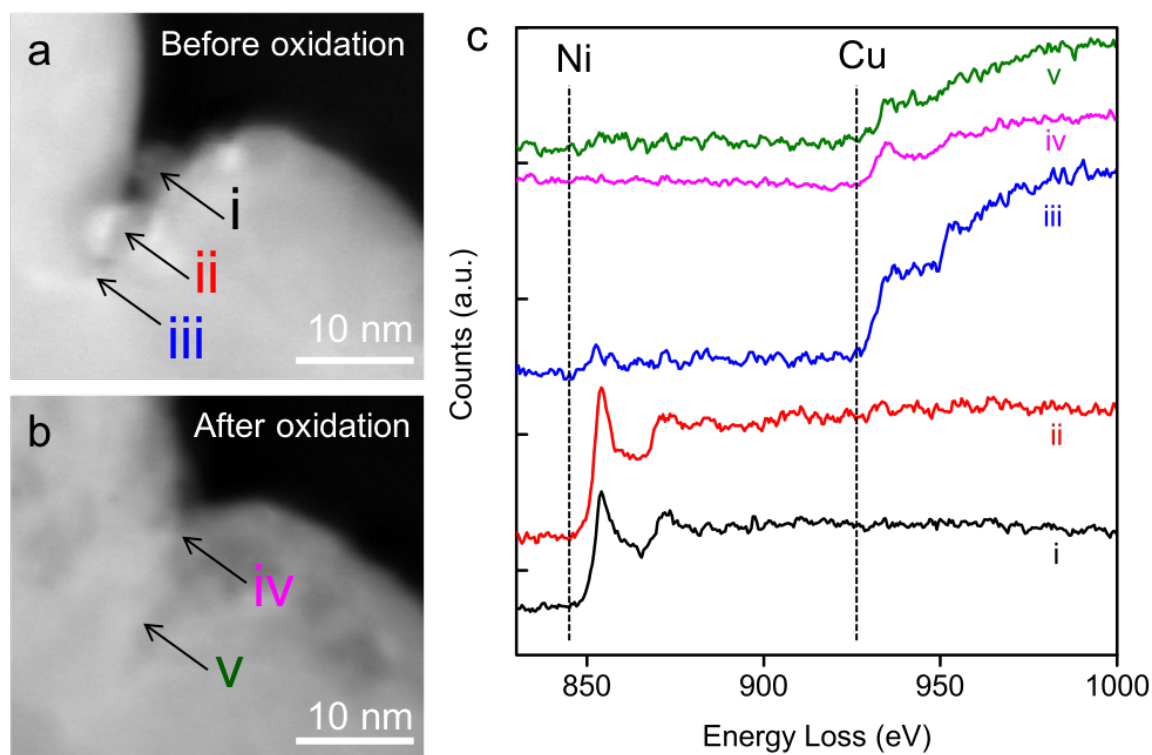


**Figure 6.9** E-TEM analysis of npNiCu demonstrate the growth of a Cu oxide overlayer covering Ni nanoparticles at the surface of a npNiCu ligament. In situ HAADF-STEM images of the same area a) before and b) after oxidation (1 h, 250 °C, 1 Torr) illustrate the nanoparticles and the overlayer. c) EELS analysis of the areas indicated by the arrows identify the Ni nanoparticles (i and ii) and the edge of the ligament as metallic Cu (iii). After oxidation, the copper oxide overlayer (iv) covers the nanoparticles, which is more metallic towards the bulk (v).

To demonstrate the Cu oxide overlayer, environmental transmission electron microscopy (E-TEM) was used to analyze selected regions before and after in situ oxidation. After loading an as prepared npNiCu sample, the sample was reduced in situ (1 h, 350 °C, 1 Torr) and exposed to ethanol (17 h, 250 °C, 0.2 Torr), similar

conditions as AP-XPS. STEM imaging of the edge of a npNiCu ligament after these treatments depicts a region with two nanoparticles in a ridge (Figure 6.9a). Electron energy loss spectroscopy (EELS) analysis identified the two particles as Ni nanoparticles<sup>87</sup> (i and ii, Figure 6.9c). The Ni particles were present in the as prepared sample and after the treatments. By contrast, Ni is not detected in the ligament structure outside of these particles, only Cu is detected (iii, Figure 6.9c). Based on the peak shape of the Cu L<sub>2,3</sub> edge, the Cu is determined to be metallic Cu<sup>87</sup>. Unfortunately, due to the overlap of the Cu and Zn L<sub>2,3</sub> edges, EELS could not be used to detect the presence of Zn.

After oxidation using the same conditions as the AP-XPS (1 h, 250 °C, 1 Torr O<sub>2</sub>), the same region was imaged and nanoparticles could no longer be observed in the ridge (Figure 6.9b). The ridge was now filled-in and where a smooth edge appeared before, it was now roughened and uneven, although the general curves of the area were preserved. An EELS line-scan was conducted down the area where the particles were previously located. Ni was not detected in the region (iv - v, Figure 6.9c). EELS analysis showed the presence of copper oxide, identified by the sharp peak (iv, Figure 6.9), and more metallic copper further from the edge (v, Figure 6.9c). This limited ETEM/EELS data set is consistent with the measured AP-XPS data that copper oxide covers the surface and Ni is no longer detectable.

The migration of Ni away from the surface after oxidation was initially a surprising due to its high affinity for oxygen and previous studies that showed Ni migrates to the surface in an oxidative environment<sup>88-90</sup>. Our data showed otherwise, displaying complete overgrowth of Ni by CuO at the surface (Figures 6.5 and 6.9).

Other studies have also shown copper oxide segregation at the surface<sup>91-92</sup>, in addition to the studies on the duplex structure discussed previously<sup>83-85</sup>. To understand the discrepancy among the literature, DFT studies were conducted of Ni in bulk Cu with varying oxygen coverages of the surface (Figure 6.17c). The studies demonstrate that in the presence of a small amount of oxygen, 0 to 0.3 ML of O, Ni prefers to be in the second or third atomic layer. With more oxygen, 0.3 - 1 ML of O coverage, Ni prefers to be in the first layer of bulk Cu. With much more O present, where Cu is modeled as a complete oxide, CuO (111), Ni prefers to be in the second layer (Figure 6.17c).

The DFT study qualitatively elucidates the conflicting observations in the literature. Indeed, studies done with pressures lower than  $10^{-4}$  Torr, where less O<sub>2</sub> is adsorbed, observed segregation of NiO at the surface of the CuNi alloy<sup>88-90</sup>. Studies using above  $10^{-4}$  Torr to atmospheric pressures, including this investigation, where the amount of O atoms adsorbed is higher, observed CuO segregation at the surface<sup>83-85, 91-92</sup>. One study demonstrated that with increasing O coverage, 10 to  $10^4$  ML, the NiO segregation at the surface progressively decreased until the surface had less Ni than the bulk concentration essentially observing copper oxide segregation at the surface (> 10 ML O adsorbed)<sup>88</sup>. Although different temperatures and exposure lengths were used in the studies cited, the segregation at the surface was most sensitive to the pressure used. The O coverage and DFT studies reflect an underlying principle in oxidation studies that extends to any other alloy system. That it is the amount of O atoms adsorbed on the surface that determines whether one component

segregates to the surface or not upon oxidation. Pressure is simple one parameter used to regulate the O coverage at the surface.

#### Reaction After O<sub>2</sub> Treatment

After oxidation, the npNiCu was once again exposed to 0.2 Torr of ethanol and heated to 250 °C for 1 h after which XPS spectra were acquired under reaction conditions. CuO features were no longer present in the Cu 2p XPS spectrum (3, Figure 6.5a). NEXAFS of the Cu L-edge shows the characteristic resonance of metallic Cu, however, the main L<sub>3</sub> peak at ~933 eV is more intense than expected for pure metallic species suggesting the presence of Cu<sub>2</sub>O (Figure 6.6a). A least square fit based on the linear combination of standard Cu<sup>0</sup> and Cu<sup>+1</sup> NEXAFS spectra reveals 29% Cu<sup>1+</sup> on the ingot surface with the rest being Cu<sup>0</sup>. On the cross section, however, NEXAFS analysis of the Cu L-edge shows 100% Cu<sup>2+</sup> (Figure 6.6b).

This difference between the ingot surface and cross section demonstrates two things. First, the presence of Ni facilitates the reduction of Cu. Not only do Cu-Ni alloys reduce more easily than their monometallic counterparts<sup>93-94</sup>, but their reducibility increases with increasing nickel content<sup>93</sup>. Because the ingot surface had more Ni than the cross section (Table 6.1), it helped facilitate the reduction of Cu resulting in the ingot surface being predominantly Cu<sup>0</sup> whereas the cross section is solely Cu<sup>1+</sup>. Second, the stepwise reduction of Cu<sup>2+</sup> to Cu<sup>1+</sup> then Cu<sup>0</sup>, previously reported in hydrogen limited conditions<sup>95-96</sup>. In non-limited conditions, Cu<sup>2+</sup> directly transforms to Cu<sup>0</sup>. On the cross section, all the Cu<sup>2+</sup> reduced to Cu<sup>1+</sup>, which would then reduce to Cu<sup>0</sup>, showing the clear stepwise reduction and indicating a hydrogen limited

environment. On the ingot surface, the stepwise reduction either occurs faster due to the higher Ni content as mostly  $\text{Cu}^0$  is observed or Ni facilitates the direct reduction of  $\text{Cu}^{2+}$  to  $\text{Cu}^0$  and the 29%  $\text{Cu}^{1+}$  is from an underlying cupric oxide. Based on reduction kinetics studies of copper oxides,  $\text{Cu}^{2+}$  will completely transform to metallic Cu in reaction conditions<sup>95</sup>.

Other than the partial reduction of surface Cu, after 1 h of reaction, small amounts of Ni and Zn (~5% each) reappear on the ingot surface (Figures 6.5b and 6.5c, Table 6.1). No spectrum was collected for Ni on the cross section, however, 1% Zn was present after 1 h. Given the parallel trends thus far, Ni likely returns to the surface of the cross section as well. Least square fitting of the Ni 2p spectrum indicated a mixture of metallic Ni (19%), NiO (36%), and  $\text{Ni}(\text{OH})_2$  (45%) (Figure 6.5b and Table 6.2), whereas the Ni NEXAFS spectrum reveals only nickel oxide is present suggesting that the small portion of reduced Ni species is only at the surface. The Zn LMM Auger spectrum illustrated again the coexistence of both metallic and oxidized Zn species (3, Figure 6.5d).

The enhanced activity observed in the first hour of reaction after oxidation for both of the npCu and npNiCu catalysts (Figure 6.18) coincides with the reduction of  $\text{Cu}^{2+}$  to  $\text{Cu}^{1+}/\text{Cu}^0$  species in ethanol, given it was the only species initially present at the surface. Monitoring the ethanol dehydrogenation activity after oxidation of npNiCu by MS also reveals the reduction of oxide species and enhanced activity (Figure 6.18). As the temperature is increased from 30°C to 250 °C, the onset of reaction can be seen by the production of hydrogen (mass 2) and acetaldehyde (mass 29 and 43) alongside the consumption of ethanol (mass 31). The reaction peaks

within the first hour, after which the amount of hydrogen and acetaldehyde produced slowly declines. The data also demonstrates a clear, transient formation of water in the first half hour (Figure 6.18) indicating the reduction of oxide species.

Because both catalysts display the enhanced activity, the source of the enhanced activity in the first hour must be due to the reduction of  $\text{Cu}^{2+}$  species in the overlayer. Previous studies demonstrated that an increased formation of  $\text{H}_2$  and acetaldehyde coincides with the reduction of  $\text{Cu}^{2+}$  species by the correlation of time-resolved X-ray absorption spectroscopy (XAS), MS, and Raman techniques<sup>16</sup>. These studies also illustrated that the formation of  $\text{H}_2$  and acetaldehyde further decreased during the reduction of the  $\text{Cu}^{1+}$  species to  $\text{Cu}^0$ . Other studies also showed that  $\text{Cu}^{1+}$  species are more active than fully reduced  $\text{Cu}^0$  for the ethanol dehydrogenation reaction<sup>13-15</sup>. Thus, since the NEXAFS shows  $\text{Cu}^{1+}/\text{Cu}^0$  after 1 h in reaction, the gradual decline in activity after the 1<sup>st</sup> hour may correspond to the reduction of  $\text{Cu}^{1+}$  species to  $\text{Cu}^0$ , which is more difficult to reduce<sup>95</sup>. Because the slow reduction of  $\text{Cu}^{1+}$  would produce very small amounts of water, our mass spectrometer would not be able to detect it. Although  $\text{Cu}^0$  is still active for ethanol dehydrogenation to acetaldehyde, our study agrees with these previous studies that  $\text{Cu}^{2+}/\text{Cu}^{1+}$  species are more active, though short-lived, for the reaction.

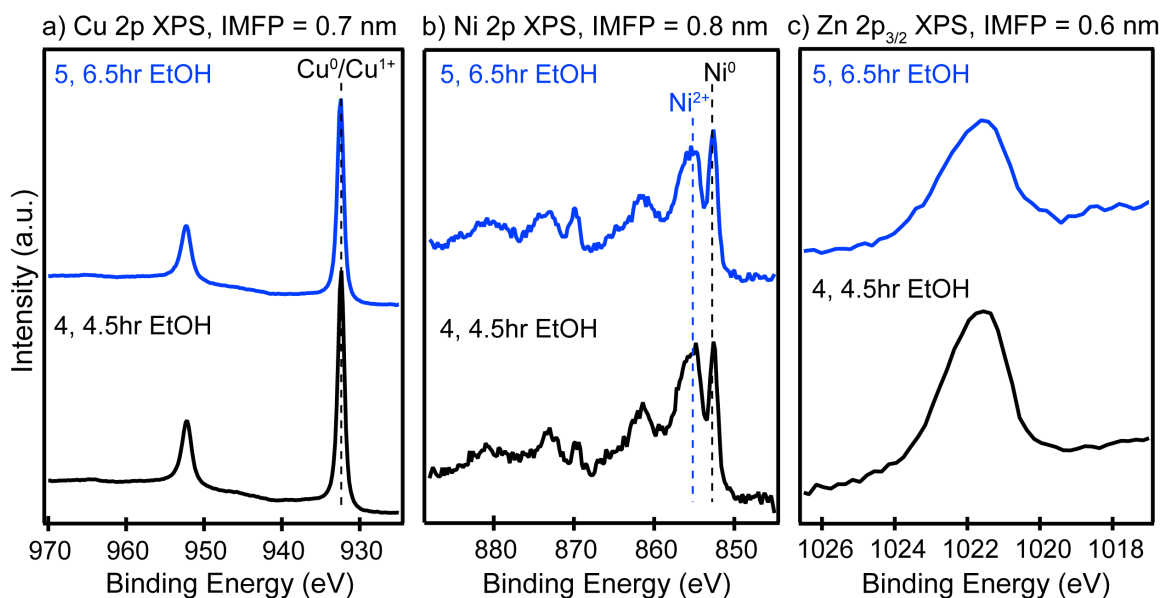


**Figure 6.10** AP-XPS analysis of O<sub>2</sub> exposed npNiCu after (4) 4.5 h and (5) 6.5 h of ethanol exposure (250 °C, 0.2 Torr) revealing Cu<sup>0</sup>/Cu<sup>1+</sup> at the surface, a mixture of Ni<sup>0</sup>, NiO, and Ni(OH)<sub>2</sub>, and a broad Zn 2p peak that cannot be identified.

After an extended period of reaction of up to 6.5 h, the XPS spectra of Cu 2p, Ni 2p, and Zn 2p were collected in situ using 1221 eV photon energy for all spectra (Figure 6.10). Therefore, the kinetic energies of the electrons measured were slightly different for Cu and Ni, 288 and 368 eV, respectively, than the 200 eV kinetic energies used for the spectra in Figures 6.3 and 6.5, corresponding to inelastic mean free paths of 0.7 nm and 0.8 nm, respectively. Since each element was probed with a different depth profile, quantification was not performed.

Qualitatively, the Cu and Zn 2p spectra remained largely unchanged compared to the spectra taken 1 h after oxidation-reaction (Figures 6.10a and 6.10c). The most significant difference is the oxidation state of Ni as it now has a clear contribution from Ni<sup>0</sup> indicated by the sharp peak at ~852 eV (Figure 6.10b). Least square fitting

of the Ni 2p spectrum reveals a mixture of Ni<sup>0</sup> (41%), NiO (21%), and Ni(OH)<sub>2</sub> (38%) after 4.5 h of reaction (Table 6.2). After 6.5 h, Ni gets more reduced as there is 47% Ni<sup>0</sup>, 15% NiO, and 38% Ni(OH)<sub>2</sub> (Table 6.2). Although Ni gets more reduced in ethanol as time progresses, the observation that Ni is not fully reduced is consistent with the literature that Ni oxide cannot be completely reduced at 250 °C with ethanol or hydrogen on this timescale<sup>80-82, 97</sup>. Because the reaction cannot be followed even longer using AP-XPS to see how the Ni oxidation state evolves after 40 h in reaction, ex situ XPS was performed at each step to track the long-term changes.

#### **6.4.4 Long-term Compositional and Chemical State Changes**

Ex situ XPS was conducted with crushed samples that expose the interior of the prepared ingots (Figure 6.11). Because the probing depths between the AP-XPS and ex situ XPS vary greatly, the two data sets cannot be compared. However, the two techniques are complementary and depict a complete picture of the catalyst, as the AP-XPS reveals surface sensitive information while the ex situ XPS provides surface and sub-surface information. Treatments for ex situ XPS analysis were conducted in two pathways. In the first pathway shown in Figure 6.11, a fresh sample (0) was hydrogen treated (1), analyzed, then returned to the flow reactor and exposed to reaction until the sample deactivated (2a). In the second pathway shown in Figure 6.11, a fresh sample was hydrogen and oxygen treated (2b), analyzed, then returned to be exposed to reaction for one hour (3b). After analysis, the sample was returned to reaction again for another 40 h until the reaction was stopped so that the sample could be analyzed (4b). This sample was then returned, the activity was recovered



and the sample was hydrogen treated and returned to reaction for 40 h, where it deactivated. XPS was conducted after this deactivation.

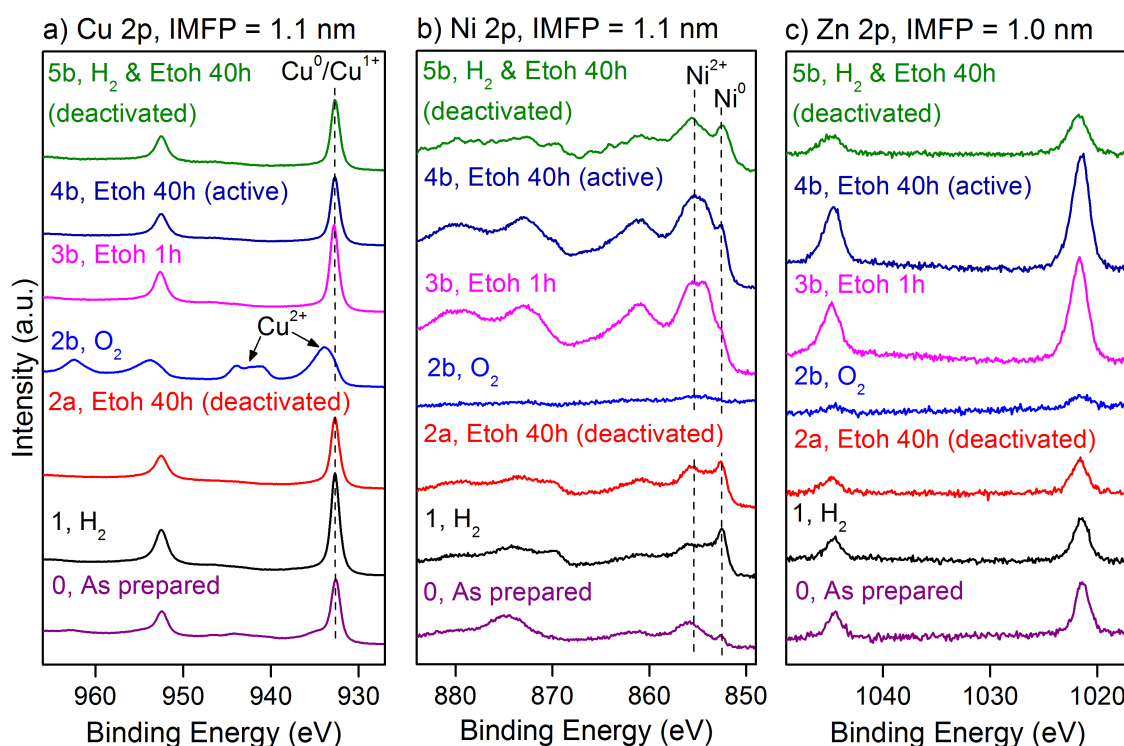


**Figure 6.11** Ex situ XPS of (0) as prepared npNiCu and after (1) hydrogen treatment (350 °C, 1 h, 10% H<sub>2</sub>, 20 mL/min), (2a) ethanol reaction until deactivation (250 °C, 40 h, 6% ethanol, 50 mL/min), (2b) oxygen treatment (250 °C, 1 h, 20% O<sub>2</sub>, 50 mL/min), (3b) ethanol reaction (250 °C, 1 h, 6% ethanol, 50 mL/min), (4b) ethanol reaction (250 °C, 40 h, 6% ethanol, 50 mL/min), and (5b) hydrogen treatment (350 °C, 1 h, 10% H<sub>2</sub>, 20 mL/min) and ethanol reaction until deactivation (250 °C, 40 h, 6% ethanol, 50 mL/min). Cu is present as Cu<sup>0</sup>/Cu<sup>1+</sup> after every treatment except after oxidation where it is Cu<sup>2+</sup>. Ni is mostly Ni<sup>2+</sup> (NiO/Ni(OH)<sub>2</sub>) in the as prepared and after the O<sub>2</sub>-ethanol exposures. Ni is mostly Ni<sup>0</sup> after H<sub>2</sub> and H<sub>2</sub>-ethanol and is hardly

present immediately after oxidation. The oxidation state of Zn is difficult to infer from its XPS spectra; however, it migrates to the bulk after oxidation.

Following the first pathway, the as prepared sample contained 1.5% Ni and 6.0% Zn at the surface. After H<sub>2</sub>, there was an increase to 10.2% Zn and 4.0% Ni (Table 6.4). Cu seems to be reduced as no satellite peak for Cu<sup>2+</sup> is present though it is not possible to distinguish the metallic Cu<sup>0</sup> peak from the Cu<sup>1+</sup> peak (1, Figure 6.11a). Although Ni exhibits some NiO/Ni(OH)<sub>2</sub> features centered around 855 eV, it also has a large metallic component at 852.5 eV (1, Figure 6.11b). The metallic component is readily seen when the spectrum is fit with three components corresponding to Ni<sup>0</sup>, Ni<sup>2+</sup>, and the 2p<sub>3/2</sub> satellite (Figure 6.19). Because in situ reduction with 1 Torr H<sub>2</sub> at 350 °C for 1 h reduces the Ni, it can be safely assumed that Ni is reduced at the higher pressure of the flow reactor with 10% H<sub>2</sub> at 1 atm (760 Torr) at 350 °C for 1 h. Furthermore, because the AP-XPS depth profile probes essentially the same depth as the lab-source XPS, 1.1 nm and 1.1 nm, respectively, the oxide component in the XPS spectrum cannot be due to unreduced Ni in the sub-surface region as in situ reduction proved that both the surface and the sub-surface regions completely reduce at 1 Torr H<sub>2</sub> (Figure 6.16b). Therefore, the Ni<sup>2+</sup> features in the XPS spectrum must be from the re-oxidation of Ni<sup>0</sup> after exposure to air as metallic Ni can easily oxidize to Ni<sup>2+</sup> under atmospheric conditions<sup>98-99</sup>.

After exposure to ethanol for 40 h, where the catalyst deactivates, the spectral features are mostly unchanged. Cu and Ni are still mostly metallic. The Ni XPS exhibits some oxide features with similar intensities as after H<sub>2</sub> treatment, attributed to the

air exposure (1, Figure 6.11b). The surface composition is also relatively unchanged with 5% Ni and 8.2% Zn (Table 6.4). Because the same spot is not analyzed by XPS after each treatment as the sample is crushed and different particle pieces are analyzed each time, small variations in the composition may not reflect changes due to the treatment.

Starting the second pathway, after reduction and oxidation, most of the nickel and zinc are gone from the surface analogous to what was observed in AP-XPS (2b, Figures 6.11b and 6.11c). A small amount of nickel and zinc (~2% each) are observed by ex situ XPS after oxidation (Table 6.4), whereas in AP-XPS they were completely removed from the surface (Table 6.1). This difference can be related to difference in probing depth between the two techniques, as the ex situ XPS probes deeper than the AP-XPS, 1.1nm for Ni and 1.0 nm for Zn, almost twice the probing depth of the AP-XPS. This difference reflects the depth at which the Ni and Zn are buried or in another sense, the thickness of the copper oxide. Copper is completely oxidized (2b, Figure 6.11), exhibiting a strong  $\text{Cu}^{2+}$  satellite, akin to the AP-XPS, demonstrating that copper oxide covers most of the surface after oxidation. The small amount of nickel left is also completely oxidized to  $\text{Ni}^{2+}$  (Figure 6.19). The correspondence between the in situ and ex situ  $\text{O}_2$ -treated samples demonstrate that the surface structure is stable.

After exposure to ethanol again, Ni and Zn return to the surface. In AP-XPS, after 1 h of 0.2 Torr ethanol at 250 °C, less Ni and Zn return to the surface than was previously present before oxidation. In ex situ XPS, after 1 h of 6% ethanol with a total pressure of 1 atm (760 Torr) at 250 °C, more Ni (10.5%) and Zn (21.2%) returned to the surface than was there before oxidation (after reduction) (Table 6.4). The

difference in probing depth reflects that there is an enrichment of Ni and Zn in the sub-surface region as the copper oxide layer subsides. Due to the disappearance of the  $\text{Cu}^{2+}$  satellite, Cu is reduced to metallic  $\text{Cu}^0$  or a mixture of  $\text{Cu}^0$  and  $\text{Cu}^{1+}$  (3b, Figure 6.11). Ni, on the other hand, is present almost completely as an oxide/hydroxide with a very small contribution by  $\text{Ni}^0$  indicated by the slight shoulder at  $\sim 852.5$  eV. As seen previously with the hydrogen treatment, although Ni partially oxidizes due to air exposure, the greater amount of oxidized Ni seen after  $\text{O}_2$  and reaction is not due to air exposure. Even after 40 h of reaction (4b, Figure 6.11), Ni is still mostly oxidized with growing contribution from  $\text{Ni}^0$  (Figure 6.19). After 40 h of reaction, some change is observed in the composition, with some Ni going into the bulk (10.5%) and Zn coming to the surface (21.2%) (Table 6.4).

After the active catalyst is hydrogen treated and returned to reaction, after which it deactivated (Figure 6.2b), the surface exhibits a large change (5b, Figure 6.11). Though some Ni has gone into the bulk (7.8%), there is now half the amount of Zn at the surface (12.2%) (Table 6.4). Interestingly, the quantification and oxidation states are similar to that of the hydrogen (1) and ethanol reaction exposed (2a) surfaces which also deactivated in a similar manner. Additionally, the Ni spectrum also reflects a mostly metallic component as the hydrogen treatment is expected to reduce Ni.

Regardless of when the sample was hydrogen treated, the hydrogen treatment induces a change in the material that leads to deactivation. An oxidation treatment, on the other hand, leads to more stable activity over the same period of time. The surface composition after both deactivations (2a and 5b) reflects moderate amounts

of Ni (5-8%) and Zn (8-12%), whereas the active surface (3b and 4b) has more Ni (10-14%) and Zn (18-21%) (Table 6.4). The hydrogen treated sample also has a similar composition to the deactivated samples, though it is initially active and deactivates over 40 hours. This indicates that it is not inherently the surface composition after reduction that causes inactivity, but rather how the hydrogen-treated surface interacts and evolves in reaction. One

A key difference between the active and deactivating surface is the presence of  $\text{Ni}^{2+}$  and  $\text{Ni}^0$ , respectively. Metallic Ni is well-known to deposit carbon on catalysts in ethanol-based reactions. The production of CO and  $\text{CH}_4$  as by-products during reaction (Figures 6.2b and 6.15) and the increase of carbon at the surface as determined by XPS (Figure 6.8) hints that carbon deposition is occurring. After oxidation, CO and  $\text{CH}_4$  are still produced as by-products due to the gradual reduction of  $\text{Ni}^{2+}$  to  $\text{Ni}^0$  and the higher quantity of Ni present near the surface. Further characterization was conducted on the catalysts to confirm if carbon deposition was the taking place.

#### **6.4.5 Characterization of Carbon Species**

After 40 h of reaction, the  $\text{H}_2$ -treated and  $\text{O}_2$ -treated npNiCu catalysts were characterized by temperature-programmed oxidation (TPO) which indicated the presence of coke in the  $\text{H}_2$ -treated catalyst which had deactivated catalyst. The TPO profiles of the used catalysts both show the evolution of  $\text{CO}_2$  (Figure 6.12a). The TPO of the  $\text{H}_2$ -treated, deactivated catalyst has one broad, asymmetric peak at  $\sim 290$  °C. The TPO of the  $\text{O}_2$ -treated, active catalyst has two symmetric peaks at  $\sim 180$  and

~300 °C indicating different types of carbon are present (Figure 6.12a). These peaks at low temperatures (< 450 °C) correspond to amorphous coke, monoatomic or polymeric in nature<sup>72, 100</sup>. The presence of one peak in the deactivated sample compared to two in the active one may indicate a transformation of one type of carbon to another during deactivation. Peaks above 450 °C would correspond to graphitic-type coke, including carbon filaments<sup>72, 100</sup>. Unfortunately, our furnace could not go to higher temperatures to check for graphitic-type carbon. However, previous studies of Ni and Co catalysts have demonstrated that encapsulating coke, which is monoatomic and polymeric, blocks metal active sites and leads to deactivation of the catalysts, whereas carbon filaments did not deactivate the catalyst<sup>72, 101</sup>. Thus, the presence of amorphous coke does not rule it out as a source of deactivation.

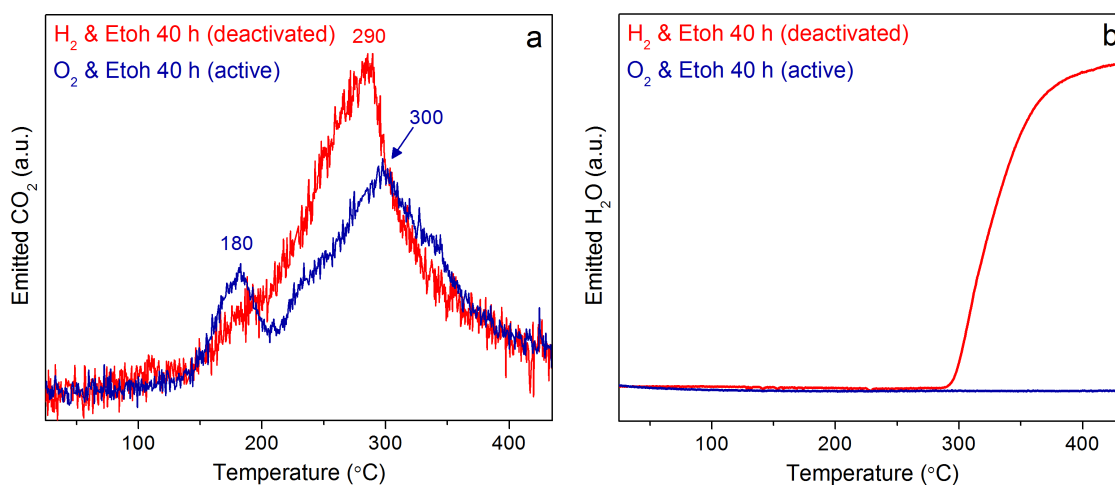


**Figure 6.12** TPO profiles displaying emitted a) CO<sub>2</sub> and b) H<sub>2</sub>O of deactivated (red) and active (dark blue) npNiCu showing the evolution of H<sub>2</sub>O only from the deactivated catalyst, an indicator of coking, and the evolution of CO<sub>2</sub> from both catalysts. The TPO was conducted on H<sub>2</sub>-treated (red) and O<sub>2</sub>-treated (dark blue) npNiCu after 40 h of

reaction where the H<sub>2</sub>-treated catalyst had deactivated and the O<sub>2</sub>-treated was still active. Temperature was ramped from 25 to 430 °C (10 °C/min).

Comparison of the intensities of the peaks at 290 and 300 °C shows that the deactivated catalyst has more carbon on its surface. The difference in temperature between the two peaks is likely within experimental error. The difference in peak shape at the same temperature also indicates a change in reaction order in the oxidation of coke. An asymmetric peak, observed in the H<sub>2</sub>-treated catalyst, indicates the reaction order is less than 1, whereas as the symmetric peak, observed in the O<sub>2</sub>-treated catalyst, indicates the reaction order is 1<sup>102</sup>. To summarize from the literature, when there is a small amount of carbon at the surface such as a monolayer or small particles (< 2nm), a reaction order of 1 is observed, because the exposed carbon is directly related to the amount of carbon being oxidized<sup>102</sup>. When larger coke particles are present, the amount of carbon exposed decreases as carbon is oxidized leading to a reaction order that is less than 1. Thus, both the intensity and the peak shape of the emitted CO<sub>2</sub> TPO profiles indicate that the deactivated H<sub>2</sub> pretreated npNiCu has more coke on its surface than the O<sub>2</sub> pretreated npNiCu that is still active for the reaction.

Analysis of the emitted H<sub>2</sub>O during the TPO demonstrates that the H<sub>2</sub>-treated, deactivated catalyst has a different type coke on its surface. Coke that is polymerized hydrocarbons consists of carbon and hydrogen as its composition is CH<sub>n</sub>, where n = 0.2 to 1.5<sup>103-104</sup>. Thus, the evolution of water during oxidation of coke is to be expected<sup>103-106</sup>. In the TPO profiles of the used H<sub>2</sub>-treated and O<sub>2</sub>-treated catalysts, only the deactivated H<sub>2</sub>-treated npNiCu emitted H<sub>2</sub>O (Figure 6.12b). This difference

indicates that a polymeric type coke covers the deactivated catalyst, in addition to its intensity and peak shape. Although the active catalyst also had carbon on its surface, it is likely a different type that does not contain H and evolve H<sub>2</sub>O during oxidation as its intensity and peak shape also indicated less carbon was present.

Raman spectroscopy of the used catalysts also shows that the deactivated npNiCu has more coke on its surface (Figure 6.20). The Raman spectrum of the H<sub>2</sub> treated npNiCu reveals a minor amount of carbon on the surface, likely corresponding to amorphous carbon from air exposure. The spectra of the O<sub>2</sub>-treated and H<sub>2</sub>-treated catalysts after reaction show an increased amount of carbon on the surface compared to the H<sub>2</sub>-treated spectrum, with even more carbon on the deactivated H<sub>2</sub>-treated catalyst than the active O<sub>2</sub>-treated catalyst. A similar intensity as the deactivated H<sub>2</sub>-treated catalyst was observed on the deactivated npNiCu that had been H<sub>2</sub> treated after being active in reaction for 40 h (5b in Figure 6.11). Deconvolution of the spectra reveal four bands: ~1570 cm<sup>-1</sup>, G band, characteristic of sp<sup>2</sup> hybridized carbon; ~1430 cm<sup>-1</sup>, D<sub>3</sub> band, attributed to amorphous carbon including adsorbed molecules, molecular fragments, and ring structures; and ~1330 cm<sup>-1</sup>, D band, characteristic of disordered aromatic structures; and 1245 cm<sup>-1</sup>, corresponding to aliphatic C-H bonds<sup>71, 107-108</sup>. Both the active and deactivated catalysts exhibit contributions from numerous types of carbon species, reflecting amorphous carbon, in agreement with the TPO. Amorphous carbon can be a mixture of sp<sup>3</sup>, sp<sup>2</sup>, and sp<sup>1</sup> sites, and may or may not be hydrogenated. The deactivated H<sub>2</sub> pretreated catalyst has a stronger contribution from the G band, which indicates a higher concentration of sp<sup>2</sup> hybridized carbon on the surface. In combination with the TPO data, this supports the



presence of more polymeric chains or aromatic structures that contain or trap hydrogen.

Characterization of the active and deactivated catalysts revealed that both catalysts had amorphous carbon on the surface. The deactivated catalyst had more carbon on its surface than the active catalyst as determined from the intensities of the Raman spectra and TPO profiles. The TPO peak shapes also indicated that the deactivated catalyst had larger amounts of coking than the active catalyst. The evolution of water in the TPO profile and increase of  $sp^2$  hybridized carbon in the Raman spectra indicate the presence of polymeric carbon, which may be leading to the deactivation of the catalyst, as it was not present in the active catalyst.

#### **6.4.6 Ni Oxidation State and Deactivation**

Characterization of the carbon species revealed that carbon deposition was occurring on the npNiCu catalyst and likely leading to the deactivation of the  $H_2$ -treated catalyst. After  $H_2$  treatment, the surface being exposed to reaction and thus, depositing carbon, consists of metallic Cu and Ni and partially reduced Zn. Of the three components, metallic Ni is well-documented to be a culprit of carbon deposition deactivating monometallic Ni catalysts as well as multi-component Ni catalysts for various reactions as metallic Ni forms Ni-carbide which is the precursor to carbon deposition<sup>34-35, 38-40, 109</sup>. Unlike Ni, Cu is not capable of forming a carbide precursor and depositing carbon. The reactivity studies support this notion that neither Cu nor Zn/ZnO nor their combination with Cu are responsible for the carbon deposition as npCu produces acetaldehyde with 100% selectivity regardless of pretreatment

(Figures 6.2a and 6.15). The combination of Ni and Zn, on the other hand, has been documented to deactivate in ethanol steam reforming due to the formation a  $\text{Ni}_3\text{ZnC}_{0.7}$  carbide<sup>39-40</sup>. Whether Ni acts on its own or with Zn as its accomplice, the reactivity and characterization studies all indicate that the npNiCu is guilty of carbon deposition.

Although the  $\text{O}_2$ -treated npNiCu catalysts exhibits an increase of carbon at its surface, it was not characterized to be polymeric like the deactivated  $\text{H}_2$ -treated catalyst. The main difference between the two catalysts leading to the observed difference in activity is the presence of metallic or oxidized Ni. Hydrogen treatment, whether it is conducted before the first reaction exposure or after the catalyst had been active in reaction, reduces the Ni and leads to deactivation. As alluded to before, it is not inherently the hydrogen-treated surface that is inactive for the reaction. It is the interaction of this surface with the reactants that leads to deactivation. Hence, the metallic Ni at the surface decomposes the reactants and products, depositing carbon and deactivating the catalyst, which also takes 20 - 30 h because of the small amount of Ni at the surface.

This mechanism could explain the gradual decline in activity of the  $\text{O}_2$ -treated catalyst. As the  $\text{Ni}^{2+}$  at the surface is reduced by the reaction, the metallic Ni species decompose the reactants and products, observed by the evolution of CO and  $\text{CH}_4$  during the reaction. Carbon species build-up on surface, blocking certain metal sites and reducing the activity, supported by the TPO and Raman studies showing an increase of carbon on the surface. One study showed that carbon deposition by Ni is not significant until 80% of NiO is reduced<sup>110</sup>. Indeed, when an  $\text{O}_2$ -treated npNiCu

catalyst is left on stream for longer periods of time, the catalyst rapidly deactivates after 70 h on stream in a similar manner as the two H<sub>2</sub>-treated deactivated catalysts. Deactivation by carbon deposition would indicate that the Ni<sup>2+</sup> at the surface stabilizes the activity by preventing significant carbon deposition until Ni<sup>2+</sup> is greatly reduced.

Alternatively, Ni<sup>2+</sup> may contribute to the stability and activity of the catalyst by either stabilizing the active structure or promoting the ethanol dehydrogenation activity. Ni<sup>2+</sup> has been cited to promote ethanol dehydrogenation to acetaldehyde<sup>39, 111</sup>, in which case the deactivation would still be related to the reduction of Ni<sup>2+</sup>, but due to the loss of active species, not carbon deposition. Furthermore, water has been identified as co-catalyst in the dehydrogenation of methanol<sup>56</sup>. Because the Ni<sup>2+</sup> identified by XPS has a contribution of Ni(OH)<sub>2</sub>, the hydroxyl species may also contribute to enhancing the activity until the oxidized species have been completely reduced. Likely, a combination of all the mechanisms discussed is involved.

Regardless of mechanism, the reduction of Ni<sup>2+</sup> is involved, revealing the enhancing role of Ni<sup>2+</sup> and the deactivating role of Ni<sup>0</sup> in the npNiCu catalyst. The key to keeping Ni<sup>2+</sup> at the surface is the low reaction temperature used resulting in a metastable material. At this low temperature, the kinetics of reducing the Ni<sup>2+</sup> are very slow, even though it is thermodynamically favorable. Thus, the Ni<sup>2+</sup> is trapped for a time-being until its reduction leads to deactivation. Deactivation by carbon deposition is supported by our studies, though the contribution of the Ni<sup>2+</sup> to the activity and structure cannot be excluded.

## 6.5 Conclusions

Nanoporous Cu, with residual Zn, was shown to be catalytically active and stable for ethanol dehydrogenation reaction regardless of H<sub>2</sub> or O<sub>2</sub> pretreatment. O<sub>2</sub>-treating led to a slight increase in the long-term activity, attributed to re-dispersion of Cu. Ni-doping nanoporous Cu to yield nanoporous NiCu initially led to higher activity for the reaction, as Ni facilitates C-H bond cleavage in the reaction mechanism. However, over ~30 h on stream H<sub>2</sub>-treated npNiCu completely deactivated. It's O<sub>2</sub>-treated counterpart was more stable, losing only 15% of its activity in the same time period, while maintaining higher activity than the npCu.

Hydrogen treatment completely reduced Cu and Ni and partially reduced the residual Zn and brought Ni and Zn to the surface. Subsequent, exposure to ethanol brought more Zn to the surface, while Ni segregated to the bulk. Exposure for 30 to 40 h in ethanol, led to the deactivation of the catalyst. Ethanol exposure was shown to increase the C at the surface by in situ XPS as was expected by the production of by-products, indicating decomposition of reactants or products. The deactivated H<sub>2</sub>-treated catalyst had a large increase of carbon at its surface, that was characterized to be polymeric in nature, due to the hydrogen content of the coke. The source of the deposition is attributed to metallic Ni species.

Oxidation treatment, on the other hand, completely oxidized Cu and led to a Cu oxide overlayer covering up the Ni and Zn at the surface. The growth of an Cu oxide overlayer in NiCu alloys was shown to be dependent on the coverage of O atoms on the surface. Ethanol exposure of the oxidized surface brought Ni and Zn back to the surface, while reducing the Cu, which was shown to be a stepwise reduction: Cu<sup>2+</sup>→

$\text{Cu}^{1+} \rightarrow \text{Cu}^0$ . Ni at the surface was oxidized after ethanol exposure and kept its oxidized state even after 40 h in reaction conditions, when it was still active. Characterization of the catalyst after 40 h revealed an increase in carbon at its surface, though less than the deactivated  $\text{H}_2$ -treated catalyst.

Hydrogen treatment of the active catalyst also led to deactivation of the catalyst, demonstrating how different pretreatments could be used to manipulate the activity of the catalyst. The key to the active surface, induced by oxygen pretreatment, is the presence of  $\text{Ni}^{2+}$ .  $\text{Ni}^{2+}$  in the form of  $\text{NiO}$  or  $\text{Ni}(\text{OH})_2$  prevents significant coking and may also participate in the reaction mechanism enhancing the activity, until it is reduced by reaction or hydrogen treatment when it deactivates again. Thus, the activated surface is metastable, being thermodynamically favorable to reduce the  $\text{Ni}^{2+}$ , but kinetically trapped due to the low reaction temperature. This allowed the use of  $\text{Ni}^{2+}$  to enhance the activity, while preventing deactivation of the Cu component. With further stabilization of the  $\text{Ni}^{2+}$ , an active and stable catalyst for the ethanol dehydrogenation reaction could be created for industrial purposes. These findings can be expanded to other alloy materials and present an interesting, new principle for the design of catalytic materials: the exploitation of kinetics to overrule thermodynamics and preserve the active species on the catalyst surface.

## 6.6 Supporting Information

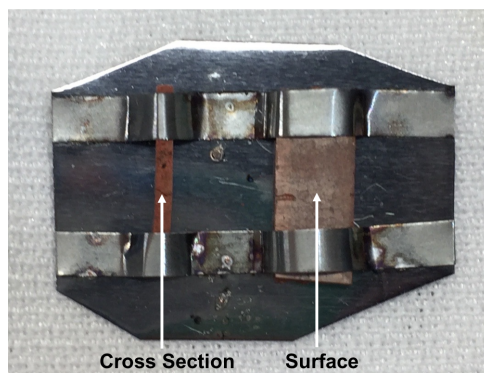


**Figure 6.13** AP-XPS ingot cross section (left) and surface (right) samples on tantalum back-plate with tantalum foils running across the top and bottom to keep samples in place

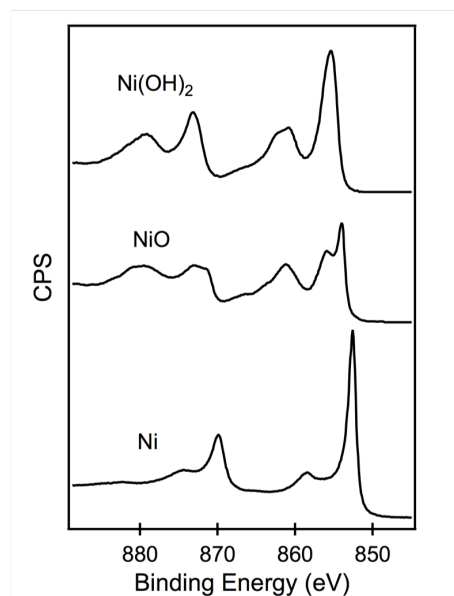


**Figure 6.14** Ni reference spectra used to fit measured spectra

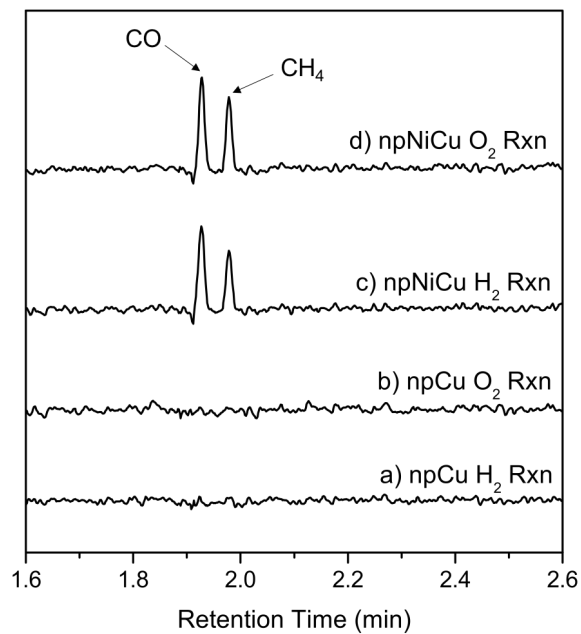


**Figure 6.15** Chromatographs of npCu in reaction after a) hydrogen and b) oxygen showing no CO or CH<sub>4</sub> production. Typical chromatographs of npNiCu in reaction after a) hydrogen and b) oxygen showing CO and CH<sub>4</sub> production.

**Table 6.1** Quantification of AP-XPS

<b>AP-XPS @ NSLSII/BNL: 200 eV Kinetic Energy</b>			
H <sub>2</sub> pre-treated sample in flow reactor: 10% H <sub>2</sub> , 1h, 350°C, 20 mL min <sup>-1</sup>			
<b>Surface</b>	<b>Cu%</b>	<b>Ni%</b>	<b>Zn%</b>
UHV, RT (As prepared)	85.3	7.6	7.1
0, UHV, RT (H <sub>2</sub> pretreated)	71.6	11.3	17.1
1, Ethanol (6h, 250°C, 0.2 torr)	67.5	10.7	21.8
2, O <sub>2</sub> (1hr, 250°C, 1 torr)	99.6	0.0	0.4
3, Ethanol (1h, 250°C, 0.2 torr)	89.8	5.2	5.0
<b>Cross Section</b>	<b>Cu%</b>	<b>Ni%</b>	<b>Zn%</b>
UHV, RT (As prepared)	91.4	3.0	5.6
0, UHV, RT (H <sub>2</sub> pretreated)	75.2	7.1	17.7
1, Ethanol (6h, 250°C, 0.2 torr)	73.7	2.1	24.2
2, O <sub>2</sub> (1hr, 250°C, 1 torr)	100.00	0.0	0.0
3, Ethanol (1h, 250°C, 0.2 torr)	99.12	No spec	0.9



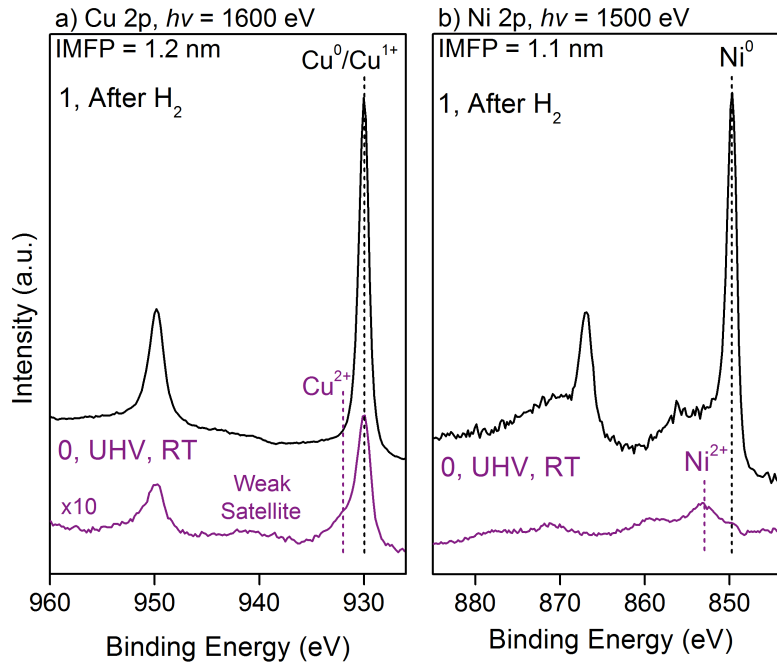


**Figure 6.16** Depth profile of as prepared npNiCu taken with a higher X-ray photon energy such that the kinetic energy of photoelectrons were 667 eV and 647 eV for Cu and Ni, respectively. AP-XPS spectra were taken in (0) UHV at RT and (1) after H<sub>2</sub> treatment (1h, 350°C, 1 torr) showing the complete reduction of (a) Cu and (b) Ni.

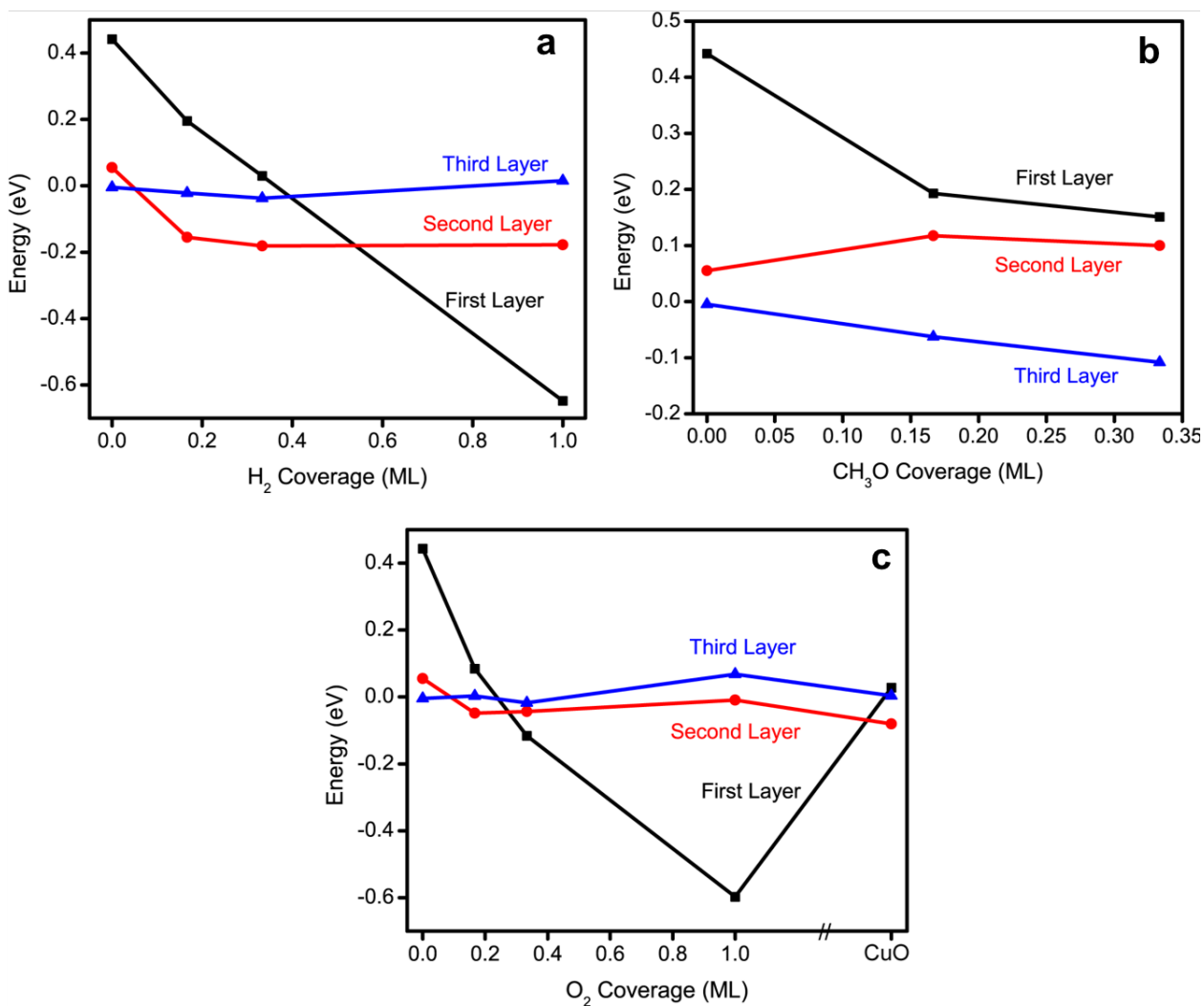


**Figure 6.17** Density Functional Theory (DFT) calculations of Ni in the first to third layer of Cu with varying coverages of a) hydrogen, b) methoxy, and c) oxygen.

**Table 6.2** Quantification of Ni oxidation states

Surface	Ni <sup>0</sup> %	NiO %	Ni(OH) %
0, UHV, RT (H <sub>2</sub> pretreated), IMFP = 0.6 nm	10	54	36
1, Ethanol (6h, 250°C, 0.2 torr), IMFP = 0.6 nm	100	0	0
2, O <sub>2</sub> (1hr, 250°C, 1 torr), IMFP = 0.6 nm	No Ni on surface		
3, Ethanol (1h, 250°C, 0.2 torr), IMFP = 0.6 nm	19	36	45
4, Ethanol (4.5h, 250°C, 0.2 torr), IMFP = 0.8 nm	41	21	38
5, Ethanol (6.5h, 250°C, 0.2 torr), IMFP = 0.8 nm	47	15	38

**Table 6.3** Quantification of C 1s XPS spectra

<b>AP-XPS @ NSLSII/BNL: 200 eV Kinetic Energy</b> H <sub>2</sub> pre-treated sample in flow reactor: 10% H <sub>2</sub> , 1h, 350°C, 20 mL min <sup>-1</sup>	
<b>Surface</b>	<b>C/Metal %</b>
UHV (H <sub>2</sub> pre-treated)	120.7
Ethanol (6h, 250°C, 0.2 torr)	988.7
<b>Cross Section</b>	<b>Cu%</b>
UHV (H <sub>2</sub> pre-treated)	34.6
Ethanol (6h, 250°C, 0.2 torr)	270.9

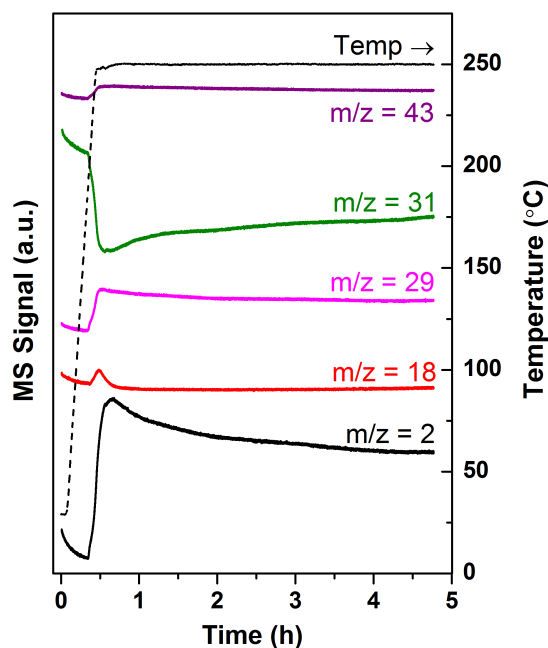


**Figure 6.18** Product evolution during ethanol dehydrogenation reaction on npNiCu immediately after O<sub>2</sub> treatment using the flow reactor monitored by an RGA as the

temperature is being ramped to 250 °C from RT in 6% ethanol at 50 mL min<sup>-1</sup>, revealing the production of acetaldehyde and hydrogen (not detected by GC-MS) and the transient production of H<sub>2</sub>O corresponding to reduction of copper oxide at the surface.

**Table 6.4** Quantification of ex situ XPS

<b>Ex-situ XPS after each specified treatment</b>			
<b>Crushed (cross section)</b>	<b>Cu%</b>	<b>Ni%</b>	<b>Zn%</b>
0, As prepared	92.5	1.5	6.0
1, H <sub>2</sub>	85.8	4.0	10.2
2a, Ethanol Reaction (40h, <b>Deactivated</b> )	86.8	5.0	8.2
2b, H <sub>2</sub> → O <sub>2</sub>	95.4	2.2	2.5
3b, Ethanol Reaction (1h)	67.7	14.4	17.9
4b, Ethanol Reaction (40h, <b>Active</b> )	68.3	10.5	21.2
5b, H <sub>2</sub> and Reaction (40h, <b>Deactivated</b> )	80.0	7.8	12.2

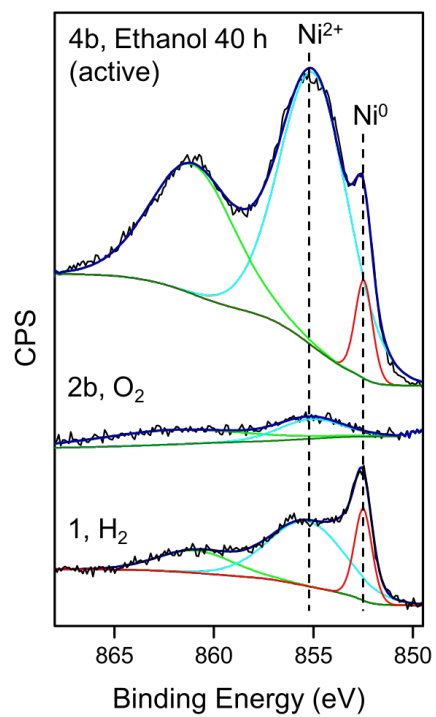


**Figure 6.19** Fitting of select Ni ex situ XPS spectra to show Ni<sup>0</sup> and Ni<sup>2+</sup> components

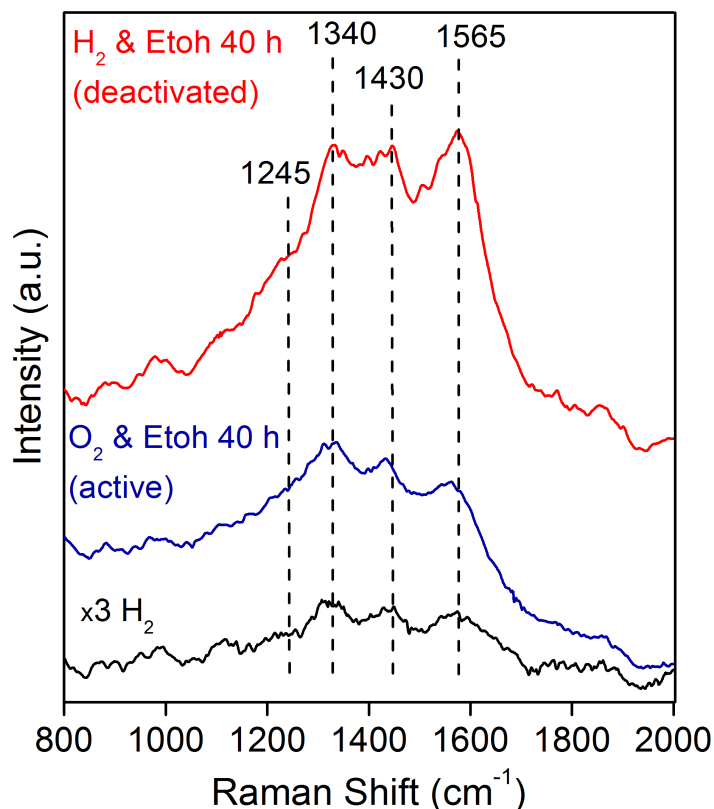


**Figure 6.20** Raman spectra (800-2000 cm<sup>-1</sup> region) of H<sub>2</sub>-treated npNiCu (black), O<sub>2</sub>-treated npNiCu after 40 h reaction (dark blue), and H<sub>2</sub>-treated npNiCu after 40 h reaction (red).

## 6.7 References

1. Eckert, M.; Fleischmann, G.; Jira, R.; Bolt, H. M.; Golka, K., Acetaldehyde. In *Ullmann's Encyclopedia of Industrial Chemistry*, Wiley-VCH Verlag GmbH & Co. KGaA: 2000.
2. Hagemeyer, H. J.; Staff, U. b., Acetaldehyde. In *Kirk-Othmer Encyclopedia of Chemical Technology*, John Wiley & Sons, Inc.: 2000.
3. Inui, K.; Kurabayashi, T.; Sato, S., Direct synthesis of ethyl acetate from ethanol over Cu-Zn-Zr-Al-O catalyst. *Applied Catalysis A: General* **2002**, 237 (1), 53-61.

4. Gao, D.; Feng, Y.; Yin, H.; Wang, A.; Jiang, T., Coupling reaction between ethanol dehydrogenation and maleic anhydride hydrogenation catalyzed by Cu/Al<sub>2</sub>O<sub>3</sub>, Cu/ZrO<sub>2</sub>, and Cu/ZnO catalysts. *Chemical Engineering Journal* **2013**, *233*, 349-359.
5. Jung, K.-D.; Joo, O.-S.; Han, S.-H.; Uhm, S.-J.; Chung, I.-J., Deactivation of Cu/ZnO catalyst during dehydrogenation of methanol. *Catalysis Letters* **1995**, *35* (3), 303-311.
6. Mušič, A.; Batista, J.; Levec, J., Gas-phase catalytic dehydrogenation of methanol to formaldehyde over ZnO/SiO<sub>2</sub> based catalysts, zeolites, and phosphates. *Applied Catalysis A: General* **1997**, *165* (1), 115-131.
7. Carotenuto, G.; Kumar, A.; Miller, J.; Mukasyan, A.; Santacesaria, E.; Wolf, E. E., Hydrogen production by ethanol decomposition and partial oxidation over copper/copper-chromite based catalysts prepared by combustion synthesis. *Catalysis Today* **2013**, *203*, 163-175.
8. Inui, K.; Kurabayashi, T.; Sato, S., Direct Synthesis of Ethyl Acetate from Ethanol Carried Out under Pressure. *Journal of Catalysis* **2002**, *212* (2), 207-215.
9. Fridman, V. Z.; Davydov, A. A., Dehydrogenation of Cyclohexanol on Copper-Containing Catalysts. *Journal of Catalysis* **2000**, *195* (1), 20-30.
10. Witzke, M. E.; Dietrich, P. J.; Ibrahim, M. Y. S.; Al-Bardan, K.; Triezenberg, M. D.; Flaherty, D. W., Spectroscopic evidence for origins of size and support effects on selectivity of Cu nanoparticle dehydrogenation catalysts. *Chemical Communications* **2017**, *53* (3), 597-600.
11. Iwasa, N.; Takezawa, N., Reforming of Ethanol –Dehydrogenation to Ethyl Acetate and Steam Reforming to Acetic Acid over Copper-Based Catalysts–. *Bulletin of the Chemical Society of Japan* **1991**, *64* (9), 2619-2623.
12. Colley, S. W.; Tabatabaei, J.; Waugh, K. C.; Wood, M. A., The detailed kinetics and mechanism of ethyl ethanoate synthesis over a Cu/Cr<sub>2</sub>O<sub>3</sub> catalyst. *Journal of Catalysis* **2005**, *236* (1), 21-33.
13. Cassinelli, W. H.; Martins, L.; Passos, A. R.; Pulcinelli, S. H.; Rochet, A.; Briois, V.; Santilli, C. V., Correlation between Structural and Catalytic Properties of Copper Supported on Porous Alumina for the Ethanol Dehydrogenation Reaction. *ChemCatChem* **2015**, *7* (11), 1668-1677.
14. Freitas, I. C.; Damyanova, S.; Oliveira, D. C.; Marques, C. M. P.; Bueno, J. M. C., Effect of Cu content on the surface and catalytic properties of Cu/ZrO<sub>2</sub> catalyst for ethanol dehydrogenation. *Journal of Molecular Catalysis A: Chemical* **2014**, *381*, 26-37.

15. Sato, A. G.; Volanti, D. P.; de Freitas, I. C.; Longo, E.; Bueno, J. M. C., Site-selective ethanol conversion over supported copper catalysts. *Catalysis Communications* **2012**, *26*, 122-126.
16. Cassinelli, W. H.; Martins, L.; Magnani, M.; Pulcinelli, S. H.; Briois, V.; Santilli, C. V., Time-resolved XAS/MS/Raman monitoring of mutual copper self-reduction and ethanol dehydrogenation reactions. *RSC Advances* **2016**, *6* (25), 20453-20457.
17. Wang, Z.-T.; Xu, Y.; El-Soda, M.; Lucci, F. R.; Madix, R. J.; Friend, C. M.; Sykes, E. C. H., Surface Structure Dependence of the Dry Dehydrogenation of Alcohols on Cu(111) and Cu(110). *The Journal of Physical Chemistry C* **2017**, *121* (23), 12800-12806.
18. Bowker, M.; Madix, R. J., XPS, UPS and thermal desorption studies of alcohol adsorption on Cu(110) II. Higher Alcohols. *Surface Science* **1982**, *116* (3), 549-572.
19. Bowker, M.; Madix, R. J., XPS, UPS and thermal desorption studies of alcohol adsorption on Cu(110) I. Methanol. *Surface Science* **1980**, *95* (1), 190-206.
20. Wachs, I. E.; Madix, R. J., The selective oxidation of CH<sub>3</sub>OH to H<sub>2</sub>CO on a copper(110) catalyst. *Journal of Catalysis* **1978**, *53* (2), 208-227.
21. Sexton, B. A.; Hughes, A. E.; Avery, N. R., Surface intermediates in the reaction of methanol, formaldehyde and methyl formate on copper (110). *Applications of Surface Science* **1985**, *22*, 404-414.
22. Chladek, P.; Croiset, E.; Epling, W.; Hudgins, R. R., Characterization of Copper Foam as Catalytic Material in Ethanol Dehydrogenation. *The Canadian Journal of Chemical Engineering* **2007**, *85* (6), 917-924.
23. Tu, Y.-J.; Chen, Y.-W., Effects of Alkali Metal Oxide Additives on Cu/SiO<sub>2</sub> Catalyst in the Dehydrogenation of Ethanol. *Industrial & Engineering Chemistry Research* **2001**, *40* (25), 5889-5893.
24. Shiau, C.-Y.; Chen, S.; Tsai, J. C.; Lin, S. I., Effect of zinc addition on copper catalyst in isoamyl alcohol dehydrogenation. *Applied Catalysis A: General* **2000**, *198* (1), 95-102.
25. Redina, E. A.; Greish, A. A.; Mishin, I. V.; Kapustin, G. I.; Tkachenko, O. P.; Kirichenko, O. A.; Kustov, L. M., Selective oxidation of ethanol to acetaldehyde over Au-Cu catalysts prepared by a redox method. *Catalysis Today* **2015**, *241*, 246-254.
26. Bauer, J. C.; Veith, G. M.; Allard, L. F.; Oyola, Y.; Overbury, S. H.; Dai, S., Silica-Supported Au-CuO<sub>x</sub> Hybrid Nanocrystals as Active and Selective Catalysts for the Formation of Acetaldehyde from the Oxidation of Ethanol. *ACS Catalysis* **2012**, *2* (12), 2537-2546.



27. Wang, Y.; Shi, L.; Lu, W.; Sun, Q.; Wang, Z.; Zhi, C.; Lu, A.-H., Spherical Boron Nitride Supported Gold–Copper Catalysts for the Low-Temperature Selective Oxidation of Ethanol. *ChemCatChem* **2017**, 9 (8), 1363-1367.
28. Homs, N.; Llorca, J.; de la Piscina, P. R., Low-temperature steam-reforming of ethanol over ZnO-supported Ni and Cu catalysts. *Catalysis Today* **2006**, 116 (3), 361-366.
29. Galetti, A. E.; Gomez, M. F.; Arrua, L. A.; Marchi, A. J.; Abello, M. C., Study of CuCoZnAl oxide as catalyst for the hydrogen production from ethanol reforming. *Catalysis Communications* **2008**, 9 (6), 1201-1208.
30. Resini, C.; Concepción Herrera Delgado, M.; Presto, S.; Alemany, L. J.; Riani, P.; Marazza, R.; Ramis, G.; Busca, G., Ytria-stabilized zirconia (YSZ) supported Ni–Co alloys (precursor of SOFC anodes) as catalysts for the steam reforming of ethanol. *International Journal of Hydrogen Energy* **2008**, 33 (14), 3728-3735.
31. He, L.; Berntsen, H.; Ochoa-Fernández, E.; Walmsley, J. C.; Blekkan, E. A.; Chen, D., Co–Ni Catalysts Derived from Hydrotalcite-Like Materials for Hydrogen Production by Ethanol Steam Reforming. *Topics in Catalysis* **2009**, 52 (3), 206-217.
32. Mariño, F.; Boveri, M.; Baronetti, G.; Laborde, M., Hydrogen production from steam reforming of bioethanol using Cu/Ni/K/ $\gamma$ -Al<sub>2</sub>O<sub>3</sub> catalysts. Effect of Ni. *International Journal of Hydrogen Energy* **2001**, 26 (7), 665-668.
33. Velu, S.; Suzuki, K.; Vijayaraj, M.; Barman, S.; Gopinath, C. S., In situ XPS investigations of Cu<sub>1-x</sub>Ni<sub>x</sub>ZnAl-mixed metal oxide catalysts used in the oxidative steam reforming of bio-ethanol. *Applied Catalysis B: Environmental* **2005**, 55 (4), 287-299.
34. Vizcaíno, A. J.; Carrero, A.; Calles, J. A., Hydrogen production by ethanol steam reforming over Cu–Ni supported catalysts. *International Journal of Hydrogen Energy* **2007**, 32 (10), 1450-1461.
35. Fierro, V.; Akdim, O.; Mirodatos, C., On-board hydrogen production in a hybrid electric vehicle by bio-ethanol oxidative steam reforming over Ni and noble metal based catalysts. *Green Chemistry* **2003**, 5 (1), 20-24.
36. Mariño, F. J.; Cerrella, E. G.; Duhalde, S.; Jobbagy, M.; Laborde, M. A., Hydrogen from steam reforming of ethanol. characterization and performance of copper-nickel supported catalysts. *International Journal of Hydrogen Energy* **1998**, 23 (12), 1095-1101.

37. Velu, S.; Satoh, N.; Gopinath, C. S.; Suzuki, K., Oxidative Reforming of Bio-Ethanol Over CuNiZnAl Mixed Oxide Catalysts for Hydrogen Production. *Catalysis Letters* **2002**, *82* (1), 145-152.
38. Anjaneyulu, C.; Costa, L. O. O. d.; Ribeiro, M. C.; Rabelo-Neto, R. C.; Mattos, L. V.; Venugopal, A.; Noronha, F. B., Effect of Zn addition on the performance of Ni/Al<sub>2</sub>O<sub>3</sub> catalyst for steam reforming of ethanol. *Applied Catalysis A: General* **2016**, *519*, 85-98.
39. Barroso, M. N.; Gomez, M. F.; Arrúa, L. A.; Abello, M. C., Hydrogen production by ethanol reforming over NiZnAl catalysts. *Applied Catalysis A: General* **2006**, *304*, 116-123.
40. Galetti, A. E.; Gomez, M. F.; Arrúa, L. A.; Abello, M. C., Hydrogen production by ethanol reforming over NiZnAl catalysts. *Applied Catalysis A: General* **2008**, *348* (1), 94-102.
41. Casanovas, A.; Llorca, J.; Homs, N.; Fierro, J. L. G.; Ramírez de la Piscina, P., Ethanol reforming processes over ZnO-supported palladium catalysts: Effect of alloy formation. *Journal of Molecular Catalysis A: Chemical* **2006**, *250* (1), 44-49.
42. Mironova, E. Y.; Lytkina, A. A.; Ermilova, M. M.; Efimov, M. N.; Zemtsov, L. M.; Orekhova, N. V.; Karpacheva, G. P.; Bondarenko, G. N.; Muraviev, D. N.; Yaroslavtsev, A. B., Ethanol and methanol steam reforming on transition metal catalysts supported on detonation synthesis nanodiamonds for hydrogen production. *International Journal of Hydrogen Energy* **2015**, *40* (8), 3557-3565.
43. Örucü, E.; Gökalliler, F.; Aksoylu, A. E.; Önsan, Z. I., Ethanol Steam Reforming for Hydrogen Production over Bimetallic Pt-Ni/Al<sub>2</sub>O<sub>3</sub>. *Catalysis Letters* **2008**, *120* (3), 198-203.
44. Sanchez-Sanchez, M. C.; Navarro Yerga, R. M.; Kondarides, D. I.; Verykios, X. E.; Fierro, J. L. G., Mechanistic Aspects of the Ethanol Steam Reforming Reaction for Hydrogen Production on Pt, Ni, and PtNi Catalysts Supported on  $\gamma$ -Al<sub>2</sub>O<sub>3</sub>. *The Journal of Physical Chemistry A* **2010**, *114* (11), 3873-3882.
45. Bi, J.-L.; Hong, Y.-Y.; Lee, C.-C.; Yeh, C.-T.; Wang, C.-B., Novel zirconia-supported catalysts for low-temperature oxidative steam reforming of ethanol. *Catalysis Today* **2007**, *129* (3), 322-329.
46. Freitas, I. C.; Gallo, J. M. R.; Bueno, J. M. C.; Marques, C. M. P., The Effect of Ag in the Cu/ZrO<sub>2</sub> Performance for the Ethanol Conversion. *Topics in Catalysis* **2016**, *59* (2), 357-365.
47. Iwasa, N.; Yamamoto, O.; Tamura, R.; Nishikubo, M.; Takezawa, N., Difference in the reactivity of acetaldehyde intermediates in the dehydrogenation of ethanol over supported Pd catalysts. *Catalysis Letters* **1999**, *62* (2), 179-184.

48. Jeroro, E.; Vohs, J. M., Exploring the Role of Zn in PdZn Reforming Catalysts: Adsorption and Reaction of Ethanol and Acetaldehyde on Two-dimensional PdZn Alloys. *The Journal of Physical Chemistry C* **2009**, *113* (4), 1486-1494.
49. Sanchez, A. B.; Homs, N.; Miachon, S.; Dalmon, J.-A.; Fierro, J. L. G.; Ramirez de la Piscina, P., Direct transformation of ethanol into ethyl acetate through catalytic membranes containing Pd or Pd-Zn: comparison with conventional supported catalysts. *Green Chemistry* **2011**, *13* (9), 2569-2575.
50. Personick, M. L.; Madix, R. J.; Friend, C. M., Selective Oxygen-Assisted Reactions of Alcohols and Amines Catalyzed by Metallic Gold: Paradigms for the Design of Catalytic Processes. *ACS Catalysis* **2017**, *7* (2), 965-985.
51. Zugic, B.; Karakalos, S.; Stowers, K. J.; Biener, M. M.; Biener, J.; Madix, R. J.; Friend, C. M., Continuous Catalytic Production of Methyl Acrylates from Unsaturated Alcohols by Gold: The Strong Effect of C-C Unsaturation on Reaction Selectivity. *ACS Catalysis* **2016**, *6* (3), 1833-1839.
52. Wang, L.-C.; Stowers, K. J.; Zugic, B.; Biener, M. M.; Biener, J.; Friend, C. M.; Madix, R. J., Methyl ester synthesis catalyzed by nanoporous gold: from 10<sup>-9</sup> Torr to 1 atm. *Catalysis Science & Technology* **2015**, *5* (2), 1299-1306.
53. Zugic, B.; Wang, L.; Heine, C.; Zakharov, D. N.; Lechner, B. A. J.; Stach, E. A.; Biener, J.; Salmeron, M.; Madix, R. J.; Friend, C. M., Dynamic restructuring drives catalytic activity on nanoporous gold-silver alloy catalysts. *Nat Mater* **2017**, *16* (5), 558-564.
54. Boucher, M. B.; Zugic, B.; Cladaras, G.; Kammert, J.; Marcinkowski, M. D.; Lawton, T. J.; Sykes, E. C. H.; Flytzani-Stephanopoulos, M., Single atom alloy surface analogs in Pd<sub>0.18</sub>Cu<sub>15</sub> nanoparticles for selective hydrogenation reactions. *Physical Chemistry Chemical Physics* **2013**, *15* (29), 12187-12196.
55. Lucci, F. R.; Liu, J.; Marcinkowski, M. D.; Yang, M.; Allard, L. F.; Flytzani-Stephanopoulos, M.; Sykes, E. C. H., Selective hydrogenation of 1,3-butadiene on platinum-copper alloys at the single-atom limit. **2015**, *6*, 8550.
56. Shan, J.; Lucci, F. R.; Liu, J.; El-Soda, M.; Marcinkowski, M. D.; Allard, L. F.; Sykes, E. C. H.; Flytzani-Stephanopoulos, M., Water co-catalyzed selective dehydrogenation of methanol to formaldehyde and hydrogen. *Surface Science* **2016**, *650*, 121-129.
57. Marcinkowski, M. D.; Liu, J.; Murphy, C. J.; Liriano, M. L.; Wasio, N. A.; Lucci, F. R.; Flytzani-Stephanopoulos, M.; Sykes, E. C. H., Selective Formic Acid Dehydrogenation on Pt-Cu Single-Atom Alloys. *ACS Catalysis* **2017**, *7* (1), 413-420.

58. Shan, J.; Janvelyan, N.; Li, H.; Liu, J.; Egle, T. M.; Ye, J.; Biener, M. M.; Biener, J.; Friend, C. M.; Flytzani-Stephanopoulos, M., Selective non-oxidative dehydrogenation of ethanol to acetaldehyde and hydrogen on highly dilute NiCu alloys. *Applied Catalysis B: Environmental* **2017**, *205*, 541-550.
59. Biesinger, M. C.; Lau, L. W. M.; Gerson, A. R.; Smart, R. S. C., Resolving surface chemical states in XPS analysis of first row transition metals, oxides and hydroxides: Sc, Ti, V, Cu and Zn. *Applied Surface Science* **2010**, *257* (3), 887-898.
60. Yeh, J. J. L., I., Atomic Subshell Photoionization Cross Sections and Asymmetry Parameters:  $1 < Z < 103$ . *Atomic Data and Nuclear Data Tables* **1985**, *33*, 1-155.
61. Kresse, G.; Furthmüller, J., Efficiency of ab-initio total energy calculations for metals and semiconductors using a plane-wave basis set. *Computational Materials Science* **1996**, *6* (1), 15-50.
62. Kresse, G.; Hafner, J., Ab initio molecular dynamics for liquid metals. *Physical Review B* **1993**, *47* (1), 558-561.
63. Perdew, J. P.; Burke, K.; Ernzerhof, M., Generalized Gradient Approximation Made Simple. *Physical Review Letters* **1996**, *77* (18), 3865-3868.
64. Kresse, G.; Joubert, D., From ultrasoft pseudopotentials to the projector augmented-wave method. *Physical Review B* **1999**, *59* (3), 1758-1775.
65. Blöchl, P. E., Projector augmented-wave method. *Physical Review B* **1994**, *50* (24), 17953-17979.
66. Tkatchenko, A.; Scheffler, M., Accurate Molecular Van Der Waals Interactions from Ground-State Electron Density and Free-Atom Reference Data. *Physical Review Letters* **2009**, *102* (7), 073005.
67. Hautier, G.; Ong, S. P.; Jain, A.; Moore, C. J.; Ceder, G., Accuracy of density functional theory in predicting formation energies of ternary oxides from binary oxides and its implication on phase stability. *Physical Review B* **2012**, *85* (15), 155208.
68. Rocquefelte, X.; Whangbo, M. H.; Villesuzanne, A.; Jobic, S.; Tran, F.; Schwarz, K.; Blaha, P., Short-range magnetic order and temperature-dependent properties of cupric oxide. *Journal of Physics: Condensed Matter* **2010**, *22* (4), 045502.
69. Marchi, A. J.; Fierro, J. L. G.; Santamaría, J.; Monzon, A., *Dehydrogenation of isopropyl alcohol on a Cu/SiO<sub>2</sub> catalyst: A study of the activity evolution and reactivation of the catalyst*. 1996; Vol. 142, p 375-386.

70. Hølse, C.; Elkjær, C. F.; Nierhoff, A.; Sehested, J.; Chorkendorff, I.; Helveg, S.; Nielsen, J. H., Dynamic Behavior of CuZn Nanoparticles under Oxidizing and Reducing Conditions. *The Journal of Physical Chemistry C* **2015**, *119* (5), 2804-2812.
71. Montero, C.; Ochoa, A.; Castaño, P.; Bilbao, J.; Gayubo, A. G., Monitoring NiO and coke evolution during the deactivation of a Ni/La<sub>2</sub>O<sub>3</sub>- $\alpha$ -Al<sub>2</sub>O<sub>3</sub> catalyst in ethanol steam reforming in a fluidized bed. *Journal of Catalysis* **2015**, *331*, 181-192.
72. Vicente, J.; Montero, C.; Ereña, J.; Azkoiti, M. J.; Bilbao, J.; Gayubo, A. G., Coke deactivation of Ni and Co catalysts in ethanol steam reforming at mild temperatures in a fluidized bed reactor. *International Journal of Hydrogen Energy* **2014**, *39* (24), 12586-12596.
73. Egle, T.; Barroo, C.; Janvelyan, N.; Baumgaertel, A. C.; Akey, A. J.; Biener, M. M.; Friend, C. M.; Bell, D. C.; Biener, J., Multiscale Morphology of Nanoporous Copper Made from Intermetallic Phases. *ACS Applied Materials & Interfaces* **2017**, *9* (30), 25615-25622.
74. Shan, J.; Liu, J.; Li, M.; Lustig, S.; Lee, S.; Flytzani-Stephanopoulos, M., NiCu single atom alloys catalyze the CH bond activation in the selective non-oxidative ethanol dehydrogenation reaction. *Applied Catalysis B: Environmental* **2018**, *226*, 534-543.
75. Chen, C.-Y. Catalyst regeneration via reduction with hydrogen. U.S. Patent 6,632,765 B1, October 14, 2003.
76. Kuld, S.; Thorhauge, M.; Falsig, H.; Elkjær, C. F.; Helveg, S.; Chorkendorff, I.; Sehested, J., Quantifying the promotion of Cu catalysts by ZnO for methanol synthesis. *Science* **2016**, *352* (6288), 969.
77. Kuld, S.; Conradsen, C.; Moses, P. G.; Chorkendorff, I.; Sehested, J., Quantification of Zinc Atoms in a Surface Alloy on Copper in an Industrial-Type Methanol Synthesis Catalyst. *Angewandte Chemie International Edition* **2014**, *53* (23), 5941-5945.
78. Pielsticker, L.; Zegkinoglou, I.; Divins, N. J.; Mistry, H.; Chen, Y.-T.; Kostka, A.; Boscoboinik, J. A.; Cuenya, B. R., Segregation Phenomena in Size-Selected Bimetallic CuNi Nanoparticle Catalysts. *The Journal of Physical Chemistry B* **2018**, *122* (2), 919-926.
79. Sinfelt, J. H.; Carter, J. L.; Yates, D. J. C., Catalytic hydrogenolysis and dehydrogenation over copper-nickel alloys. *Journal of Catalysis* **1972**, *24* (2), 283-296.
80. Coskun, F.; Cetinkaya, S.; Eroglu, S., Reduction of Nickel Oxide with Ethanol. *JOM* **2017**, *69* (6), 987-992.

81. Manukyan, K. V.; Avetisyan, A. G.; Shuck, C. E.; Chatilyan, H. A.; Rouvimov, S.; Kharatyan, S. L.; Mukasyan, A. S., Nickel Oxide Reduction by Hydrogen: Kinetics and Structural Transformations. *The Journal of Physical Chemistry C* **2015**, *119* (28), 16131-16138.
82. Jeangros, Q.; Hansen, T. W.; Wagner, J. B.; Damsgaard, C. D.; Dunin-Borkowski, R. E.; Hébert, C.; Van herle, J.; Hessler-Wyser, A., Reduction of nickel oxide particles by hydrogen studied in an environmental TEM. *Journal of Materials Science* **2013**, *48* (7), 2893-2907.
83. Castle, J. E.; Nasserian-Riabi, M., The oxidation of cupronickel alloys—I. XPS study of inter-diffusion. *Corrosion Science* **1975**, *15* (6), 537-543.
84. Castle, J. E., The oxidation of cupro-nickel alloys—II. The kinetics of diffusion in porous inner layers. *Corrosion Science* **1979**, *19* (7), 475-487.
85. Souchet, R. L., M.; Miche, P.; Weber, S.; Scherrer, S., Study of copper-nickel alloy oxidation by FTIR and SIMS. *Analisis* **1993**, *21*, 173-176.
86. Castle, J. E., Use of Shake-up Satellites in Photoelectron Spectra for Analysis of Oxide Layers on Metals. *Nature, Phys. Sci.* **1971**, *234*, 93.
87. Leapman, R. D.; Grunes, L. A.; Fejes, P. L., Study of the L23 edges in the 3d transition metals and their oxides by electron-energy-loss spectroscopy with comparisons to theory. *Physical Review B* **1982**, *26* (2), 614-635.
88. Kamiya, I.; Hashizume, T.; Sakai, A.; Sakurai, T.; Pickering, H., Chemisorption Induced Surface Segregation in Cu-Ni Alloys. *Journal de Physique Colloques* **1986**, *47* (C7), 195-201.
89. Tsong, T. T.; Ng, Y. S.; McLane, S. B. J., Surface segregation of Ni-Cu alloy in nitrogen and oxygen: An atom-probe field-ion microscope study. *Journal of Applied Physics* **1980**, *51* (12), 6189-6191.
90. Helms, C. R.; Yu, K. Y., Determination of the surface composition of the Cu-Ni alloys for clean and adsorbate-covered surfaces. *Journal of Vacuum Science and Technology* **1975**, *12* (1), 276-278.
91. Beaumont, S. K.; Alayoglu, S.; Pushkarev, V. V.; Liu, Z.; Kruse, N.; Somorjai, G. A., Exploring surface science and restructuring in reactive atmospheres of colloiddally prepared bimetallic CuNi and CuCo nanoparticles on SiO<sub>2</sub> in situ using ambient pressure X-ray photoelectron spectroscopy. *Faraday Discussions* **2013**, *162* (0), 31-44.

92. Takasu, Y.; Shimizu, H.; Maru, S.-i.; Matsuda, Y., Auger spectroscopic study on the surface composition of CuNi alloys oxidized with nitric oxide. *Surface Science* **1976**, *61* (1), 279-282.
93. Chen, C.-S.; You, J.-H.; Lin, J.-H.; Chen, C.-R.; Lin, K.-M., The effect of a nickel promoter on the reducibility of a commercial Cu/ZnO/Al<sub>2</sub>O<sub>3</sub> catalyst for CO oxidation. *Catalysis Communications* **2008**, *9* (6), 1230-1234.
94. Robertson, S. D.; McNicol, B. D.; De Baas, J. H.; Kloet, S. C.; Jenkins, J. W., Determination of reducibility and identification of alloying in copper-nickel-on-silica catalysts by temperature-programmed reduction. *Journal of Catalysis* **1975**, *37* (3), 424-431.
95. Kim, J. Y.; Rodriguez, J. A.; Hanson, J. C.; Frenkel, A. I.; Lee, P. L., Reduction of CuO and Cu<sub>2</sub>O with H<sub>2</sub>: H Embedding and Kinetic Effects in the Formation of Suboxides. *Journal of the American Chemical Society* **2003**, *125* (35), 10684-10692.
96. Rodriguez, J. A.; Kim, J. Y.; Hanson, J. C.; Pérez, M.; Frenkel, A. I., Reduction of CuO in H<sub>2</sub>: In Situ Time-Resolved XRD Studies. *Catalysis Letters* **2003**, *85* (3), 247-254.
97. Rodriguez, J. A.; Hanson, J. C.; Frenkel, A. I.; Kim, J. Y.; Pérez, M., Experimental and Theoretical Studies on the Reaction of H<sub>2</sub> with NiO: Role of O Vacancies and Mechanism for Oxide Reduction. *Journal of the American Chemical Society* **2002**, *124* (2), 346-354.
98. D'Addato, S.; Grillo, V.; Altieri, S.; Tondi, R.; Valeri, S.; Frabboni, S., Structure and stability of nickel/nickel oxide core-shell nanoparticles. *Journal of Physics: Condensed Matter* **2011**, *23* (17), 175003.
99. Prieto, P.; Nistor, V.; Nouneh, K.; Oyama, M.; Abd-Lefdil, M.; Díaz, R., XPS study of silver, nickel and bimetallic silver-nickel nanoparticles prepared by seed-mediated growth. *Applied Surface Science* **2012**, *258* (22), 8807-8813.
100. Großmann, K.; Dellermann, T.; Dillig, M.; Karl, J., Coking behavior of nickel and a rhodium based catalyst used in steam reforming for power-to-gas applications. *International Journal of Hydrogen Energy* **2017**, *42* (16), 11150-11158.
101. Wang, H.; Liu, Y.; Wang, L.; Qin, Y. N., Study on the carbon deposition in steam reforming of ethanol over Co/CeO<sub>2</sub> catalyst. *Chemical Engineering Journal* **2008**, *145*, 25-31.
102. Querini, C. A.; Fung, S. C., Temperature-programmed oxidation technique: kinetics of coke-O<sub>2</sub> reaction on supported metal catalysts. *Applied Catalysis A: General* **1994**, *117*, 53-74.

103. Hughes, R.; Parvinian, M., *Regeneration kinetics of coked silica-alumina catalyst*. 1989; Vol. 34.
104. Barbier, J.; Churin, E.; Parera, J. M.; Riviere, J., Characterization of coke by hydrogen and carbon analysis. *Reaction Kinetics and Catalysis Letters* **1985**, 29 (2), 323-330.
105. Tone, S.; Miura, S.-i.; Otake, T., Kinetics of Oxidation of Coke on Silica-Alumina Catalysts. *Bulletin of The Japan Petroleum Institute* **1972**, 14 (1), 76-82.
106. Nakasaka, Y.; Tago, T.; Konno, H.; Okabe, A.; Masuda, T., Kinetic study for burning regeneration of coked MFI-type zeolite and numerical modeling for regeneration process in a fixed-bed reactor. *Chemical Engineering Journal* **2012**, 207-208, 368-376.
107. Garcia-Calzada, R.; Rodio, M.; Bagga, K.; Intartaglia, R.; Bianchini, P.; Chirvony, V. S.; Martinez-Pastor, J. P., Facile laser-assisted synthesis of inorganic nanoparticles covered by a carbon shell with tunable luminescence. *RSC Advances* **2015**, 5 (62), 50604-50610.
108. Sadezky, A.; Muckenhuber, H.; Grothe, H.; Niessner, R.; Pöschl, U., Raman microspectroscopy of soot and related carbonaceous materials: Spectral analysis and structural information. *Carbon* **2005**, 43 (8), 1731-1742.
109. Zeng, G.; Liu, Q.; Gu, R.; Zhang, L.; Li, Y., Synergy effect of MgO and ZnO in a Ni/Mg-Zn-Al catalyst during ethanol steam reforming for H<sub>2</sub>-rich gas production. *Catalysis Today* **2011**, 178 (1), 206-213.
110. Cho, P.; Mattisson, T.; Lyngfelt, A., Carbon Formation on Nickel and Iron Oxide-Containing Oxygen Carriers for Chemical-Looping Combustion. *Industrial & Engineering Chemistry Research* **2005**, 44 (4), 668-676.
111. Frusteri, F.; Freni, S.; Chiodo, V.; Donato, S.; Bonura, G.; Cavallaro, S., Steam and auto-thermal reforming of bio-ethanol over MgO and CeO<sub>2</sub> Ni supported catalysts. *International Journal of Hydrogen Energy* **2006**, 31 (15), 2193-2199.



## Chapter 7.

# Structural Evolution of Nanoporous NiCu

### 7.1 Introduction

Nanoporous copper (npCu) is bimetallic alloy with small amounts of Zn that is active, selective, and stable for the ethanol dehydrogenation reaction. Nickel doping npCu to produce nanoporous nickel-copper (npNiCu) improves the activity for the reaction, though it reduces the stability of the catalyst during ethanol dehydrogenation reaction. By using an O<sub>2</sub> pretreatment instead of a H<sub>2</sub> pretreatment, the reduced stability of the npNiCu catalyst can be overcome (Chapter 6). X-ray photoelectron spectroscopy (XPS) studies demonstrated that Ni<sup>2+</sup> was a key component in sustaining activity, whereas Ni<sup>0</sup> was the culprit for carbon deposition and subsequent deactivation.

In this investigation, we demonstrate the structural changes npNiCu undergoes that lead to its deactivation (due to hydrogen pretreatment and subsequent reaction) or its improved activity (due to oxygen pretreatment and subsequent reduction by ethanol). While XPS provided the overall surface composition and oxidation states of the metal species on the surface, as it is an averaging technique, more local techniques are needed to provide insight into the local structures and compositions. Several imaging and related spectroscopic tools were used in this report to investigate the catalyst morphology and surface structures and how they may influence the activities observed. Both in situ and ex situ experiments were performed under similar conditions of pressure, gas composition, and temperature as

the XPS studies in Chapter 6 to directly correlate surface composition and structure to the catalytic activity.

We show that H<sub>2</sub> treatment creates dense, metallic Ni nanoparticles that deactivate the catalyst through carbon deposition, whereas O<sub>2</sub> treatment and subsequent reaction creates numerous NiO crystals at the surface that stabilize the catalytic activity and endure at the surface in a metastable state. The stability of this species is strongly linked to the reaction conditions which slow the reduction kinetics of NiO, preventing the creation of metallic Ni and deactivating the catalyst. Purposeful reduction of the active O<sub>2</sub>-treated catalyst, leads to deactivation through the aforementioned mechanism. This work demonstrates how the catalyst behavior can be manipulated using carefully chosen pretreatments and reaction conditions. In addition, this investigation demonstrates how catalyst activation is a critical step in the development of sustainable catalytic processes.

This chapter is to be adapted for publication.

## **7.2 Methods**

### **7.2.1 Ex situ Characterization Techniques**

All ex situ electron microscopy studies were conducted on npCu and npNiCu powder catalysts. See Chapter 6 (Section 6.3.1) for catalyst synthesis details and Chapter 2 for more microscopy details. To summarize, scanning electron microscopy (SEM) was performed using a Zeiss Supra55VP field-emission SEM equipped with an energy-dispersive X-ray spectroscopy (EDS) detector at the Center for Nanoscale Systems (CNS) at Harvard University. Scanning and transmission electron microscopy (STEM and TEM) along with EDS

mapping was performed using an aberration-corrected JEOL ARM 200F STEM at CNS as well as a FEI Talos F200X. To prepare TEM and STEM samples, powder samples were dispersed in deionized water and drop-casted onto lacey C/Au mesh grids from Ted Pella.

### **7.2.2 Environmental Transmission Electron Microscopy (E-TEM)**

Environmental-TEM (E-TEM) studies were conducted at the Center for Functional Nanomaterials (CFN) at Brookhaven National Laboratory (BNL) using a FEI Titan aberration-corrected TEM operating at 300 kV equipped with an electron energy loss spectrometer (EELS). The instrument has a base pressure of  $3\text{-}4 \cdot 10^{-7}$  Torr. As prepared npNiCu powder was dispersed in deionized water and drop-casted onto a DENS Solutions sample holder. After drying, the holder was inserted in the microscope. Gases and vapors were introduced into the microscope using a gas-handling manifold equipped with dosing valves. Gases were introduced into the sample stage area with the beam blanked. The sample was then heated to the specified temperatures and held for the treatment duration. After cooling, the gases were evacuated to vacuum pressure for imaging and EELS analysis. EELS spectra were analyzed using TEM Imaging and Analysis (TIA) software.

### **7.2.3 Surface Area Approximation**

Due to the low mass of catalyst yielded by the synthesis and used for catalytic testing, Brunauer-Emmett-Teller (BET) surface area measurements could not be conducted after each treatment. One BET measurement was conducted using N<sub>2</sub> adsorption on an as prepared npCu sample to yield a surface area of 2.7 m<sup>2</sup>/g. For npCu after a specified treatment, the ligament size was used to estimate the surface area of the nanoporous

structure following the published procedure<sup>1</sup>. The as prepared npCu sample was used as a reference to determine the dimensionless constant of the porous structure. To account for any spherical nanoparticles at the surface, the surface area per gram was calculated using the radius of the particle. The total surface area of the nanoporous structure and particles was then calculated by taking a weighted average with the number of particles and ligaments measured.

## **7.3 Results and Discussion**

### **7.3.1 Characterization of npCu**

As discussed in Chapter 6, npCu are active and stable for the ethanol dehydrogenation reaction regardless of H<sub>2</sub> or O<sub>2</sub> pretreatment. To understand the effect of each treatment and reaction on the morphology, the catalyst was characterized using SEM and TEM. As prepared npCu has an interconnected ligament and pore structure with a ligament size of  $135 \pm 35$  nm and a BET surface area of  $2.7 \text{ m}^2/\text{g}$  (Figure 7.1a). When npCu is H<sub>2</sub> treated in the flow reactor (350 °C, 1 h, 10 H<sub>2</sub>), the ligament size increases to  $295 \pm 75$  nm and the estimated surface area is  $2.2 \text{ m}^2/\text{g}$  (Figure 7.1b).

As discussed in Chapter 6, when the H<sub>2</sub>-treated npCu is exposed to ethanol dehydrogenation reaction, it is active and stable for the reaction for over 40 h on stream. After reaction, the catalyst was characterized and exhibited even larger ligaments of  $605 \pm 190$  nm with a range of smaller particles at its surface (Figure 7.1c). Incorporating the surface area of these smaller particles (black arrows, Figure 7.1c) in the surface area calculation, as described in Section 7.2, yielded a surface area of  $1.9 \text{ m}^2/\text{g}$ . The activity lost during reaction was determined to be insignificant in Chapter 6 (~7%), which corresponds

well with the  $\sim 9\%$  decrease in the surface area. Therefore, the exposed Cu surface area is responsible for the observed activity.

The SEM image of the H<sub>2</sub> and reaction exposed samples also exhibited small, white masses at its surface that were not present in the as prepared sample (white arrows, Figure 7.1c). TEM imaging of the reaction exposed sample revealed similar features. In the STEM and TEM images, masses are observed have a lower Z-contrast on the main Cu ligament,  $\sim 89 \pm 20$  nm in size (Figures 7.2a and 7.2b). Elemental mapping revealed that the masses correspond to ZnO (Figures 7.2b – 7.2f). Specifically, the Zn masses are ZnO as metallic Zn would have a higher Z-contrast similar to that of Cu and due to the high densities of oxygen that overlap with Zn in the oxygen elemental map (Figures 7.2e and 7.2f). In TEM images, some ZnO masses are crystalline, whereas others are amorphous (Figure 7.12). Analysis of the white masses in the SEM reveal sizes of  $83 \pm 40$  nm, corresponding well to the size measured in the STEM. Thus, the masses covering the surface in the SEM and TEM are ZnO. The presence of Zn/ZnO does not affect the activity of the catalyst (see Chapters 5 and 6).

Oxygen treatment of the npCu catalyst resulted in roughening of the surface likely due to copper oxide (Figure 7.1d). When returned to reaction conditions, the O<sub>2</sub>-treated npCu had short-lived enhancement, corresponding to the reduction of copper oxide, followed by a 15% increase in its baseline activity compared to the H<sub>2</sub>-treated catalyst (Chapter 6). This was attributed to the re-dispersion of Cu by the oxidation treatment. SEM analysis of the O<sub>2</sub> and reaction exposed npCu sample revealed more Cu nanoparticles that were also smaller in size at the surface of the nanoporous structure (black arrows, Figure 7.1e). TEM imaging also revealed small Cu particles ( $\sim 26$  nm in diameter) supported on the surface that was not observed on the H<sub>2</sub> pretreated catalyst after reaction (pink arrows, Figure 7.3a).

The small Cu particles seem to be supported on ZnO as this feature (0.71 nm in size) is similar to those observed in the TEM image of the H<sub>2</sub>-treated sample. Measurement of the lattice fringes in the crystalline mass also reveals a 0.26 nm interplanar spacing, which could correspond to ZnO (002). Given the similarity in size, crystalline nature, and Z-contrast to the H<sub>2</sub> pretreated sample after reaction, the masses are likely ZnO as well. The estimated surface area of the O<sub>2</sub>-treated catalyst after reaction is 2.6 m<sup>2</sup>/g, a 27% increase from the H<sub>2</sub>-treated npCu after reaction, which can be used to explain the 15% increase difference in activity. Although the estimated surface area is higher than the increase in activity, this could be due to ZnO blocking surface sites or the method used as it is a rough estimate of the surface area. Thus, the surface area increase is responsible for the increase in activity further confirming the re-dispersion of Cu by oxidation.

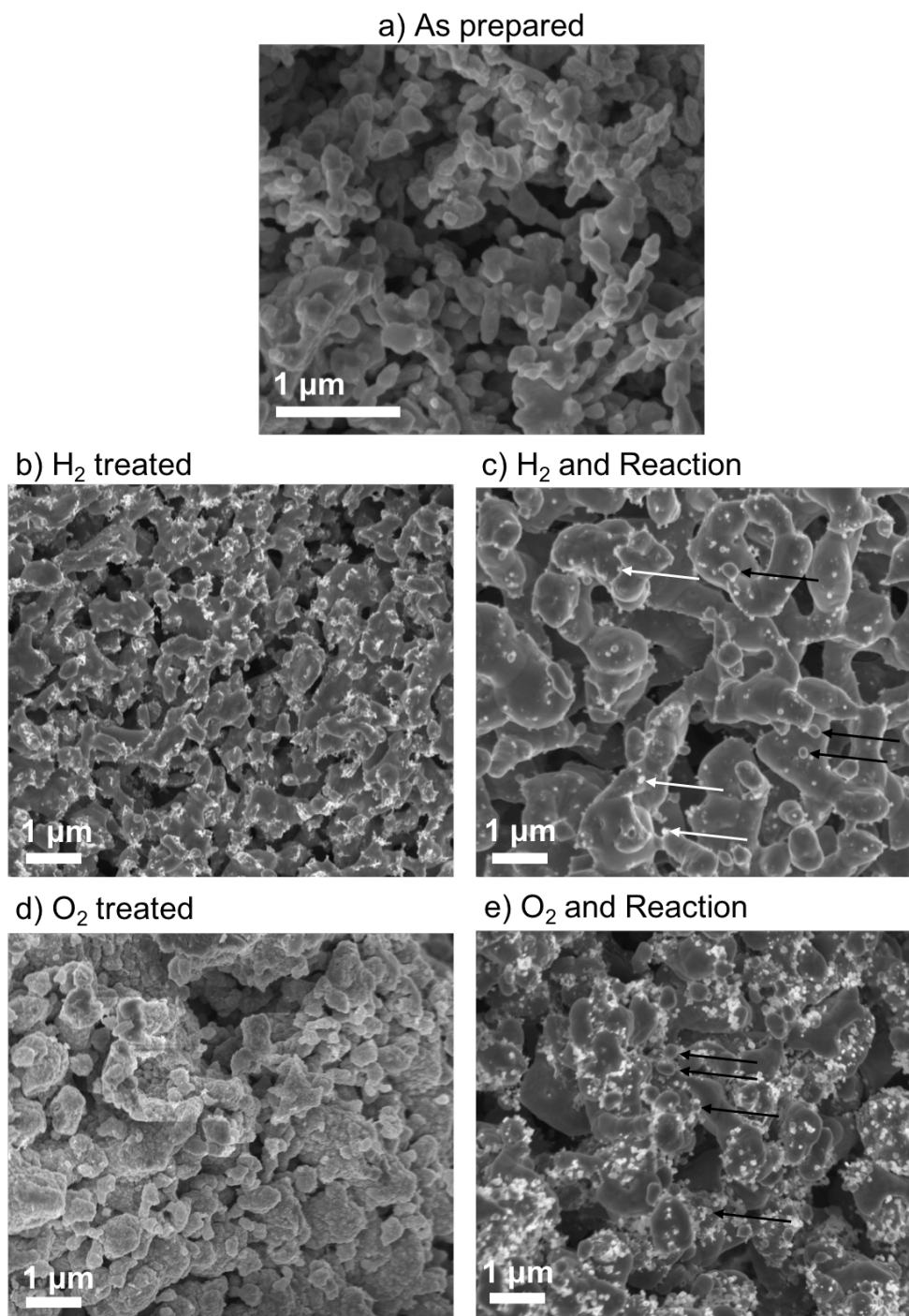


**Figure 7.1** Scanning electron microscopy (SEM) images of npCu a) as prepared npCu, b) H<sub>2</sub> treated, c) H<sub>2</sub> treated and exposed to ethanol dehydrogenation reaction for > 40 h, d) O<sub>2</sub> treated, and e) O<sub>2</sub> and reaction exposed for > 40 h. Both catalysts in c) and e) are active for the reaction (see Chapter 6). Black arrows indicate smaller Cu particles, whereas white

arrows indicate white masses. H<sub>2</sub> pretreatment: 350 °C, 1 h, 20 mL min<sup>-1</sup>, 10 vol.% hydrogen. O<sub>2</sub> pretreatment: 250 °C, 1 h, 50 mL min<sup>-1</sup>, 20 vol.% oxygen. Reaction conditions: 250 °C, > 40 h, 50 mL min<sup>-1</sup>, 6 vol.% ethanol.

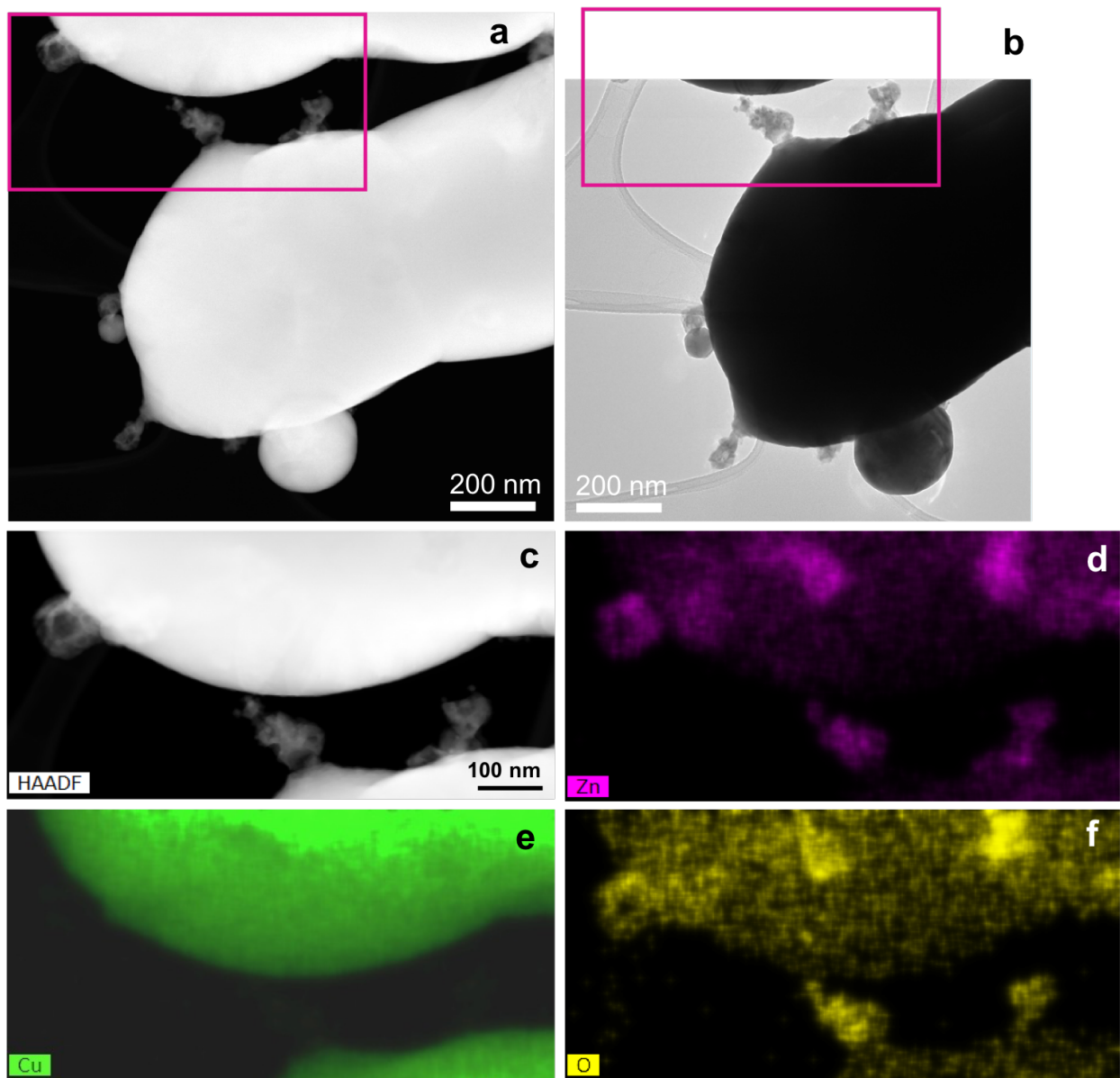


**Figure 7.2** a) High angle annular dark field (HAADF) STEM image and b) TEM image of npCu after H<sub>2</sub> and reaction. c) Higher magnification STEM of the region indicated in a) and b) and corresponding elemental maps of d) Zn, e) Cu, and f) O. The elemental maps identify the



crystalline masses with lower Z-contrast decorating the Cu ligament surface in the STEM images as ZnO.

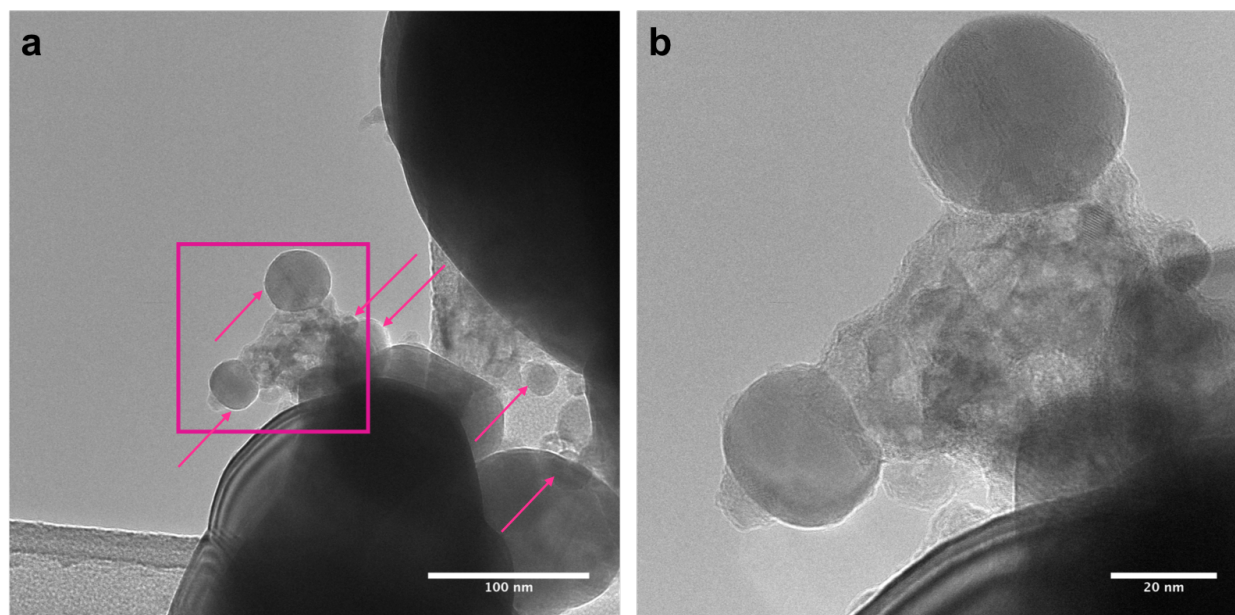


**Figure 7.3** a) TEM image of npCu after O<sub>2</sub> and reaction. Arrows indicate re-dispersed particles, ~26 nm in diameter. b) Higher magnification image of region indicated in a) illustrating the Cu nanoparticles supported on what is identified as ZnO due to its interplanar spacing, crystalline nature, and lower Z-contrast.

### 7.3.2 Characterization of H<sub>2</sub>-treated npNiCu

When nanoporous NiCu (npNiCu) is H<sub>2</sub>-treated and exposed to ethanol dehydrogenation reaction, it deactivates over a 30 to 40 h period. When it is O<sub>2</sub>-treated and exposed to reaction, it is stable in the reaction, losing only 15% of its activity in the same time period (Chapter 6). Characterization of the morphology was performed to see if changes in morphology and surface structure correlated with this difference in stability. SEM analysis

of H<sub>2</sub>-treated npNiCu revealed a ligament size of  $313 \pm 95$  nm (Figure 7.4a). H<sub>2</sub>-treated npNiCu also had white ZnO particles on its surface (in some areas more than others). H<sub>2</sub>-treated npNiCu has a similar surface area as H<sub>2</sub>-treated npCu, yet its initial activity was twice that the peak activity of npCu. This is due to the Ni-doping and not the surface area as Ni reduces the activation energy for the ethanol dehydrogenation reaction (Chapters 5 and 6).

TEM imaging revealed that the npNiCu had Ni nanoparticles at its surface. Using environmental TEM (E-TEM) and electron energy loss spectroscopy (EELS) Ni nanoparticles were identified on the surface of the as prepared (as loaded) sample. Zn cannot be detected by EELS due to overlap of the Cu and Zn L<sub>2,3</sub> edges. These particles were still present after H<sub>2</sub> treating in situ (1 h, 350 °C, 1 Torr) (Figures 7.5a – 7.5c). Parts of the Cu ligament edges also exhibited an amorphous layer or mass at the surface with a crystalline bulk (Figure 7.5d). The amorphous layer corresponds to an oxygen-deficient metal oxide likely ZnO as XPS studies determined that H<sub>2</sub> brings Zn to the surface and only partially reduces it (Chapter 6). The crystalline bulk has an interplanar spacing of 0.21 nm corresponding to Cu (111). Ex situ TEM imaging of H<sub>2</sub>-treated npNiCu also depicted particles at the surface (Figures 7.13a and 7.13b). It also depicted areas of amorphous material at the edge with some portions showing some crystallinity (Figure 7.13c). The correspondence between the in situ and ex situ H<sub>2</sub> treated sample indicates that the surface structure is stable regardless of air exposure.

Based on the Cu-Ni phase diagram, Cu and Ni phase separate at low temperatures below ~600 °C. Above these temperatures, Cu and Ni form a miscible alloy. At a bulk concentration of 3% Ni, the two-phase field lies at 400 °C and below. Thus, it is not surprising that the Cu and Ni phase separated in npNiCu, especially with 7% Ni at the surface after H<sub>2</sub> treatment<sup>2</sup>. The presence of Ni nanoparticles accounts for the Ni-like behavior observed such

as the production of CO and CH<sub>4</sub> as by-products. As Chapter 5 demonstrated, NiCu nanoparticles with 1% or less Ni do not produce CO as Ni is highly dispersed. When the Ni content is ~3%, the selectivity dropped and CO started being produced even at low temperatures indicating large Ni ensembles were present<sup>62</sup>. Large Ni ensembles or particles also favor carbon deposition which was also observed (Chapter 6)<sup>3-4</sup>. Previous studies of NiCu catalysts also observed that Cu and Ni mostly phase separate though a small fraction of the metals alloyed<sup>5-7</sup>. Even with the small fraction that alloyed, these studies observed an appreciable increase in the catalytic synthesis of dimethyl carbonate<sup>5</sup>, reverse water gas shift reaction<sup>6</sup>, and synthesis of methanol<sup>7</sup>. Due to the promotion of acetaldehyde production observed here, some NiCu alloy likely still occurs.

After reaction for over 40 h, the npNiCu completely deactivated, yet its ligament size only increased modestly to 420 ± 125 nm (Figure 7.4b). Other sample batches exhibited increased coarsening similar to that of npCu with smaller particles at the surface. Coarsening does not explain the complete deactivation of the npNiCu catalyst, while npCu was still stable in same time frame and for even longer periods.

Analysis of the surface structures reveal that the deactivated surface is decorated with Ni particles (Figure 7.6). The Cu has a clean edge where the particles sit on top of. The Ni is metallic from the density and high Z-contrast of the particles to which Ni corresponds to in the elemental map, also determined by the XPS studies in Chapter 6. Zn is more oxidized, though parts of it may be more reduced, as seen from the amorphous and low Z-contrast areas and the overlap of O, whereas some areas have higher densities of Zn in more particle forms which could indicate regions of more crystalline ZnO (Figure 7.6). The amorphous areas to which Zn corresponds are more apparent in the larger bright field and STEM images

of the area in Figure 7.14. It is apparent from the elemental maps that the Ni particles are in close contact with the Zn and seem to partially overlap. Some Ni is also dissolved in the Cu ligament, which could be the source of the initial enhanced activity compared to the npCu.

As discussed in Chapter 6, metallic Ni particles deposit carbon and deactivate catalysts through a Ni-carbide precursor<sup>3-4, 8-11</sup>, while Ni and Zn can form a  $\text{Ni}_3\text{ZnC}_{0.7}$  carbide<sup>8-9</sup> which would also lead to carbon deposition. Carbon deposition is apparent in the C elemental map as the carbon extends past the Cu edge and past some of the Ni and Zn particles filling some of the pore space (Figure 7.6). Another region at higher magnification better demonstrates the carbon deposition at the surface (Figure 7.15). This area shows a mass of material on the Cu surface mostly corresponding to carbon and oxygen and small amounts of Ni (Figure 7.15). The observation of carbon on the surface by EDS further supports the conclusion in Chapter 6 that the npNiCu deactivates due to carbon deposition.

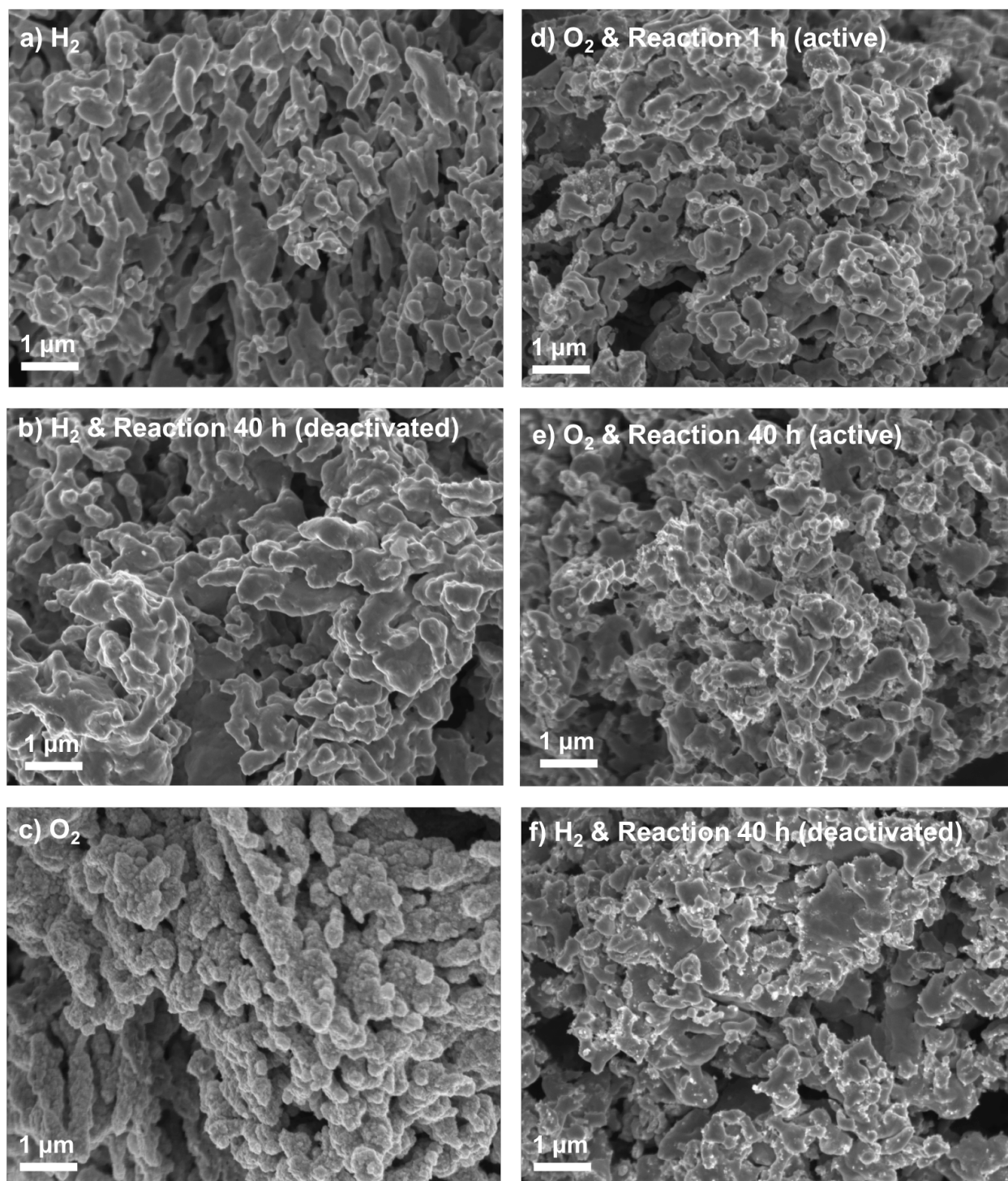


**Figure 7.4** SEM images of npNiCu a) H<sub>2</sub> treated, b) H<sub>2</sub> treated and exposed to ethanol dehydrogenation reaction for > 40 h (deactivated), c) H<sub>2</sub> and O<sub>2</sub> treated, d) O<sub>2</sub> and reaction

*Chapter 7. Structural Evolution of Nanoporous NiCu*

exposed for 1 h, e) O<sub>2</sub> and reaction exposed for > 40 h (active), and f) subsequently H<sub>2</sub> treated and exposed to reaction for ~30 h (deactivated). Figure nomenclature a-f follows that of 1-5b in Chapter 6, respectively. H<sub>2</sub> pretreatment: 350 °C, 1 h, 20 mL min<sup>-1</sup>, 10 vol.% hydrogen. O<sub>2</sub> pretreatment: 250 °C, 1 h, 50 mL min<sup>-1</sup>, 20 vol.% oxygen. Reaction conditions: 250 °C, > 40 h, 50 mL min<sup>-1</sup>, 6 vol.% ethanol.



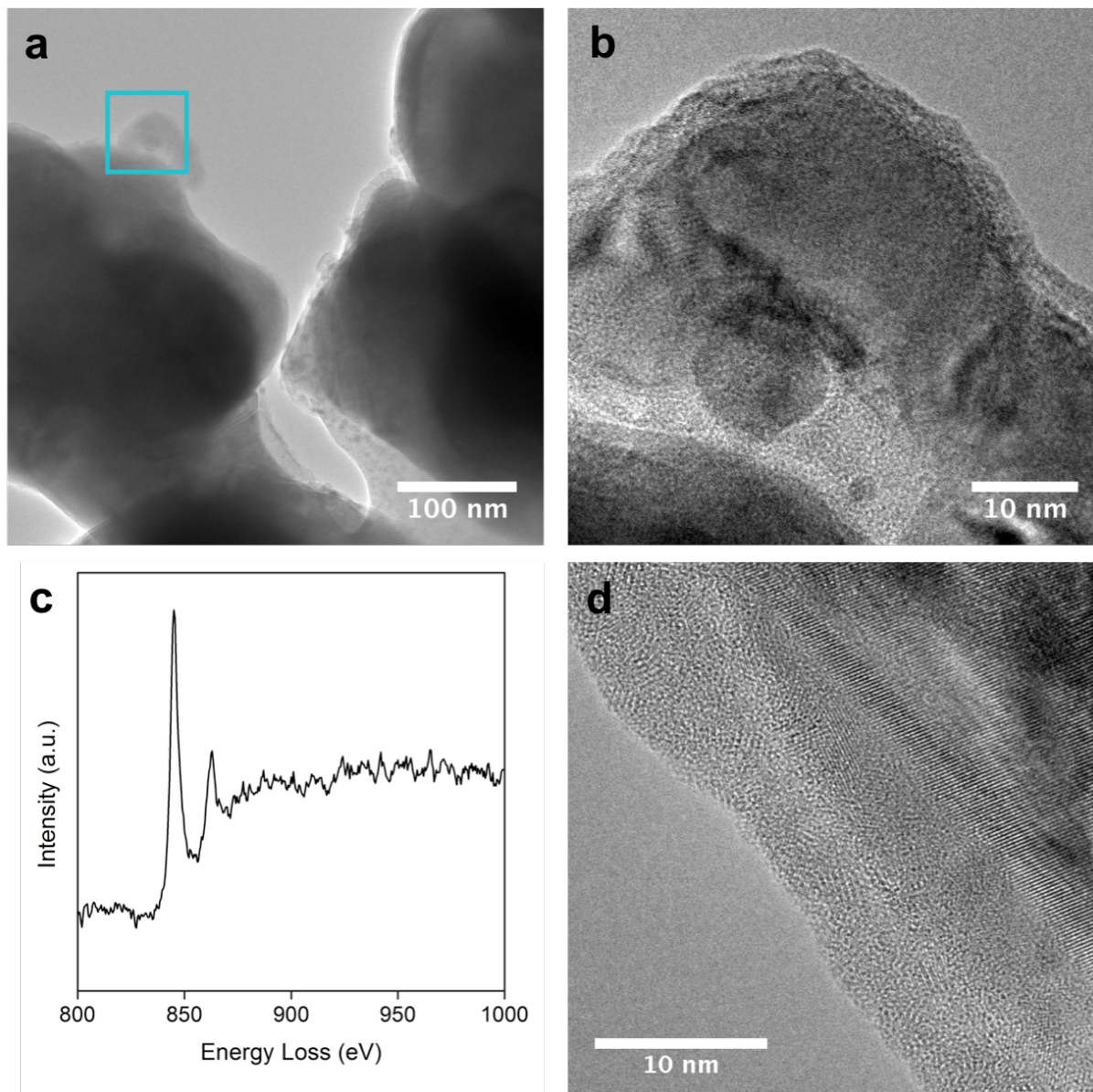


**Figure 7.5** a) E-TEM image of in situ H<sub>2</sub>-treated (1 h, 350 °C, 1 Torr) npNiCu. b) Higher magnification of particle indicated in a) and corresponding EELS spectrum identifying the particle as Ni. d) Edge of a Cu ligament showing an amorphous layer at its surface with a crystalline bulk.

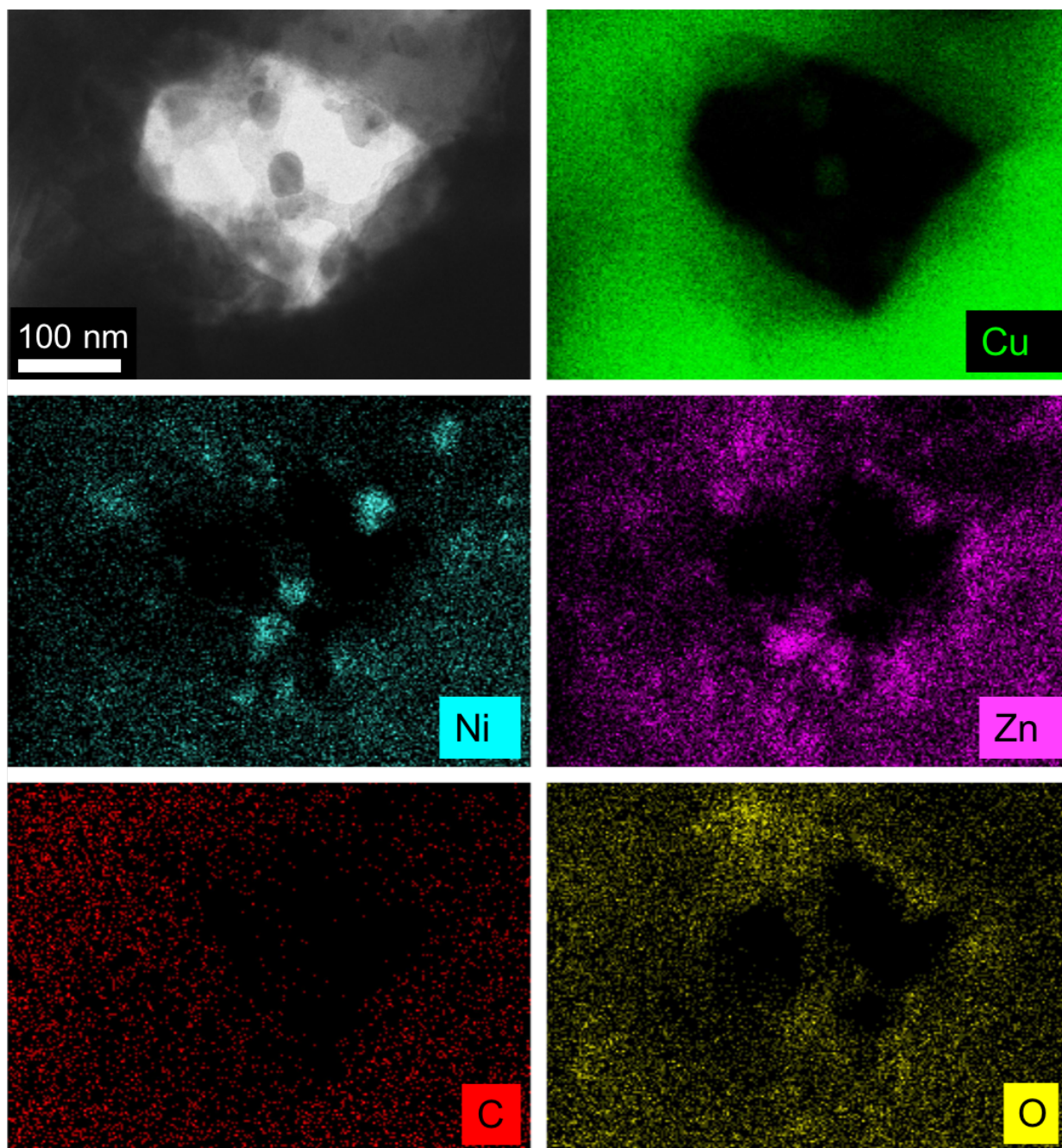


**Figure 7.6** Bright field image and elemental maps of a typical region in the H<sub>2</sub>-treated catalyst after deactivation showing Ni particles in close contact with Zn and an increase of carbon at the surface.



### 7.3.3 Characterization of O<sub>2</sub>-treated npNiCu

Oxygen treatment of npNiCu resulted in more stable activity for a long period of time than H<sub>2</sub>-treated npNiCu. Similar to npCu, O<sub>2</sub> treatment results in roughening of the npNiCu surface (Figures 7.4c and 7.7a). Ni particles are no longer observed at the surface after oxidation and the roughening can be attributed to the creation and growth of copper oxide crystallites in different orientations (Figure 7.7b). CuO and Cu<sub>2</sub>O have similar interplanar spacings so they cannot be used to identify oxide at the surface. However, XPS studies in Chapter 6 determined that CuO was at the surface after oxidation and that it overgrew the Ni and Zn at the surface as determined by E-TEM and XPS. To expand further, after 10 minutes of in situ oxidation (250 °C, 1 Torr), copper oxide can already be observed at the Cu ligament edge (Figure 7.15a). However, it was only after a full hour of oxidation (250 °C, 1 Torr), that complete overgrowth of Ni by Cu oxide was observed (Figures 7.15b and 7.15c). The correspondence between the ex situ and in situ oxidized npNiCu samples demonstrates that the surface structure is stable.

Immediately after oxidation, O<sub>2</sub>-treated npNiCu exhibits a short enhancement in activity, ~1-2 h, similar to npCu, corresponding to the reduction of copper oxide at the surface. Thus, the corresponding roughening by copper oxide subsides and smooth ligaments return to the surface after 1 h of reaction (Figure 7.4d). After the 1 h of reaction, the catalyst has similar sized ligaments as the H<sub>2</sub>-treated catalyst, but with numerous small particles at its surface, which may be attributed to the re-dispersion of Cu by oxidation such as in npCu (Figure 7.4d).

Both in situ and ex situ XPS studies demonstrated that Ni and Zn return to the surface after 1 h of reaction and that Ni is still oxidized (Chapter 6). TEM analysis demonstrates that

Ni and Zn return in the form of NiO and ZnO particles at the surface of a typical region (Figure 7.8). The elemental map of Ni shows two Ni particles and one Zn particle. The oxygen encompasses both particles and XPS studies determined Ni is an oxide after oxidation and reaction. It is clear that the Ni in lower corner purely Ni. However, it is difficult to confirm if separate overlapping NiO and ZnO particles coexist in the larger particle located in the upper right or if it is a NiZn alloy. Because Ni in the upper right region is not as fully dense as the Zn, it is more likely that two separate particles of each overlap. In other regions, Cu nanoparticles can also be observed at the surface. Similar to the npCu, the oxygen treatment re-dispersed Cu and demonstrates that the nanoparticles form soon,  $\sim 1$  h, after the copper oxide overlayer is reduced by the reaction. The oxygen treatment also oxidized the Ni and the exposure to the reaction formed NiO particles at the surface. Because Zn already existed as a mixture of reduced and oxidized Zn (Chapter 6), it is likely that the oxygen treatment oxidized any reduced Zn at the surface and formed ZnO particles.

After reaction for  $\sim 40$  h, the O<sub>2</sub>-treated catalyst still has NiO particles at its surface and its activity stabilizes, with only 15% activity loss over time. The catalyst morphology and ligament sizes are similar to the 1 h reaction exposed sample with small particles still apparent at the surface (Figure 7.4e). Thus, the surface area is retained during reaction exposure. It should be noted that other sample batches exhibited coarsening similar to that of npCu, though the activity was still stable for  $> 40$  h. Thus, the surface area does not account for its improved activity over its H<sub>2</sub>-treated counterpart, nor its enhanced activity compared to the npCu.

Investigation of the surface structures by TEM and EDS reveals that the most prevalent structure in the O<sub>2</sub>-treated catalyst after reaction is Ni oxide particles at the Cu

ligament surface (Figure 7.9). XPS analysis revealed that Ni is oxidized after oxidation and after reaction exposure (Chapter 6). In the STEM image, the surface feature seems more like an aggregate likely due to numerous overlapping particles. Some Zn may also be a part of the structure. In other regions, ZnO and Cu particles can also be observed at the surface similar to the npCu after reaction. In some other regions, Cu ligaments and particles are enveloped by NiO (Figure 7.17). The region presented shows one large Cu particle or small ligament with several smaller Cu particles engulfed in a web of NiO and a smaller amount of Zn. The NiO seems to be a web, but more particle like features can be distinguished (Figure 7.17). Similar to the region presented in Figure 7.9, the web is likely an aggregate of small, overlapping NiO crystals and possibly ZnO particles similar to Figure 7.8. Thus, the most prevalent and distinctive feature of the O<sub>2</sub>-treated npNiCu after reaction (the active surface) is the presence of NiO as an aggregate of smaller particles.

In another region, Cu particles decorate the surface of the Cu ligament. In the two particles in the upper right corner, Ni and Zn are also present with the Cu (Figure 7.18). They may constitute an alloy or more likely there are particles underneath the Cu that cannot be distinguished as the Ni and Zn spread to the top overlapping with two very small particles on the right of the Cu particle. In the middle of the region, a large Zn particle can be seen with smaller particles surrounding it. Two of these particles on the top and bottom can be attributed to Cu. The smaller particles in between the Zn particle and the Cu particle on the left can be attributed to Ni (Figure 7.18).

Comparison of the npCu and npNiCu reveal analogous structures at the surface. Both catalysts after H<sub>2</sub> or O<sub>2</sub> treatment and reaction display Zn aggregates or particles that are crystalline or amorphous. After oxidation, re-dispersed Cu nanoparticles are observed at the

surface of both catalysts. These features are not unique to either catalyst or pretreatment used and would not explain the difference in stability of npNiCu after H<sub>2</sub> versus O<sub>2</sub> treatment. The distinct feature is therefore the Ni doping in the npNiCu catalyst. As described before, H<sub>2</sub> treated npNiCu has metallic Ni particles decorating its surface, which are still present after reaction and deactivation. These particles are responsible for depositing carbon and deactivating the catalyst. After oxidation, the Ni at the surface is no longer metallic, but is an oxide present in the form of small particles. XPS studies in Chapter 6 confirm that the Ni is an oxide after reaction even up to 40 h. The key to keeping Ni as an oxide at the surface is the use of a low reaction temperature where the kinetics of reducing Ni is very slow. Additionally, the reducing agent in reaction conditions is ethanol whose reduction potential is lower than H<sub>2</sub> further lengthening the reduction process of NiO.

The presence of Ni oxide particles has a distinct effect on the npNiCu catalyst. By not being metallic, the NiO particles do not deposit carbon and deactivate the catalyst in 30 -40 h, unlike the metallic particles in its H<sub>2</sub>-treated counterpart. Previous studies have also demonstrated that NiO promotes the ethanol dehydrogenation reaction to acetaldehyde<sup>9, 12</sup>. Another study demonstrated that NiO crystals in proximity to Cu had higher activity for acetaldehyde production than the reduced catalyst for ethanol steam reforming<sup>13</sup>. The authors concluded that the NiO and Cu interface was responsible for the improvement. Given that the npNiCu maintains the NiO and Cu interface from 1 h to 40 h of reaction after oxidation, the interface between the may also be contributing to the improved performance of the O<sub>2</sub>-treated catalyst. Clearly, NiO plays a key role in stabilizing the performance of npNiCu and preventing its deactivation, whereas metallic Ni leads to deactivation.

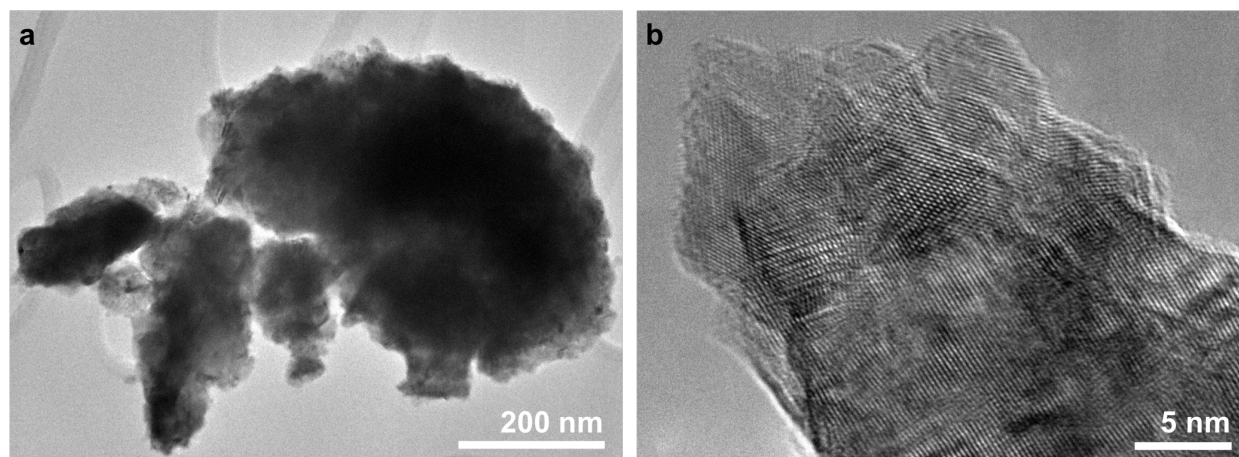


**Figure 7.7** a) Low magnification and b) high magnification TEM images of npNiCu after ex situ  $O_2$  treatment (1 h, 250 °C, 20%  $O_2$ , 1 atm) showing roughening at the surface by copper oxide crystallites.

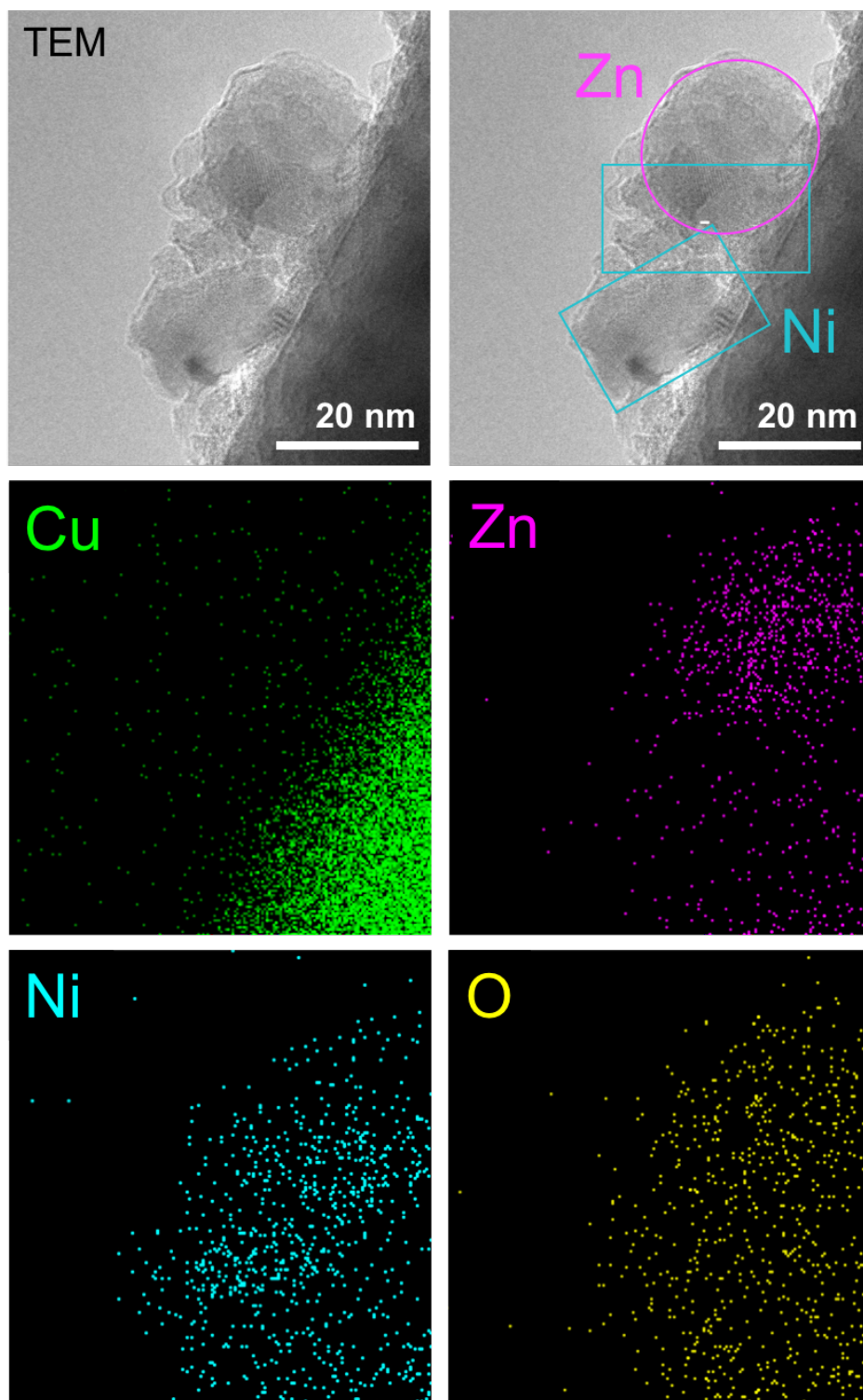


**Figure 7.8** TEM image and corresponding elemental maps of a typical region of the surface of  $O_2$ -treated npNiCu after 1 h of reaction. NiO and ZnO particles are outlined in the TEM image in the upper right.

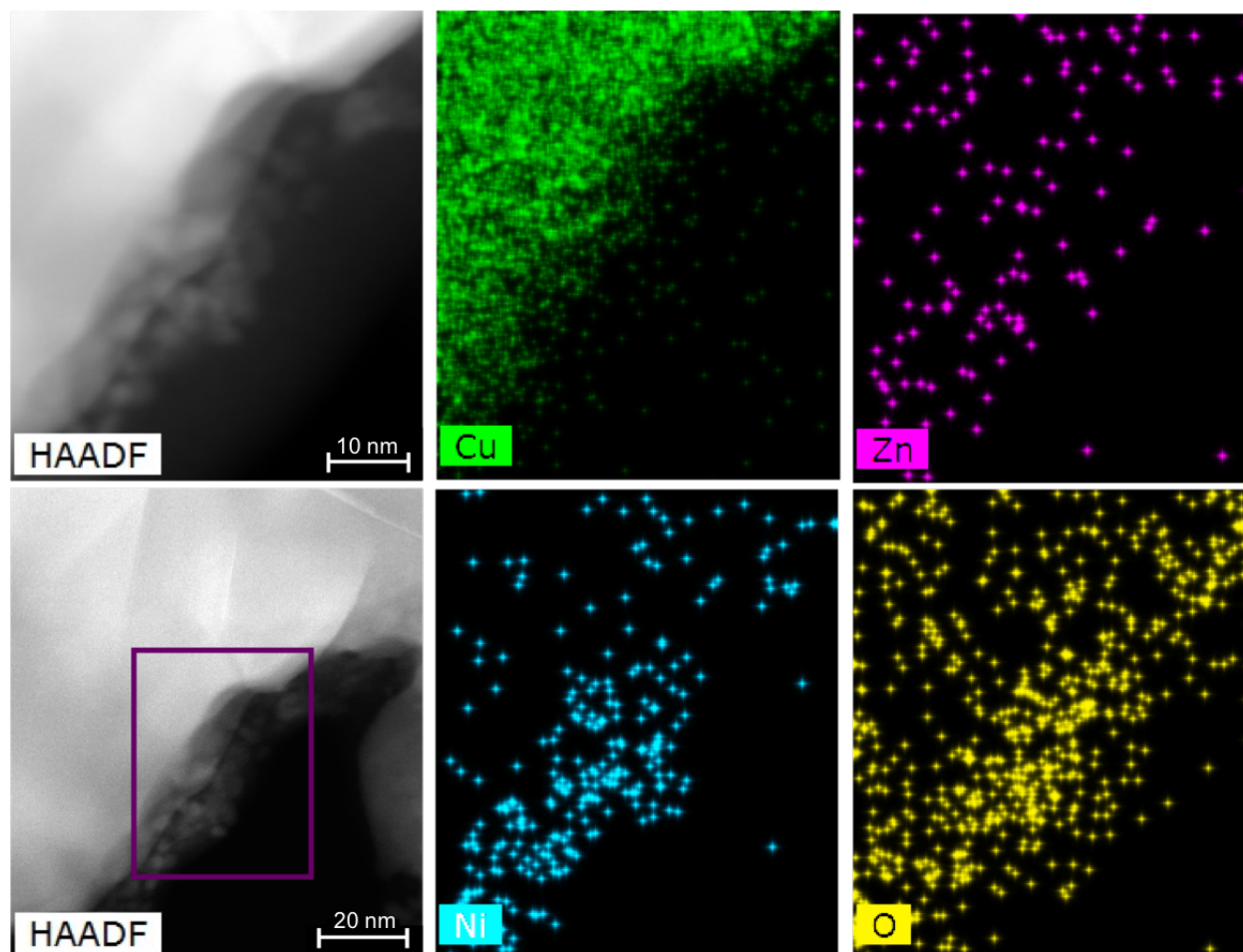


**Figure 7.9** Low magnification and high magnification HAADF images of  $O_2$ -treated npNiCu after reaction with corresponding elemental maps showing Ni oxide particles at the surface of the Cu ligament.

#### 7.3.4 Reduction-Oxidation Behavior of npNiCu

Sequential in situ reduction and oxidation cycling shows parallel behavior to the ex situ treated analysis. In situ reduction of npNiCu (1 h, 550 °C, 1 Torr  $H_2$ ) using an E-TEM shows nanoparticles at the surface of the ligament (Figure 7.11a). EELS analysis of the particles and the ligament edge confirm that the particles are Ni and the ligament is Cu (i-ii,

Figure 7.11d). Several points were analyzed by EELS in addition to those indicated to conclude that the particles are Ni identified by the  $L_2$  and  $L_3$  peaks located at  $\sim 850$  and  $\sim 870$  eV in the EELS spectrum. The EELS spectrum reveals that ligament edges is metallic Cu after seen from the stepped shape of the EELS spectrum (ii, Figure 7.11d) After oxidation, copper oxide roughens and completely covers the Ni nanoparticles (iii, Figures 7.11b). The EELS spectrum illustrates copper oxide due to its sharp  $L_2$  and  $L_3$  peaks at  $\sim 930$  eV and  $\sim 952$  eV. These observations are consistent with the XPS and E-TEM studies presented in Chapter 6.

After oxidation, reducing the sample again (1 h,  $550^\circ\text{C}$ , 1 Torr  $\text{H}_2$ ) reveals Ni particles back at the surface with the Cu ligament edges reformed and smoothed (Figure 7.11c and 7.11d). Higher temperatures were used for the reduction and oxidation treatments to ensure full reduction and oxidation in the E-TEM. Because Ni reduces at such a high temperature, the Ni particles will be metallic, suggesting that reduction of the oxidized sample would revert it back to its  $\text{H}_2$ -treated form which would then deactivate.

To illustrate this effect, the  $\text{O}_2$ -treated npNiCu was  $\text{H}_2$  treated after being active in reaction for 40 h. After the  $\text{H}_2$  treatment (1 h,  $350^\circ\text{C}$ , 10%  $\text{H}_2$ , 1 atm) using conditions known to reduce Ni, the sample was exposed to reaction where it subsequently deactivated over a 30 h period similar to the purely  $\text{H}_2$ -treated catalyst. XPS of the sample after deactivation indicated metallic Ni was present (Chapter 6). Morphologically, the sample exhibits some coarsened regions, but still retains numerous nanoparticles at its surface (Figure 7.4f). Thus, the loss of surface area cannot account for its complete deactivation.

Similar to the purely  $\text{H}_2$ -treated npNiCu, the now deactivated  $\text{O}_2$  and  $\text{H}_2$ -treated catalyst exhibits a string of Ni particles at its surface adjacent to Zn particles (Figure 7.10). From the XPS studies (Chapter 6), it is known that Ni is completely reduced by the  $\text{H}_2$



treatment and it is evident here by the high density of Ni in the particle structures indicating metallic Ni particles. Additionally, carbon can be seen overlapping with the Ni nanoparticles well-beyond the Cu ligament edge. Another area of the sample displays Cu nanoparticles at the surface which are encapsulated by a layer Ni which is further encapsulated by carbon (Figure 7.19). Zn particles are also present adjacent to the Cu particles. The carbon deposition observed in this area demonstrates that Ni does not need to be a fully formed nanoparticle to deposit carbon on the surface, even small ensembles can deposit carbon. These observations support carbon deposition as the deactivation mechanism of H<sub>2</sub>-treated npNiCu samples in accordance with the observations presented in Chapter 6.

The reduction-oxidation behavior indicates that the catalyst activity can be manipulated and reversed using O<sub>2</sub> or H<sub>2</sub> treatments. H<sub>2</sub> treatment can be used to create metallic Ni particles which deactivate the catalyst by carbon deposition. O<sub>2</sub>-treatment can create a more stable and active catalyst by creating NiO particles at the surface. NiO particles do not reduce in reaction conditions due to the low reaction temperature and reducing potential of ethanol, even though it is thermodynamically favorable. They also do not deposit carbon like metallic Ni and thus, lengthen the deactivation mechanism until they are greatly reduced. NiO may also participate in the ethanol dehydrogenation reaction, promoting the production of acetaldehyde, whereas metallic Ni promotes decomposition to CO and CH<sub>4</sub>. Thus, the key to the active catalyst is the kinetic trapping of NiO at the surface due to the reaction conditions used.

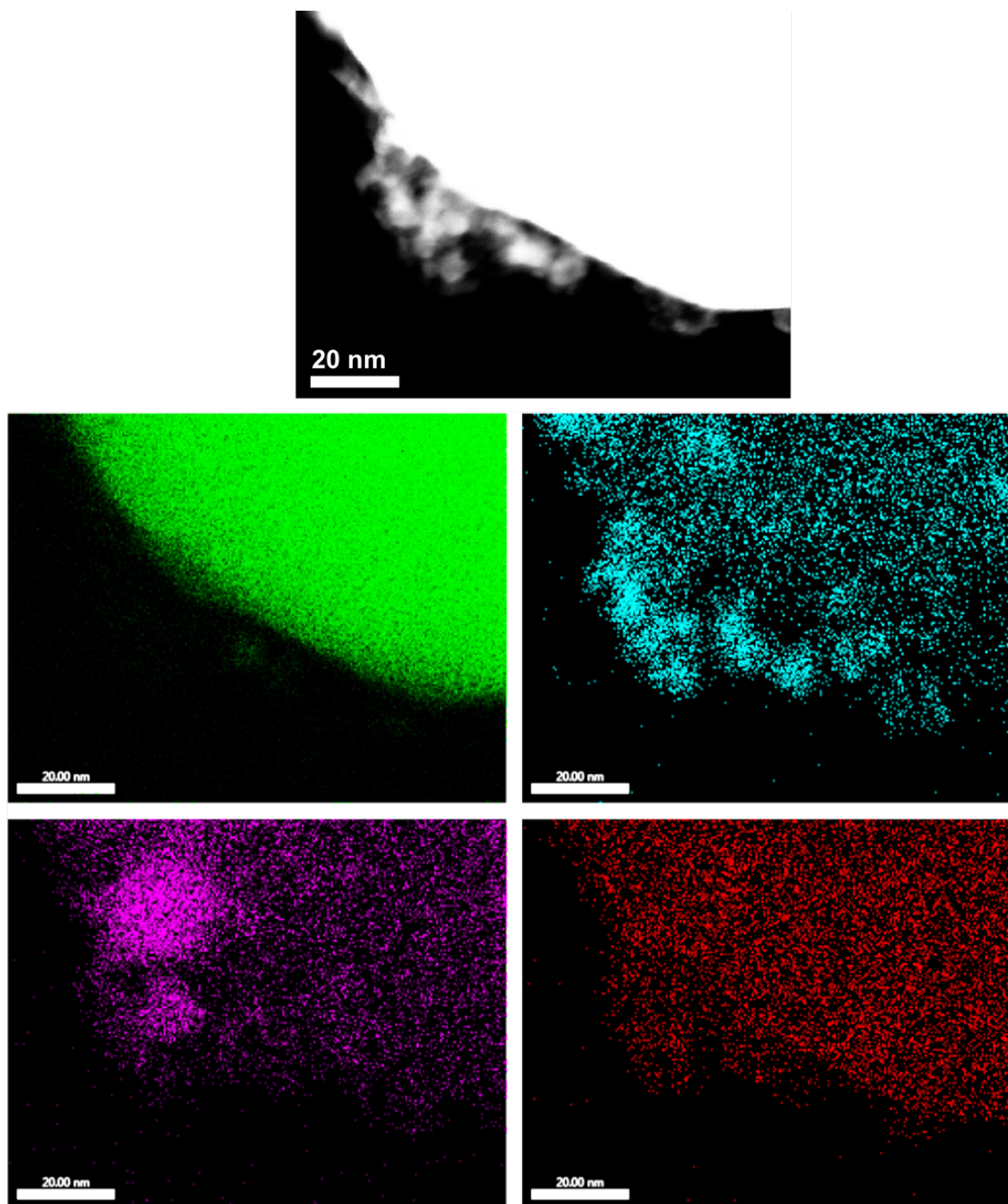


**Figure 7.10** STEM image and corresponding EDS maps of deactivated npNiCu showing numerous Ni nanoparticles and a large amount of C surrounding the particles. The active O<sub>2</sub>-treated catalyst was H<sub>2</sub>-treated and exposed to reaction where it deactivated.

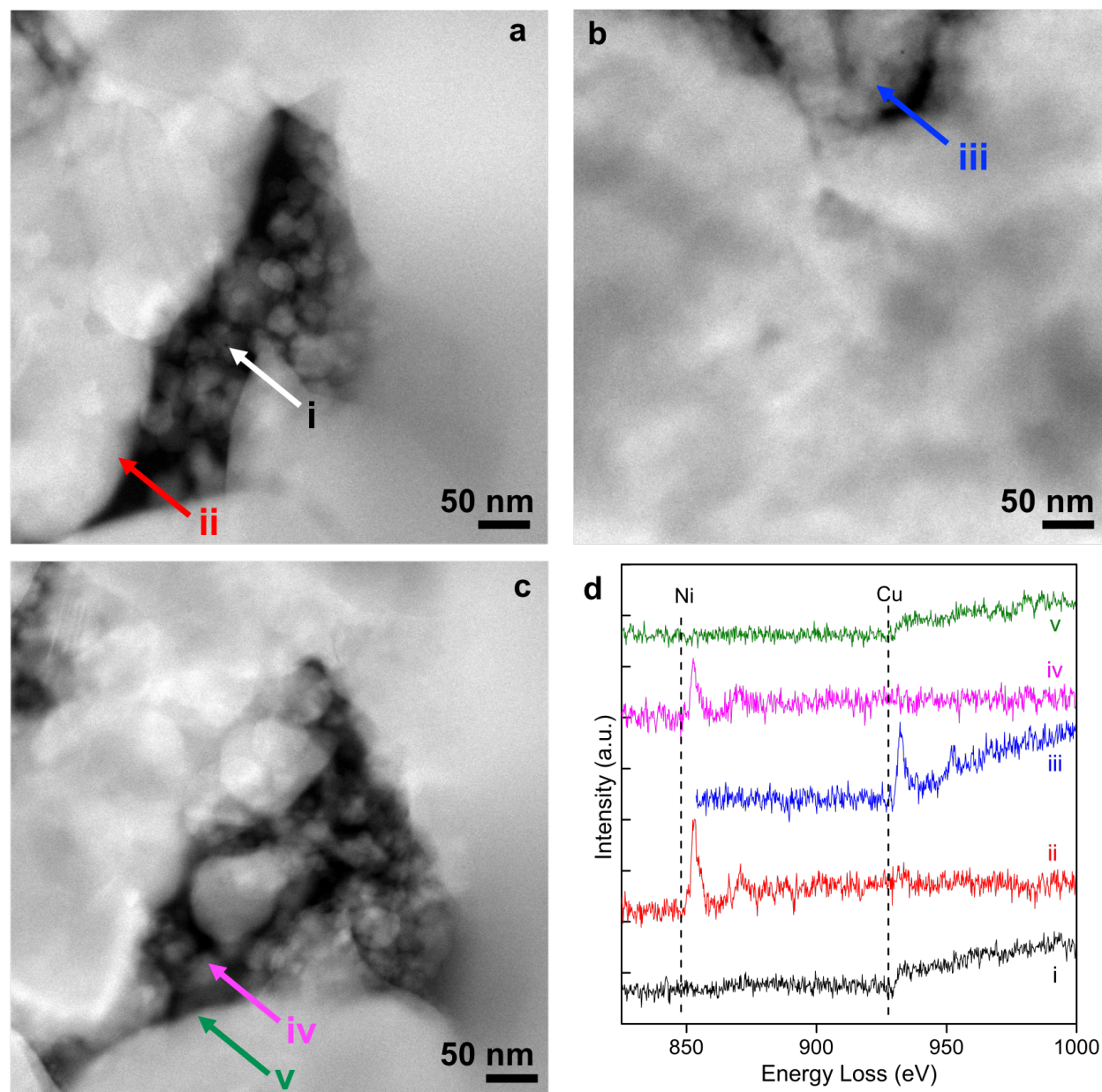


**Figure 7.11** STEM imaging of npNiCu after sequential in situ a) reduction (1 h, 550 °C, 1 Torr H<sub>2</sub>), b) oxidation (1 h, 350 °C, 10 Torr O<sub>2</sub>), c) reduction again (1 h, 550 °C, 1 Torr H<sub>2</sub>), and d) EELS spectra of areas indicated by arrows.

## **7.4 Conclusions**

In this report, the morphology and surface structures of npCu and npNiCu were investigated to understand their contribution in ethanol dehydrogenation reaction. After H<sub>2</sub> or O<sub>2</sub> treatment, the npCu had ZnO particles at its surface. O<sub>2</sub> treatment re-dispersed Cu resulting in Cu nanoparticles at the surface which was also observed in the npNiCu sample. The increase in surface area of npCu due to the re-dispersed particles can account for the increased activity of the O<sub>2</sub>-treated catalyst versus the H<sub>2</sub>-treated catalyst, both of which are stable in reaction for prolonged periods of time. The presence of particles at the surface even with coarsening of the Cu ligaments can also account for the stable activity even with the larger morphological change.

For npNiCu, morphology does not account for the difference in activity observed between the H<sub>2</sub>-treated and O<sub>2</sub>-treated samples. The distinguishing feature between the two is the presence of metallic versus oxidized Ni particles at the surface. Metallic Ni leads to deactivation by carbon deposition, whereas NiO particles prevent carbon deposition. In situ and ex situ analysis of npNiCu reveal that the structures observed are stable. The O<sub>2</sub>-treated npNiCu catalyst exhibits NiO particles at its surface even after 40 h of ethanol dehydrogenation reaction. Thus, the NiO is kinetically trapped due to the reaction conditions. This principle of kinetic trapping can be extended to other catalytic systems to synthesis novel catalysts for sustainable catalytic applications.



## 7.5 Supporting Information

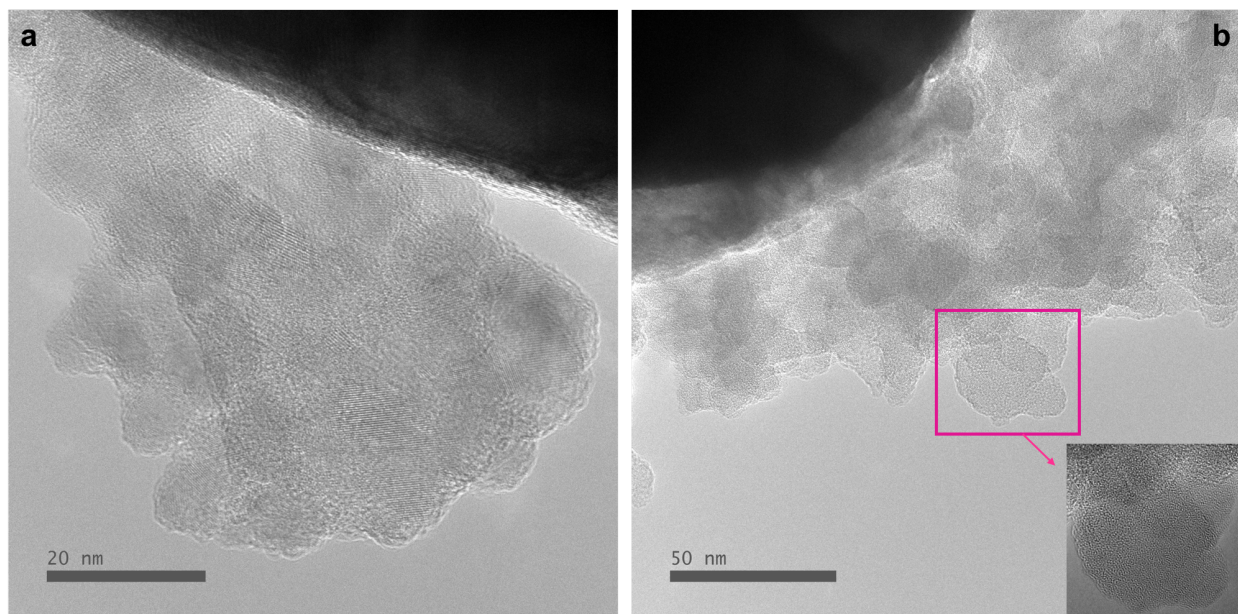


**Figure 7.12** TEM images of H<sub>2</sub>-treated npCu after reaction exposure showing a) crystalline and b) amorphous ZnO agglomerates at the surface.

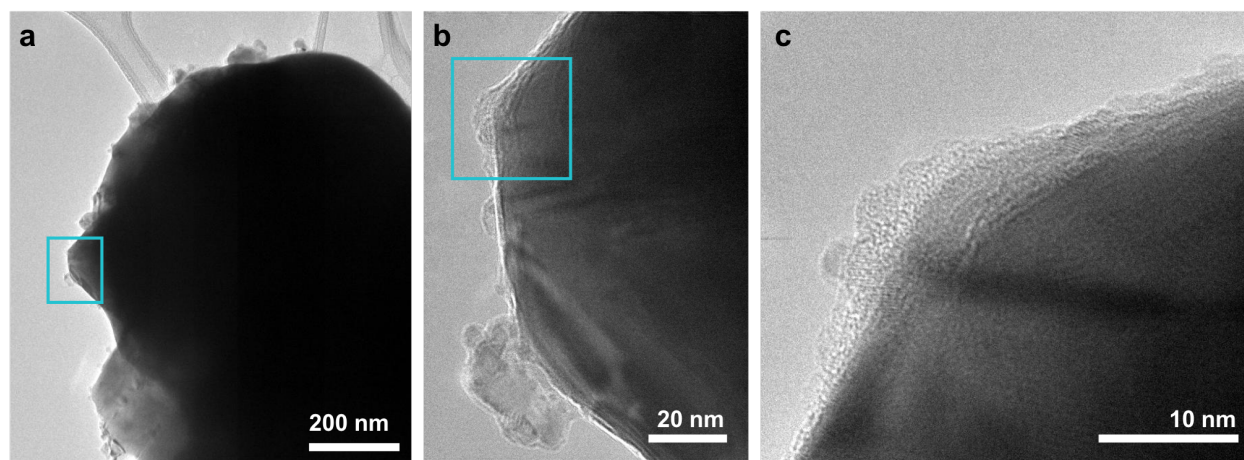


**Figure 7.13** a) – c) Low to high magnification TEM images of ex situ H<sub>2</sub>-treated npNiCu showing particles and amorphous material at the surface, in accordance with the features observed by in situ H<sub>2</sub> treatment.

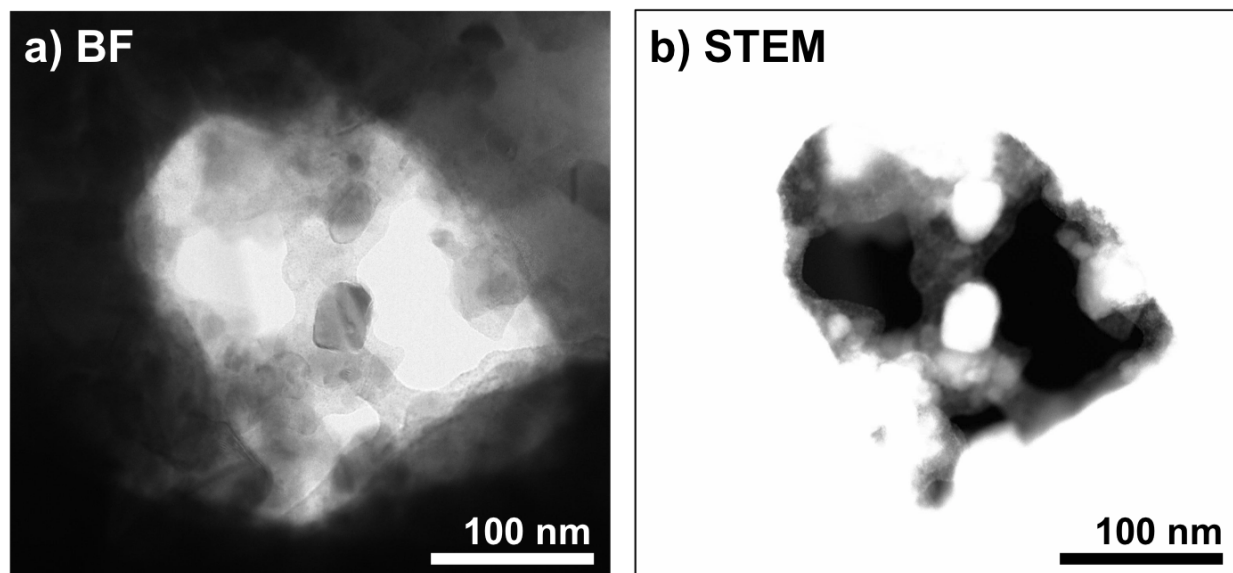


**Figure 7.14** a) Larger bright field and b) STEM images of the region shown in Figure 7.6.

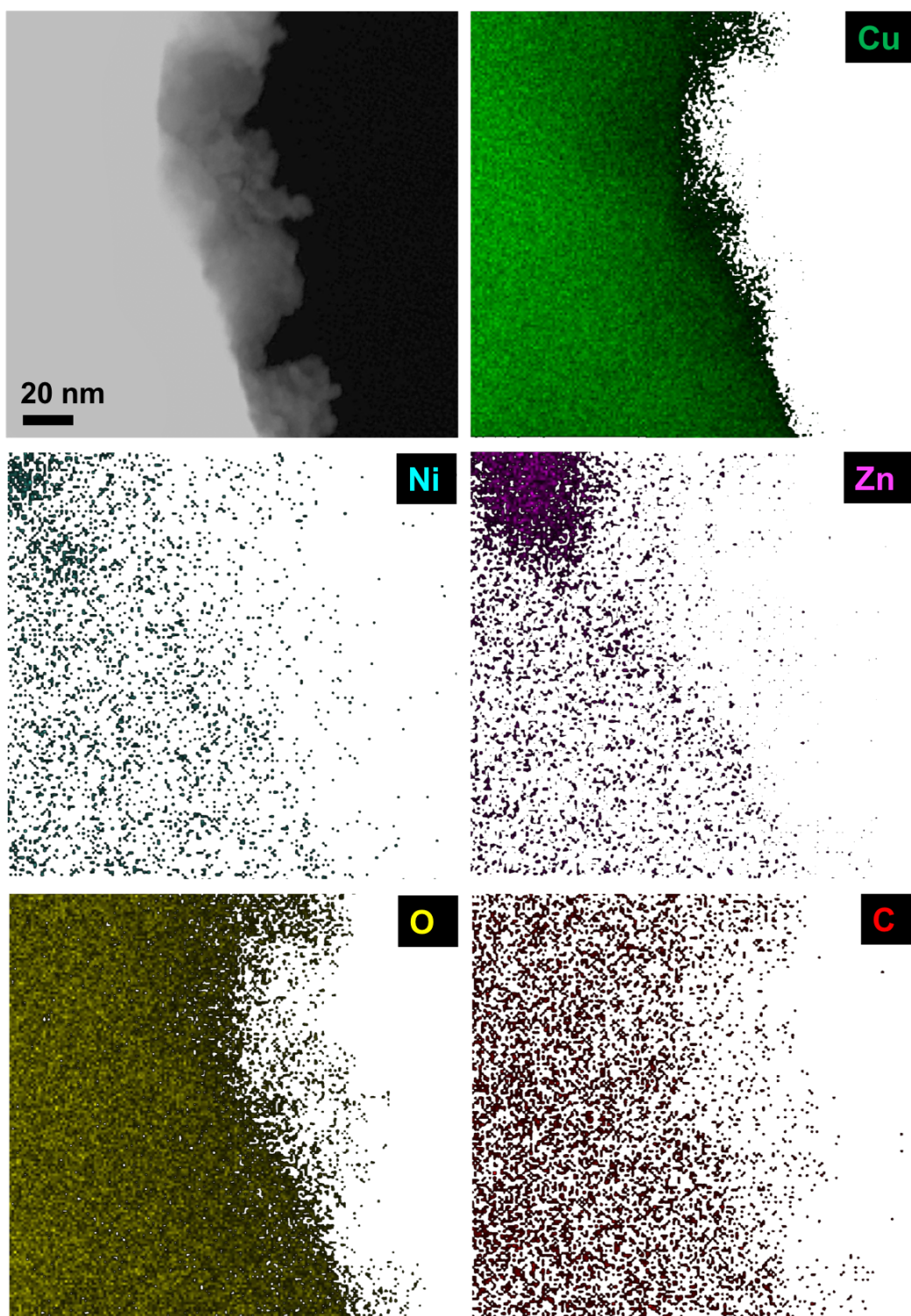


**Figure 7.15** STEM image and corresponding elemental maps of H<sub>2</sub>-treated npNiCu after reaction until deactivation showing large amounts of carbon at the surface. The common black background was made transparent to highlight the features on the surface.



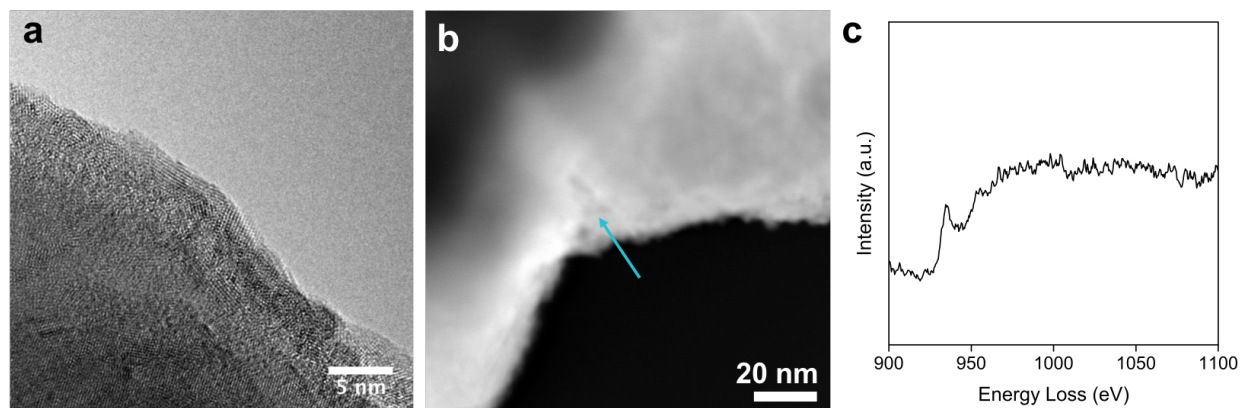


**Figure 7.16** npNiCu ligament edge after a) 10 min of in situ oxidation (250 °C, 1 Torr) showing the beginning of copper oxide formation and b) 1 h of oxidation showing the full formation of the copper oxide overlayer where a Ni nanoparticle was previously observed (blue arrow) with the corresponding EELS spectrum after oxidation in c).



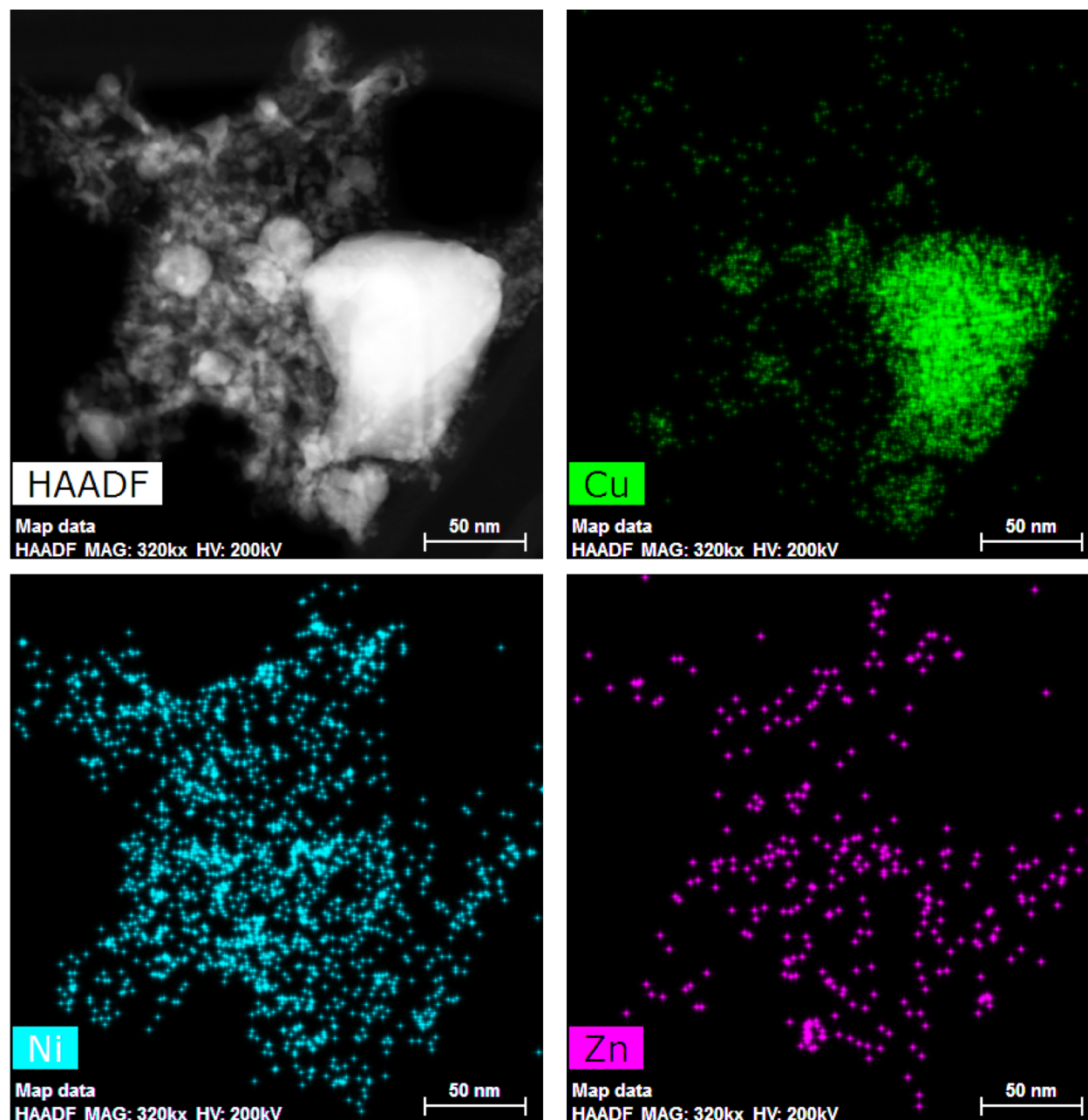


**Figure 7.17** STEM image of region of O<sub>2</sub>-treated npNiCu after reaction with corresponding elemental maps showing the envelopment of Cu ligaments by NiO.

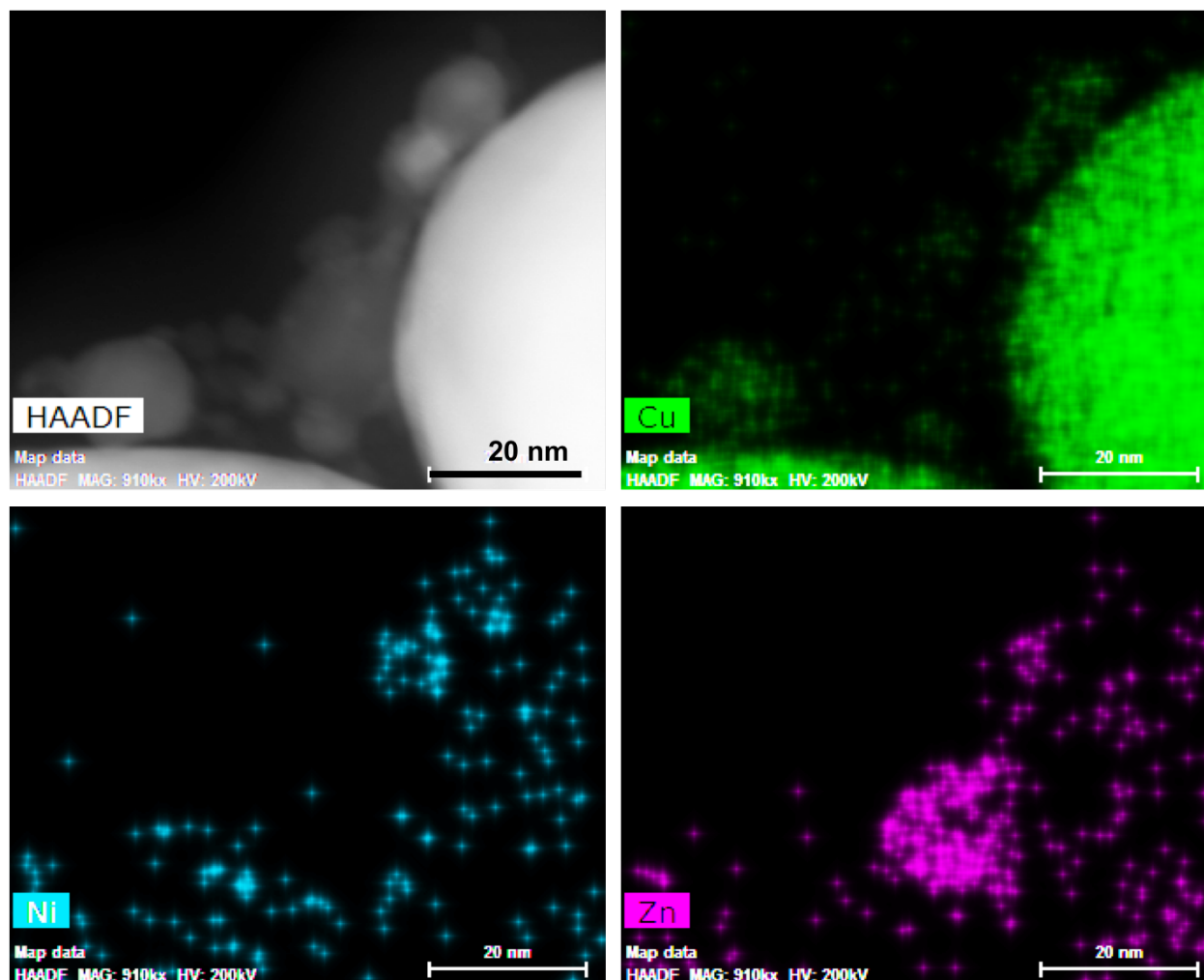


**Figure 7.18** HAADF image of another region at the surface of O<sub>2</sub>-treated npNiCu after reaction with corresponding elemental maps showing Cu, NiO, and ZnO particles at the surface of the Cu ligament.

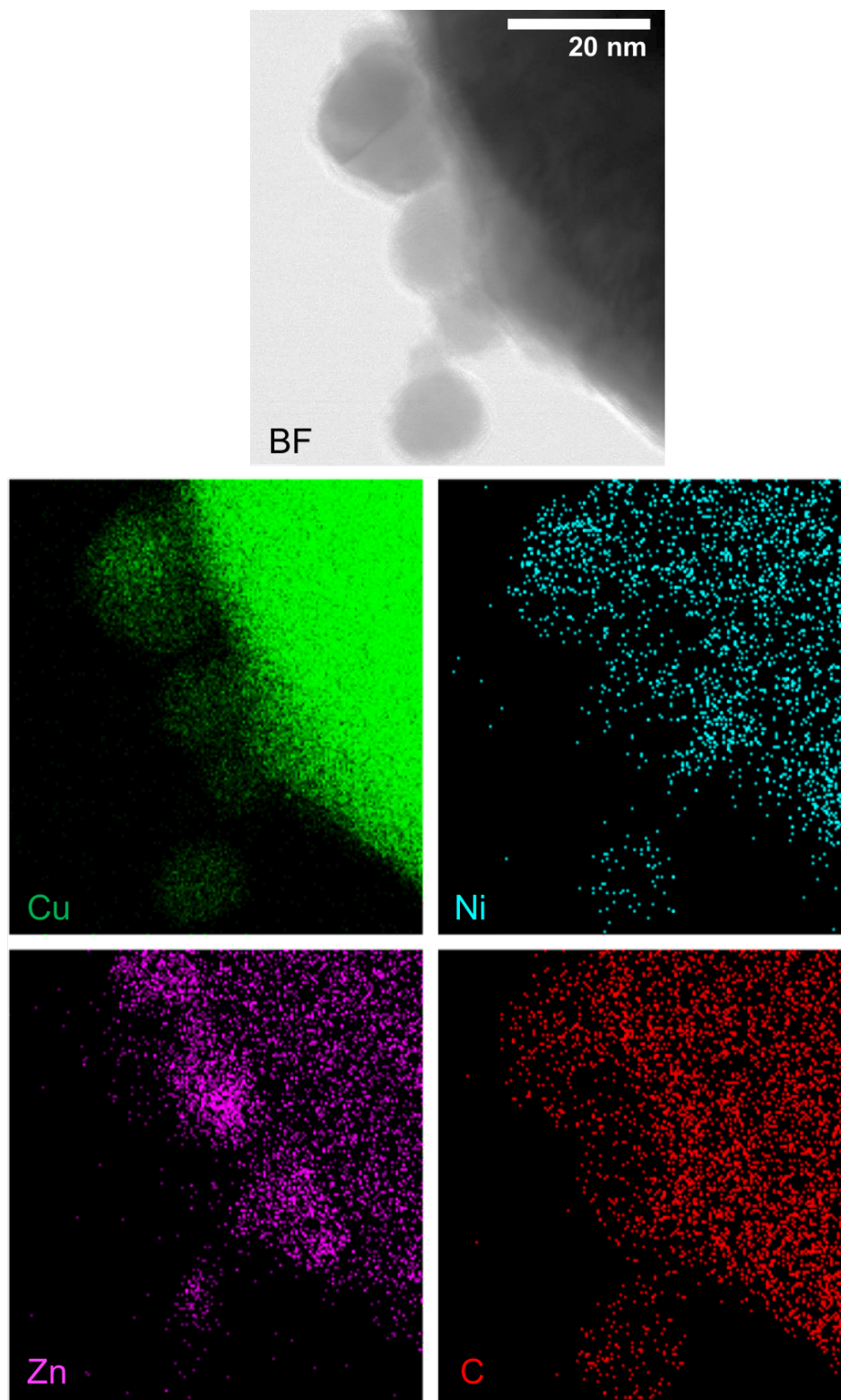


**Figure 7.19** Bright field image and elemental maps of deactivated npNiCu showing Cu particles first encapsulated by Ni then by C. The active O<sub>2</sub>-treated catalyst was H<sub>2</sub>-treated

and exposed to reaction where it deactivated. Zn particles are also present but cannot be distinguished in the bright field image possibly indicating that they are located below the Cu ligament.

## 7.6 References

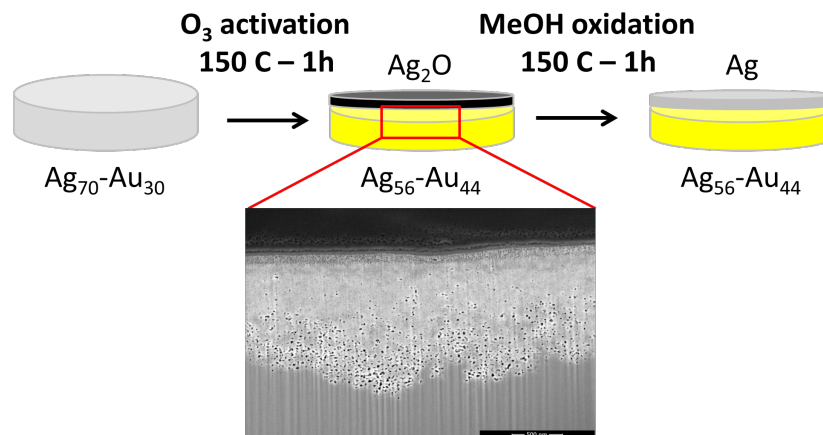
1. Detsi, E.; Jong, E. D.; Zinchenko, A.; Vukovic, I.; Punzhin, S.; Loos, K.; Brinke, G. t.; Raedt, H. A. D.; Onck, P. R.; Hosson, J. T. M. D., On the specific surface area of nanoporous materials. *Acta materialia* **2011**, *59*, 7488-7497.
2. Guisbiers, G.; Khanal, S.; Ruiz-Zepeda, F.; Roque de la Puente, J.; Jose-Yacaman, M., Cu-Ni nano-alloy: mixed, core-shell or Janus nano-particle? *Nanoscale* **2014**, *6* (24), 14630-14635.
3. Anjaneyulu, C.; Costa, L. O. O. d.; Ribeiro, M. C.; Rabelo-Neto, R. C.; Mattos, L. V.; Venugopal, A.; Noronha, F. B., Effect of Zn addition on the performance of Ni/Al<sub>2</sub>O<sub>3</sub> catalyst for steam reforming of ethanol. *Applied Catalysis A: General* **2016**, *519*, 85-98.
4. Vizcaíno, A. J.; Carrero, A.; Calles, J. A., Hydrogen production by ethanol steam reforming over Cu–Ni supported catalysts. *International Journal of Hydrogen Energy* **2007**, *32* (10), 1450-1461.
5. Bian, J.; Xiao, M.; Wang, S.; Wang, X.; Lu, Y.; Meng, Y., Highly effective synthesis of dimethyl carbonate from methanol and carbon dioxide using a novel copper–nickel/graphite bimetallic nanocomposite catalyst. *Chemical Engineering Journal* **2009**, *147* (2), 287-296.
6. Lortie, M.; Isaifan, R.; Liu, Y.; Mommers, S., Synthesis of CuNi/C and CuNi-/Al<sub>2</sub>O<sub>3</sub> Catalysts for the Reverse Water Gas Shift Reaction. *International Journal of Chemical Engineering* **2015**, *2015*, 9.
7. Studt, F.; Abild-Pedersen, F.; Wu, Q.; Jensen, A. D.; Temel, B.; Grunwaldt, J.-D.; Nørskov, J. K., CO hydrogenation to methanol on Cu–Ni catalysts: Theory and experiment. *Journal of Catalysis* **2012**, *293*, 51-60.
8. Galetti, A. E.; Gomez, M. F.; Arrúa, L. A.; Abello, M. C., Hydrogen production by ethanol reforming over NiZnAl catalysts. *Applied Catalysis A: General* **2008**, *348* (1), 94-102.
9. Barroso, M. N.; Gomez, M. F.; Arrúa, L. A.; Abello, M. C., Hydrogen production by ethanol reforming over NiZnAl catalysts. *Applied Catalysis A: General* **2006**, *304*, 116-123.

10. Zeng, G.; Liu, Q.; Gu, R.; Zhang, L.; Li, Y., Synergy effect of MgO and ZnO in a Ni/Mg–Zn–Al catalyst during ethanol steam reforming for H<sub>2</sub>-rich gas production. *Catalysis Today* **2011**, *178* (1), 206-213.
11. Fierro, V.; Akdim, O.; Mirodatos, C., On-board hydrogen production in a hybrid electric vehicle by bio-ethanol oxidative steam reforming over Ni and noble metal based catalysts. *Green Chemistry* **2003**, *5* (1), 20-24.
12. Frusteri, F.; Freni, S.; Chiodo, V.; Donato, S.; Bonura, G.; Cavallaro, S., Steam and auto-thermal reforming of bio-ethanol over MgO and CeO<sub>2</sub> Ni supported catalysts. *International Journal of Hydrogen Energy* **2006**, *31* (15), 2193-2199.
13. Chen, L.-C.; Lin, S. D., Effects of the pretreatment of CuNi/SiO<sub>2</sub> on ethanol steam reforming: Influence of bimetal morphology. *Applied Catalysis B: Environmental* **2014**, *148-149*, 509-519.

## Chapter 8.

# Macroscopic 3D Nanoporosity Formation by Dry Oxidation of AgAu Alloys

### 8.1 Abstract



3D nanoporous metals made by alloy corrosion have attracted much attention due to various promising applications ranging from catalysis and sensing to energy storage and actuation. In this work we report a new process for the fabrication of 3D open nanoporous metal networks that phenomenologically resembles the nano-Kirkendall hollowing process previously reported for Ag/Au nanowires and nanoparticles, with the difference that the involved length scales are 10-100 times larger. Specifically, we find that dry oxidation of  $\text{Ag}_{70}\text{Au}_{30}$  bulk alloy samples by ozone exposure at  $150^\circ\text{C}$  stimulates extremely rapid Ag outward diffusion towards the gas/alloy-surface interface, at rates at least 5 orders of magnitude faster than predicted based on reported Ag bulk diffusion values. The micrometer-thick Ag depleted alloy region thus formed transforms into a 3D open

nanoporous network morphology upon further exposure to methanol-O<sub>2</sub> at 150°C. These findings have important implications for practical applications of alloys, for example as catalysts, by demonstrating that large-scale compositional and morphological changes can be triggered by surface chemical reactions at low temperatures, and that dilute alloys such as Ag<sub>0.03</sub>Au<sub>0.97</sub> are more resilient against such changes.

This paper was published in *J. Phys. Chem. C* **2017**, *121*, 5115-5122.

## 8.2 Introduction

The synthesis and properties of nanoporous metals in the form of monolithic 3D bulk materials, nanowires and nanoparticles have recently been widely studied in the physical-chemistry community using various imaging and characterization techniques (TEM, SEM, XPS, XRD...) as well as simulations. Different materials systems have been used to study various aspects of porosity formation, morphology evolution and reactivity towards certain chemical transformations. Pt-based alloys have, for example, been used to study the correlation between the barrier for vacancy diffusion with the alloying energy of the alloy<sup>1</sup>; Pd-based intermetallic alloys were used to study the effect of composition on void formation via the nanoscale Kirkendall effect<sup>2</sup>, and Cu-Au alloys<sup>3</sup> were used to study the effect of alloy composition on both dealloying kinetics and morphology. In-situ imaging and spectroscopy techniques were used, for example, to study the effect of surface defects on electrochemical surface alloying/dealloying kinetics in the PbCu alloy system<sup>4</sup>, and to study the dealloying mechanism of PtY alloy nanoparticles during the oxygen reduction reaction in a fuel cell

environment<sup>5</sup>. Similar, in-situ imaging and spectroscopy techniques were used to study the morphological and compositional changes in CuCo core-shell nanoparticles during exposure to oxygen and syngas<sup>6</sup>. Exposure to reactive gases has also been shown to change the local chemical composition of AgAu alloys. For example, DFT simulations on (AuAg)<sub>147</sub> nanoclusters have shown that Au favors surface sites<sup>7</sup>, while the presence of adsorbed oxygen seems to create surface sites of high local Ag concentration that then facilitate O<sub>2</sub> dissociation<sup>8,9</sup>.

A mechanistic study on dealloying of silver-gold alloys by Erlebacher et al.<sup>10</sup> in 2001 sparked broad interest in 3D nanoporous metals such as nanoporous gold (np-Au), leading to a series of discoveries revealing surprising mechanical<sup>11</sup>, optical<sup>11</sup> and catalytic<sup>13,14</sup> properties of this class of materials. In dealloying, selective dissolution of one or more components from a suitable starting alloy, such as Ag<sub>70</sub>Au<sub>30</sub> for np-Au, results in the formation of a characteristic three-dimensional bicontinuous nanoporous morphology with a uniform feature size on the nm length scale. Pore formation during dealloying is the consequence of selective dissolution of surface atoms of one (or more) alloy component(s) by a corrosive liquid environment. The dissolution process generates adatoms and vacancies on the surface, which nucleate into adatom and vacancy islands to form a pit-and-mound surface morphology. Local passivation by the more inert adatom clusters then leads to the development of a full 3D nanoporous morphology. The fast outward diffusion of the dissolved species through either the liquid phase or along the alloy-liquid interface makes this process amenable to macroscopic, millimeter-sized samples.



By contrast, nanoporosity formation in metal nanoparticles or nanowires by the nanoscale Kirkendall effect does not involve selective dissolution of an alloy component, but is caused by an inward flux of vacancies balancing the outward diffusion of the metal core which typically is driven by a chemical reaction at the nanoparticle surface, e.g. by dry oxidation<sup>15</sup>. Coalescence of inward diffusing vacancies then leads to nanopore formation. The bulk diffusion responsible for the nano-Kirkendall effect is much slower than surface diffusion or mass transport through a liquid phase, thus limiting the size of the particles to which this process can be applied. It is important to note that less dramatic compositional changes triggered by surface chemistry can critically affect the functionality of metal nanoparticles and nanoporous metals. For example, ozone exposure induces Ag surface segregation in np-Au with a Au<sub>97</sub>Ag<sub>3</sub> bulk composition, which can dramatically affect the catalytic activity and selectivity of np-Au<sup>16</sup>.

In this work, we report on Ag surface segregation and the formation of 3D nanoporosity in Ag<sub>70</sub>Au<sub>30</sub> bulk alloys triggered by surface-chemistry-driven processes that phenomenologically resemble the nano-Kirkendall hollowing process previously reported for Ag/Au nanowires and nanoparticles, with the difference that the involved length scales are 10-100 times larger. The 3D nanoporosity formation in Ag<sub>70</sub>Au<sub>30</sub> alloys studied in this work is triggered by dry oxidation with ozone at 150°C followed by methanol/O<sub>2</sub> gas exposure. The ozone-stimulated outward diffusion of Ag is extremely fast, with diffusion rates at least 5 orders of magnitude faster than predicted based on reported Ag bulk diffusion values. Kinetic Monte Carlo (kMC) simulations based on energetics from density functional theory (DFT) are used to analyze the observed diffusion kinetics.

### 8.3 Methods

In this work, we studied the compositional and morphological changes that result from the interaction of homogeneous AgAu bulk alloy samples with gas phase ozone (30 s to 4 h at 150°C in 3% O<sub>3</sub>/O<sub>2</sub>-He at a flow rate of 100 mL/min) and methanol-O<sub>2</sub> mixtures (1 h at 150°C in 6.5% MeOH / 20% O<sub>2</sub>-He at a flow rate of 50 mL/min). These conditions were selected because the ozone treatment is typically used to activate np-Au samples for selective methanol oxidation. The compositional and morphological changes induced by ozone exposure and by methanol-O<sub>2</sub> exposure were studied using a combination of focused ion beam (FIB) cross-sectional scanning electron microscopy (X-SEM) and cross sectional energy dispersive X-ray spectroscopy (X-EDX). X-ray photoelectron spectroscopy (XPS) was used to monitor the oxidation state of Ag as well as the surface composition of the alloy sample. To further study the mechanism of Ag diffusion and the effect of ozone induced vacancy injection on diffusion kinetics of Ag, we performed kMC simulations based on energetics from plane-wave DFT. These methods are described below.

#### 8.3.1 Physicochemical treatments

The various catalyst treatments were performed in an atmospheric pressure flow reactor. The thermal treatment was performed by heating the sample for 1 hour at 150°C (10°C/min ramp) under a flow of 100% He at 50 mL/min. The ozone treatments were performed at 150°C under a flow of 3% O<sub>3</sub> in O<sub>2</sub>-He at 100 mL/min with different exposure durations. In these experiments, ozone was introduced in the reactor once the temperature reached 150°C and was stable. The reaction conditions were 6.5% MeOH and 20% O<sub>2</sub>-He at a flow of

50 mL/min at 150°C for 1 hour. In the standard mode of operation, the sample is exposed to reaction conditions immediately after ozone treatment, without exposure to air between the two treatments.

### **8.3.2 FIB-SEM studies and analysis**

FIB-SEM analyses were performed using an FEI Helios Nanolab 660 Dualbeam FIB-SEM. The procedure is as follows: 1) deposition of a W protective layer (3 kV, 13 nA in SEM mode, then 30 kV 0.45 nA in FIB mode with  $W(CO)_6$  as gas precursor); 2) milling the sample in the vicinity of the protective layer (Ga beam at 30 kV, 2.5 nA in FIB mode); 3) cleaning the cross-section (30 kV or lower, 80 pA in FIB mode).

SEM images were acquired at 2-3 kV and 50-100 pA. Due to the configuration of the system, the SEM images of the cross sections were acquired at an angle of 52°. Consequently, a tilt correction was applied to measure the thickness of the different layers. EDX analyses were performed with an EDAX system (Model: Octane Plus), and acquired at 15 kV and 1.6 nA. Results were analyzed with the TEAM software from EDAX.

### **8.3.3 Density functional theory and kinetic Monte Carlo**

DFT calculations were performed using the VASP code<sup>17,18</sup>, and the PBE<sup>19</sup> exchange correlation functional was employed, with the Tkatchenko-Scheffler method<sup>20</sup> for van der Waals corrections. A 4x4x3 unit cell was used, with a k-point mesh of 7x7x9, and the plane-wave basis set was cut off at 400 eV. The projector-augmented wave method was used to model core electrons<sup>21,22</sup>.

For the kMC calculations, it is necessary to predict the energy barriers as a function of the local environment. The energy of a particular configuration of Ag, Au, and vacancies was predicted as a linear function of the number of each type of nearest neighbor interaction (Ag-Au, Ag-Ag, Ag-vacancy, etc.), fit to the DFT results. This allowed predictions of our database of 83 formation energies of Ag-Au-vacancy systems with a variety of compositions with a mean absolute error of 7.6 meV/atom. Further exploration showed that all three-body and second-nearest neighbor interactions were negligible, except vacancy-metal-vacancy interactions, which improved the accuracy of the predictions somewhat but were not included due to the significant complexity this would add to kinetic Monte Carlo simulations. The energy barriers were predicted based only on (1) the number of vacancies that are nearest neighbors to the diffusing atom at the transition state, and (2) the number of vacancies on the opposite side of these atoms from the diffusing atoms, as explained in the main text. A linear model was fit to these two parameters using 9 climbing-image nudged elastic band calculations (CI-NEB)<sup>23</sup>. (For one calculation, the climbing-image algorithm did not converge due to a very flat potential energy surface near the transition state, and therefore a regular NEB calculation was performed.) It was found to be more accurate to always predict the lower barrier of the forward and reverse diffusion steps; this resulted in a mean absolute error of 0.043 eV. By combining the formation energy predictions with the barrier predictions, we can predict rates for an arbitrary diffusion step. We assumed a pre-exponential factor of  $10^{15}$  for all rate calculations. To ensure we did not extrapolate too far outside our barrier database, a minimum barrier of 0.18 eV was enforced in the kMC; the results are insensitive to this value.

KMC calculations were performed using the KMCLib code<sup>24</sup> and periodic boundary conditions in the lateral directions. The bottom two layers were fixed, and vacancies were allowed to annihilate at this interface, with a 70% chance of becoming Ag and a 30% chance of becoming Au. Several kMC simulations were performed with various unit cell sizes, and all showed similar results. The results are shown from a 5x5x44 cell.

## 8.4 Results and Discussion

The first evidence of ozone-induced, large-scale compositional and morphological changes of a Ag<sub>70</sub>Au<sub>30</sub> bulk alloy (Figure 8.1) comes from a simple visual inspection of the sample: Exposure to ozone for 1 hour at 150°C leads to the formation of a thin black layer on top of the originally silver colored Ag<sub>70</sub>Au<sub>30</sub> alloy sample (Figure 8.1a). The black layer can be easily removed mechanically to expose a now golden-colored sample, indicating Au enrichment. Subsequent exposure to methanol-O<sub>2</sub> at 150°C turns the black layer into a 'greyish' powder which also can be easily mechanically removed to, once again, expose a golden-colored surface. It is important to note that annealing at 150°C under an inert gas atmosphere did not change the appearance of the silver colored Ag<sub>70</sub>Au<sub>30</sub> alloy sample, thus excluding a pure thermal effect.

XPS spectra collected from the sample surface confirm that these macroscopic changes induced by O<sub>3</sub> exposure and by methanol-O<sub>2</sub> exposure were caused by silver surface segregation (Table 8.1): The black surface layer formed during ozone exposure at 150°C consists of pure Ag<sub>2</sub>O as indicated by the Ag3d binding energy (BE) shift from 368.3 eV to 367.8 eV and the simultaneous disappearance of the Au4f peak. The greyish powder formed after subsequent methanol-O<sub>2</sub> exposure consists of metallic Ag, as indicated by another shift

of the Ag3d BE from 367.8 eV to 368.2 eV. Analysis of the Ag3d and Au4f intensity ratio of the original alloy sample (as well as of the thermally treated sample) confirms the nominal alloy composition of Ag<sub>70</sub>Au<sub>30</sub>.

FIB/X-SEM reveals that the Ag<sub>2</sub>O film that covers the Ag<sub>70</sub>Au<sub>30</sub> sample after 1 h ozone exposure at 150°C is approximately 1.5-2 μm thick and apparently delaminated (Figure 8.1b). A roughly 1-μm-thick region of the alloy sample directly below the Ag<sub>2</sub>O layer appears lighter and less homogeneous than the unreacted alloy. XPS reveals that the Ag-to-Au ratio at the sample surface (after removal of the Ag<sub>2</sub>O layer) changed from Ag<sub>70</sub>Au<sub>30</sub> to Ag<sub>56</sub>Au<sub>44</sub>, indicating that approximately one-half of the Ag atoms that were originally in this region of the alloy sample diffused outward to form the Ag<sub>2</sub>O layer. X-EDX line analysis (Figure 8.2) of a FIB cross-section prepared in a sample after 4 h ozone exposure revealed that the Ag depletion is uniform throughout the modified alloy region below the Ag<sub>2</sub>O layer, with a Ag-to-Au ratio of Ag<sub>40(±3)</sub>Au<sub>60</sub>, in fair agreement with the XPS surface composition of Ag<sub>56</sub>Au<sub>44</sub>. XSEM micrographs further reveal the formation of a few seemingly isolated 20-30 nm pores mostly towards the bottom of the modified layer, but their density and size is too small to account for the void space that one would expect to be present after removing roughly one third of the atoms of this region.

Subsequent exposure to the methanol-O<sub>2</sub> mixture at 150°C dramatically changes the morphology of the Ag depleted alloy region. The porosity increases and the pore morphology transitions from isolated pores to a 3D interconnected porous network with 50-70 nm pores (Figures 8.1c and 8.6). XPS reveals that the methanol-O<sub>2</sub> exposure does not lead to further changes of the Ag-to-Au ratio at the sample surface.

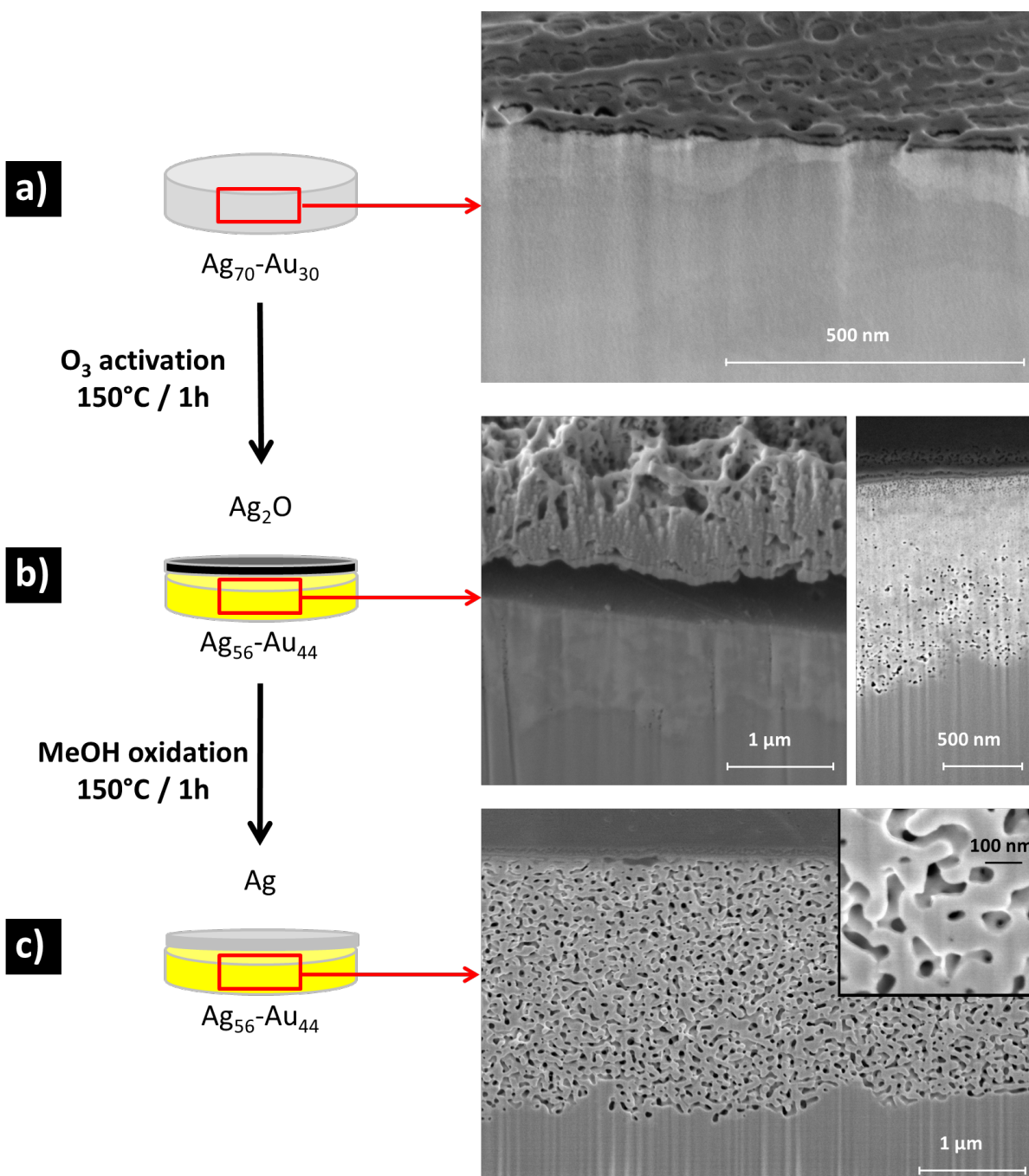


**Figure 8.1** FIB/X-SEM reveals Ag surface segregation induced by ozone exposure and 3D nanoporosity formation in a Ag<sub>70</sub>Au<sub>30</sub> alloy: **a)** the unexposed Ag<sub>70</sub>Au<sub>30</sub> alloy is very uniform (the darker top layer is a W protective layer), and looks identical before and after heat treatment at 150°C (not shown); **b)** Ozone exposure leads to the formation of an approximately one-micron thick detached layer of Ag<sub>2</sub>O. The region directly below looks less

uniform, and high magnification XSEM images reveal the formation of isolated pores with pore diameters in the 20-30 nm range; **c)** subsequent methanol/O<sub>2</sub> exposure at 150°C transforms the apparently isolated pore morphology into a three-dimensional interconnected porous network with pore diameters of 50-70 nm.

As mentioned above, methanol-O<sub>2</sub> exposure of the ozone treated alloy sample induces a transition from a few isolated pores towards a homogeneous 3D interconnected pore morphology. It is important to note that the 3D pore morphology of np-Au prepared by traditional wet chemistry can be imaged by FIB/X-SEM (Figure 8.7), thus ruling out that the lower-than-expected porosity observed after O<sub>3</sub> exposure is an artifact of the FIB technique used to prepare the cross-section. The apparent increase in porosity during exposure to methanol-O<sub>2</sub> thus indicates that much of the Ag-depletion-related porosity formed during O<sub>3</sub> exposure was either too small to be detected by SEM and/or that the porosity formation resulting from removing ~50% of the Ag atoms in this sample region was at least partially compensated by oxidation of the remaining Ag and the accompanying volume expansion by a factor of ~1.5<sup>25</sup>. The existence of this 'hidden' porosity also rules out that the observed Ag outward diffusion was balanced by an equivalent Au inward diffusion (see Figure 8.8 for TEM imaging).



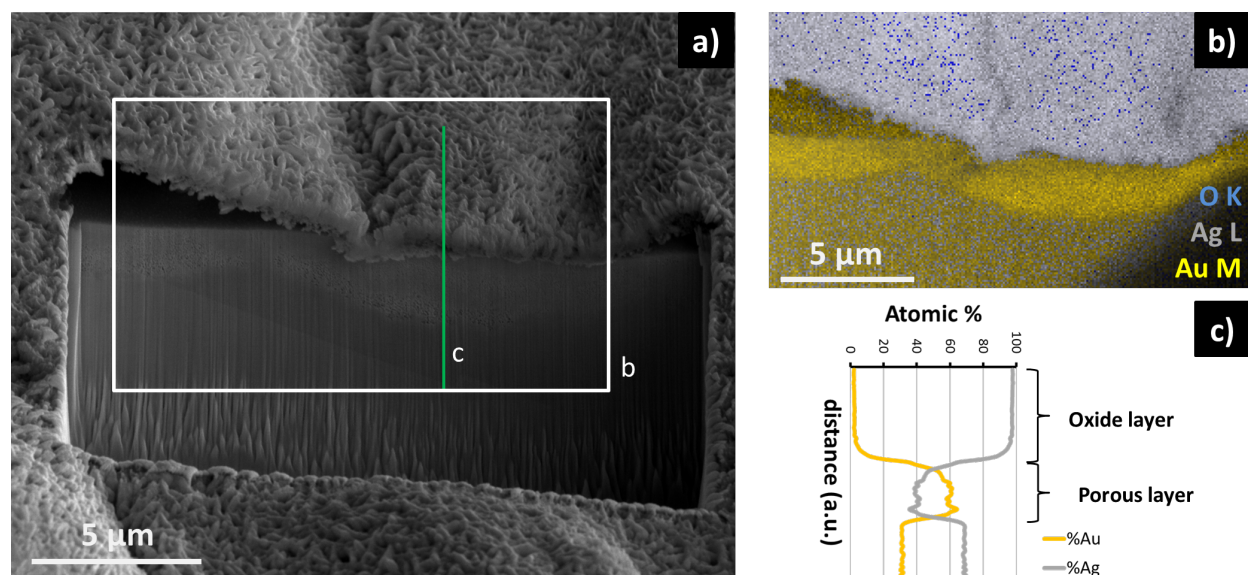


**Figure 8.2** Composition and morphology of the  $\text{Ag}_{70}\text{Au}_{30}$  alloy sample after 4 h of ozone treatment: **a)** FIB/X-SEM; **b)** EDX map of the gold (Au M), silver (Ag L) and oxygen (O K) distribution in the white rectangular region shown in **a**. The delaminated surface layer contains only Ag and O, and the  $\sim$ one-micron-thick porous layer directly below is enriched in Au (Au-to-Ag ratio of  $\sim 1.5$ ) compared to the unperturbed  $\text{Ag}_{70}\text{Au}_{30}$  alloy below (Au-to-Ag ratio of  $\sim 0.43$ ); **c)** Au-to-Ag ratio along the green line shown in **a**.

The  $\text{O}_3$  induced Ag surface segregation and porosity formation occurs on the whole alloy surface, but the depth of modified alloy layer varies laterally (Figure 8.3a). The flow of reactants (either pure  $\text{O}_3$  or a mix of  $\text{MeOH-O}_2$ ) that arrives at the sample surface can be considered to be homogeneous<sup>26</sup>; thus surface and/or bulk defects seem to be responsible for the observed lateral variation in the Ag surface segregation/porosity formation kinetics<sup>27,28</sup>. For example, it is well known that the diffusion rate along the grain boundaries is higher than the corresponding lattice diffusion rate<sup>29</sup>. Indeed, the preferential Ag depletion along grain boundaries is evidenced by the observation of porosity line defects (highlighted

by arrows) that extend beyond the average depth of the porous region and seem to mark the position of grain boundaries (Figure 8.3b).

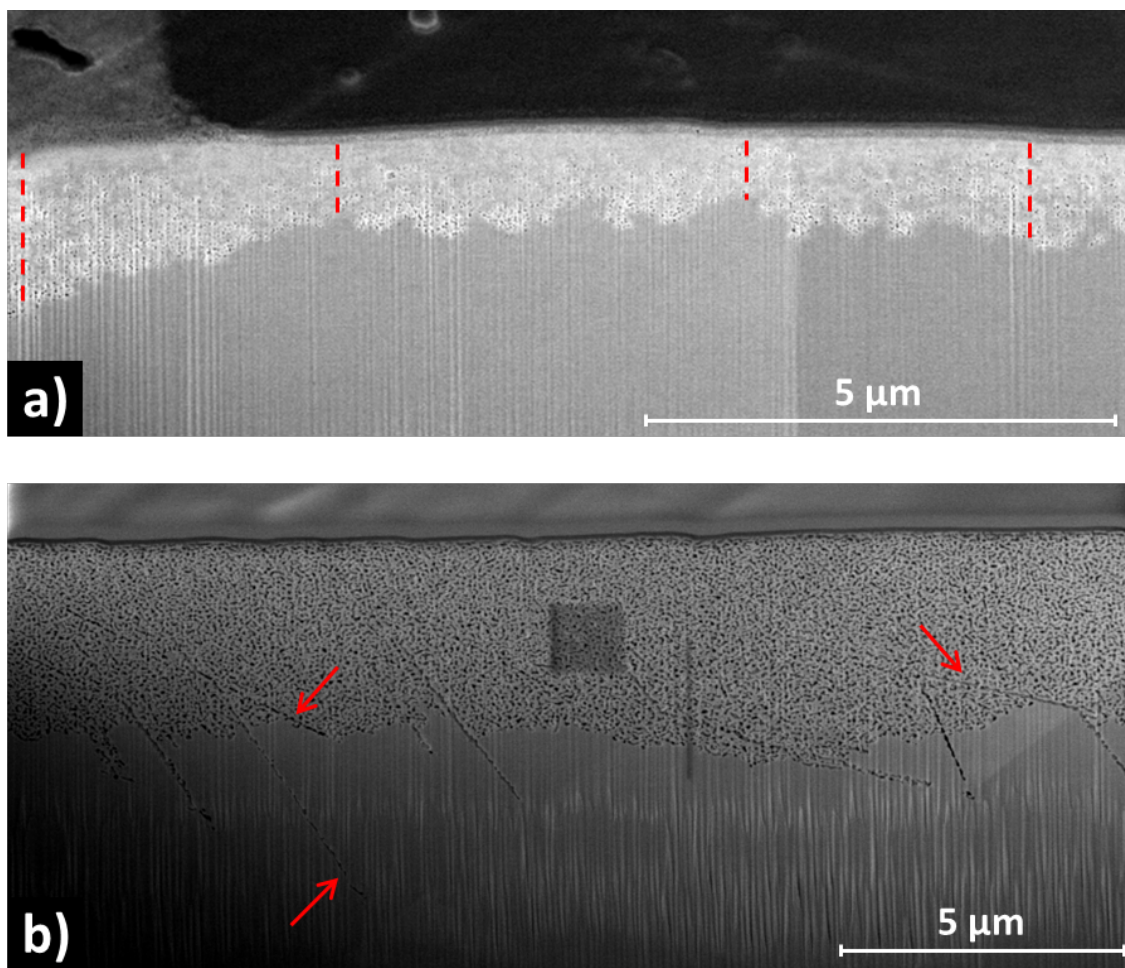


**Figure 8.3** Depth of penetration and preferential growth of the porous network: **a)** Alloy after 1 h of ozone treatment exhibits significant variations in porosity depth. The red lines correspond to the presence of pores 2.05 μm, 980 nm, 940 nm and 1.5 μm deep (from left to right). **b)** Alloy after ozone treatment and reaction conditions. In some cases, it is possible to observe the presence of ‘porosity lines’ with well-defined directions. These ‘lines’ expand deeper than the average depth of the porous structure, suggesting a nucleation and growth process initiated at surface and/or bulk defects.

It is well documented that bulk Ag samples form tens of micron thick layers of Ag oxides upon exposure to dilute ozone<sup>25,30</sup>. Consistent with thermodynamic data, only Ag(I) oxide ( $\text{Ag}_2\text{O}$ ) forms upon dilute ozone exposure at  $T > 150^\circ\text{C}$ <sup>30</sup>.  $\text{Ag}_2\text{O}$  is thermally stable up to  $227^\circ\text{C}$  where it decomposes into metallic Ag and molecular oxygen. By contrast, Au surfaces passivate upon ozone exposure after forming a one-nm-thick amorphous surface oxide<sup>31</sup>. The continuous oxidation of Ag by ozone has been explained by the  $\sim 55\%$  volume expansion of the Ag lattice upon oxidation, from  $68.23 \text{ \AA}^3$  for Ag to  $105.02 \text{ \AA}^3$  for  $\text{Ag}_2\text{O}$ ; the resulting stress-induced delamination of the growing  $\text{Ag}_2\text{O}$  film continuously exposes fresh Ag surfaces for further oxidation. However, the oxidation product,  $\text{Ag}_2\text{O}$ , is also a highly reactive catalyst for ozone decomposition<sup>32</sup>, thus providing a constant source of atomic oxygen even in the absence of freshly exposed Ag surfaces. Transport of atomic oxygen through the  $\text{Ag}_2\text{O}$  surface layer to the  $\text{Ag}_2\text{O}/\text{Ag}$  interface does not seem to be necessarily required for continuous Ag oxidation; a recent in-situ imaging study of the oxidation of Ag nanowires revealed the formation of Kirkendall voids at the interface between the growing  $\text{Ag}_2\text{O}$  shell and the Ag core which continued to grow in size until the Ag nanowires were completely transformed into hollow  $\text{Ag}_2\text{O}$  nanotubes<sup>33</sup>. The authors of the study<sup>33</sup> thus concluded that the outward diffusion of Ag through the growing  $\text{Ag}_2\text{O}$  oxide shell is faster than the oxygen inward diffusion. Fast Ag outward diffusion coupled with oxidation driven  $\text{Ag}_2\text{O}$  shell growth and void formation has also been observed for Ag-Au core-shell and AgAu alloy nanoparticles<sup>34</sup>.

In contrast to the oxidation of pure Ag, the oxidation of a  $\text{Ag}_{70}\text{Au}_{30}$  alloy not only requires Ag mass transport through the growing  $\text{Ag}_2\text{O}$  surface layer, but also through the

AgAu alloy. The Ag<sub>2</sub>O layer formation starts with the oxidation of the Ag atoms at the AgAu alloy surface. Once the surface Ag atoms have been consumed by the oxidation reaction, additional Ag atoms need to be transported to the interface between the growing Ag<sub>2</sub>O layer and the Ag depleted alloy surface. Indeed, the XPS analysis indicates that even within the Ag-depleted layer, there is Ag enrichment at the surface Ag<sub>56</sub>Au<sub>44</sub> by XPS as compared to Ag<sub>40</sub>Au<sub>60</sub>. In contrast to traditional wet chemistry dealloying where Ag diffuses as a solvated Ag ion through pores filled with a corrosive liquid medium, the ozone-induced dealloying mechanism described in this work requires fast solid state Ag diffusion at 150°C, either via surface or bulk diffusion. The diffusion length  $L$  can be estimated using Fick's law,  $L = \sqrt{2 D \cdot t}$ , where  $D$  is the diffusion coefficient, and  $t$  is the diffusion time. Here, the diffusion coefficient is defined as  $D = D_0 e^{(-E_a/RT)}$ , where  $D_0$  is the temperature-independent diffusion coefficient (m<sup>2</sup>/s),  $E_a$  the activation energy for diffusion (J/mol),  $R$  is the gas constant (J/mol•K) and  $T$  is the absolute temperature (K). Despite the lateral variation of the thickness of the Ag depletion layer, experiments with different ozone exposure times, ranging from 30 s for 4 h, indeed confirm the square root dependence of the diffusion length suggested by Fick's law (Figure 8.4). For this, an averaged value of depth of the porous layer was used. However, the Ag diffusion coefficient calculated from the time dependence of the Ag depletion layer thickness (~ one micron per hour) is  $\sim 1.4 \times 10^{-12}$  cm<sup>2</sup>/s, many orders of magnitude higher than the reported diffusion coefficient of  $9 \times 10^{-24}$  cm<sup>2</sup>/s for Ag self-diffusion in a Ag-Au solid solution at 150°C<sup>35</sup> that predicts an estimated diffusion length of only  $\sim 2.5 \times 10^{-8}$  m for 1 h. This is a much lower value than our experimental observations

( $\approx 1 \times 10^{-6}$  m) which proves that reactive gas exposure greatly increases the rate of diffusion of Ag through a bulk alloy as compared to the self-diffusion of Ag. (see Figure 8.4).

Ag diffusion along grain boundaries in Au thin films<sup>36,37</sup> is considerably faster than the Ag self-diffusion, with an estimated diffusion length of  $\sim 7.2 \times 10^{-1}$   $\mu\text{m}$ , which is much closer to our experimental values. However, in view of Figure 8.3b and the observation of a more or less uniform diffusion front, grain boundary diffusion cannot explain the observed dealloying kinetics. A surface diffusion mediated mechanism can be ruled out because the continuous open porosity required for this process is experimentally not observed in corresponding FIB/X-SEM micrographs (Figure 8.1b).

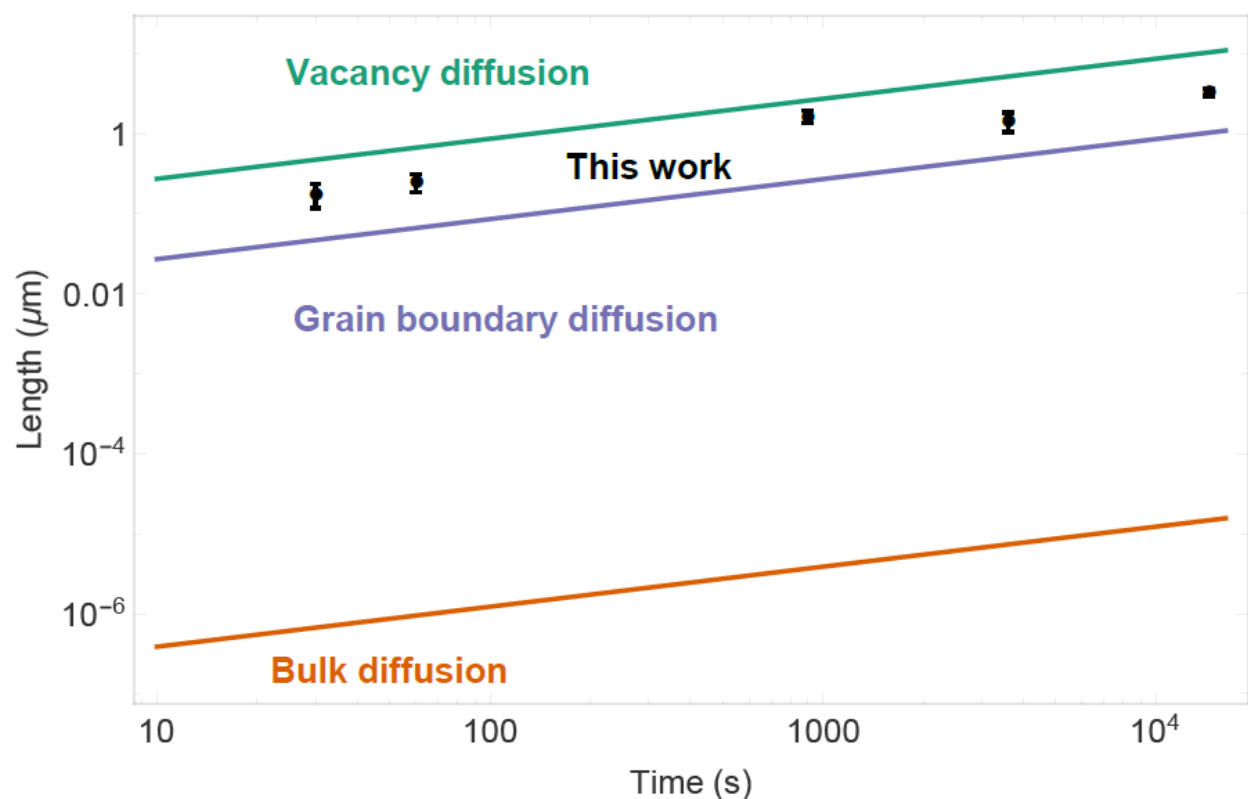


**Figure 8.4** Time dependence of porosity formation: Diffusion length as a function of time simulated for the bulk diffusion (based on parameters  $D_0 = 2.3 \text{ cm}^2/\text{s}$  and  $E_a = 1.888 \text{ eV}$  from reference<sup>35</sup>), the grain boundary diffusion (based on parameters  $D_0 = 1.1 \times 10^{-2} \text{ cm}^2/\text{s}$  and  $E_a = 0.88 \text{ eV}$  from reference<sup>36,37</sup>), and the vacancy diffusion (based on parameters from<sup>38</sup> and our DFT calculations), as well as the experimental results from this work (black dots): 30 sec:  $176 \pm 59 \text{ nm}$ , 1 min:  $247 \pm 64 \text{ nm}$ , 15 min:  $1.64 \pm 0.29 \text{ } \mu\text{m}$ , 1 h:  $1.43 \pm 0.39 \text{ } \mu\text{m}$ , 4 h:  $3.30 \pm 0.36 \text{ } \mu\text{m}$ .

Possible explanations for the faster than expected Ag outward diffusion are 1) accelerated Ag bulk diffusion by Ag-O reaction-driven vacancy injection at the  $\text{Ag}_2\text{O}/\text{Ag-Au}$  alloy interface, and 2) Ag diffusion through a Ag oxide phase embedded in the Ag depleted

alloy region. To explore how Ag diffusion in a  $\text{Ag}_{70}\text{Au}_{30}$  alloy is affected by the presence of a high, non-equilibrium vacancy concentration, we performed kinetic Monte Carlo (kMC) simulations based on energetics from density functional theory (DFT). DFT calculations of vacancy diffusion barriers show that the barrier depends strongly on the local vacancy configuration, but not on the identities of the atoms (see Figure 8.5a). In particular, if any of the four atoms that are closest to the diffusing atom at the transition state are vacancies, the barrier decreases, as noted in previous work on Ni<sup>39</sup>. Similarly, if these atoms can easily move away from the diffusing atom at the transition state because there are vacancies opposite these atoms from the diffusing atom, the barrier decreases. Because the probability of these low activation barrier diffusion configurations increases with increasing vacancy concentration, we expect the apparent activation barrier to decrease with increasing vacancy concentration. We find excellent agreement between experiment and the vacancy mediated diffusion mechanism based on parameters from our DFT calculations (Figure 8.4).

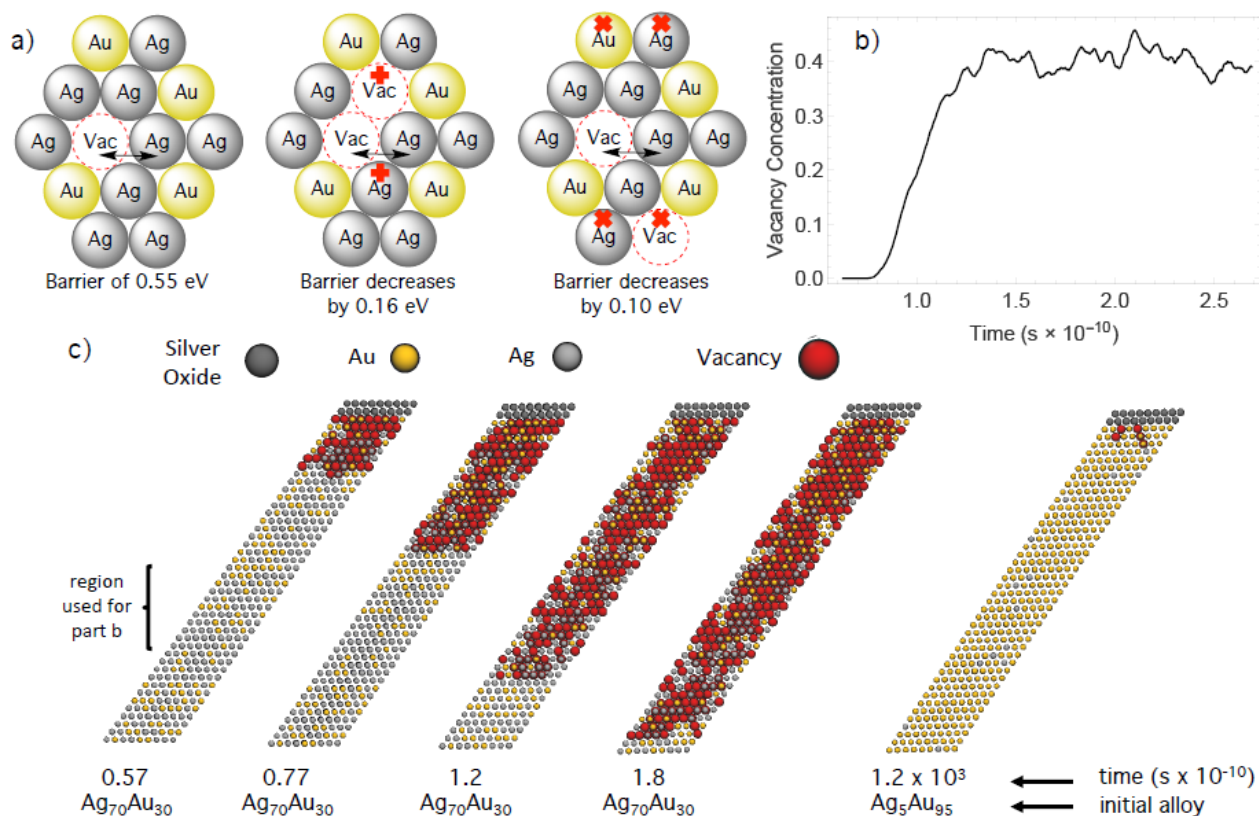


**Figure 8.5** Kinetic Monte Carlo simulations demonstrating the effect of vacancy concentration on Ag diffusion: **a)** Diagram showing schematically how the vacancy diffusion barrier depends on only two factors: the number of vacancies that are nearest-neighbors to the transition state (sites next to the diffusing atom are marked with red crosses +), and the number of vacancies that are opposite these nearest-neighbor positions from the transition state (sites opposite to the diffusing atom are marked with red X). **b)** vacancy concentration in 10 layers of material as a function of time, from kinetic Monte Carlo, with some mild smoothing; **c)** selected configurations from kinetic Monte Carlo for Ag<sub>70</sub>Au<sub>30</sub> and Ag<sub>5</sub>Au<sub>95</sub> alloys.

The kMC simulations consisted of an alloy, initially Ag<sub>70</sub>Au<sub>30</sub>, in contact with a model of silver oxide at one end, and with a vacancy annihilation mechanism (simulating vacancy



diffusion farther into the material) at the other end. Ag atoms at the metal-oxide interface were allowed to hop to the silver oxide layer, thereby creating vacancies in the alloy. As shown in Figures 8.5b and 8.5c, these vacancies propagate into the material as a sharp front, instead of as a smooth increase in the vacancy density, similar to the experimental observation. After an initial sharp increase, the vacancy concentration levels off at roughly 40%, comparable to the experimental vacancy concentration of 35% inferred from the final Ag-to-Au ratio of  $\text{Ag}_{40(\pm 3)}\text{Au}_{60}$ . Because vacancy-vacancy interactions are unfavorable, the vacancies spread out throughout the material, effectively causing Ag to leach from the  $\text{Ag}_{70}\text{Au}_{30}$  bulk, rather than from the partially dealloyed  $\text{Ag}_{40}\text{Au}_{60}$  layer. Interestingly, kMC calculations on a  $\text{Ag}_5\text{Au}_{95}$  starting alloy show that only a much smaller fraction of Ag ( $\sim 5\%$  in the  $\text{Ag}_5\text{-Au}_{95}$  case vs.  $\sim 50\%$  in the  $\text{Ag}_{70}\text{-Au}_{30}$  case) is removed due to the low vacancy concentration in the  $\text{Au}_{95}\text{-Ag}_5$  case. However, to be consistent with the experiment, one needs to postulate that the vacancies are stabilized and do not form larger clusters (pores) because the full porosity is only observed after the methanol- $\text{O}_2$  reaction step.

One way to explain that the continuous 3D porosity develops only after exposing the  $\text{O}_3$  treated alloy sample to the methanol- $\text{O}_2$  reaction mixture is that the initially formed small scale porosity (that is too small to be detected by FIB/X-SEM) is stabilized by atomic oxygen<sup>16,40,41</sup> Previous work from your group<sup>16</sup> showed that methanol- $\text{O}_2$  exposure almost completely reduces the Au and Ag oxides formed on Ag-Au alloys during ozone treatment. The lattice expansion (x1.5) that accompanies the oxidation of Ag (the residual Ag content in the Ag depleted alloy region is still 40 at.%) could further account for some of the missing Ag depletion related porosity. In any case, reduction of the Au/Ag oxides species upon exposure to the methanol- $\text{O}_2$  reaction mixture<sup>16</sup> would reverse the oxidation-induced Ag lattice

expansion and remove the stabilizing effect of oxygen, thus triggering rapid coarsening. Both explanations require that atomic oxygen diffuses through the Ag<sub>2</sub>O surface layer and into the bulk of the AgAu alloy sample. Indeed, extrapolation of the oxygen diffusion coefficient measured at 400-600°C<sup>42</sup> suggests that atomic oxygen can diffuse through bulk Ag at a rate of several tens of microns per hour at 150°C. Unfortunately, neither X-EDX (data shown in Figure 8.2, large noise level of the EDX O signal) nor XPS (insufficient spatial resolution) allowed us to directly measure the oxygen concentration and the Ag oxidation state in the Ag depleted AgAu alloy region. If oxygen indeed diffuses into the Ag depleted region of the alloy sample and forms an embedded Ag<sub>2</sub>O phase, then the accelerated Ag outward diffusion may also be the consequence of Ag diffusion through this embedded Ag oxide phase, similar to the situation in liquid metal dealloying<sup>43</sup>. The diffusion coefficient of Ag through Ag<sub>2</sub>O at ambient temperatures has recently been calculated to be  $1.2 \times 10^{-13}$  cm<sup>2</sup>/s based on the morphological evolution of Ag nanowires observed during exposure to an oxidative environment created by radiolysis of air. Unfortunately, the experiment did not allow the measurement of the actual sample temperature. Nevertheless, the reported diffusion value has at least the same order of magnitude as the diffusion coefficient calculated from our experimental observations ( $\sim 1.4 \times 10^{-12}$  cm<sup>2</sup>/s).

The observations reported in this work have several important implications: From a fundamental point of view, our results provide new insights into the mechanism of dealloying. There is evidence that the vacancy mediated Ag diffusion process discussed in this work is also active in wet chemistry dealloying. Both the presence of small pores within the ligaments and the observation of macroscopic sample shrinkage during dealloying<sup>44</sup> cannot be explained by the generally accepted coherent surface diffusion mediated

dealloying mechanism, but would be a natural consequence of the vacancy mediated dealloying mechanism.

From an application point of view, our work provides a new understanding of 3D open porous network formation. More specifically, our results demonstrate that alloy catalysts can undergo low-temperature surface-chemistry-driven large-scale compositional and morphological changes, which can be either desired or undesired. Our results also indicate that dilute alloy catalysts with a more reactive minority component such as  $\text{Ag}_{0.03}\text{Au}_{0.97}$  alloys are more resilient against these large-scale compositional changes. Finally, we speculate that a nanoporous catalyst architecture is intrinsically more stable against surface-chemistry-driven large-scale compositional changes because the confinement provided by nanoscale ligaments limits the reservoir available for surface-chemistry induced phase segregation.

## **8.5 Conclusions**

Our experiments reveal that ozone exposure of  $\text{Ag}_{70}\text{Au}_{30}$  alloy samples at  $150^\circ\text{C}$  triggers fast Ag outward diffusion leading to the formation of micrometer thick  $\text{Ag}_2\text{O}$  surface films accompanied by Ag depletion in a near-surface alloy region of similar thickness. Some isolated nano-pores, mostly near the bottom of the Ag depletion region, can be found after the  $\text{O}_3$  exposure, but the full extent of Ag depletion-induced porosity becomes evident only after subsequent exposure to a methanol- $\text{O}_2$  mixture. The width of the Ag depletion region follows the square-root time dependence predicted by Fick's law, but the Ag diffusion coefficient ( $\sim 1.4 \times 10^{-12} \text{ cm}^2/\text{s}$ ) calculated from the observed morphological changes is many

orders of magnitude higher than the reported values for the Ag diffusion coefficient. The oxidation-induced Ag outward diffusion results in a Ag<sub>2</sub>O surface film and void formation, thus resembling the nano-Kirkendall phenomena previously reported for Ag/Au nanowires and nanoparticles, with the difference that the involved length scales are 10-100 times larger. Possible explanations for the faster than expected Ag outward diffusion include the presence of non-equilibrium vacancy concentrations by Ag-O reaction-driven vacancy injection at the Ag<sub>2</sub>O/Ag-Au alloy interface and/or Ag diffusion through a Ag oxide phase embedded in the Ag depleted alloy region.

## 8.6 Supporting Information

**Table 8.1** XPS results: Au and Ag contents (C and O were not taken into account) for the Ag<sub>70</sub>-Au<sub>30</sub> bulk sample under different conditions.

Sample	Ag3d (%)	BE (eV)	Au4f (%)	BE (eV)
No treatment	71.51	368.28	28.49	84.35
Ozone treatment: Black layer	100	367.79	0	
Ozone treatment; Below black layer	56.71	368.2	43.29	84.47 (+shoulder at 85.6)
Reaction: Grey powder	100	368.23	0	
Reaction: Below grey powder	55.36	368.28	44.64	84.34

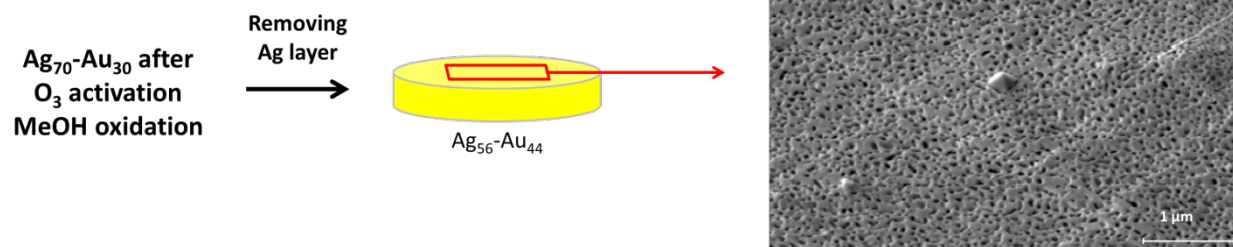


**Figure 8.6** Imaging the formation of nanoporosity: SEM image of top surface of the catalyst below the 'greyish' powder, highlighting the extent of the nanoporous network over the whole surface.

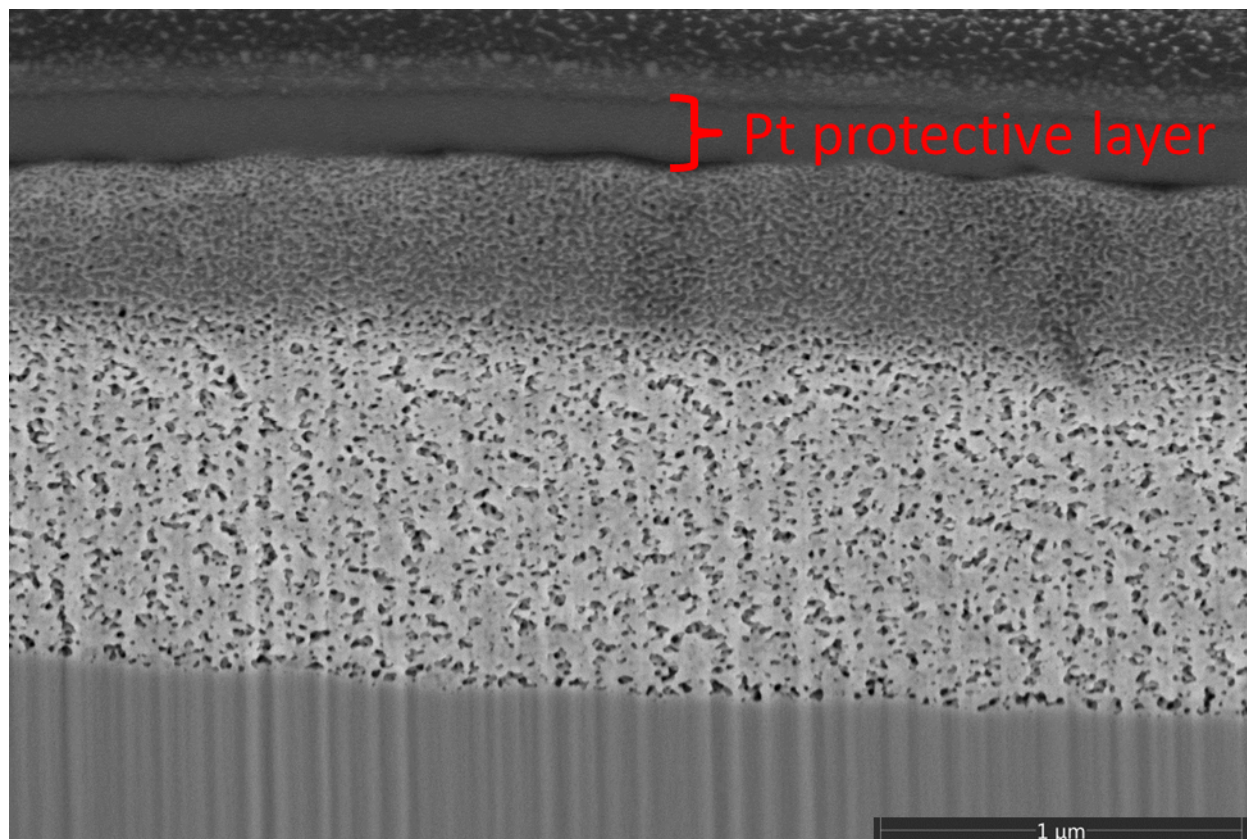


**Figure 8.7** Formation of porosity in a bulk Ag<sub>70</sub>Au<sub>30</sub> alloy via wet chemistry etching in HNO<sub>3</sub> solution (2 min of treatment) showing a completely different porous structure than in the case of ozone treatment. The upper part corresponds to the Pt protective layer which infiltrated in the porous network.

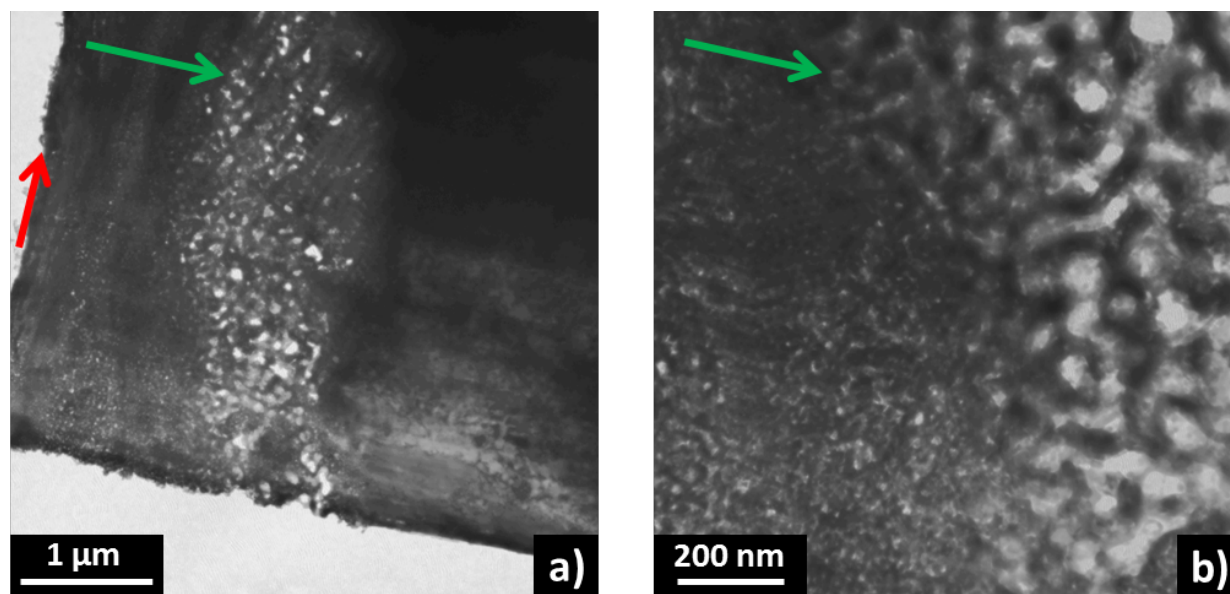


**Figure 8.8** TEM analysis of the Ag-depleted region of an ozone-treated Ag<sub>70</sub>-Au<sub>30</sub> sample. Preparation of the TEM sample by the FIB lift-out technique obviously triggered changes of the morphology towards the three-dimensional interconnected porous network structure with pores up to ~100 nm which normally is only observed after subsequent methanol/O<sub>2</sub> exposure at 150°C. The observed morphology change indicates FIB-induced oxygen desorption which destabilizes the original small scale porosity. While the experiment did not allow direct imaging of the proposed small scale porosity, the FIB induced large scale porosity formation still demonstrates the presence of “hidden” porosity after the ozone treatment (scales bars are 1 μm (a) and 200 nm (b)). The etching direction is indicated by the green arrow. The Pt protective layer is located on the upper part and indicated by the red arrow on a).

## 8.7 References

1. Vej-Hansen, U. G.; Rossmeisl, J.; Stephens, I. E. L.; Schiøtz, J. Correlation Between Diffusion Barriers and Alloying Energy in Binary Alloys. *Phys. Chem. Chem. Phys.* **2016**, *18*, 3302-3307.
2. Götsch, T.; Stöger-Pollach, M.; Thalinger, R.; Penner, S. The Nanoscale Kirkendall Effect in Pd-Based Intermetallic Phases. *J. Phys. Chem. C* **2014**, *118*, 17810-17818.
3. Xia, J.; Ambrozik, S.; Crane, C. C.; Chen, J.; Dimitrov, N. Impact of Structure and Composition on the Dealloying of  $\text{Cu}_x\text{Au}_{(1-x)}$  Bulk and Nanoscale Alloys. *J. Phys. Chem. C* **2016**, *120*, 2299-2308.
4. Taranovskyy, A.; Guézo, S.; Matsushima, H.; Gründer, Y.; Magnussen, O. M. Studies of Electrochemical Surface Alloying and Dealloying by In Situ High-Speed STM. *Phys. Chem. Chem. Phys.* **2012**, *14*, 10579-10588.
5. Malacrida, P.; Sanchez Casalongue, H. G.; Masini, F.; Kaya, S.; Hernández-Fernández, P.; Deiana, D.; Ogasawara, H.; Stephens, I. E. L.; Nilsson, A.; Chorkendorff, I. Direct Observation of the Dealloying Process of a Platinum–Yttrium Nanoparticle Fuel Cell Cathode and its Oxygenated Species During the Oxygen Reduction Reaction. *Phys. Chem. Chem. Phys.* **2015**, *17*, 28121-28128.
6. Carenco, S.; Tuxen, A.; Chintapalli, M.; Pach, E.; Escudero, C.; Ewers, T. D.; Jiang, P.; Borondics, F.; Thornton, G.; Alivisatos, A. P.; et al. Dealloying of Cobalt from CuCo Nanoparticles under Syngas Exposure. *J. Phys. Chem. C* **2013**, *117*, 6259-6266.
7. Gould, A. L.; Heard, C. J.; Logsdail, A. J.; Catlow, C. R. A. Segregation Effects on the Properties of  $(\text{AuAg})_{147}$ . *Phys. Chem. Chem. Phys.* **2014**, *16*, 21049-21061.
8. Montemore, M. M.; Madix, R. J.; Kaxiras, E. How Does Nanoporous Gold Dissociate Molecular Oxygen? *J. Phys. Chem. C* **2016**, *120*, 16636-16640.
9. Montemore, M. M.; Cubuk, E. D.; Klobas, J. E.; Schmid, M.; Madix, R. J.; Friend, C. M., Kaxiras, E. Controlling O Coverage and Stability by Alloying Au and Ag. *Phys. Chem. Chem. Phys.* **2016**, *18*, 26844-26853.
10. Erlebacher, J.; Aziz, M. J.; Karma, A.; Dimitrov, N.; Sieradzki, K. Evolution of Nanoporosity in Dealloying. *Nature* **2001**, *410*, 450-453.
11. Biener, J.; Hodge, A. M.; Hayes, J. R.; Volkert, A. V.; Zepeda-Ruiz, L. A.; Hamza, A. V.; Abraham, F. F. Size Effects on the Mechanical Behavior of Nanoporous Au. *Nano Lett.* **2006**, *6*, 2379-2382.



12. Kucheyev, S. O.; Hayes, J. R.; Biener, J.; Huser, T.; Talley, C. E.; Hamza, A. V. Surface-Enhanced Raman Scattering on Nanoporous Au. *Appl. Phys. Lett.* **2006**, *89*, 053102.
13. Xu, C.; Su, J.; Xu, X.; Liu, P.; Zhao, H.; Tian, F.; Ding, Y. Low Temperature CO Oxidation over Unsupported Nanoporous Gold. *J. Am. Chem. Soc.* **2007**, *129*, 42-43.
14. Wittstock, A.; Zielasek, V.; Biener, J.; Friend, C. M.; Bäumer, M. Nanoporous Gold Catalysts for Selective Gas-Phase Oxidative Coupling of Methanol at Low Temperature. *Science* **2010**, *327*, 319-322.
15. Fan, H. J.; Gosele, U.; Zacharias, M. Formation of Nanotubes and Hollow Nanoparticles Based on Kirkendall and Diffusion Processes: a Review. *Small* **2007**, *3*, 1660-1671.
16. Zugic, B.; Wang, L.; Heine, C.; Zakharov, D. N.; Lechner, B. A. J.; Stach, E. A.; Biener, J.; Salmeron, M.; Madix, R. J.; Friend, C. M. Dynamic Restructuring Drives Catalytic Activity on Nanoporous Gold-Silver Alloy Catalysts. *Nat. Mater.* **2016**
17. Kresse, G.; Furthmüller, J. Efficiency of Ab-initio Total Energy Calculations for Metals and Semiconductors Using a Plane-Wave Basis Set. *Comput. Mater. Sci.* **1996**, *6*, 15-50.
18. Kresse, G.; Hafner, J. Ab Initio Molecular Dynamics for Liquid Metals. *Phys. Rev. B* **1993**, *47*, 558-561.
19. Perdew, J.; Burke, K.; Ernzerhof, M. Generalized Gradient Approximation Made Simple. *Phys. Rev. Lett.* **1996**, *77*, 3865-3868.
20. Tkatchenko, A.; Scheffler, M. Accurate Molecular van der Waals Interactions from Ground-State Electron Density and Free-Atom Reference Data. *Phys. Rev. Lett.* **2009**, *102*, 073005.
21. Blöchl, P. E. Projector Augmented-Wave Method. *Phys. Rev. B* **1994**, *50*, 17953.
22. Kresse, G.; Joubert, D. From Ultrasoft Pseudopotentials to the Projector Augmented-Wave Method. *Phys. Rev. B* **1999**, *59*, 1758-1774.
23. Henkelman, G.; Uberuaga, B. P.; Jónsson, H. A Climbing Image Nudged Elastic Band Method for Finding Saddle Points and Minimum Energy Paths. *J. Chem. Phys.* **2000**, *113*, 9901-9904.
24. Leetmaa, M.; Skorodumova, N. V. KMCLib: a General Framework for Lattice Kinetic Monte Carlo (KMC) Simulations. *Comput. Phys. Commun.* **2014**, *185*, 2340-2349.
25. Waterhouse, G. I. N.; Bowmaker, G. A.; Metson, J. B. Oxidation of a Polycrystalline Silver Foil by Reaction with Ozone. *Appl. Surf. Sci.* **2001**, *183*, 191-204.

26. Falcucci, G.; Montessori, A.; Succi, S.; Zugic, B.; Barroo, C.; Biener, M. M.; Biener, J.; Bell, D. C.; Kaxiras, E. Mapping Reactive Flow Patterns in Monolithic Nanoporous Catalysts. *Microfluid. Nanofluid.* **2016**, *20*, 105.
27. Chen-Wiegart, Y.-C. K.; Wang, S.; Lee, W.-K.; McNulty, I.; Voorhees, P. W.; Dunand, D. C. *In Situ* Imaging of Dealloying During Nanoporous Gold Formation by Transmission X-Ray Microscopy. *Acta Mater.* **2013**, *61*, 1118-1125.
28. Renner, F. U.; Ankah, G. N.; Bashir, A.; Ma, D.; Biedermann, P. U.; Shrestha, B. R.; Nellesen, M.; Khorashadizadeh, A.; Losado-Pérez, P.; Duarte, M. J.; et al. Star-Shaped Crystallographic Cracking of Localized Nanoporous Defects. *Adv. Mater.* **2015**, *27*, 4877-4882.
29. Chung, Y.-C.; Kim, C. K.; Wuensch, B. J. Calculation of the Contribution to Grain Boundary Diffusion in Ionic Systems that Arises from Enhanced Defect Concentrations Adjacent to the Boundary. *J. Appl. Phys.* **2000**, *87*, 2747-2752.
30. Suzuki, R. O.; Ogawa, T.; Ono, K. Use of Ozone to Prepare Silver Oxides. *J. Am. Ceram. Soc.* **1999**, *82*, 2033-2038.
31. Biener, J.; Wittstock, A.; Zepeda-Ruiz, L. A.; Biener, M. M.; Zielasek, V.; Kramer, D.; Viswanath, R. N.; Weissmüller, J.; Bäumer, M.; Hamza, A. V. Surface-Chemistry-Driven Actuation in Nanoporous Gold. *Nat. Mater.* **2009**, *8*, 47-51.
32. Imamura, S.; Ikebata, M.; Ito, T.; Ogita, T. Decomposition of Ozone on a Silver Catalyst. *Ind. Eng. Chem. Res.* **1991**, *30*, 217-221.
33. Yu, L.; Yan, Z.; Cai, Z.; Zhang, D.; Han, P.; Cheng, X.; Sun, Y. Quantitatively In-Situ Imaging Silver Nanowire Hollowing Kinetics. *Nano Lett.* **2016**, *16*, 6555-6559.
34. Lewis, E. A.; Slater, T. J. A.; Prestat, E.; Macedo, A.; O'Brien, P.; Camargo, P. H. C.; Haigh, S. J. Real-Time Imaging and Elemental Mapping of AgAu Nanoparticle Transformations. *Nanoscale* **2014**, *6*, 13598-13605.
35. Mallard, W. C.; Gardner, A. B.; Bass, R. F.; Slifkin, L. M. Self-Diffusion in Silver-Gold Solid Solutions. *Phys. Rev.* **1963**, *129*, 617-625.
36. Bukaluk, A. Determination of the Activation Energy of Ag Diffusion through Grain Boundaries of Thin Au Films by Using AES in a Simplified Accumulation Method. *Appl. Surf. Sci.* **1988-89**, *35*, 317-326.
37. Bukaluk, A. AES Depth Profile Studies of Interdiffusion in Thin Polycrystalline Au-Ag Multilayer Films. *Appl. Surf. Sci.* **1990**, *45*, 57-64.
38. Peterson, N. L. Self-Diffusion in Pure Metals. *J. Nucl. Mater.* **1978**, *69-70*, 3-37.

39. Megchiche, E. H.; Mijoule, C.; Amarouche, M. First Principles Calculations of Vacancy-Vacancy Interactions in Nickel: Thermal Expansion Effects. *J. Phys. Condens. Matter.* **2010**, *22*, 485502.
40. Biener, J.; Wittstock, A.; Biener, M. M.; Nowitzki, T.; Hamza, A. V.; Bäumer, M. Effect of Surface Chemistry on the Stability of Gold Nanostructures. *Langmuir* **2010**, *26*, 13736-13740.
41. Cattarin, S.; Kramer, D.; Lui, A.; Musiani, M. M. Preparation and Characterization of Gold Nanostructures of Controlled Dimension by Electrochemical Techniques. *J. Phys. Chem. C* **2007**, *111*, 12643-12649.
42. Outlaw, R. A.; Sankaran, S. N.; Hoflund, G. B.; Davidson, M. R. Oxygen Transport Through High-Purity, Large-Grain Ag. *J. Mater. Res.* **1988**, *3*, 1378-1384.
43. McCue, I.; Gaskey, B.; Geslin, P.-A.; Karma, A.; Erlebacher, J. Kinetics and Morphological Evolution of Liquid Metal Dealloying. *Acta Mater.* **2016**, *115*, 10-23.
44. Parida, S.; Kramer, D.; Volkert, C. A.; Rösner, H.; Erlebacher, J.; Weismuller, J. Volume Change During the Formation of Nanoporous Gold by Dealloying. *Phys. Rev. Lett.* **2006**, *97*, 035504.